2012

Development and validation of an electron Monte Carlo model for the Elekta Infinity accelerator

Guy Merritt Harris

Louisiana State University and Agricultural and Mechanical College

Follow this and additional works at: https://digitalcommons.lsu.edu/gradschool_theses

Part of the Physical Sciences and Mathematics Commons

Recommended Citation

DEVELOPMENT AND VALIDATION OF AN ELECTRON MONTE CARLO MODEL FOR THE ELEKTA INFINITY ACCELERATOR

A Thesis

Submitted to the Graduate Faculty of the
Louisiana State University and
Agricultural and Mechanical College
in partial fulfillment of the
requirements for the degree of
Master of Science

in

The Department of Physics and Astronomy

by
Guy Merritt Harris
B.S., Georgia Institute of Technology, 2009
August 2012

Acknowledgements

Table of Contents

List of Tables

List of Figures

ix

Abstract

Purpose: The purpose of this work was to create a Monte Carlo BEAMnrc/EGSnrc model of the electron beam delivery system of an Elekta Infinity linear accelerator that could simulate electron percent depth doses and off-axis profiles to within a specified tolerance criteria, $\pm 2\%$ relative quantities (D_{max}) or 1 mm distance to agreement (DTA), when compared to a subset of the measured commissioning data for the accelerator's existing set of scattering foils and applicators.

Methods: The model was constructed with the BEAMnrc user code from vendor provided schematics and correspondence with manufacturer engineers under a nondisclosure agreement. The spatial distribution of the initial electron source was derived by matching the large field (open-insert 25x25 cm^2 applicator) cross beam profiles calculated by the model with the measured data. The measured data was re-sampled and symmetrized about the central axis (CAX) and the simulation data was smoothed before the two data sets were normalized to reference values along the CAX. The two data sets were compared to test to the hypothesis.

Results: The model was able to meet the tolerance criteria (2% of D_{max} or 1 mm DTA) for all large-field %DD curves. The model was unable to meet the criteria for any large field, shallow depth cross-beam profiles. The low energy (7-, 9-MeV) and high energy (16-, 20-MeV) models over-predict off-axis dose. The medium energy (10-, 11-, 13-MeV) beam model under-predict off-axis dose. These off-axis dose discrepancies were not pronounced at smaller field-sizes (6x6 and 14x14 cm^2) for the subset of the clinical beam energies (7-, 13-, 20-MeV) that were compared.

Conclusions: The Monte Carlo model of the Elekta Infinity electron beam delivery system could not simulate the considered subset of measured beam data to within the tolerance criteria of the study. The model could accurately reproduce the smaller field-sizes that were compared but could not reproduce the measured large field data. The large-field off-axis dose discrepancies observed with the medium beam energies (10-, 11-, 13-MeV) could be resolved by introducing a small initial angular spread ($\sim 2°$) to the incident electron source of the model.

Chapter 1
Introduction/Background

1.1 Electron Beam Therapy

1.1.1 History and Clinical Use

Clinical electron beams have played an important role in radiation therapy for over half a century. The early treatment machines were developed in the 1930s and 1940s and using Van de Graaff generators. This technology was proceeded by betatron accelerators, which allowed for higher electron energies. Today, microwave-based accelerators have become the clinical standard (Karzmark 1984). Figure 1.1 shows a generic percent depth-dose (%DD) curve for a clinically acceptable electron beam, with a most probable beam energy of 10-MeV, as defined by ICRU report 35 (1984) . This curve represents normalized dose as a function of depth in water along the central axis (CAX) of the beam.
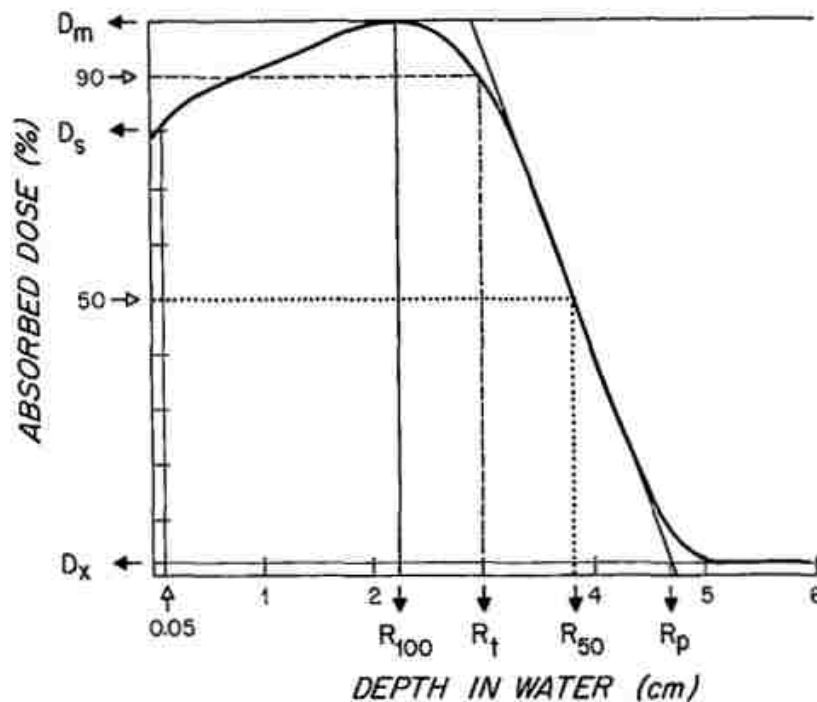
Figure 1.1: Parameters used to characterize electron beam central-axis depth-dose curve. These parameters are discussed in Section 1.1.2. Figure from ICRU report 35 (1984).

1

The finite range and sharp distal falloff distal of the electron beam provide unique clinical characteristics. In particular, electrons offer advantages over photons when the clinical goal is the treatment of superficial sites while sparing the distal tissues of dose. However, these clinically desirable properties of electron dose distributions begin to degrade as the beam energy exceeds 20-MeV, above which the lateral penumbra, distal falloff, and Bremsstrahlung production increase rapidly (see Figure 1.2). Therefore, typical electron beam energies currently in use at radiation therapy centers range from about 6-MeV to 20-MeV.

AAPM Task Group No. 70 outlines several clinical sites where the clinical properties of electron beams have shown to be advantageous (Gerbi et al. 2009). Electrons are often used to deliver boost dose to surgical scars for post-lumpectomy breast treatments following tangential photon fields. Electron arc therapy is an excellent choice for delivering uniform dose to curved surfaces, such as the treatment of double post-mastectomy chest walls. Electron treatment is useful for total skin and total scalp where the goal is to deliver a uniform dose to the skin while sparing the deeper structures. Electrons have played an important role in the treatment of superficial sites in the head and neck region. Electron therapy is the primary treatment for retinoblastoma patients that have a chance for vision preservation in the afflicted eye. Additionally, the matching of photon and electron fields have greatly reduced both the acute, and more importantly, the late complications associated with craniospinal irradiation of pediatric patients.

1.1.2   Basic Interactions and Dosimetric Properties

The clinically applicable section of the beam delivers a reasonably uniform dose of radiation to the tissues that are within the therapeutic range (R_t), recommended to be defined as the depth that receives 90% of the dose (R_{90}) by Khan et al. (1991) in AAPM Task Group No. 25. The physics governing the interactions (mainly, multiple coulomb scattering and collisional energy loss) of electrons result in a sharp distal falloff from R_{90} to the 10% of the maximum dose, R_{10}. The practical range of the beam, R_p, corresponds to the intersection of a line tangent to the point of inflection ($\sim R_{50}$) along the distal falloff of the %DD curve. As the finite range of the electron beam is reached, the %DD curve approaches a horizontal asymptote as depth increases. This asymptote
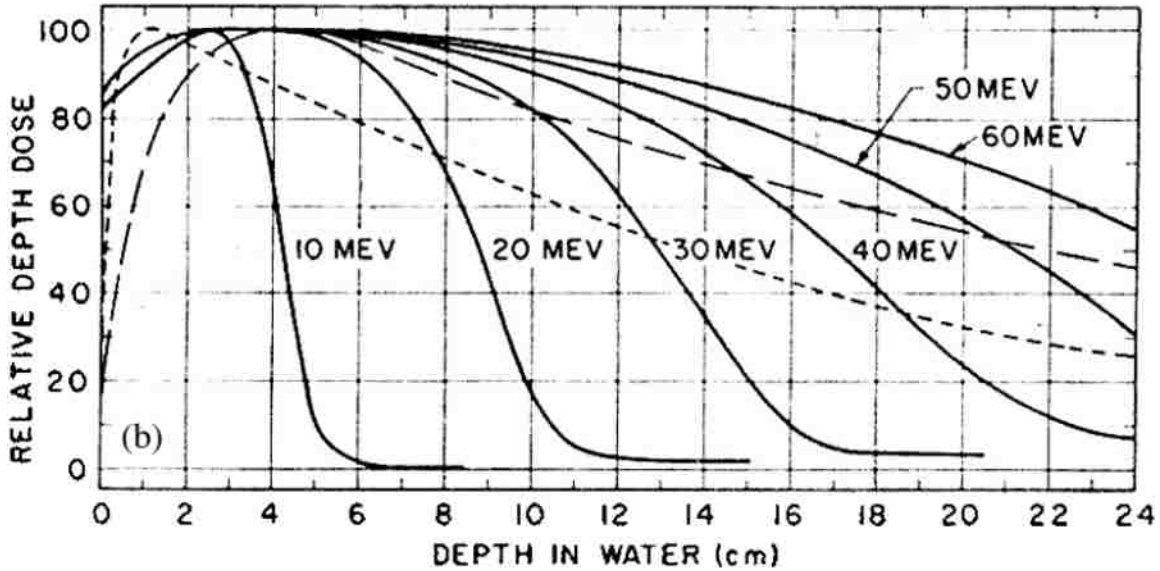
Figure 1.2: %DD curves as a function of electron energy. Figure from Loevinger, Karzmark, and Weissbluth (1961).
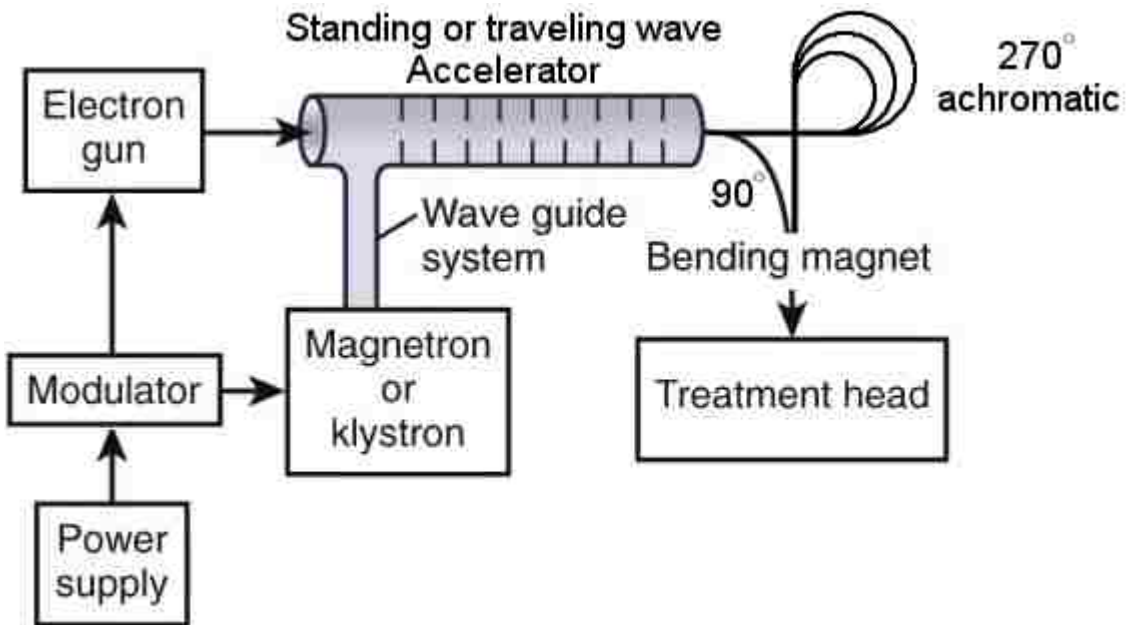
Figure 1.3: Block diagram of medical linear accelerator. Figure adapted from Khan (2010).

value, denoted D_x, is the dose contribution from bremsstrahlung photons generated primarily by the beam-line components. The parameters defined in this section are all of clinical importance and have been shown to be influenced by small changes in the scattering foils, beam collimation, source-to-surface distance (SSD), and beam energies (Hogstrom and Almond 2006).

1.1.3 Generation of Clinical Beam

The accelerated electron beams produced by modern medical linear accelerators are too narrow to be clinically useful. The most common approach for producing usable field sizes is to use direct the electron beam through a dual scattering foil system. The modern medical linear accelerator, shown in Figure 1.3, achieves microwave-based acceleration of electrons using either a magnetron or a klystron, with an accelerator structure, which is either traveling wave or standing wave depending on the manufacturer of the device. This accelerated electron beam is directed towards the patient plane by an achromatic bending magnet and leaves the vacuum environment of the acceleration system via a metal exit window.

A simplified example of the dual scattering foil system is shown in Figure 1.4. The primary foil, denoted in Figure 1.4, is a high-Z material of uniform thickness and is intended to scatter the initial electron beam into a broadened Gaussian distribution. The secondary foil, denoted in Figure 1.4, is constructed with lower-Z materials, such as aluminum, and has a varying thickness that decreases with distance from the CAX. This geometry results in a decrease in electron scatter as the distance from the CAX increases. The two foils combined effect results in a beam which is flat and symmetric over a large field size (a minimum of the diagonal field across the largest electron applicator) at isocenter, usually specified as approximately 100 cm from the exit window. One combination of primary foil and secondary foil cannot produce an acceptable broad and flat field for all clinical energies. Therefore, linear accelerator manufacturers generally design a set of scattering foils for a predetermined set of electron energies (Bieda 1999). Deviation from these beam energies can cause failure to achieve minimum acceptable flatness ($\pm 3\%$ of CAX value) and symmetry (2% of CAX value) as specified in AAPM Task Group No. 25 (Khan et al. 1991).
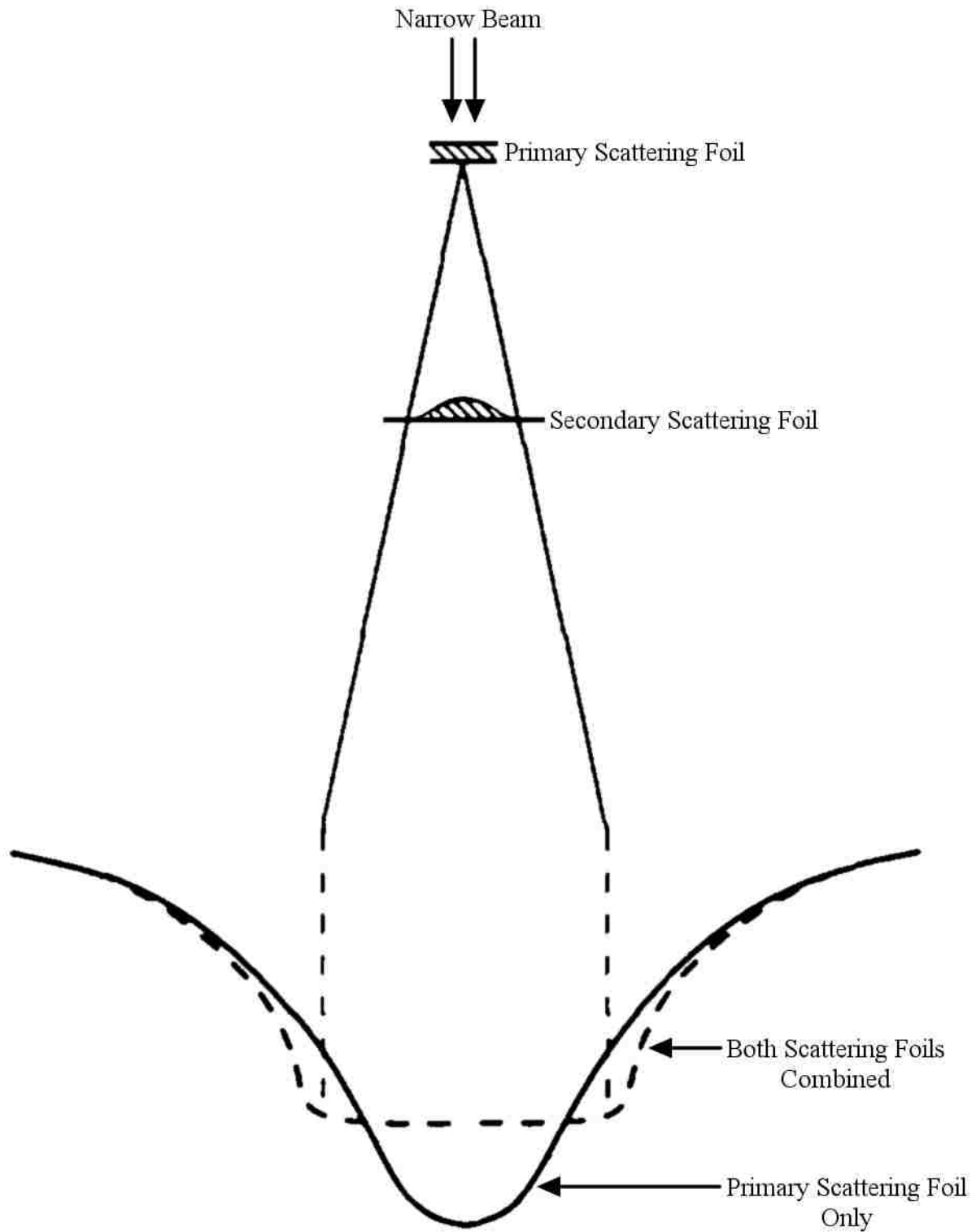
Figure 1.4: Dual scattering foil system. Figure adapted from Karzmark (1993).

This broadened beam is impacted by the position of the photon jaws. Side scatter equilibrium affects the penumbra of the field near the projection of the edges of the jaws, particularly at low beam energies. Additionally, scatter off and out through the edges of the photon jaws is most prominent at higher energies (Lax and Brahme 1980). Furthermore, electron scatter off the applicator system contributes to the shape of the off-axis dose profiles. To account for these effects, the jaw positions are different for each applicator/beam energy combination. Although these positions should be precalculated and optimized, sometimes a procedure is used where adjustments to the jaw positions are made during the acceptance of a new linear accelerator. These types of adjustments are not recommended without first looking at the radiation leakage outside of the field.
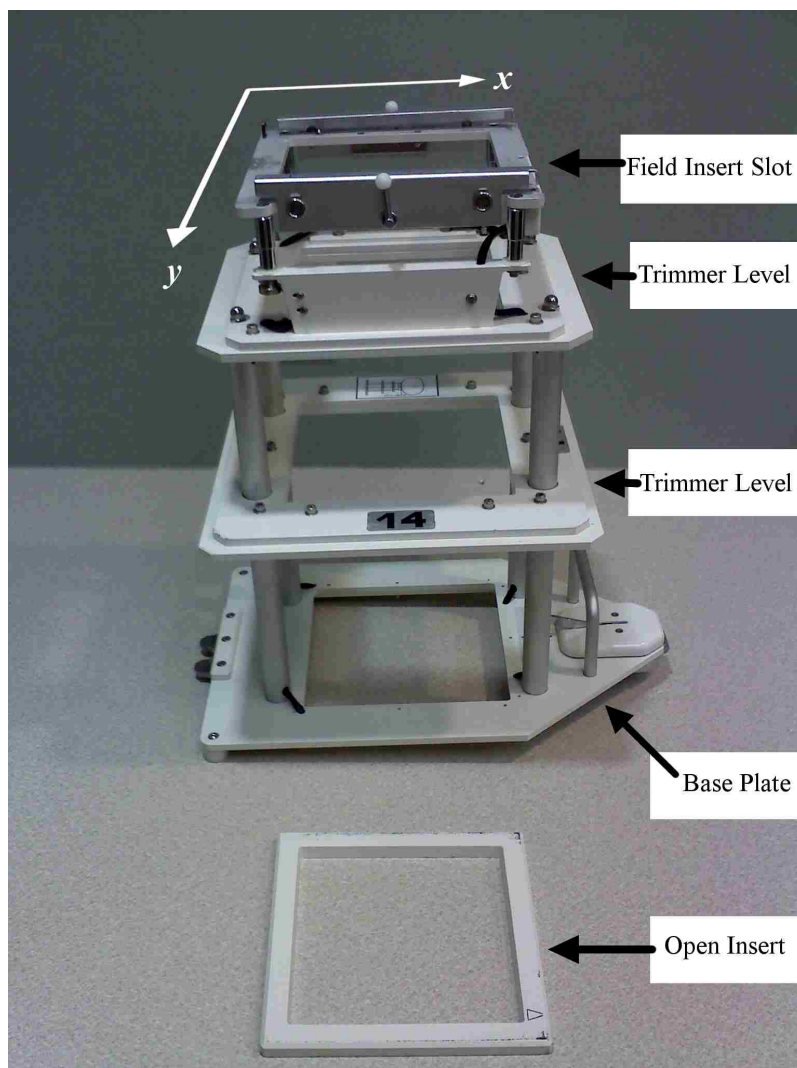
Figure 1.5: Elekta Infinity electron applicator (14x14 cm^2).

1.1.4 Ancillary Hardware

Since electrons scatter easily in air, additional beam collimation is needed near the patient surface to reduce lateral penumbra. The typical approach for this purpose has been to use an electron applicator (Elekta applicator shown in Figure 1.5). The electron applicator generally attaches to the bottom of the treatment head via a sliding or latching mechanism. The applicator consists of multiple trimmer bars constructed of high-Z material to prevent electrons from reaching beyond the desired field size. The patient surface (level of isocenter) and the downstream face of the applicator are separated by 5 cm of air. A removable collimator, or "insert", allows for definition of irregular field shapes.

1.2 Motivation for Study

Mary Bird Perkins Cancer Center (MBPCC) contracted a linear accelerator manufacturer, Elekta (Elekta Limited, Stockholm, Sweden), to provide five Elekta Infinity linear accelerators with unique requirements. MBPCC specified the electron beam energies such that the accelerators would have the following R_{90} depths: 2.0, 2.5, 3.0, 3.5, 4.0, 5.0, and 6.0 cm. This specification resulted in electron beam energies that were non-standard for the design of Elekta's dual scattering foil system. Additionally, MBPCC flatness requirements ($\pm 3\%$ for points 2 cm inside the 50% OAR along the principal axes and $\pm 4\%$ for points $2\sqrt{2}$ cm inside the 25% OAR along the diagonals of the field) for the electron beams of the Elekta accelerators were more stringent than industry standards. Furthermore, MBPCC required very strict tolerances for the dosimetric matching of each of the installed accelerators so that a single set of commissioning data could be used at the five MBPCC sites.

While Elekta was able to achieve all of MBPCC requirements, two of the three secondary scattering foils had to be modified in order to achieve the required beam flatness at the specified beam energies. Additionally, Elekta has needed to send factory engineers to each MBPCC site during machine installation to assist in the accelerator tuning process to match the dosimetry of the new machines with the original commissioning data. In order to make this process more efficient for future institutions with requirements similar to MBPCC, Elekta entered into a research agreement

7

with MBPCC to redesign the dual scattering foil system of the Elekta Infinity linear accelerator. Concurrently, the electron applicators for the Infinity accelerator will also be redesigned to provide optimal beam flatness for the newly designed scattering foil system while achieving optimal geometry and mass for ease of user operation and providing acceptable leakage.

In order to redesign beam-line components of an accelerator, certain materials and tools are necessary. First, fast analytical calculation tools are needed to quickly optimize the design of the components. Once initial designs are created, a more robust and intensive calculation tool is then needed to validate and fine-tune the analytical designs. This more intensive calculation tool is also needed to verify that the accelerator will meet the specifications for leakage as defined in international industry (IEC) standard 6061-2-1 (1998) after the beam-line components are redesigned. Monte Carlo modeling and simulation is considered the "gold standard" of intensive calculation tools in the field of radiation therapy (Rogers 2006). Before a Monte Carlo model of the beam line components can be used to validate analytical designs it must be benchmarked against the current system with the existing scattering foil system. Measured beam data of the current system is required to benchmark the Monte Carlo model and measured beam data taken with the redesigned components is needed to confirm the Monte Carlo results as well as the new beam-line components.

Analytical code to optimize the design of a scattering foil system for mono-energetic electron beams was developed by Green (1991). This work was updated by Kainz et al. (2005) include poly-energetic electron beams. These analytical codes are available for in-house use at MBPCC. Analytical methods to optimize the Elekta electron applicators are currently being developed from previous work by Hogstrom et al. (1990). Additionally, the necessary measured beam data for the current system was acquired during the commissioning of the first MBPCC Infinity accelerator. This work focused on delivering a Monte Carlo model of the existing electron beam delivery system of the Elekta Infinity linear accelerators that was validated by the measured beam data of the accelerators installed at the MBPCC sites.

1.3 Monte Carlo Simulations

Monte Carlo algorithms are often used to estimate solutions to problems for which analytical solutions are very difficult or impossible using deterministic methods. The Monte Carlo method can be used to model any statistical process that can be described by probability distributions. A process can be simulated by sampling the individual probability distribution of the events that compose the process with random numbers. Computers are able to generate pseudo-random numbers via an algorithm that uses one or more number seeds. Radiation transport is one such problem that is well-suited for simulation using Monte Carlo methods since an electron/photon shower is created by compiling a large number of repetitions of physical processes that follow probability distributions. When a sufficiently large number of particles are used, the average value of macro-scopic properties, like dose deposited in a material or fluence at a plane, can be determined. In radiation therapy, a benchmarked Monte Carlo model is generally accepted as the "gold standard" for electron-photon transport inside of complex three dimensional geometries (Rogers 2006).

1.3.1 EGSnrc and History

EGSnrc is a Monte Carlo transport code which grew out of the need to model electron-photon transport at high energies for the research occurring at the Stanford Linear Accelerator Center (SLAC). The Electron Gamma Shower (EGS) code was originally created for tasks such as the optimization and validation of calorimeters designed for use with charged particles reaching energies of several hundred-GeV (Guerra and Nelson 1988). The third revision of the code, EGS3, was released in 1978 and extended the low energy limits of the package. The extended low energy simulation abilities gave the code utility to other disciplines, such as the medical physics community (Nelson, Hirayama, and Rogers 1985). The fourth revision of the code, EGS4, was released to the public as an open source package in 1985. The current version of the code, the EGSnrc user package, made numerous improvements to the radiation transport that are listed in the manual (Kawrakow et al. 2011). The most notable improvements were improved low energy cross sections, a new multiple scattering theory, corrected Bremsstrahlung routines, and improved accuracy in the calculation of energy loss (Kawrakow et al. 2011). The improved energy loss accu-

racy is due mainly to the replacement of the original algorithm for condensed history electron step, `PRESTA-I`, with `PRESTA-II`. `PRESTA-II` improves the lateral and longitudinal corrections for elastic scattering to improve the description of the spread of electrons in a single condensed history (Kawrakow et al. 2011). The current version at the time of this publication, EGSnrc V4 2.3.2, was considered physically valid for photons, electrons, and positrons over a wide dynamic of energies. Kawrakow et al. (2011) documented that the transport of charged particles with kinetic energies from 10-keV to a few hundred GeV and photon energies from 1-keV to several hundred GeV were considered valid.

1.3.2   BEAMnrc and History

The original BEAM code came about as a solution to the difficulty presented in building the complex geometry of a linear accelerator using the EGS4 user code. BEAM was developed at the NRC in conjunction with the Ottawa Madison Electron Gamma Algorithm (OMEGA) project, a project to develop a dose calculation algorithm for electron beam radiotherapy using Monte Carlo methods. This code was documented and released for public use in 1995 by Rogers et al. (1995). The BEAM user package has been updated to BEAMnrc, to correspond with update of EGS4 to EGSnrc. The BEAMnrc user package includes a program, DOSXYZnrc, that can score dose from the output of a BEAMnrc simulation as well as other arbitrary sources in a user-defined phantom. The description of the source options in DOSXYZnrc are located in the manual (Walters, Kawrakow, and Rogers 2011). Another program, BEAMDP, provides the user with a powerful analysis tool capable of gathering information from the contents of the phase-space output of a BEAMnrc simulation without any additional Monte Carlo simulation. The BEAMnrc user package and its programs will be discussed in further detail in Section 2.3. Rogers et al. (1995) demonstrated the ability of the BEAM user code to accurately model the beam characteristics of several of the major manufacturers. Figure 1.6 shows agreement of simulation results with the measured data %DD curves for linear accelerators from three manufacturers over a wide range of clinical electron beam energies (6-MeV to 20-MeV). In each case, the accelerator geometry was simulated in the BEAM user code and the dose was scored in a DOSXYZ water phantom. The simulation of

the electron beams with a 10x10 cm^2 applicator was compared with measured data from various institutions.

The Therac20 accelerator shown in Figure 1.6 was scanning beam accelerator produced by AECL (Atomic Energy of Canada Limited, Chalk River, Ontario, Canada). Scanning beams achieve broad beams by quickly scanning a narrow electron beam across a field with a magnetic field. The Clinac 2100C accelerator shown in Figure 1.6 was a dual scattering foil accelerator produced by Varian (Varian Medical Systems, Palo Alto, CA). The SL75-20 accelerator shown in Figure 1.6 was a dual scattering foil accelerator produced by the radiotherapy division of Philips (Philips Medical Systems, Crawley, England). Elekta (Elekta Limited, Stockholm, Sweden) acquired the radiotherapy division of Philips in 1997. The Elekta Infinity linear accelerator studied in this work is based off of the design of the SL-series of accelerators.

1.3.3 Applications of BEAMnrc in Medical Physics

BEAMnrc models of linear accelerators have been used for a variety of medical physics applications. Ali et al. (2011) were able to validate an Elekta linear accelerator electron beam as a dose calculation tool using a two-source model (one point source for photon dose and one for electron dose) in DOSXYZnrc. Similarly, a method developed by Jiang, Kapur, and Ma (2000) that utilized a four-source model in BEAM was able produce accurate Monte Carlo distributions for the electron beams of a Varian Clinac 2100C. BEAMnrc simulations of a Siemens Oncor (Siemens Medical Solutions, Malvern, PA) accelerator head that was dismantled for additional measurements led to the discovery of an undetected magnetic field inside of the treatment head (Faddegon et al. 2009). BEAMnrc has also been used as a verification tool for cone-beam CT flat panel detectors (Kim et al. 2011) and the beam characteristics of multi-detector CT simulators (Kim et al. 2012).

Accurate Monte Carlo simulations containing all the beam-line components of an electron beam delivery system and one initial electron source have been difficult to achieve. The dosimetric properties of a clinical electron beam are sensitive to changes in the scattering foil geometry. Bieda, Antolak, and Hogstrom (2001) showed that off-axis profiles are most affected by the dis-
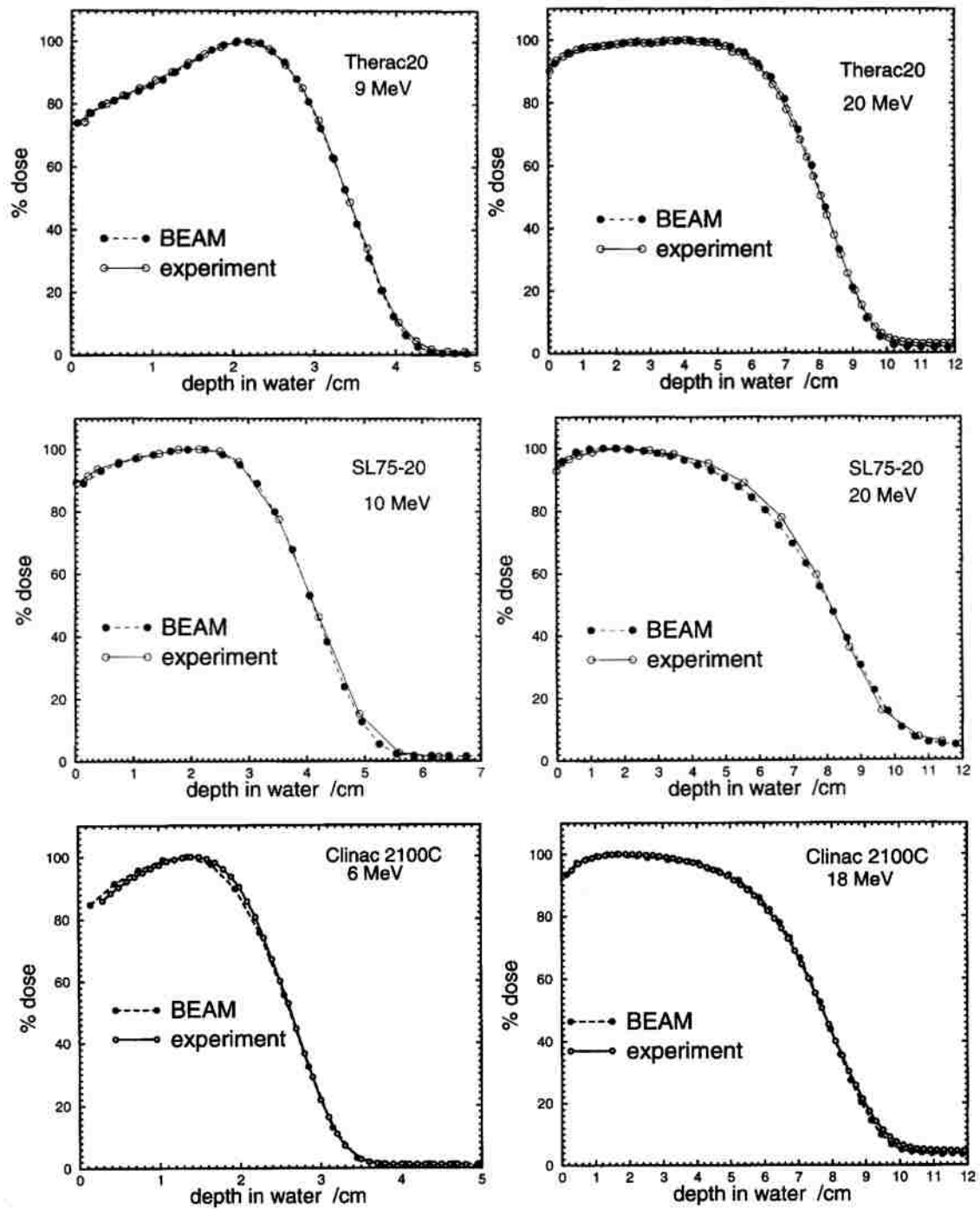
Figure 1.6: BEAM calculated %DD curves with 10x10 cm^2 applicators. Figure adapted from Rogers et al. (1995).

tance between the foils and the thickness of the secondary foil layers in a sensitivity study on slight variations of the scattering foil system geometry for a Varian Clinac 2100C. Further works have shown these effects are most pronounced at large fields (Schreiber and Faddegon 2005). Antolak, Bieda, and Hogstrom (2002) investigated the feasibility of using a one-source Monte Carlo model of the full beam-line of a Varian 2100C accelerator to reproduce a set of electron beam commissioning data. Although agreement was good, the Monte Carlo model was unable to reproduce all of the commissioning data. The failures of the model often occurred when attempting to match the measured beam data for the largest electron applicator (25x25 cm^2). Antolak, Bieda, and Hogstrom (2002) challenged the medical physics community to reproduce all measured commissioning data accurately with a one-source model of an accelerator's entire beam-line.

1.4 Hypothesis and Aims

The hypothesis of the study was that a Monte Carlo BEAMnrc/EGSnrc model of the electron beam delivery system of an Elekta Infinity linear accelerator could simulate electron percent depth doses and off-axis profiles to within a specified tolerance criteria, $\pm 2\%$ relative quantities (D_{max}) or 1 mm distance-to-agreement (DTA), when compared to a subset of the measured commissioning data for the accelerator's existing set of scattering foils and applicators. The subset of measured commissioning data is described in Section 2.2.2. The method used to determine if the simulated results meet the tolerance criteria of the hypothesis is discussed in Section 2.6.2.

The aim of this study was to simulate the complete geometry of the Elekta Infinity treatment head when the machine is in electron mode with the BEAMnrc user code for all clinical beam energies. Using schematics and information provided by the manufacturer under a nondisclosure agreement, the accelerator was modeled from the exit window of accelerating structure to the field insert of the electron applicator. The provided vendor schematics were validated with physical measurement whenever possible. The source parameters were determined for all seven clinically commissioned electron beams (7-, 9-, 10-, 11-, 13-, 16-, and 20-MeV) using the method described in Section 2.4.2. The simulation results were compared against the measured beam data for the subset of data listed in Section 2.2.2.

Chapter 2
Methods and Materials

2.1 Elekta Infinity Linear Accelerator

A Monte Carlo Model was constructed for the electron beam delivery system of the Elekta Infinity series linear accelerator. The machine, shown in Figure 2.1, contains a traveling wave accelerator structure, and the microwave system is magnetron-based. The accelerated electron beam ($22°$ above horizontal) is directed towards isocenter via a three-pole, achromatic slalom bending magnet arrangement (total bend angle= $112.5°$), shown in Figure 2.2(a). The electron beam then exits a nickel vacuum window and impinges upon the dual scattering foil system (schematic is

Figure 2.1: Elekta Infinity series linear accelerator in electron mode. Note the wall-mounted gantry with the 14x14 cm^2 applicator attached and that the imaging components are retracted during electron mode.

y

x

z

45° Down
Sector

45° Up
Sector

112.5° Down

Accelerator
at 22°

(a)

**Vacuum
Bellows**
Allows
movement
of Flight
Tube

**Bending
Magnet
Flight Tube**
Selects two
different
beam
trajectories.

**Flight Tube
Exit
Windows**
One
contains
xray target.

112.5° Down
Sector

**Flight Tube Output
Windows**
- **W** target in
photons position
-**Ni** window in
electrons position

Flight Tube
(shown in
electron position)

(b)

Primary Foil Carrier

Dual Port Primary Collimator
-**Hi-X** portion of flattening filter
-Open port

**Secondary Foil Carrier
(carrousel)**
-Electron secondary foils
-Lo-X flattening filter

Figure 2.2: Visualization of Elekta Infinity upper treatment head geometry and bending magnet system. (a) shows the achromatic slalom bending magnet arrangement. (b) shows the dual scattering foil arrangement. Figures adapted from Waldron (2002).

15

shown in Figure 2.2(b)). There are multiple levels of collimation downstream of the scattering foil system. The Infinity series accelerator has a Multi-Leaf Collimator (MLC) with a backup diaphragm as the upper photon jaw. The MLC motion is parallel to the cross-plane direction (perpendicular to the bending plane, the clinical X direction) when the machine is in the default position (collimator angle=0° and gantry angle=0°). Both the MLC leafs and the backup diaphragm have rounded, non-focused edges. The lower jaw is a divergent, focused photon jaw. The lower jaw motion is parallel to the in-plane direction (parallel to the bending plane, the clinical Y direction) when the machine is in the default position (collimator angle=0° and gantry angle=0°).

In electron delivery mode, the MLC leaves are "parked" (opened completely to a field size of 40 cm at isocenter), and the backup diaphragm is used as the initial beam collimation in the cross-plane direction. The lower photon jaws are used as the initial beam collimation in the in-plane direction. Because electron side scatter equilibrium impacts beam flatness (particularly at lower energies) and electron scatter from the photon collimators increases dose near the edge of the field, the photon collimator positions were adjusted during acceptance testing to achieve MBPCC flatness specification. Table 2.1 contains a list of the photon jaw settings for Elekta accelerators at MBPCC sites. The jaw positions listed in Table 2.1 define the half-field sizes at isocenter.

Table 2.1: Jaw Positions of Y/X photon jaws projected to isocenter for MBPCC Elekta Infinity Accelerators as a function of beam energy and applicator. Also indicated are primary and secondary foil positions for each beam energy. Note that the position of the X photon jaws is always greater because of the increased distance from isocenter.

Energy (MeV)	1° foil position	2° foil position	25x25cm^2 applicator (Y/X cm)	20x20cm^2 applicator (Y/X cm)	14x14cm^2 applicator (Y/X cm)	10x10cm^2 applicator (Y/X cm)	6x6cm^2 applicator (Y/X cm)
7	3	3	17.0/18.0	14.3/15.1	12.3/12.9	11.2/11.9	7.4/8.1
9	5	3	18.4/19.5	14.4/15.2	11.9/12.6	10.6/11.3	7.3/8.0
10	3	4	16.8/18.0	13.0/14.0	10.7/11.7	10.0/11.0	7.0/8.0
11	4	4	16.3/17.5	12.8/13.4	10.5/11.3	10.0/11.0	7.0/7.7
13	5	4	17.0/18.0	12.7/13.3	9.9/10.6	8.9/9.6	7.0/7.7
16	3	1	15.8/16.8	12.2/12.8	9.2/9.8	8.5/9.5	7.0/7.7
20	5	1	16.8/17.3	11.7/12.6	8.7/9.6	8.0/8.8	7.0/7.5

The columns labeled "1° foil position" and "2° foil position" in Table 2.1 correspond to the positions in the primary foil and secondary foil carriers (shown in Figure 2.2), respectively. The primary foil carrier rotates on an arc to allow five tantalum thickness options and one position with no tantalum (used during photon mode). The material thickness of each carrier position is varied by stacking tantalum layers of uniform thickness. The tantalum thickness provided by Elekta for each carrier position was verified by hand measurement of a removed primary foil carrier.

The secondary foil in carousel position 3 and the secondary foil in carousel position 1 were modified by Elekta engineers in order to meet the Mary Bird Perkins Cancer Center (MBPCC) acceptance criteria. The modification consisted of adding additional layers to the bottom of the existing foils. The secondary foil in carousel position 4 did not require modification. The three secondary foils were removed from the machine and measured by hand to verify the geometries provided in the vendor schematics and the dimensions of the additional layers.

The beam was then collimated by the trimmer bars of the electron applicator. The final and most downstream component is a frame that holds the field inserts. Each applicator has a beveled edge, square open-insert that defines the standard field-size. The machine has five applicator sizes available with open insert field-sizes of 6x6, 10x10, 14x14, 20x20, and 25x25 cm^2 at 95 cm SSD.

2.2 Measured Dosimetric Data

2.2.1 Commissioning Equipment and Protocol

The measured data used in this study was collected during the commissioning of an Elekta Infinity linear accelerator at the Gonzales campus of Mary Bird Perkins Cancer Center. Clinical medical physicists at MBPCC performed the accelerator commissioning using data collection procedure and techniques in accordance with the recommendations of AAPM Task Group No. 106 (Das et al. 2008).

The beam dosimetry measurements were performed with a three-dimensional dosimetry scanning system (Blue Phantom, IBA dosimetry, Bartlett, TN). A compact, 0.13-cm^3 volume ionization chamber (CC13, IBA dosimetry, Bartlett, TN) with a 3 mm air cavity radius and a 5.8 mm air

cavity length, was used for diagonal profiles and %DD curves. An electron diode (EFD^{3G}, IBA dosimetry, Bartlett, TN) with an active diameter of 2 mm was used to measure the cross-beam profiles. Because the effective depth of an ionization chamber measurement is uncertain at depths shallower than the cavity radius due to meniscus effects, measurements at depths less than 3 mm were excluded.

The measured data was collected using OmniPro-Accept 6.2 software. This software was used to operate the scanning dosimetry system, convert ion chamber readings to relative dose, and record the dosimetric information during the scans. Following acquisition, the data was exported to the Pinnacle[3] treatment planning system (Philips Medical Systems, Fitchburg, WI). The treatment planning system (TPS) imported and stored all of the commissioned beam data needed for commissioning of the electron therapy treatment planning model.

A computer program was written using MATLAB R2008b (MathWorks, Natick, MA) to extract all of the measured commissioning data from the treatment planning system. Sample extracted profiles were compared against original data in scanning software for verification. Because they are not needed as part of the Pinnacle[3] commissioning data set, diagonal profiles for the 25x25 cm^2 applicator were extracted directly from the dosimetry scanning software. Additionally, the measured data was re-sampled and symmetrized about the CAX axis before comparisons were made with the simulation results. This procedure is discussed in Section 2.2.3.

2.2.2 Measured Cross-Beam Profile Data Set

In-plane and cross-plane profiles were taken for each beam energy. Table 2.2 lists the depths of the cross-beam profiles for each beam energy. These profile depths were taken for all applicators at 100 cm SSD. Additional cross-beam profiles were taken with the 6x6 and the 14x14 cm^2 applicators to aid in constructing isodose plots which were used to validate the commissioning of the electron pencil beam dose algorithm in Pinnacle[3]. Table 2.3 lists the additional depths for each beam energy. These additional measurements were only taken in the cross-plane (X) direction. Cross-beam profiles were also measured at extended SSD (110 cm SSD) with the 10x10 and the 14x14 cm^2 applicators.

Table 2.2: Commissioned data for Elekta Infinity Accelerator

Energy (MeV)	Commissioned Profile Depths (cm)				Measured R_x depth (cm)
	$\sim R_{100}$	R_{90}	$\sim R_{70}$	$\sim R_{50}$	1-2 cm past R_p
7	1.0	2.0	2.5	2.8	5.5
9	1.3	2.5	3.1	3.5	6.3
10	1.5	3.0	3.6	4.0	6.9
11	1.7	3.5	4.1	4.5	7.6
13	2.0	4.0	4.8	5.3	8.5
16	2.5	5.0	6.0	6.6	10.0
20	3.0	6.0	7.5	8.3	12.1

Table 2.3: Additional cross-beam profile depths for the 6x6, 14x14 cm^2 applicators

Energy (MeV)	Profile depths (cm)				
7	0.5	3.5	–	–	–
9	0.5	4.3	–	–	–
10	0.5	1.0	4.9	–	–
11	0.5	1.0	5.6	–	–
13	0.5	1.0	1.5	6.5	–
16	0.5	1.0	1.5	2.0	8
20	0.5	1.0	1.5	2.0	10.1

Table 2.4: Diagonal profile depths for the 25x25cm^2 applicator

Energy (MeV)	Profile depth (cm)
7	1.0
9	1.0
10	1.0
11	2.0
13	2.0
16	2.0
20	2.0

The extended SSD data set consisted of cross-plane profiles taken at the depths listed in both Table 2.2 and Table 2.3. No in-plane (Y) profiles were recorded at 110 cm SSD. In addition to the commissioned data set, diagonal field profiles were recorded for the 25x25 cm^2 applicator. Table 2.4 lists the depth of the diagonal profile for each beam energy. Both diagonal field directions were measured for each beam energy.

The following subset of measured beam data was used for the validation of the Monte Carlo model of the Elekta Infinity linear accelerator:

1. CAX %DD curves at 100 cm SSD for open-insert applicators sizes 6x6, 14x14, and 25x25 cm^2.

2. In-plane and cross-plane off-axis profiles at measured commissioned depths listed in Table 2.2 for the 25x25 cm^2 open-insert applicator at 100 cm SSD.

3. Cross-beam profiles at 100 cm SSD for the open-insert 6x6 and 14x14 cm^2 applicators at the depths listed in Table 2.2 and Table 2.3.

4. Large-field diagonal profiles taken with the open-insert 25x25 cm^2 applicator at the depths listed in Table 2.4.

5. CAX %DD curves and cross-beam profiles at 110 cm SSD for the open-insert 14x14 cm^2 applicator at the depths listed in Table 2.2 and Table 2.3..

2.2.3   Re-Sampling and Symmetrization of Measured Data

Measured data was acquired using an adaptive sampling resolution of 5 mm in the low dose gradient regions and 1 mm in the high dose gradient regions. Additionally, systematic scanning system alignment errors were observed in some profiles. Therefore, all measured off-axis data was re-sampled and symmetrized by requiring 50% OAR points to be equidistance off-axis in order to reduce systematic errors and standardize the data set. First, the measured data were re-sampled (using linear interpolation between existing data points) such that the data points were centered

20
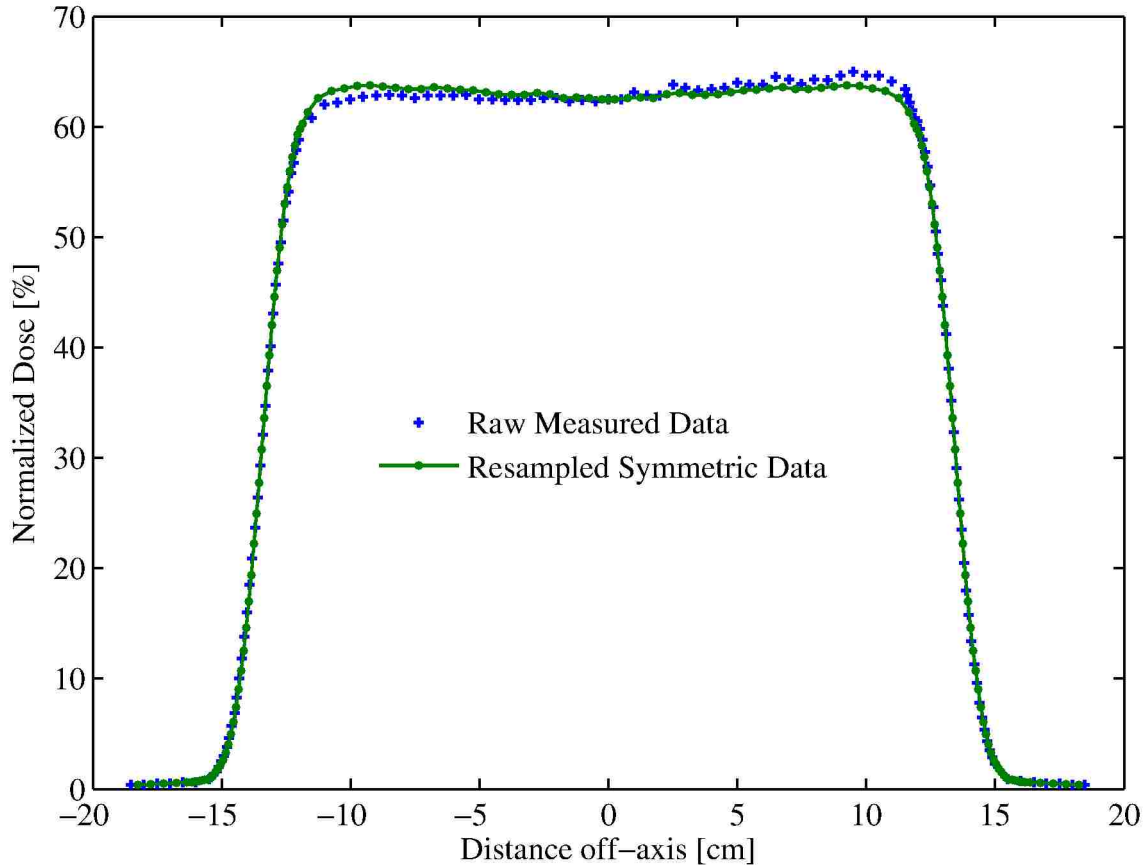
Figure 2.3: Example of re-sampling and symmetrization of a 7-MeV, 25x25 cm^2 cross-beam profile (100 cm SSD, depth z=2.8 cm).

about the CAX and positioned midway between the simulated data points of the DOSXYZnrc water phantom, which is described in Section 2.5.6. Then the average of the two points that were equidistance off-axis was taken and assigned to both points to symmetrize the measured data. The procedure applied to diagonal profiles averages the four points that were equidistance off-axis since there were scans recorded across both diagonals for the applicator. The results of the re-sampling and symmetrization procedure applied to a cross-beam profile are exemplified in Figure 2.3.

2.3 Monte Carlo Simulations

EGSnrc V4 2.3.2 and its user package, BEAMnrc V4 2.3.2, was the Monte Carlo radiation transport code used to model the Elekta Infinity linear accelerator electron beams. EGSnrc provided a versatile package that contains a robust model of the physics governing the radia-

tion transport of photons, electrons, and positrons. The physics for electron transport includes Moliere multiple scattering, inelastic scattering off of atomic electrons, positron annihilation, and bremsstrahlung photon production. The physics for photon transport includes Compton scattering, pair production, photoelectric effect, and optionally, Rayleigh scattering. Figure 2.4 provides a flow diagram for the algorithm construct of Monte Carlo radiation transport with the EGSnrc system.

2.3.1 Creating Models in BEAMnrc

As mentioned in Section 1.3.2, the development of BEAMnrc arose from a need to simplify the modeling of complex linear accelerator treatment head geometries with the EGS4 code. BEAM was designed to allow users to model treatment heads by breaking the geometry down into independent blocks, referred to as component modules (CMs). Each component module (CM) is designed to model a particular geometric shape, and the user orders these CMs along the z-axis inside of a module file that defines the overall structure of the linear accelerator. Descriptions of the original CMs included with the release of the BEAM code were given by Rogers et al. (1995).

To build an accelerator in the BEAMnrc user code, the user needs to start by determining the number and order of CMs necessary to construct the linear accelerator. Unique names must be given to each CM in order to avoid duplicate names even if a certain type of CM is used more than once in a model. Once the CM order and names are specified in the module file, the BEAM code will build the necessary EGSnrc code from the file by using the source code for each CM as specified in the HEN_HOUSE library. The actual geometry of each CM is determined by ASCII inputs into a master input file. The input file is also where the user specifies the type of radiation (photon or electron), the number of initial particles (`NCASE`), the geometry of the radiation source and its energy spectrum, `ECUT` and `PCUT` as discussed in Section 2.3.3, and other variables that are discussed in detail in the BEAMnrc user manual (Rogers, Walters, and Kawrakow 2011).

BEAMnrc is capable of outputting multiple phase-space files during a simulation of an accelerator build. A phase-space contains the charge, position, momentum, energy and LATCH information (discussed in Section 2.3.2) for all particles that cross a defined plane. BEAMnrc allows
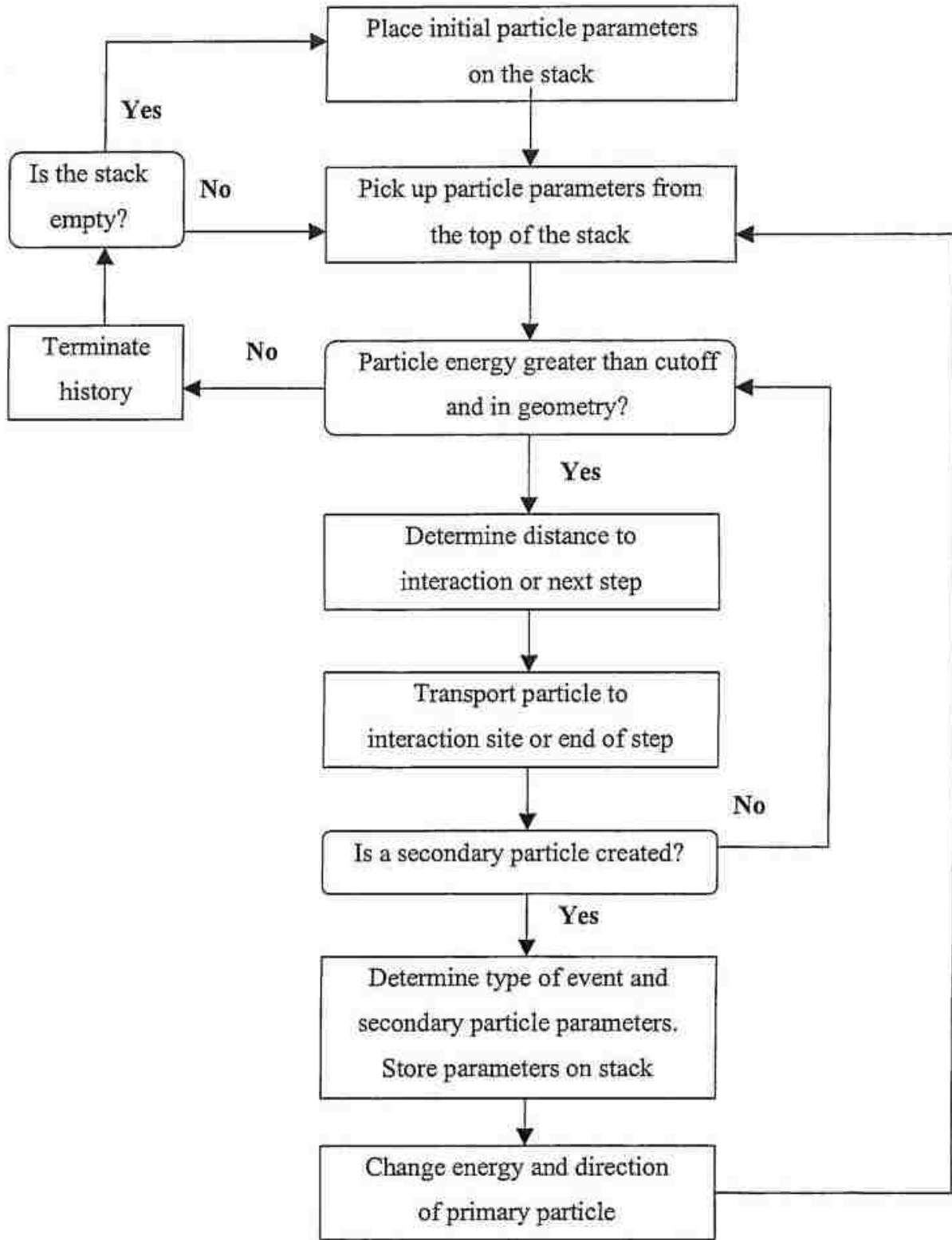
Figure 2.4: Flow chart for Monte Carlo radiation transport. Figure from Bieda (1999)

the user to simultaneously generate up to three phase-space files at any specified CM in the simulation. This phase-space can be used as the source of another BEAMnrc simulation or the source of a DOSXYZnrc simulation, a user code used for scoring absorbed dose in an arbitrary 3D phantom. It can also be divided into bins and analyzed using an axillary program, BEAMDP, a user code that can sort through the and analyze the particles contained in a phase-space. The phase-space can be useful as a model of a stationary and unchanging part of the treatment head. Scoring a phase-space behind fixed beam components, such as after the scattering foil system, to use as a source to the moving components in the treatment head, such as the photon jaw positions and the different applicators, can be more time efficient than rerunning a full simulation of the accelerator if computing resources are limited. When a phase-space source is used in either BEAMnrc or DOSXYZnrc, the particles in the phase-space will be recycled as many times as necessary to reach the user-defined `NCASE` for the simulation. The user has the option to reflect the phase-space about the CAX each time the phase space is recycled. This feature can aid in the reduction of statistical error but can also introduce systematic errors. If the phase-space is recycled too many times or systematic errors will be magnified in the final results of the simulation.

2.3.2 LATCH Variable

A particle's detailed history information can be recorded into a 32-bit variable called `LATCH`. The user can specify `LATCH` bit values to the different geometrical regions of an accelerator model. A particle can then be tagged with a geometry's `LATCH` bit if the particle has been in or interacted with the region. There are three `LATCH_OPTION` choices that determine if secondary particles inherit `LATCH` bit values from ancestor particles. If `LATCH_OPTION` is set to 1 then secondary particles do not inherit any `LATCH` information from ancestor particles. If `LATCH_OPTION` is set to 2 then secondary particles inherit the `LATCH` values corresponding to the regions any ancestor particles have passed through. If `LATCH_OPTION` is set to 3, then photons record and inherit the `LATCH` values for the regions where ancestor particles have interacted. All BEAMnrc simulations performed during this study used the default `LATCH_OPTION` value (`LATCH_OPTION=2`).

The particles can be filtered further by charge and type as well. The LATCH and charge/type filtering can be used when analyzing a phase-space with BEAMDP, to isolate dose components in a phantom using DOSXYZnrc, or to isolate particles for a phase-space input into another BEAMnrc simulation. In the case of clinical electron beam simulation, LATCH and charge filtering can be used for a number of purposes, such as determination of bremsstrahlung production from individual beam components. The LATCH variable was used in this work to aid in the development and refinement of the analytical optimization codes used to re-design to the beam line components. It was also used to quantify the electron scatter contribution to off-axis profiles for the lower-photon jaw and the backup MLC diaphragm. This contribution was found to be small enough that the photon jaw electron scatter effect could safely be left out of the analytical optimization codes.

2.3.3 EGSnrc Transport Parameters

There are several parameters in EGSnrc that correspond to energy thresholds for particle tracking and generation. `AE` and `AP` are parameters that determine the cutoff energy for the production of secondary electrons and photons, respectively. `ECUT` and `PCUT` are the threshold energies for determining when to terminate tracking a charged particle or photon history, respectively. The global electron cutoff (`ECUT`) and photon cutoff (`PCUT`) must be greater than or equal to corresponding values for AE and AP. The user code limits allow the tracking of electrons to .521 MeV (10-keV kinetic energy) and photons to 1-keV. The values for global transport cutoffs, `ECUT` and `PCUT`, used in a BEAMnrc simulation are provided in the ASCII input file described in Section 2.3.1.

The values for AE and AP are determined when generating the PEGS4 data files that contain the cross-sectional data and stopping powers for the materials that are used in the simulation. The user must also specify an upper limit (`UE` and `UP`) for secondary particle generation. The details concerning the generation of PEGS4 data files are provided in the EGSnrc manual (Kawrakow et al. 2011). Table 2.5 lists the global parameters used in all simulations and generated materials. The lower limit was used for the global electron transport parameters (`AE` and `ECUT`) to prevent the introduction of energy-loss straggling artifacts observed by Rogers et al. (1995). Kawrakow et al. (2011) recommended the global photon transport cutoffs (`AP` and `PCUT`) to be set to .01 MeV for

Table 2.5: Global parameters used in EGSnrc Monte Carlo simulations

Global Parameter	Value
ECUT	.521 MeV
AE	.521 MeV
UE	50.521 MeV
PCUT	.01 MeV
AP	.01 MeV
UP	50.00 MeV

normal operation of the EGSnrc user code. The upper limits of 50 MeV were chosen to sufficiently cover the energy range relevant to medical physics applications.

All custom mediums and alloys used in the linear accelerator were created from schematics that detailed the elemental composition of the materials. The materials generated in the PEGS4 data file used the radiative stopping power information from ICRU Report 37 (1984) and included the optional cross sections for Rayleigh scatter.

Additionally, every region where a material is defined in a simulation has regional cutoff energies for photons and electrons (PCUTIN and ECUTIN). This allows the user to make regional optimizations to reduce the simulation run-time with little to no degradation in the quality of the calculated results. The ECUTIN and PCUTIN values were set equal to the global values for all regions except for the geometries designed for photon collimation. All of the photon collimation components were made from a high density tungsten alloy. In this study, the primary collimator, MLC, backup diaphragm, and lower photon jaw were assigned ECUTIN = .7 MeV, PCUTIN = .01 MeV. This choice reduced the simulation run-time approximately 30 % by ignoring the transport of low-energy electrons that were unlikely to contribute to the dosimetric properties observed at the accelerator isocenter.

There were multiple global input parameters in addition to the energy threshold options. These parameters, described in depth by Kawrakow et al. (2011), were all given the default values that are listed in the manual.

2.4 Initial Source Parameters

The spatial distribution, energy spectrum characteristics, and the angular orientation of the initial electron beam in the vacuum environment were the definable parameters in the Monte Carlo model. The initial source parameters for the model were determined from the simulation results for the open insert 25x25 cm^2 applicator.

2.4.1 Incident Electron Energy Spectrum

The incident electron energy spectrum is potentially complex. Deasy, Almond, and McEllistrem (1996) showed that Elekta accelerator electron beams can have multi-modal energy spectra. Since there were no measured data concerning the energy spectra of the MBPCC Elekta accelerator beams at the time of this project (although such measurements are currently in progress), single Gaussian distributions, adjusted to best match the measured %DD curves, were determined.

The energy spectrum of each electron beam, defined on the upstream side of the nickel exit window, was assumed to be Gaussian in shape. Three parameters were adjusted in order to determine the optimal energy spectrum solution for a given applicator. The peak energy of each spectrum (E_p) was chosen to match the R_{50} value of the measured %DD curve. The full-width half maximum (FWHM) was chosen to match the slope of the R_{90} to R_{10} falloff observed in the measured %DD curves. The FWHM is related to the standard deviation (σ) of the Gaussian distribution by the following equation:

$$FWHM = 2\sqrt{2\ln 2}\sigma \approx 2.355\sigma \qquad (2.1)$$

Finally, the limits of the Gaussian distribution were varied if a Gaussian distribution symmetric about the mean energy was unable to reproduce the measured %DD data. The limits of the distribution where specified by multiples of sigma (σ), where Table 2.6 illustrates the parameters of the initial energy spectrum for all of the clinical electron energies. BEAMDP was used to analyze the energy spectra after Monte Carlo particle transport through the full accelerator geometry. The results from BEAMDP were obtained by binning the energies of the electrons recorded in a

27

Table 2.6: Incident energy spectrum parameters

Clinical energy (MeV)	Peak spectrum value E_p (MeV)	FWHM (% of $\bar{E}$)	Limits of distribution
7	7.8	20	-3.0σ to $+3.0\sigma$
9	9.9	15	-3.0σ to $+3.0\sigma$
10	10.7	15	-3.0σ to $+3.0\sigma$
11	12.3	12	-3.0σ to $+3.0\sigma$
13	14.0	15	-3.0σ to $+3.0\sigma$
16	17.5	15	-3.0σ to $+1.5\sigma$
20	22.0	15	-3.0σ to $+1.5\sigma$

phase-space acquired at the open insert of the 14x14 cm^2 applicator. BEAMDP was set to sample all electrons of the phase-space within a 1 cm radius of the central axis. Figure 2.5 shows the incident spectrum for the 7-MeV model, as defined by the parameters in Table 2.6, along with the resultant energy spectra after transport through the accelerator. Appendix B contains similar plots for all seven of the clinical beam energies. The lower energy limit of the BEAMDP output was set to .621 MeV in order to truncate the large number of low energy electrons that appeared beneath that threshold.
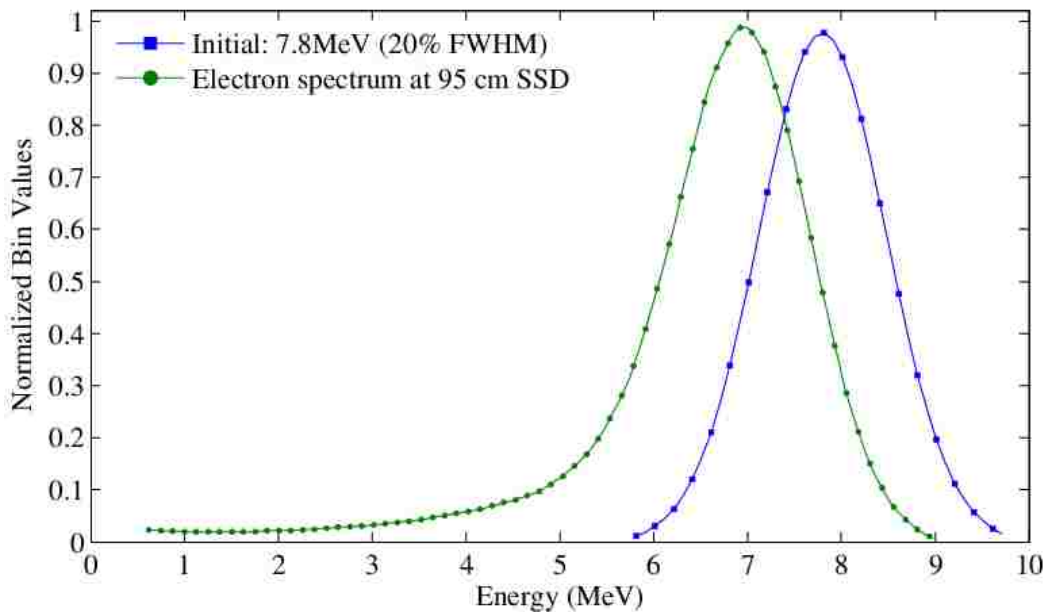

Figure 2.5: 7MeV - 14x14 cm^2 applicator - incident energy spectra compared with BEAMDP spectrum at the field insert (95 cm SSD)

2.4.2 Initial Electron Source Definition

The source option 19 in BEAMnrc, as shown in Figure 2.6, was chosen to model the spatial and angular orientation of the initial electron beam. Source option 19 allows the user to define an elliptical Gaussian electron spot size with either an arbitrary parallel direction or with a mean angular spread with respect to the central axis. The FWHM of Gaussian distributions that describe the spatial spot of the electron beam can be set independently in the X- and the Y-direction to create an elliptical spot size. If the FWHM values are both set to zero, the source collapses down to a point beam for further utility.
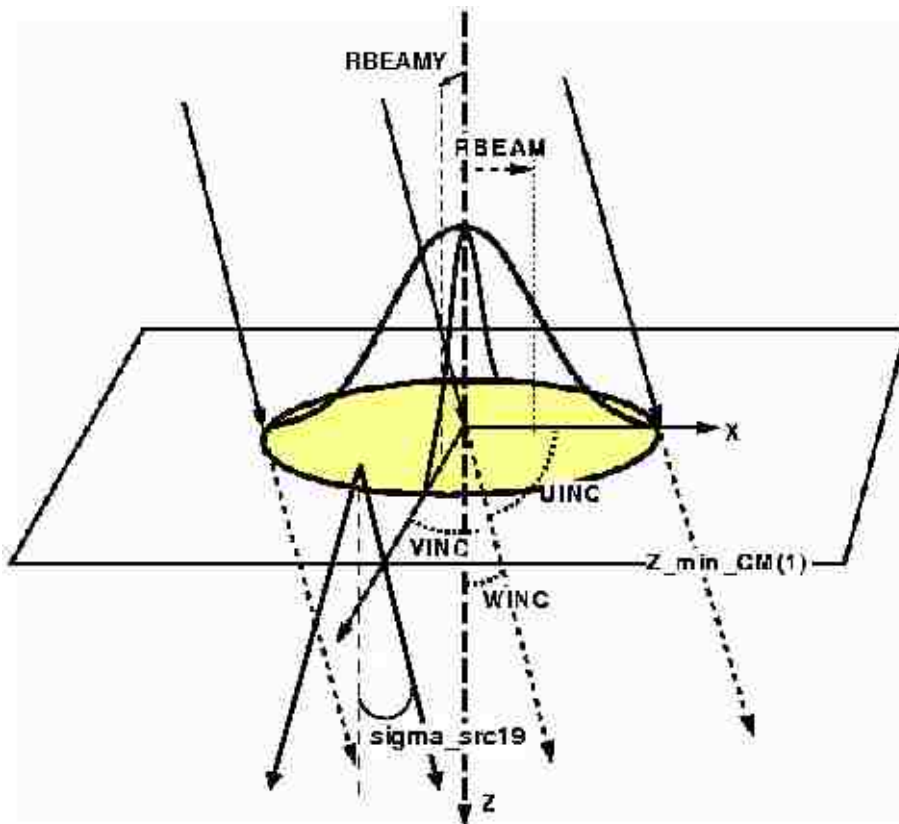
Figure 2.6: Description of parameters available in source option 19 of BEAMnrc. `REAM` and `REAMY` determine the width of the spatial distributions in the X- and Y-direction, respectively. The orientation of particles in the source in Cartesian space are determined by (`UINC`, `VINC`, `WINC`). The Z-axis value where the source is defined is determined by the front of first CM in the BEAM-nrc simulation (`Z_min_CM(1)`). The mean angular spread, in terms of degrees, is determined by `sigma_src19`. If a mean angular spread is used (`sigma_src19>0`), then (`UINC`, `VINC`, `WINC`) automatically default to (0, 0, 1). This requires the mean angular spread to be radially symmetry with respect to the central axis. Figure from Rogers, Walters, and Kawrakow (2011).

The mean angular spread of the source can be set to approximate the scattering effects of the exit window as well as the primary scattering foil or to give the incident beam a mean angular spread within the vacuum window. The mean angular spread value must be radially symmetry about the central axis. The source was defined on the upstream side of the nickel exit window and the FWHM values and the mean angular spread values were adjusted to determine the optimal source definition for the Elekta Infinity linear accelerator. The spatial distribution of the incident electron beam on the nickel exit window was deduced from the 20-MeV cross-beam profiles.

Figure 2.7(a) shows a comparison of the in-plane and cross-plane measured commissioning beam data at 3 cm depth in water for the 20-MeV beam. Figure 2.7(b) shows the Monte Carlo calculated profiles at 3 cm depth in water for a point beam source incident on the nickel window. Comparison of the two figures suggests the spot size must be elliptically shaped for the measured data to achieve comparable flatness in both profile directions with a secondary foil that lacks radial symmetry (see Figure 2.9). Figure 2.7(c) shows an elliptical spot size with a full-width half maximum (FWHM) of 2 mm in the in-plane (Y) direction and a FHWM of 1 mm in the cross-beam direction. This spot size shape was determined to give the best agreement of the calculated in-plane and cross-plane profiles without degradation of the beam flatness in either cross-beam direction.

Björk, Knöös, and Nilsson (2002) reported that the FWHM of the initial electron beam for Elekta accelerators is usually between 1 mm and 2 mm. Additionally, it has been demonstrated that electron spot size is a relatively insensitive parameter for Monte Carlo simulations (Chibani, Moftah, and Ma 2011). Since no quantitative data concerning the spatial distribution of the initial electron source was available at the time of this study, the elliptical Gaussian determined for the 20-MeV beam was used to describe the spatial distribution of the incident electron beam for all beam energies.

2.4.3 Mean Angular Spread

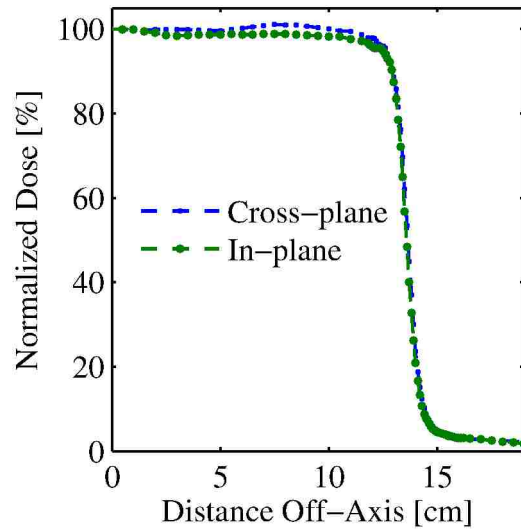The mean angular spread of the incident electron beam was set to $0°$ for all of the beam energies. This choice was made since additional initial angular spread greatly deteriorated agreement between measured and simulated profiles at low (7-MeV and 9-MeV) and high (16-MeV and
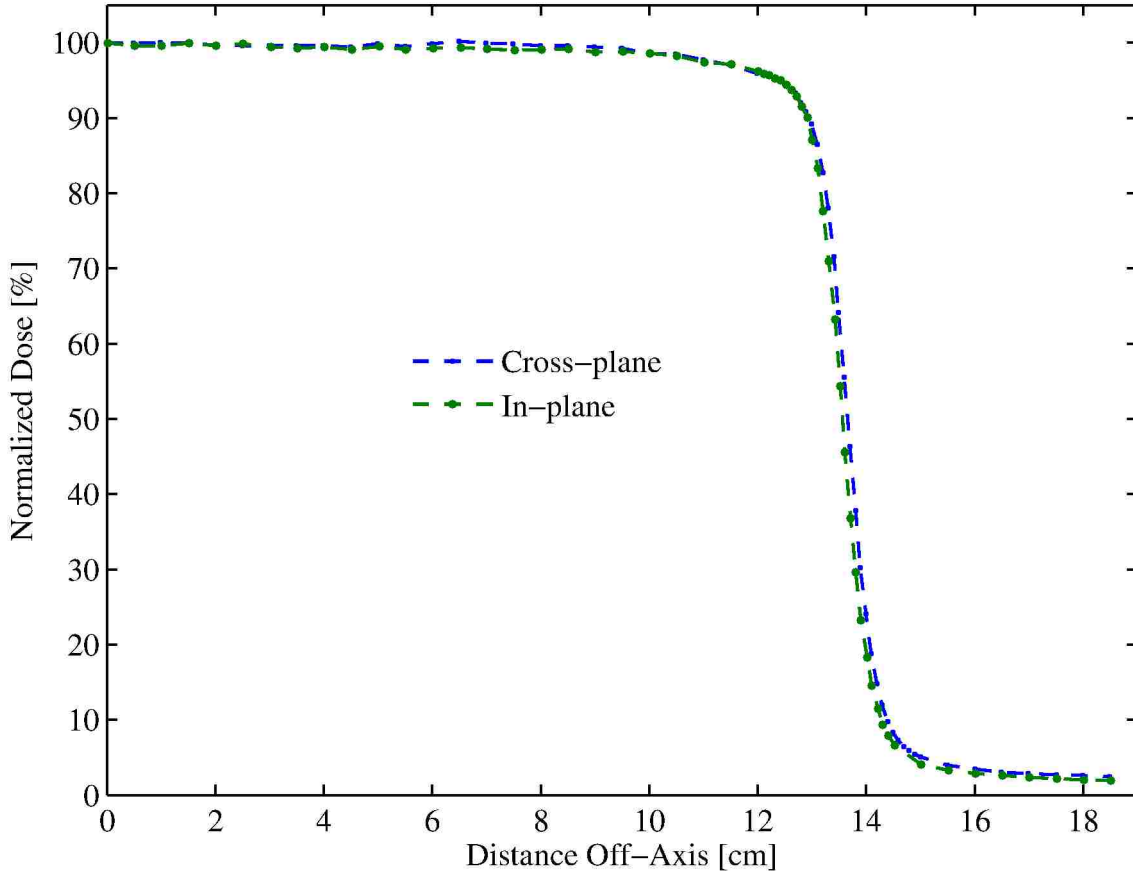
(a) Measured Profiles
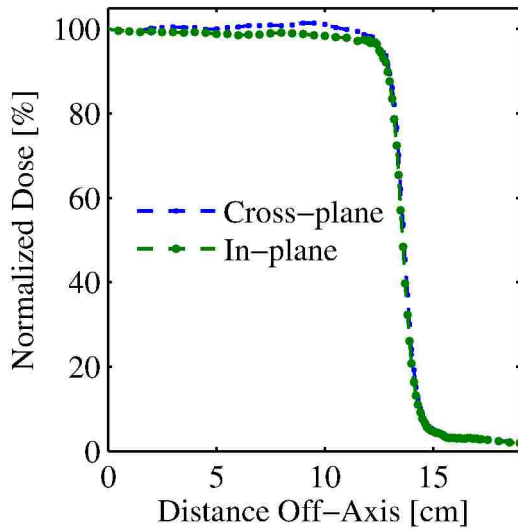
(b) Point Beam Source

(c) Elliptical Gaussian Source

Figure 2.7: Determination of beam spot size using cross-beam profiles for the 20-MeV beam with the 25x25 cm^2 open applicator.(a) Shows the measured cross-beam profiles. (b) Shows the comparison of cross-beam profiles with a point beam source. (c) Shows the comparison of cross-beam profiles with an elliptical Gaussian source (FWHM$_y$=2 mm, FWHM$_x$=1 mm).

20-MeV) beam energies. The middle energies (10-MeV, 11-MeV, and 13-MeV) were improved using a slight initial angular spread ($\sim$1-2°). However, because no overall trend of angular spread value as a function of beam energy across the clinical range was observed, the angular spread was set to 0° for all simulations.

2.5 Monte Carlo Linear Accelerator Model

The Monte Carlo model of the Elekta Infinity linear accelerator,shown in Figure 2.8, was built using the standard CMs included in BEAMnrc V4 2.3.2. The model was constructed from schematics provided by Elekta engineers under a non-disclosure agreement. The schematics provided detailed information of the geometries and material compositions of treatment head components that are impossible to measure directly without disassembly of the accelerator. Additionally, components were verified with physical measurement whenever it was possible and practical to do so.

2.5.1 Upper Head Geometry

The upper head of the accelerator consisted of the stationary beam-line components above the photon jaws. The upper head was modeled using six CMs for the 7-MeV through the 13-MeV beams, which are listed in Table 2.7. FLATFILT modules are defined by stacking an arbitrary number of coaxial cones together. Since the radii of these cones can be independently defined for each layer, the CM can model complex flattening filters and scattering foils. The simplicity of the CM input parameters also makes it an ideal choice for primary foils, the accelerator exit window, and the ionization monitor chamber. The main shortcoming of the FLATFILT CM is the requirement for objects to have cylindrical symmetry. This limitation presented an issue when modeling the additional foil layer present on the scattering foil used in the 16-MeV and 20-MeV beams. This additional layer, shown in Figure 2.9(a), was symmetric with respect to both the x-axis and the y-axis, but did not possess cylindrical symmetry about the z-axis.
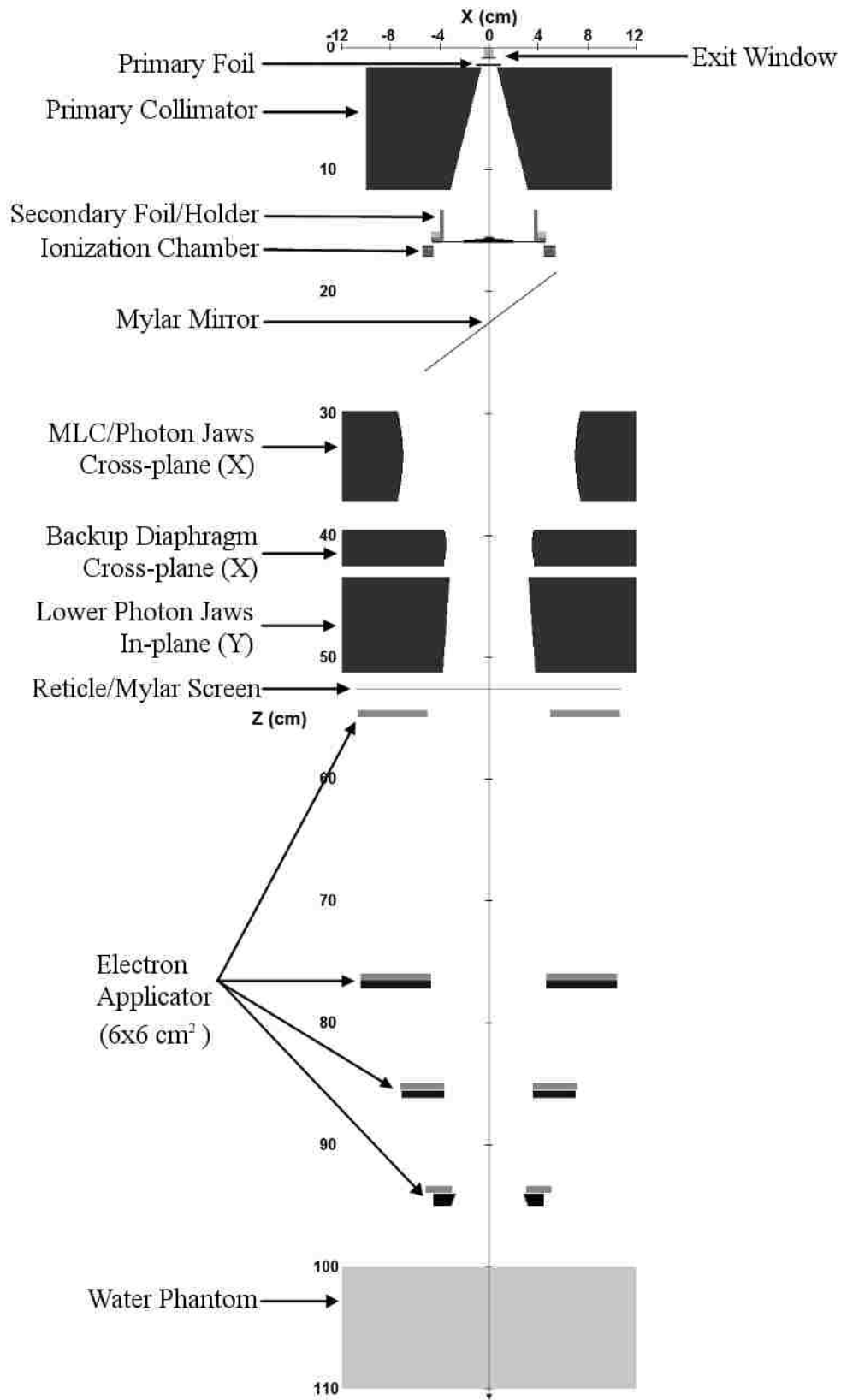
Figure 2.8: Complete model of the Elekta Infinity linear accelerator as rendered by the BEAMnrc accelerator preview

Table 2.7: Component modules in upper head (7-13 MeV)

Order of CM	CM type	Beam-line component modeled
1	FLATFILT	vacuum, exit window
2	FLATFILT	primary scattering foil
3	CONS3R	primary collimator
4	FLATFILT	secondary scattering foil
5	FLATFILT	ionization monitor chamber
6	FLATFILT	light field mirror

2.5.2   Approximation of Additional Foil Layer

Since the secondary foil for the high energy (16, 20-MeV) beams was not symmetric about the CAX through all layers, it could not be fully modeled with the standard FLATFILT module. Therefore, the additional secondary foil layer was modeled by adding an additional CM module called BLOCK immediately downstream of the cylindrically-symmetric disks of the secondary foil, which were still modeled with the FLATFILT module. This created an offset in the CM order of the high energy accelerator models as shown in Table 2.8.

Table 2.8: Component modules in upper head (16,20 MeV)

Order of CM	CM type	Beam-line component modeled
1	FLATFILT	vacuum, exit window
2	FLATFILT	primary scattering foil
3	CONS3R	primary collimator
4	FLATFILT	secondary scattering foil
5	FLATFILT	ionization monitor chamber
6	*BLOCK*	*additional asymmetric foil layer*
7	FLATFILT	light field mirror

The BLOCK module was designed to simulate photon blocks of arbitrary shapes and sizes. An arbitrary shape within the field can be modeled by setting the outer material to air and the inner material, in the case of the secondary foil layer, to aluminum. The additional foil was replicated using the BLOCK module with 20 user-defined polygonal points that defined the boundary of the additional foil layer according to the dimensions provided by Elekta. Figure 2.9 shows a photograph of the additional foil layer (left) and its representation within BEAMnrc (right).

34
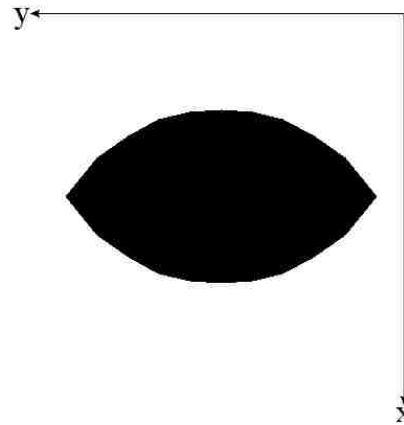
(a) Bottom of foil   (b) Approximation of layer

Figure 2.9: Approximation of the additional asymmetric foil layer. (a) shows a photograph of the additional foil layer on the secondary foil that is used in the MBPCC accelerators. (b) shows the rendered approximation of the additional foil layer using the BLOCK module in BEAMnrc

2.5.3 Lower Head Geometry

The lower head of the accelerator consisted of the photon jaws and the Mylar screen that protects the treatment head from the outside environment. The lower head was modeled with four CMs, which are provided in Table 2.9. The MLCQ component module was used to model both the actual multi-leaf collimator (MLC) and the backup diaphragm that is positioned behind it. This CM was specifically designed to model MLC leafs that have rounded leaf ends. The backup diaphragm is roughly half the thickness of the MLC and possesses no leafs, but the component does have rounded edges. The MLCQ module is the only standard CM that allows the user to define rounded (radiused) edges on a beam-line component. The radius of the backup diaphragm and the radius for the MLC leafs were specified by schematics. As mentioned in Section 2.1, when operating in

Table 2.9: Component modules in lower head

Order of CM	CM type	Beam-line component modeled
7	MLCQ	MLC
8	MLCQ	backup diaphragm
9	JAWS	lower photon jaws
10	SLABS	Mylar window

35

electron mode, the MLC leaves are "parked" to define a 40x40 cm^2 field at isocenter while the backup diaphragm defines the beam edge and performs the initial electron field collimation. While in photon mode, the backup diaphragm is set to be 2 to 3 mm behind the most open leaf position of the MLC. All machine readouts of the field size (in both photon or electron mode) are in terms of the lower jaw location in the Y direction and the photon mode location of the MLC in the X direction. Thus, the actual field size in the Y-direction projected to isocenter is larger than listed on the machine when in electron mode due to the built in offset of the backup diaphragm behind what would be the light field position for the MLC when in photon mode. This offset was confirmed by measuring the light fields for each applicator and energy combination with the applicator removed. The offset at the backup diaphragm was determined to be 2 mm on average. Figure 2.10 illustrates the configuration of the MLC and the backup diaphragm when the machine is in photon mode. Using the variables listed on Figure 2.10 and the half field-sizes (*HFS*) denoted in Table 2.2, the off-axis position of the backup diaphragm, X_{BACKUP}, in electron mode can be determined by the following equation:

$$X_{BACKUP} = (\frac{HFS}{SAD})Z_{BACKUP} + 2mm \tag{2.2}$$

The lower photon jaw was approximated with the JAWS module. The JAWS module allows the user to define slabs of a material with arbitrary openings. A photon collimator may be approximated by specifying the beginning and end of the slab along z-axis (the jaw thickness) and the off-axis position of the jaw opening at the front, beam-side, and back, patient-side, to define the beam divergence of the photon jaw. Elekta engineers provided the z-axis coordinates of the beam-side and the patient-side of the lower photon jaw when it is completely closed. The motion of the lower photon jaw is defined in terms of the variables shown in Figure 2.11. Point P is located at distance, d_p, off-axis and depth, t_p, from the beam-side of the photon jaw edge, where the thickness of the photon jaw is equal to $2t_p$. The motion of the jaw is such that the z-axis coordinate of point P, labeled Z_p, remains constant as the jaw moves. Given this information, and the half-field size (*HFS*) at isocenter (z=100 cm), the coordinates needed to define the photon jaw in
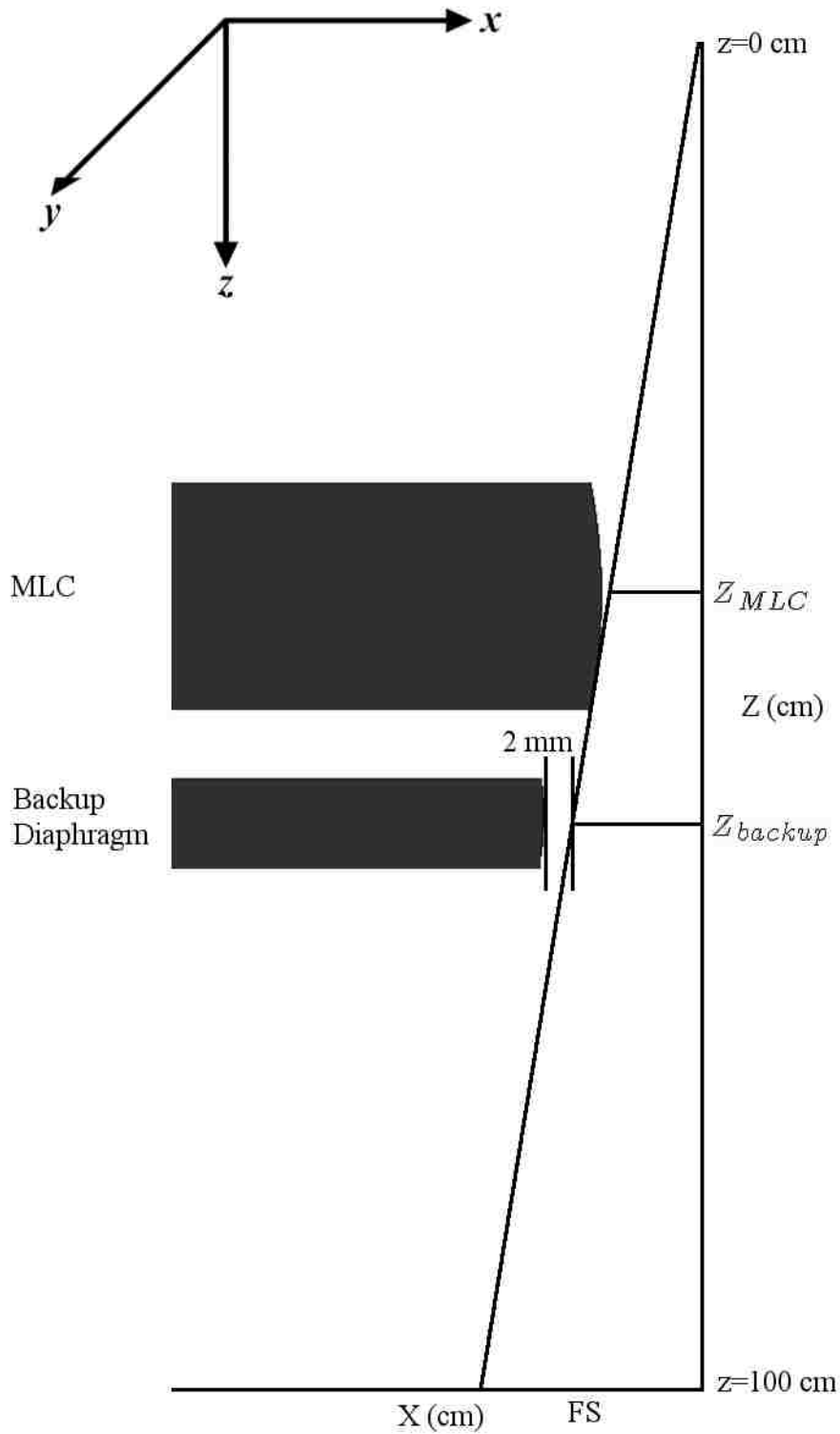
36

Figure 2.10: Elekta Infinity linear accelerator MLC and backup diaphragm configuration in photon mode.
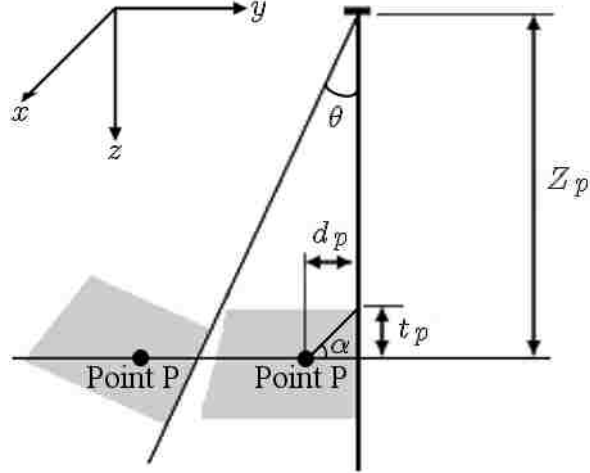
Figure 2.11: Description of lower jaw motion with necessary variables to define the motion.

BEAMnrc can be specified by the y-coordinate and z-coordinate of the beam-side (z_{upper},y_{upper}) and the patient-side (z_{lower},y_{lower}) of the photon jaw. The coordinates for the beam-side edge of the photon jaw, (z_{upper},y_{upper}), were determined by the following equations:

$$y_{upper} = y_p - H\cos(\alpha - \theta) \tag{2.3}$$

$$z_{upper} = Z_p - H\sin(\alpha - \theta) \tag{2.4}$$

$$H = \sqrt{(t_p^2 + d_p^2)} \tag{2.5}$$

$$\alpha = \arctan\frac{t_p}{d_p} \tag{2.6}$$

$$\theta = \arctan\frac{HFS}{SAD} \tag{2.7}$$

Given the position of the beam-side edge of the photon jaw, (z_{upper},y_{upper}), the patient-side edge of the photon jaw can be found using the following expressions:

$$y_{lower} = y_{upper} + 2t_p\sin\theta \tag{2.8}$$

$$z_{lower} = z_{upper} + 2t_p\cos\theta \tag{2.9}$$

38

The magnitude of shift in photon jaw position with respect to the z-axis is illustrated in Figure 2.12. This image shows the lower jaw positions and shapes modeled in the BEAMnrc model of the clinical 13-MeV beam for the 6x6 and the 25x25 cm^2 applicators. The 6x6 cm^2 applicator settings have the lighter shading while the 25x25 cm^2 applicator settings have the darker shading.
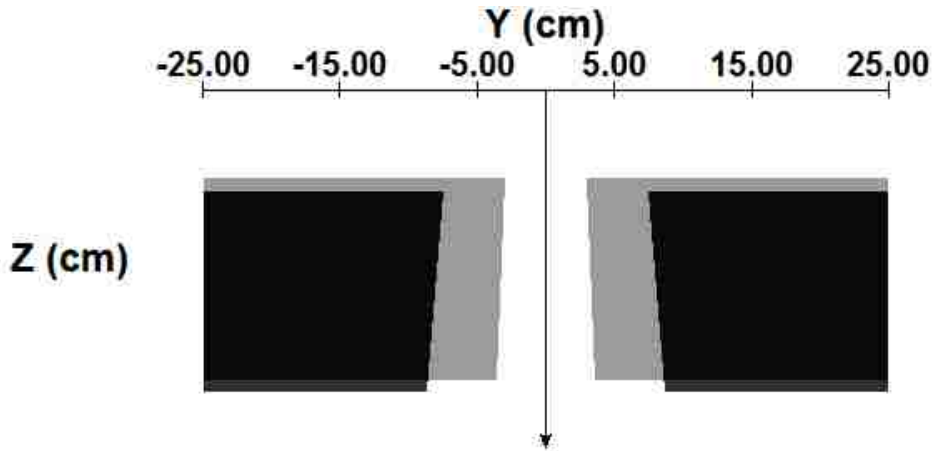
Figure 2.12: Comparison of photon jaw positions for the 6x6 (lighter shading) and the 25x25 (darker shading) cm^2 applicators for the 13-MeV beam. Note that the angulation of the jaws, shown in Figure 2.11, is not modeled. This approximation should not be significant.

2.5.4 Electron Applicator and Field Insert

The applicator and the field insert were modeled with two CMs, which are listed in Table 2.10. The dimensions, thicknesses, and z-coordinate locations of all the trimmer bars and open inserts were detailed in the schematics provided by Elekta. The APPLICAT module was used to model the fixed trimmer bars of the applicator. Since the APPLICAT module could not model beveled edges, the open insert required the use of a separate module. The PYRAMIDS module allowed for the bevel angle, which was necessary for all open inserts, to be correctly modeled. Figure 2.13 shows the electron applicator with the divergent open insert. The support rods that hold the trimmer bars together were not included in the model. All trimmer layers were approximated in the APPLICAT module as rectangular in shape.

Table 2.10: Component modules in electron applicator

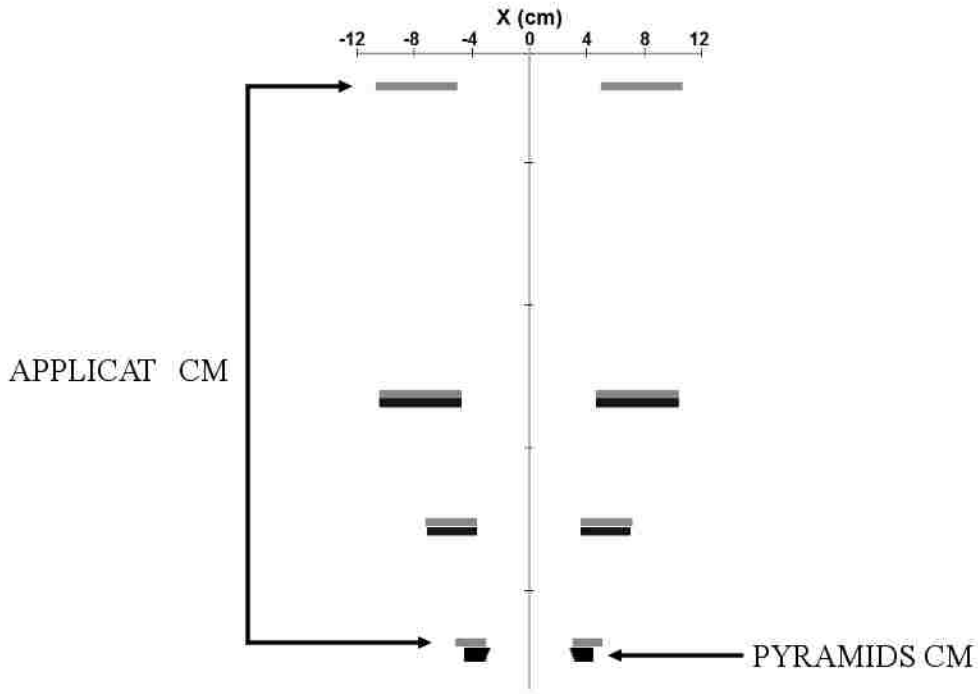| Order of CM	CM type	Beam-line component modeled
11	APPLICAT	electron applicator
12	PYRAMIDS	applicator insert

Figure 2.13: Schematic of CMs for 6x6 cm^2 electron applicator with open insert.

2.5.5 Phase Spacing Scoring and PDD Chamber

The phase-space for the production runs was scored behind the field insert of the applicator (the PYRAMIDS module) at 95 cm SSD. The recorded phase space was used as the DOSXYZnrc input for scoring cross-beam dose profiles as described in Section 2.5.6. This allowed the full model to be recorded before the beam was passed into a CM that efficiently scored the dose deposited along the central axis. After scoring the phase space, the BEAMnrc simulation continued and transported the particles through the final component module, a CHAMBER module, which began at 100 cm SSD. The CHAMBER module was designed to simulate a parallel-plate ion chamber. The geometry and number of the planes within the chamber, as well as the chamber materials,

could be arbitrary selected. The choice of a large diameter outer radius, a small radius inner wall, and a large number of uniformly spaced inner chamber regions with water as the material for all regions results in a central axis water phantom. When dose scoring is enabled (BEAMnrc will score absorbed dose in any region where dose scoring has been enabled) in the inner radius region, the CHAMBER module allows for an efficient method to acquire %DD curves without the need for an additional DOSXYZnrc simulation. The use of the CHAMBER in this manner is well documented by Rogers, Walters, and Kawrakow (2011) and has been applied in similar works by Bieda (1999). The BEAMnrc GUI allows the user to define the input parameters for the CHAMBER module in terms of an actual parallel-plate chamber or in terms of the simple water phantom described above. The labeling of the input parameters for both cases are shown in Figure 2.14.

The inner radius the chamber was set to 6 mm and outer radius of the chamber wall was set to 20 cm. The inner region consisted of 160 layers with 1 mm spacing. These settings allowed the CHAMBER module to score dose along the central axis to a depth of 16 cm with a resolution of 1 mm. The CHAMBER module was able to cover the full range of measured depth dose data for all of the beam energies without a change in spacing resolution. The maximum number of dose-scoring zones, defined by the variable, `MAX_DOSE_ZONE`, in the BEAMnrc user macros file, had to be increased to accommodate the number of dose-scoring zones required by the CHAMBER module. The default value for `MAX_DOSE_ZONE` was 50.

2.5.6   Water Phantom Models in DOSXYZnrc

The phase space file collected at the back of the field insert of the applicator was used as the input for water phantom simulations in DOSXYZnrc. Since the back of the insert module is located at z = 95 cm, a 5 cm and 15 cm gap was placed between the water surface and the phase space when running DOSXYZnrc simulations at 100 cm and 110 cm SSD, respectively. The DOSXYZnrc water phantom was used to generate all calculated cross-beam and diagonal profiles. For comparison against commissioning data, the water phantom was constructed with non-uniform spacing in the X and Y direction that was symmetric about the CAX. The spacing for the voxel in the X and Y direction was chosen to be either 5 mm or 1 mm, which were the two spacing options
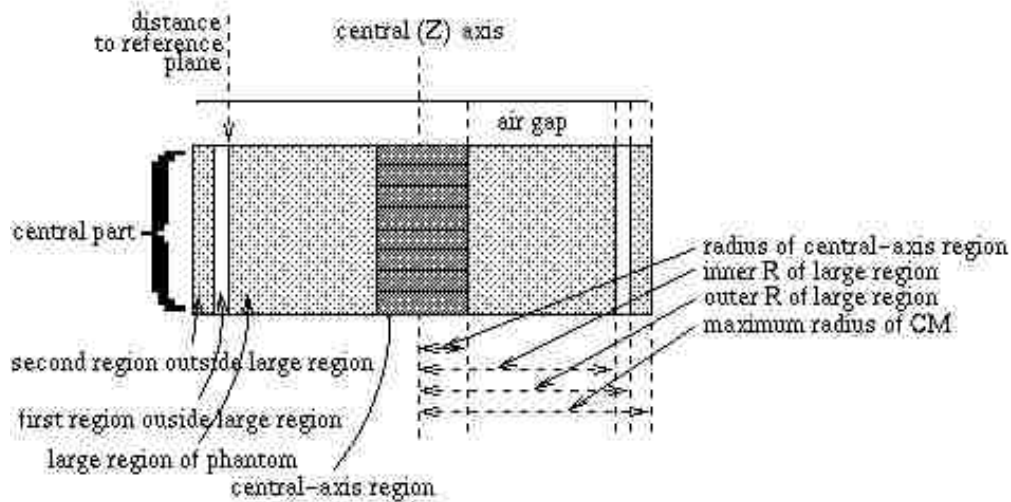
CHAMBER
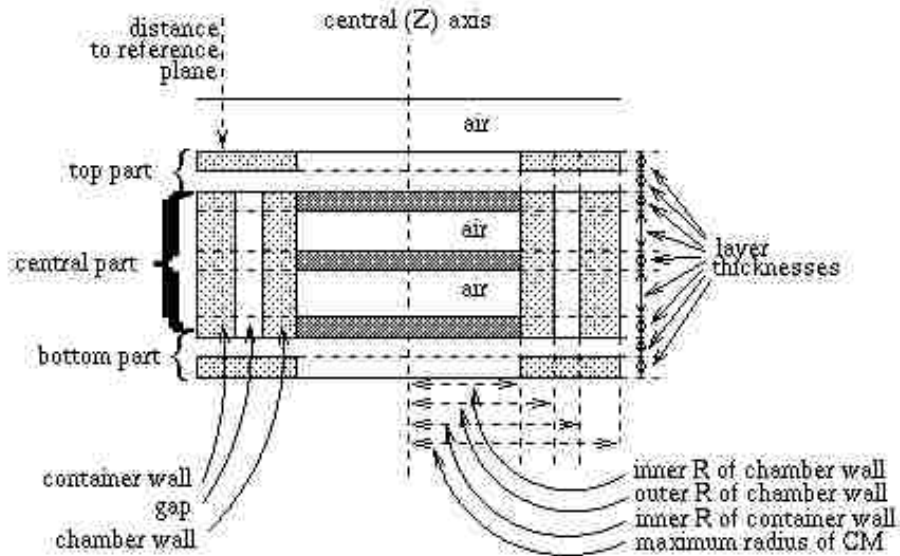
PHANTOM

Figure 2.14: CHAMBER CM options and input parameters. Figure from Rogers, Walters, and Kawrakow (2011).

of the commissioning data. The 1 mm spacing was used in the high dose gradient regions of the profile (the penumbra region), while the 5 mm spacing was used in the low dose gradient regions (the in-field and out-of-field regions).

Additionally, a DOSXYZnrc input file was created to score %DD curves. The %DD input file contained a $0.6\,\mathrm{cm^2}$ region in the X and Y directions that was centered on the CAX. Two additional

regions, with a thickness of 24.7 cm, were defined in both the X and Y directions. This extended the water phantom to a 50x50 cm^2 area in the X-Y plane. The Z direction had uniform spacing of 1 mm for 161 regions. This choice of phantom spacing created a DOSXYZnrc CAX %DD phantom that was the rectangular equivalent of the %DD phantom created with the CHAMBER module. Both methods, DOSXYZnrc simulations and CHAMBER CM with dose scoring enabled, output dose information in terms of absorbed dose per incident particle at the center of the voxel. Figure 2.15 shows a comparison of the raw, un-normalized outputs of the CHAMBER module and the DOSXYZnrc simulation for the 13-MeV beam with the 14x14 cm^2 applicator at 100 cm SSD. The dose output contained all particle types (electrons, photons, and positrons) and the water surface for both phantoms was located at 100cm SSD.

The 6x6 and 14x14 cm^2 applicator simulations compared the simulation against an expanded set of measured cross-plane profiles as described in Section 2.2.2. The DOSXYZnrc cross-beam
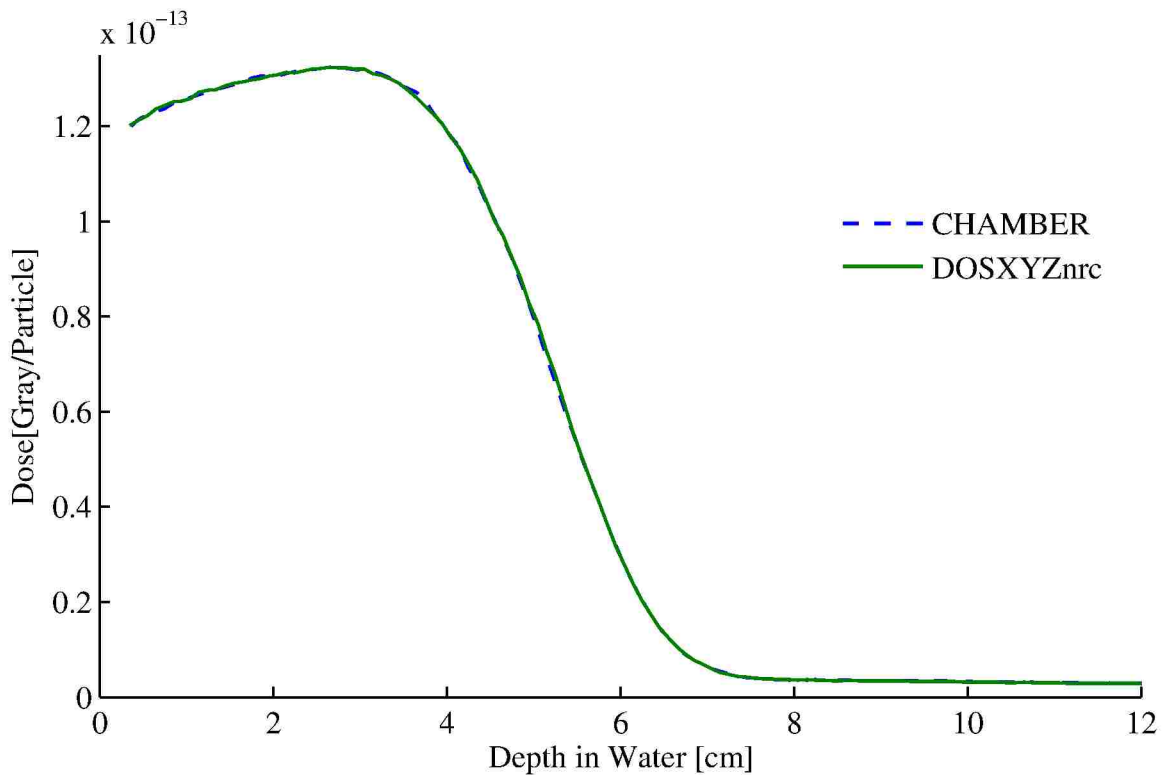
Figure 2.15: Comparison of CHAMBER and DOSXYZnrc output for the 13-MeV 14x14 cm^2 applicator at 100 cm SSD

input files for these applicators only collected dose information along the cross-plane (X) direction. The spacing of these water phantom simulations were assigned a 5 mm width about the Y-axis for all cross-plane only DOSXYZnrc simulations.

The 110 cm SSD simulations for the 14x14 cm^2 applicator were performed by increasing the air gap between the phase-space output and the surface of the DOSXYZnrc water phantom. To avoid re-running the BEAM simulation to obtain %DD information from the CHAMBER module, DOSXYZnrc was run to score %DD curves at extended SSDs using the input parameters described above.

The initial particle number (`NCASE`) for all DOSXYZnrc simulations was chosen to be 1 billion. The phase-space collected during the BEAM simulation was recycled until 1 billion initial particles were transported into the water phantom. The redistribution function (`ISMOOTH`) was enabled for all DOSXYZnrc simulations in order to reduce statistical uncertainties when recycling the phase-space. This was acceptable for all setups since the accelerator geometry was always symmetric with respect to both the Y-axis and X-axis.

2.5.7 Extraction of Simulation Data

When a CHAMBER module with dose scoring enabled is used in a BEAMnrc simulation, an additional file (.egsplot file) is output at the end of BEAMnrc simulation. This .egsplot file contains the dose information in terms of absorbed dose per incident particle (Gray/particle) for the location of each region defined along the CAX. The %DD data for all runs at 100 cm SSD was extracted from the corresponding .egsplot files.

The cross-beam profile data calculated for the water phantom in DOSXYZnrc was taken from the .3ddose output file, which is in ASCII format. The structure of this file type is described by Walters, Kawrakow, and Rogers (2011). A computer program was written to extract the profile information for each desired depth in the water phantom.

2.5.8 Smoothing of Simulated Dose

All simulated cross-beam and diagonal profile data had the dose values smoothed via a moving average filter before comparisons to the measured data were performed. The span of the moving

window was set to 3 points, which is the least amount of smoothing this type of filter can perform. The dose values for the simulated %DD curves were not smoothed before comparison with the measured data.

2.6 Data Normalization and Comparison

2.6.1 Normalization

The Monte Carlo dose results were output in terms of absorbed dose (Gray) per incident particle. In order to compare the simulated data against the measured data, the two data sets needed to be normalized in a systematic and meaningful manner. For the purpose of this study, the following protocol was followed for the normalization of all simulated and measured data.

1. Simulated and measured %DD curves were normalized to each profile's R_{100} value.

2. The in-plane and cross-plane profiles for the simulated and the measured data sets were first normalized to the average value of all data points within ± 1 cm of the central axis, then normalized to the %DD value of the measured data at the depth of the profile.

3. The measured and simulated diagonal profiles were normalized to the average value of all data points within ± 1 cm of the central axis.

2.6.2 Comparison Method

The following method was used for comparing the measured and simulated data. First, the tolerance criteria were defined in terms of distance-to-agreement, denoted α, and percent difference, denoted β. For the tolerance criteria specified in the hypothesis of this work, let $\alpha = .1$ cm and $\beta = 2\%$ of D_{max}. Then, let any normalized and smoothed simulation data point be described with coordinates: (P_{sim},%D_{sim}). Similarly, let any normalized and symmetrized measured data point be described with coordinates: (P_{meas},%D_{meas}). The pass/fail algorithm will then analyze the data in the following manner:

1. Iteratively, beginning with i=1, for every measured data point along a curve, a line is drawn from: $(P_{meas,i}, \%D_{meas,i}-\beta)$ to $(P_{meas,i}, \%D_{meas,i}+\beta)$.

2. Iteratively, beginning with j=1, for all simulated data points along a curve, a line is drawn from: $(P_{sim,j}, \%D_{sim,j})$ to $(P_{sim,j+1}, \%D_{sim,j+1})$.

3. The lines segments created by all adjacent simulated points are then tested for either intersection or boundary contact with the line that spans $\pm 2\%$ of the measured point being tested $(P_{meas,i}, \%D_{meas,i})$.

4. If any lines are found to intersect or touch, the data point is determined to meet the tolerance criteria of the hypothesis. The algorithm will then move to the next measured data point (set i=i+1 and return to the first step).

5. If no intersection is found for any line formed by adjacent simulated data points, then for the same measured data point, $(P_{meas,i}, \%D_{meas,i})$, a line is drawn from: $(P_{meas,i}-\alpha, \%D_{meas,i})$ to $(P_{meas,i}+\alpha, \%D_{meas,i})$.

6. Once again, beginning with j=1, for all simulated data points along a curve, a line is drawn from: $(P_{sim,j}, \%D_{sim,j})$ to $(P_{sim,j+1}, \%D_{sim,j+1})$.

7. The line segments created by all adjacent simulated points are then tested for either intersection or boundary contact with the line that spans ± 1 mm of the measured point being tested $(P_{meas,i}, \%D_{meas,i})$.

8. If any lines are found to intersect or touch, the data point is determined to meet the tolerance criteria of the hypothesis. The algorithm will then move to the next measured data point (set i=i+1 and return to the first step).

9. If no intersection is found for any line formed by adjacent simulated data points, then the measured data point, $(P_{meas,i}, \%D_{meas,i})$, is determined to fail the criteria tolerance of the hypothesis.

The mathematics of the line segment intersection test can be explained by defining two line segments with 4 points. Let the first line segment have endpoints, $Point_A$ and $Point_B$, and the second line segment have endpoints, $Point_C$ and $Point_D$: These two line segments can be described by the following equations:

$$Line_1 = Point_A + t_1(Point_B - Point_A) \tag{2.10}$$

$$Line_2 = Point_C + t_2(Point_D - Point_C) \tag{2.11}$$

If the location where $Line_1 = Line_2$ is solved for, the solution yields two equations:

$$P_A + t_1(P_B - P_A) = P_{sim,i} + t_2(P_{sim,i+1} - P_{sim,i}) \tag{2.12}$$

$$D_A + t_1(D_B - D_A) = D_{sim,i} + t_2(D_{sim,i+1} - D_{sim,i}) \tag{2.13}$$

Equation 2.12 and Equation 2.13 are then used to produce solutions in terms of the two unknowns, t_1 and t_2:

$$t_1 = \frac{(P_{sim,i+1} - P_{sim,i})(D_A - D_{sim,i}) - (D_{sim,i+1} - D_{sim,i})(P_A - P_{sim,i})}{(D_{sim,i+1} - D_{sim,i})(P_B - P_A) - (P_{sim,i+1} - P_{sim,i})(D_B - D_A)} \tag{2.14}$$

$$t_2 = \frac{(P_B - P_A)(D_A - D_{sim,i}) - (D_B - D_A)(P_A - P_{sim,i})}{(D_{sim,i+1} - D_{sim,i})(P_B - P_A) - (P_{sim,i+1} - P_{sim,i})(D_B - D_A)} \tag{2.15}$$

The denominator is the same in Equation 2.14 and Equation 2.15. If the denominator term produces zero as an output then $Line_1$ and $Line_2$ are parallel. In order to test if the line segments intersection, the values of t_1 and t_2 must both return values that are between zero (0) and one (1). If both t_1 and t_2 meet this condition then the line segments intersect. Figure 2.16 shows a graphical representation of the analysis technique for two 11-MeV 25x25 cm^2 applicator cross-plane profiles.
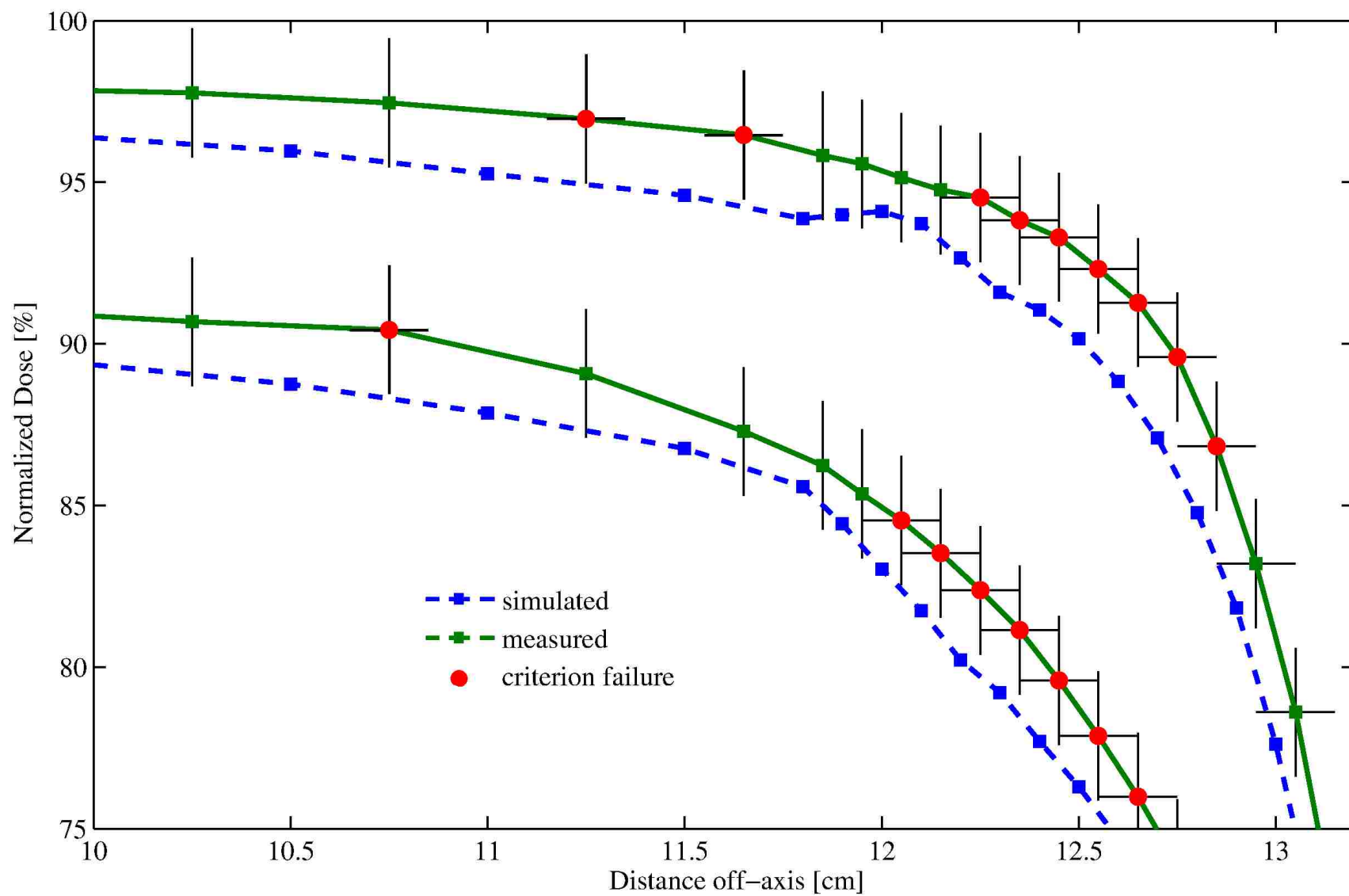
Figure 2.16: Visual representation of the tolerance criteria algorithm applied to 11-MeV 25x25 cm^2 applicator cross-beam profiles

Chapter 3
Results

3.1 Summary of Run-Time Statistics

The simulation results of the Monte Carlo model were compared against measured %DD curves, cross-beam profiles at depths listed in Table 2.2, and diagonal profiles for the open-insert 25x25 cm^2 applicator for all seven energies. Additionally, model results were compared against measured %DD curves and the extended set of measured cross-plane profiles with the 6x6 and the 14x14 cm^2 applicator for the 7-, 13-, and 20-MeV beam energies. The 14x14 cm^2 applicator results were compared at both 100 cm and 110 cm SSD. Table 3.1 lists the run-time statistics for the open-insert 25x25 cm^2 applicator accelerator simulations. The initial particle number (NCASE) was chosen to produce phase-space files with comparable total particle numbers. The total CPU times are in terms of equivalent time elapsed if the simulation were run on a single processing core. All simulations were performed on Linux clusters provided by the high performance computing (HPC) center at Louisiana State University and 4.772 teraflop Linux clusters provided through a computing allocation granted by the Louisiana Optical Network Initiative (LONI). The details of the computing resources and the parallel run environment are discussed in Appendix A.

Table 3.1: Run statistics for 25x25 cm^2 applicator

Energy (MeV)	# of Cores	NCASE (millions)	Total # particles in PHSP	# photons in PHSP	Size (GB)	CPU time (hr)	CPU sec/history
7	80	600	189010588	91035798	5.29	195.53	0.00117
9	80	500	205619614	119791861	5.76	217.04	0.00156
10	80	500	279433433	144584794	7.82	244.74	0.00176
11	80	400	250113652	141454700	7.00	218.07	0.00196
13	80	300	221332919	135432453	6.20	192.80	0.00231
16	80	300	326544476	203606036	9.14	251.00	0.00301
20	80	200	283866124	195841630	7.95	212.05	0.00382

Note: Phase-space file is denoted (PHSP) and initial particle number is denoted (NCASE).

The `NCASE` value for all water phantom simulations in DOSXYZnrc was 1 billion. This combination of `NCASE` values produced %DD curves from the CHAMBER module with less than 0.5% fractional uncertainty in the electron dominant depths and less than 2.0% fractional uncertainty in the photon dominant depths. The fractional uncertainty of the dose outputs from DOSXYZnrc simulated cross-beam profiles were less than 0.5% for the in-field points and less than 2.5% for out-of-field points. The same `NCASE` values from Table 3.1 were used for 6x6 and 14x14 cm^2 applicator simulations in BEAMnrc. The %DD curves for the 6x6 cm^2 applicator were recalculated with the DOSXYZnrc depth dose phantom in order to reduce statistical noise. The CHAMBER output from these runs had higher uncertainties due to the smaller number of particles that reach isocenter when compared with larger field-sizes.

Comparisons of the simulation results with the measured data for smaller field-sizes (6x6 and 14x14 cm^2 applicators), shown in Appendix C, demonstrate the ability of the model to produce simulated results that match the measured beam data within the tolerance criteria of the hypothesis (2% of D$_{max}$ or 1 mm DTA) for nearly 100% of the data points compared. Please refer to Appendix C for the additional data concerning the 6x6 and 14x14 cm^2 applicator simulations for the 7-, 13-, and 20-MeV beams.

Since the model showed the greatest sensitivity to modeling errors at large field-sizes, the comparison of open-insert 25x25 cm^2 applicator data are the main focus of the results of this work. The results are discussed in terms of low energy (7-, 9-MeV), medium energy (10-, 11-, 13-MeV), and high energy (16-, 20-MeV) beams. These groupings were determined by the beams which shared a common secondary scattering foil. Only figures and tables from the large-field simulation results will be shown in this Chapter.

3.2   Low Energy (7-, 9-MeV) Large-Field Results

The simulated %DD curves for both low energy beam models matched the measured data within the criteria of the hypothesis for the large-field simulations (cf. Figures 3.1 and 3.7). However, for the shallowest cross-beam depths of 1.0 cm at 7-MeV and 1.3 cm at 9-MeV, simulated profiles provided a larger off-axis dose relative to the CAX than measured (cf. Figures 3.3(a),

3.5(a), 3.9(a), and 3.11(a)). The largest difference between measured and simulated doses was on the order of 3% of D$_{max}$. The trend of over-prediction of off-axis dose by the Monte Carlo simulations continued with depth for all low energy large-field cross-beam profiles. The simulated diagonal profiles at depths of 1 cm for both energies also over-predicted the off-axis dose and exhibited a maximum dose difference from the measured diagonal profiles on the order of 4% of D$_{max}$ (cf. Figures 3.2 and 3.8).

The shape of simulated Bremsstrahlung dose profiles agreed reasonably well with the measured photon dose profiles for both energies (cf. Figures 3.3(e), 3.5(e), 3.9(e), and 3.11(e)). The slight under-prediction of the simulated photon dose could be resolved by adding mean angular spread ($\sim 1°$) to the initial electron source of the model. However, any initial angular spread with the low energy beam models would increase the off-axis dose differences observed (by $\sim$1% per degree of spread) between the simulated and measured cross-beam profile data at shallower depths.

3.3 Medium Energy (10-, 11-, 13-MeV) Large-Field Results

The simulated %DD curves for the three medium energy beam models matched the measured data within the criteria of the hypothesis for the large-field simulations (cf. Figures 3.13, 3.19, and 3.25). However, for the shallowest cross-beam depths of 1.5 cm at 10-MeV, 1.7 cm at 11-MeV, and 2.0 cm at 13-MeV, simulated profiles provided a smaller off-axis dose relative to the CAX than measured (cf. Figures 3.15(a), 3.17(a), 3.21(a), 3.23(a), 3.27(a), and 3.29(a)). The largest difference between measured and simulated cross-beam profile doses was on the order of 3% of D$_{max}$. The trend of over-prediction of off-axis dose by the Monte Carlo simulations continued with depth for all medium energy large-field cross-beam profiles. The simulated diagonal profiles at a depth of 1 cm for 10-MeV and 2 cm for 11-MeV and 13-MeV also under-predicted off-axis dose and exhibited a maximum dose difference from the measured diagonal profiles on the order of 3% of D$_{max}$ (cf. Figures 3.14, 3.20, and 3.26). Additionally, the simulated medium energy beam models failed to match the measured profiles within the DTA criteria in the penumbra region for a large number of cross-beam profiles. This DTA difference was greater in the cross-plane direction than the in-plane direction. The DTA differences observed in the penumbra of the medium energy

beams was much less pronounced for the 14x14 cm^2 applicator cross-beam comparisons of the 13-MeV beam.

The simulated Bremsstrahlung dose profiles slightly under-predicted the shape of the measured photon dose profiles for all three energies (cf. Figures 3.15(e), 3.17(e), 3.21(e), 3.23(e), 3.27(e), and 3.29(e)). The difference between the simulated and measured photon profiles increased with the energy of the beam. Including a mean angular spread ($\sim 1 - 2^\circ$) in the incident electron source of the model improved the agreement of the simulated and measured photon dose profiles. This mean angular spread term also resolved the under-prediction of simulated off-axis dose as well as the DTA failures in the penumbra region observed with the medium energy beam models. The determined mean angular spread values agreed closely with the mean angular spread of 1.75° reported by Björk, Knöös, and Nilsson (2002) for a 12-MeV electron beam from a similar Elekta linear accelerator. The results shown in this work have the mean angular spread parameter set to 0° for all beam energies. This was done to fully display the differences in dosimetric qualities between the different scattering foils of the MBPCC accelerators.

3.4   High Energy (16-, 20-MeV) Large-Field Results

The simulated %DD curves for both high energy beam models matched the measured data within the criteria of the hypothesis for the large-field simulations (cf. Figures 3.31 and 3.37). The simulated in-plane (Y) profiles matched the measured in-plane planes within the criteria of the hypothesis at every depth for both high energy beam models. However, for the shallowest cross-plane (X) depths of 2.5 cm at 16-MeV and 3.0 cm at 20-MeV, simulated profiles provided a larger off-axis dose relative to the CAX than measured (cf. Figures 3.33(a), 3.35(a), 3.39(a), and 3.41(a)). The largest difference between measured and simulated doses was on the order of 3% of D$_{max}$. The simulated cross-plane profiles matched the measured data within the criteria of the hypothesis for the deeper cross-plane comparisons. The simulated diagonal profiles at depths of 2 cm for both energies also over-predicted the off-axis dose near the penumbra edge and exhibited a maximum dose difference from the measured diagonal profiles on the order of 4% of D$_{max}$ (cf. Figures 3.32 and 3.38).

The simulated Bremsstrahlung dose profiles under-predicted the shape of the measured photon dose profiles for both energies (cf. Figures 3.33(e), 3.35(e), 3.39(e), and 3.41(e)). Including a mean angular spread ($\sim 2°$) in the incident electron source of the model could improve the agreement of the simulated and measured photon dose profiles. However, adding angular spread to the initial electron source greatly increased the off-axis dose relative to the CAX for the simulated cross-beam profiles. This parameter would ruin the agreement observed between the simulated and measured cross-beam profile data for the high energy beams.

3.5   7-MeV Large-Field Results
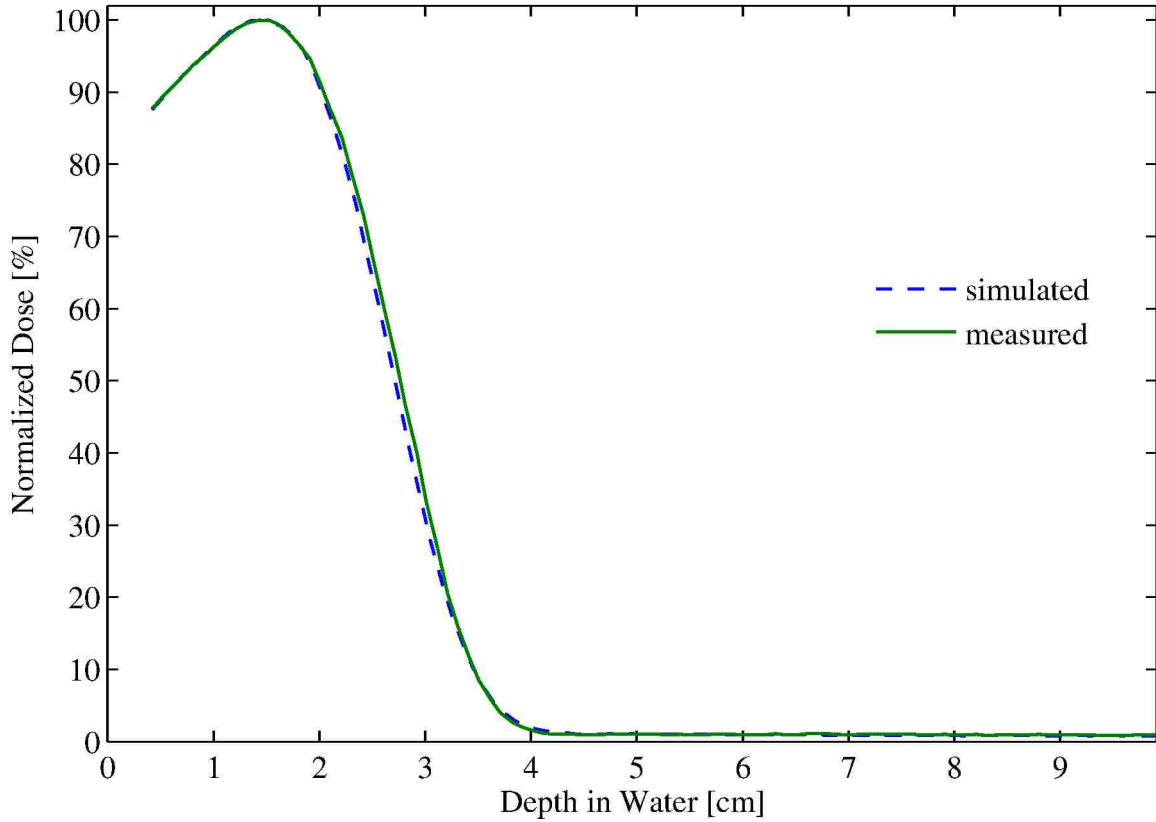
Figure 3.1: %DD: 7MeV - 25x25 cm^2 applicator

Table 3.2: 7MeV-25x25 cm^2 applicator comparison summary

Profile type (%DD, X, Y)	Profile depth (cm)	Percent of points passing		
		2%/1mm	2%/2mm	3%/3mm
%DD	–	100.0%	–	–
Diagonal	1.0	66.7%	75.0%	100.0%
Cross-plane (X)	1.0	92.4%	93.1%	100.0%
	2.0	99.3%	99.3%	100.0%
	2.5	100.0%	–	–
	2.8	100.0%	–	–
	5.5	100.0%	–	–
In-plane (Y)	1.0	95.9%	95.9%	100.0%
	2.0	96.6%	97.2%	100.0%
	2.5	96.6%	96.6%	100.0%
	2.8	100.0%	–	–
	5.5	100.0%	–	–
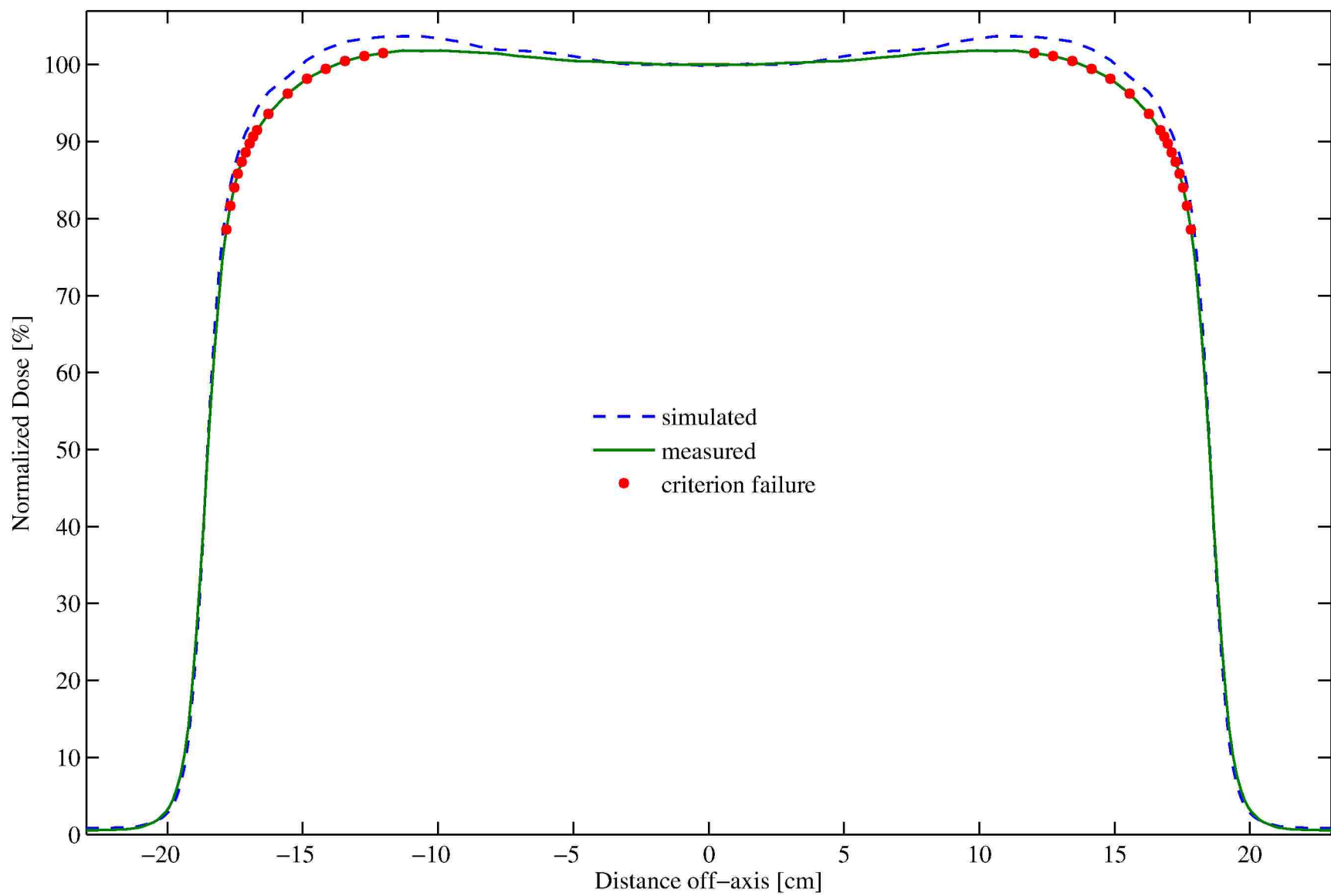
Figure 3.2: Diagonal profile: 7MeV - 25x25 cm^2 applicator at z=1 cm

(a) z=1.0 cm

(b) z=2.0 cm

(c) z=2.5 cm

(d) z=2.8 cm

(e) z=5.5 cm
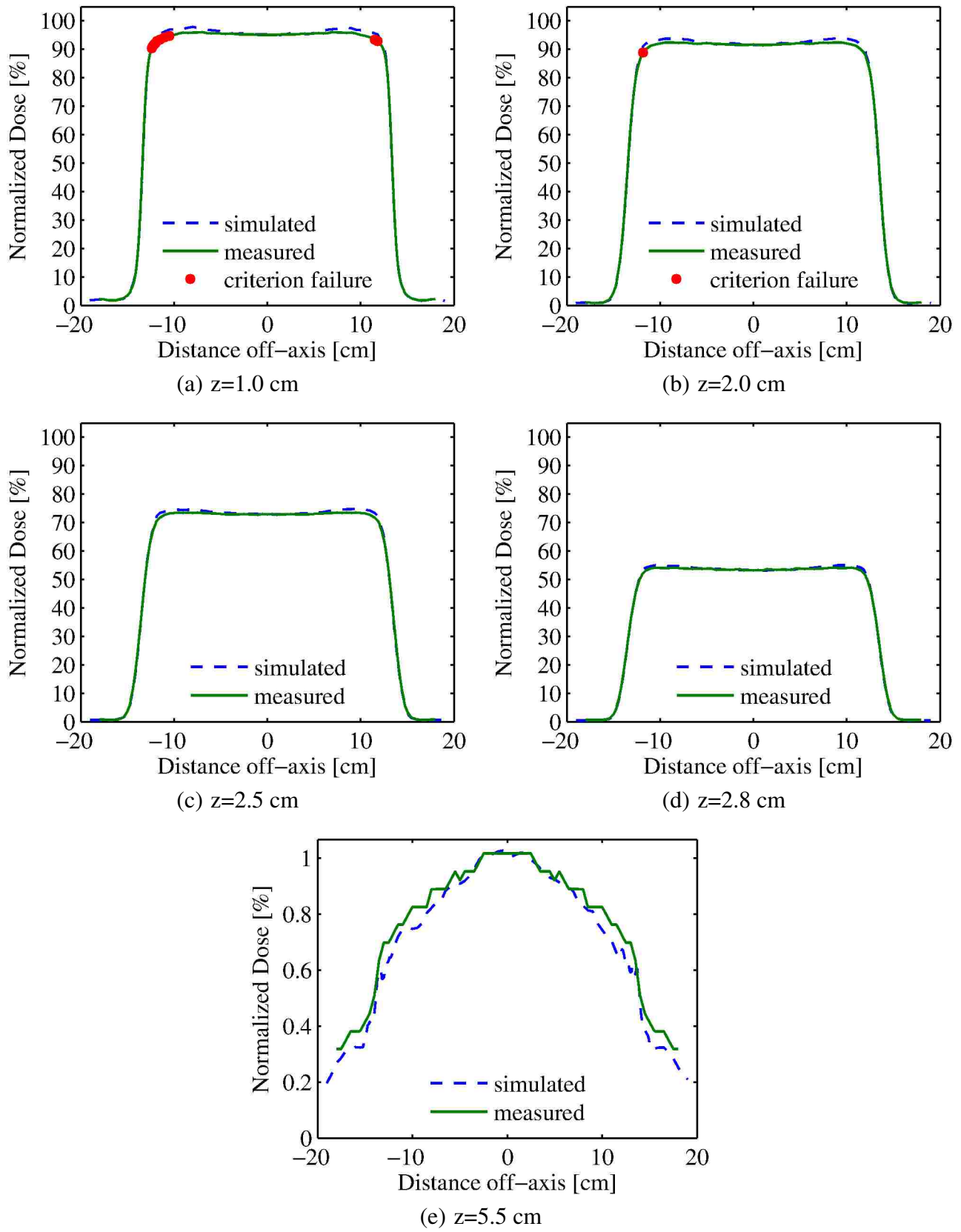
Figure 3.3: 7MeV-25x25 cm^2 cross-plane (X) profiles at five depths (1.0, 2.0, 2.5, 2.8, and 5.5 cm)
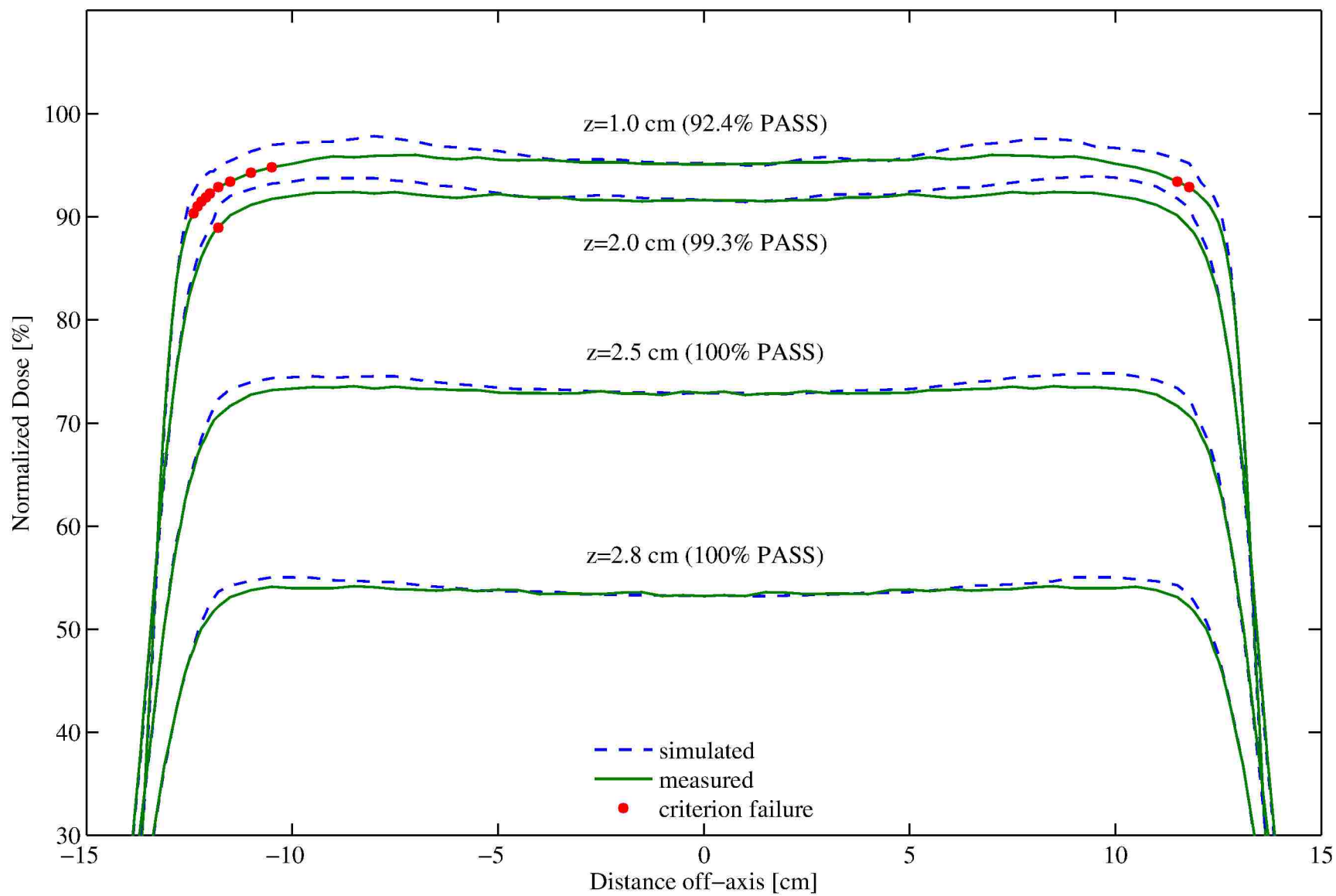
Figure 3.4: 7MeV-25x25 cm^2 cross-plane (X) profiles: zoomed view of Figure 3.3(a)-(d)

(a) z=1.0 cm

(b) z=2.0 cm

(c) z=2.5 cm

(d) z=2.8 cm

(e) z=5.5 cm
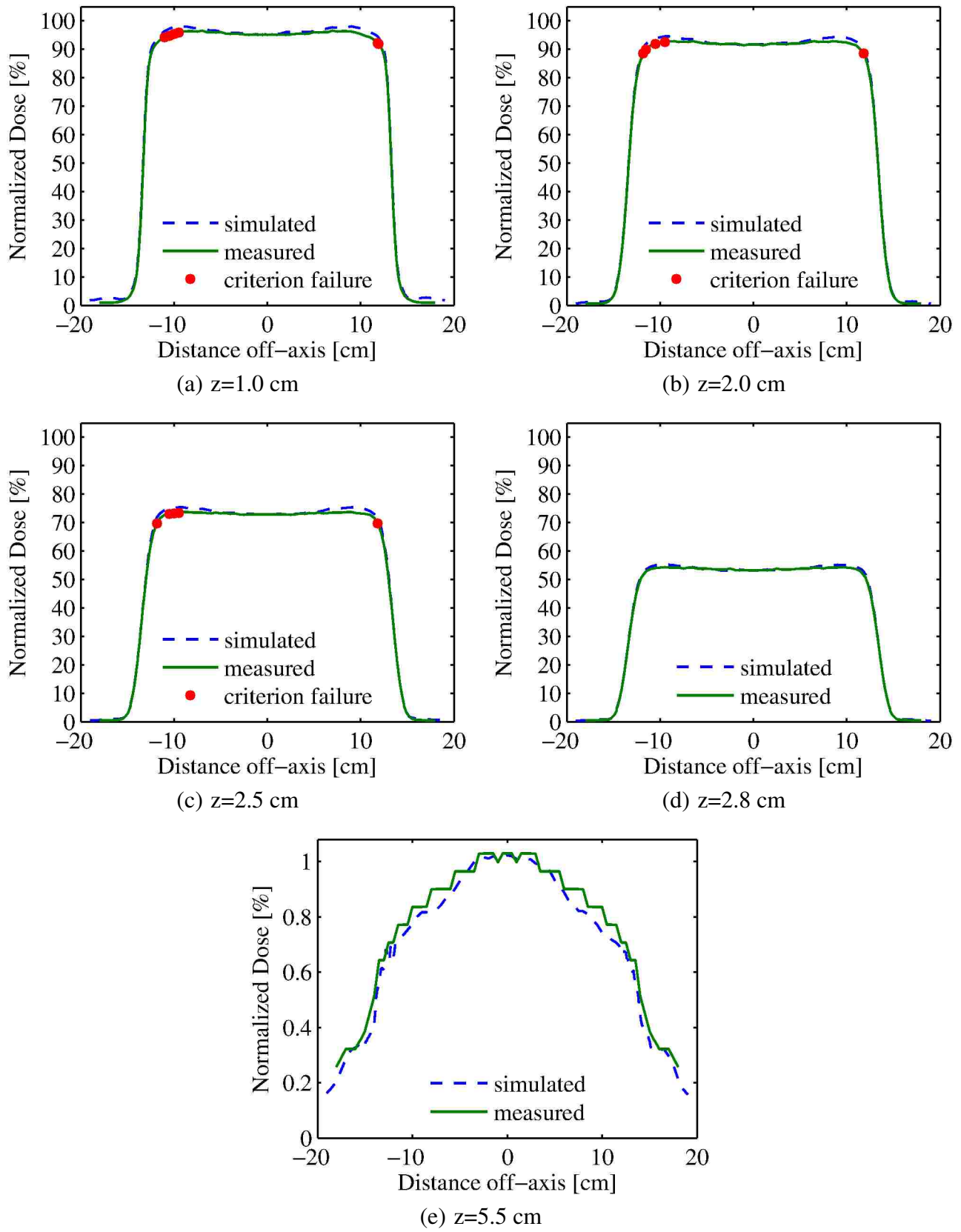
Figure 3.5: 7MeV-25x25 cm^2 in-plane (Y) profiles at five depths (1.0, 2.0, 2.5, 2.8, and 5.5 cm)
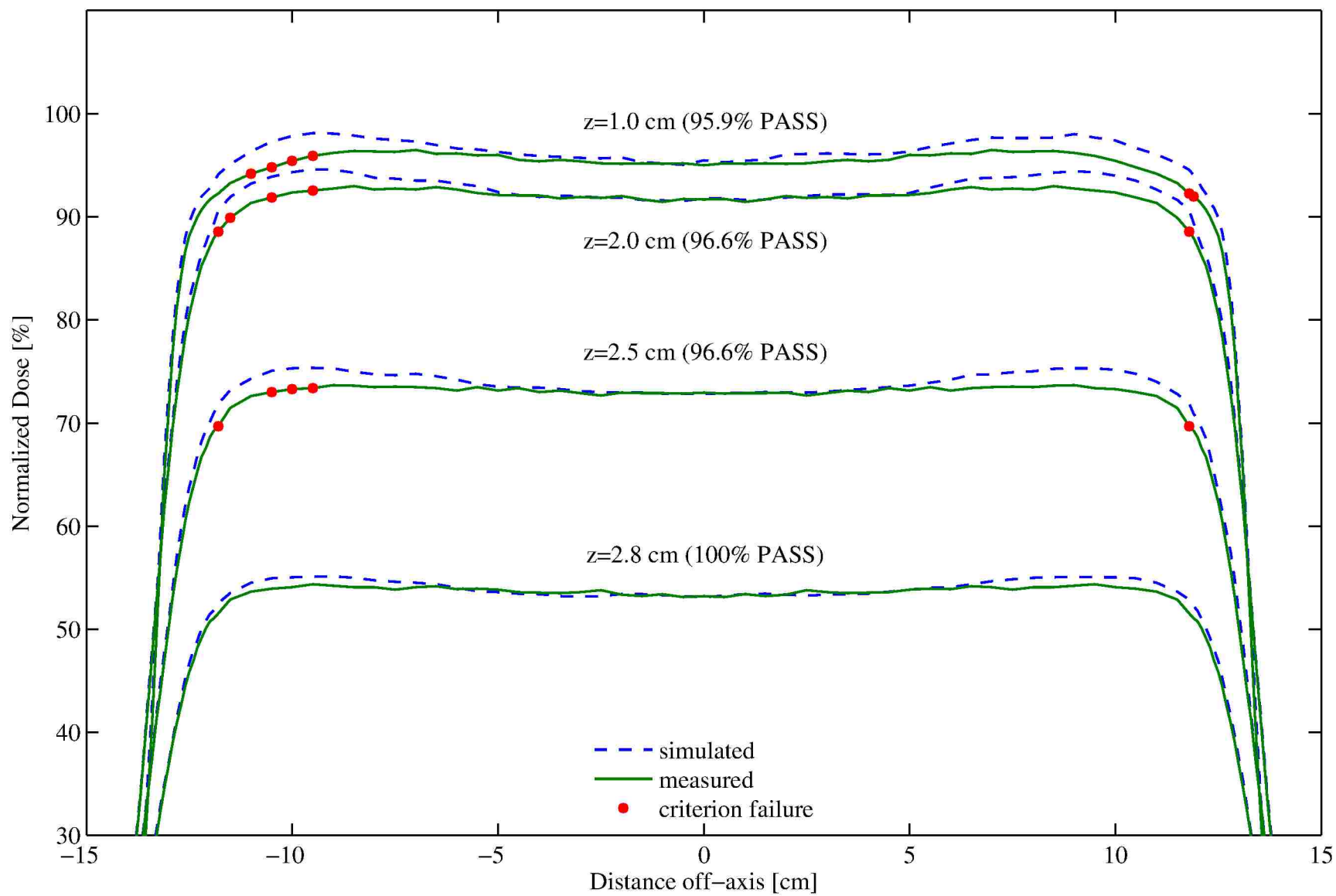
Figure 3.6: 7MeV-25x25 cm^2 in-plane (Y) profiles: zoomed view of Figure 3.5(a)-(d)

3.6 9-MeV Large-Field Results
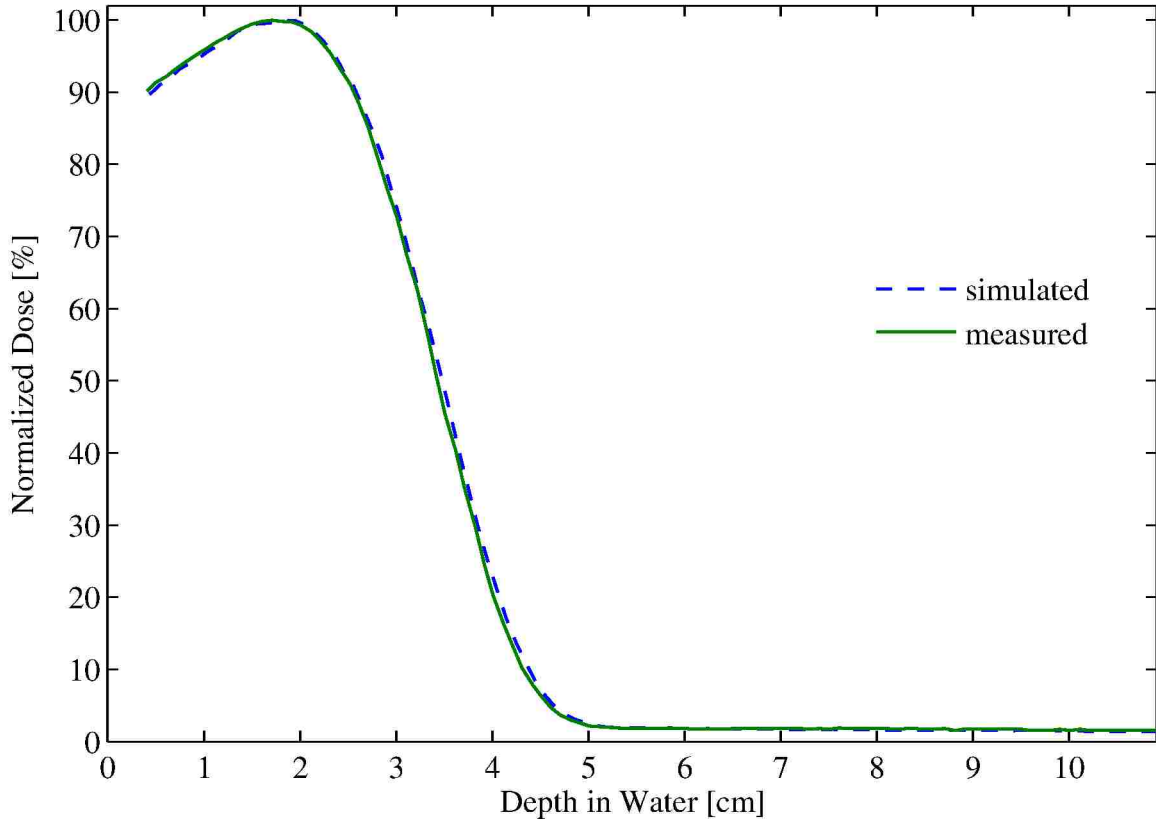
Figure 3.7: %DD: 9MeV - 25x25 cm^2 applicator

Table 3.3: 9MeV-25x25 cm^2 applicator comparison summary

Profile type (%DD, X, Y)	Profile depth (cm)	Percent of points passing		
		2%/1mm	2%/2mm	3%/3mm
%DD	–	100.0%	–	–
Diagonal	1.0	69.8%	75.5%	86.8%
Cross-plane (X)	1.3	91.0%	91.0%	100.0%
	2.6	98.6%	98.6%	100.0%
	3.1	100.0%	–	–
	3.4	100.0%	–	–
	6.3	100.0%	–	–
In-plane (Y)	1.3	81.4%	84.1%	98.6%
	2.6	96.6%	97.9%	100.0%
	3.1	99.3%	99.3%	100.0%
	3.4	97.9%	99.3%	100.0%
	6.3	100.0%	–	–
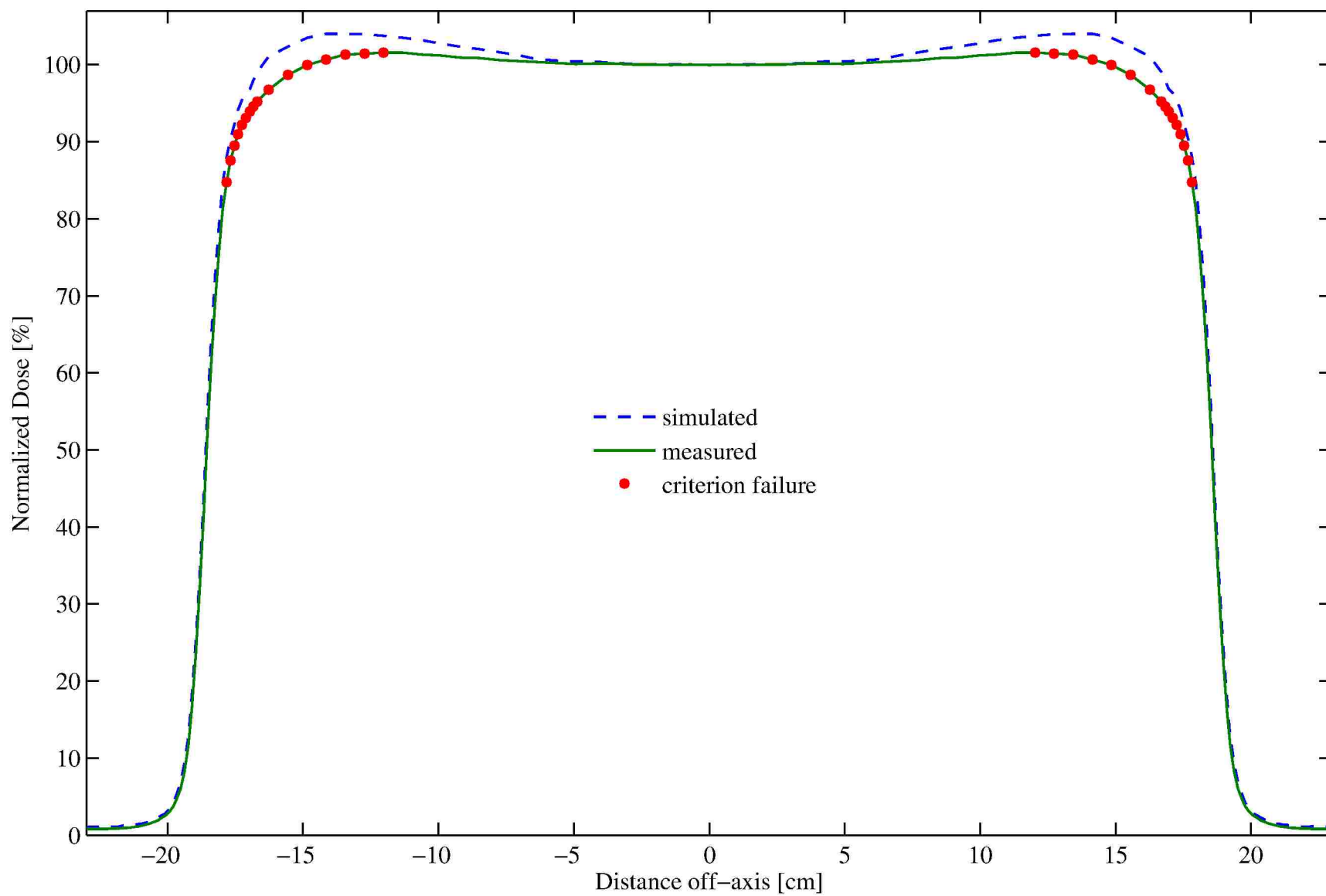
Figure 3.8: Diagonal profile: 9MeV - 25x25 cm^2 applicator at z=1 cm
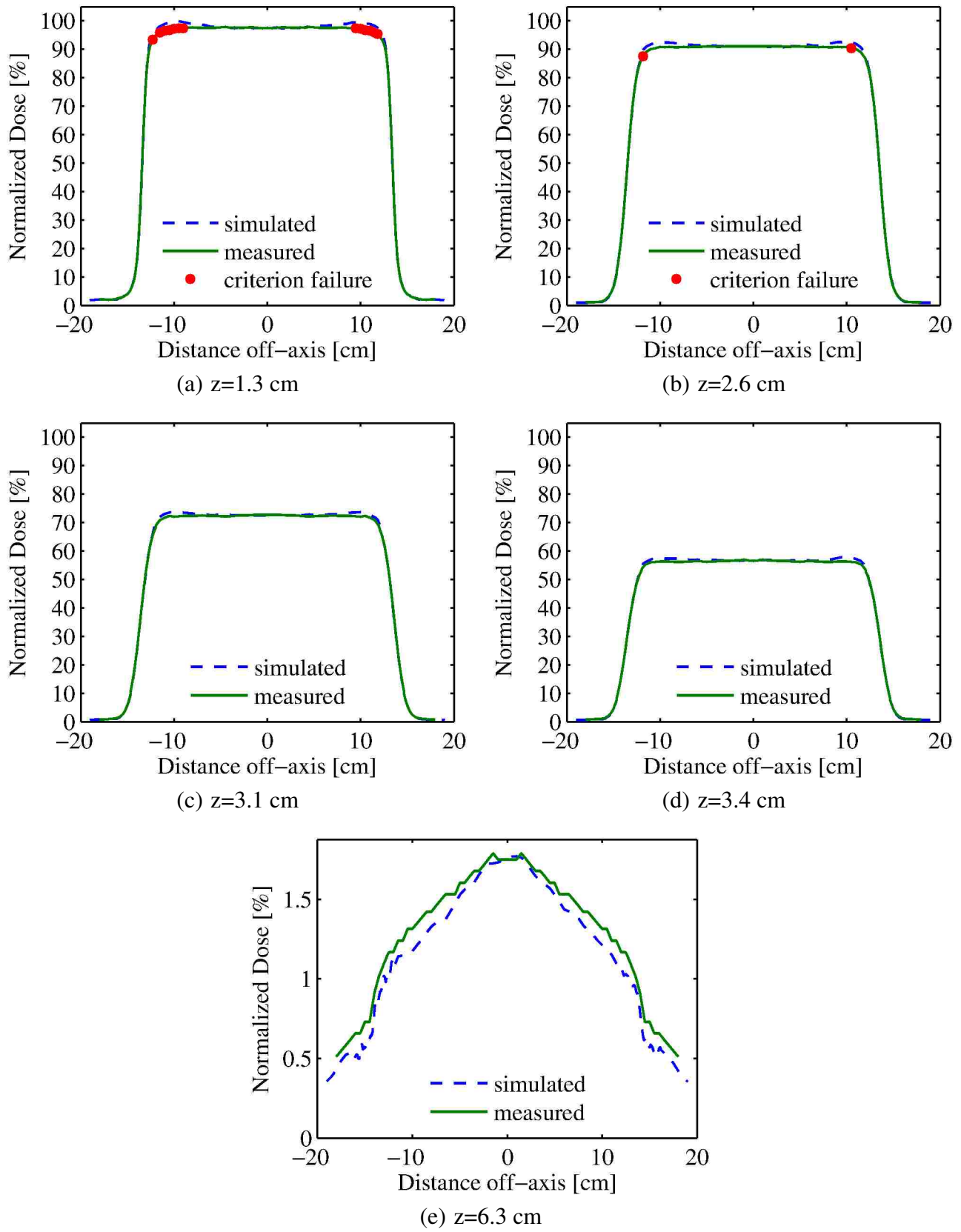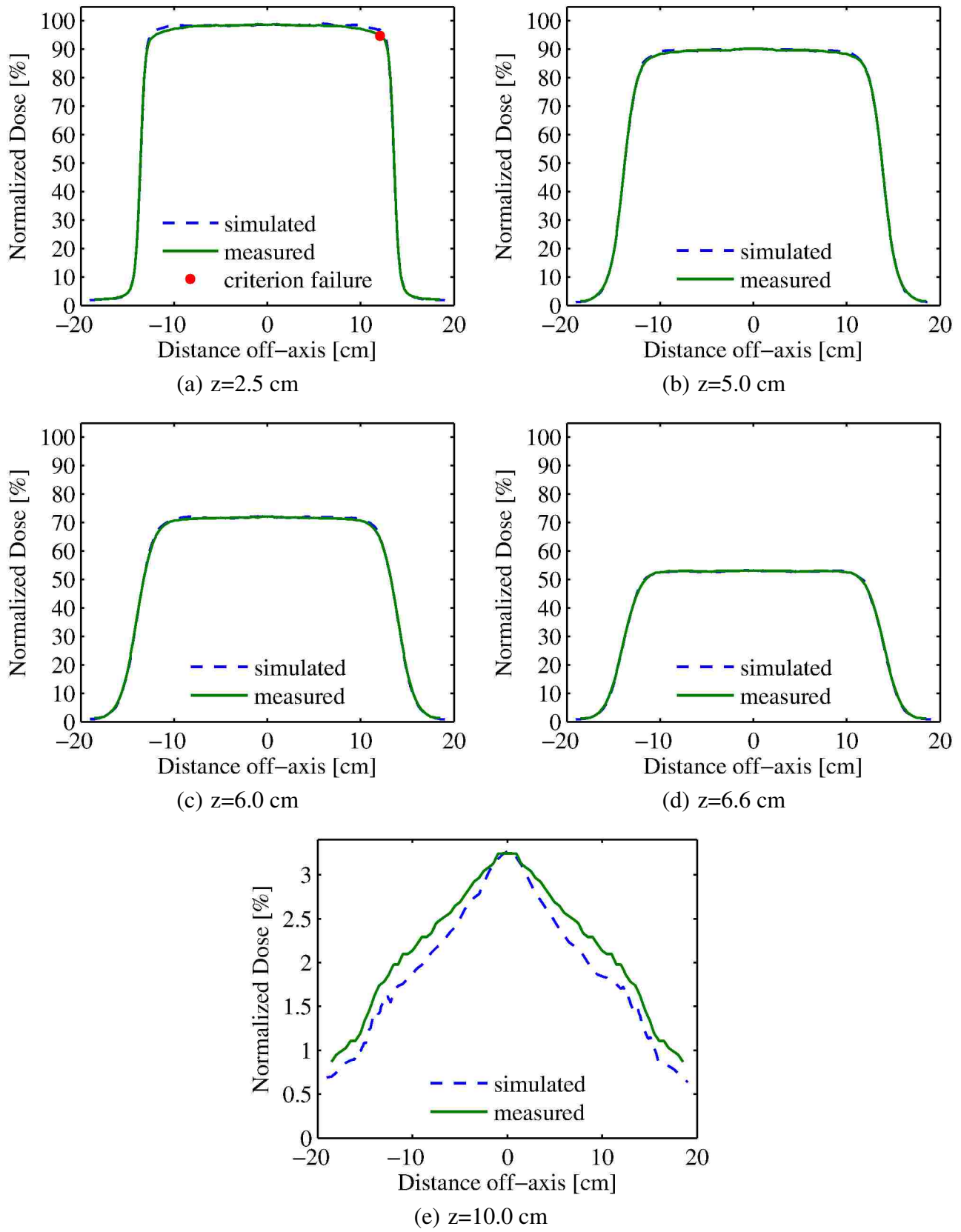
Figure 3.9: 9MeV-25x25 cm^2 cross-plane (X) profiles at five depths (1.3, 2.6, 3.1, 3.4, and 6.3 cm)
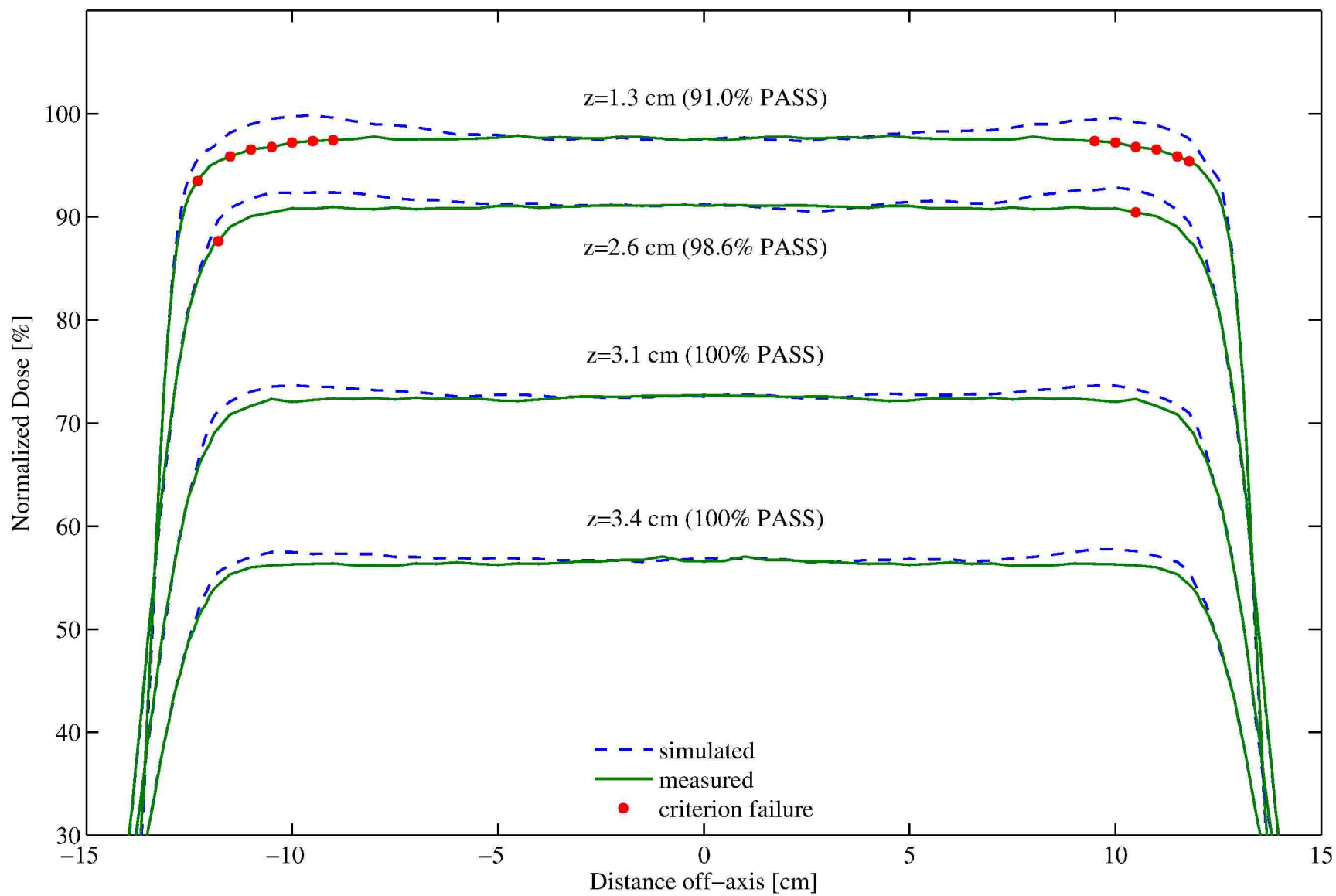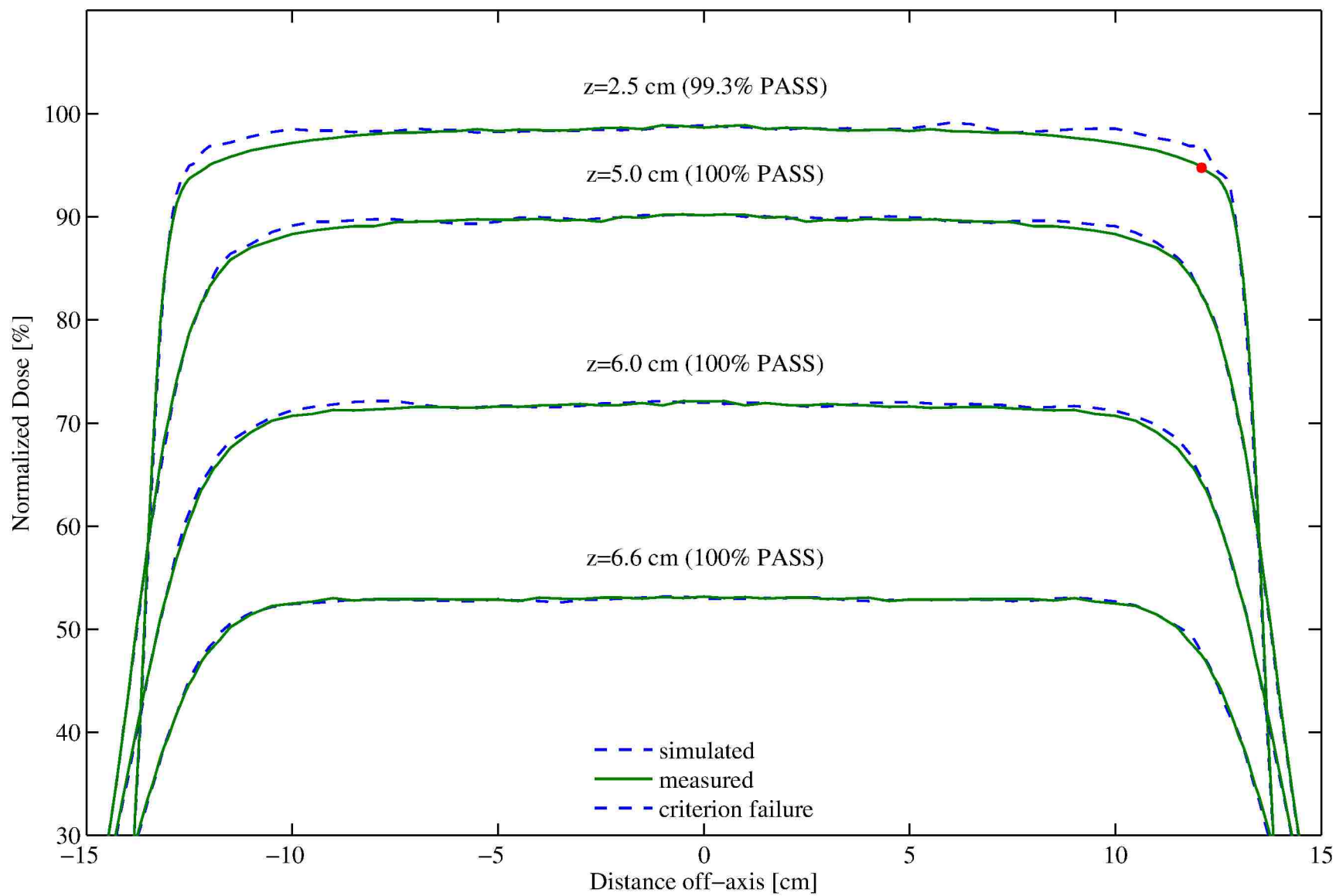
Figure 3.10: 9MeV-25x25 cm^2 cross-plane (X) profiles: zoomed view of Figure 3.9(a)-(d)

(a) z=1.3 cm

(b) z=2.6 cm

(c) z=3.1 cm

(d) z=3.4 cm

(e) z=6.3 cm
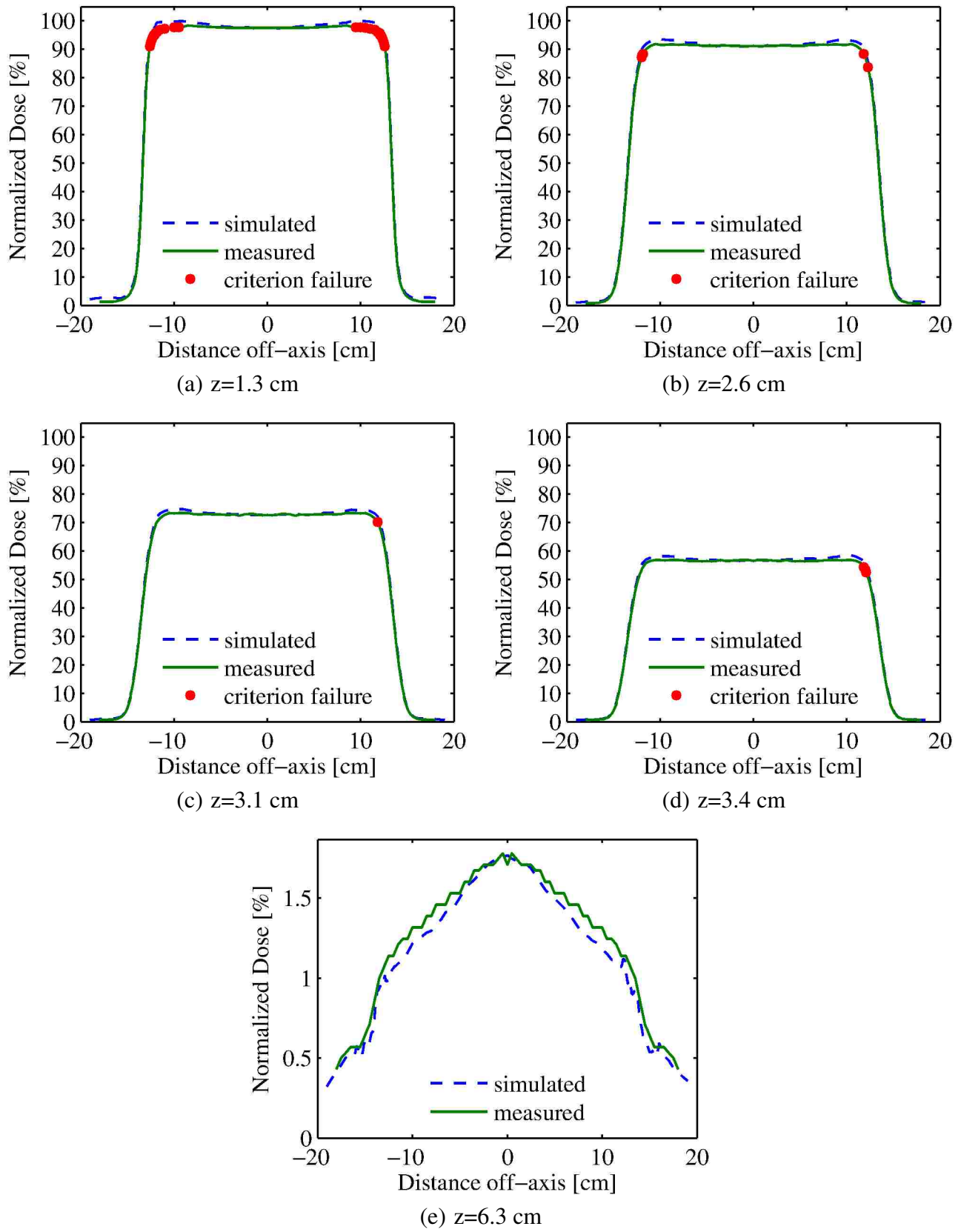
Figure 3.11: 9MeV-25x25 cm^2 in-plane (Y) profiles at five depths (1.3, 2.6, 3.1, 3.4, and 6.3 cm)
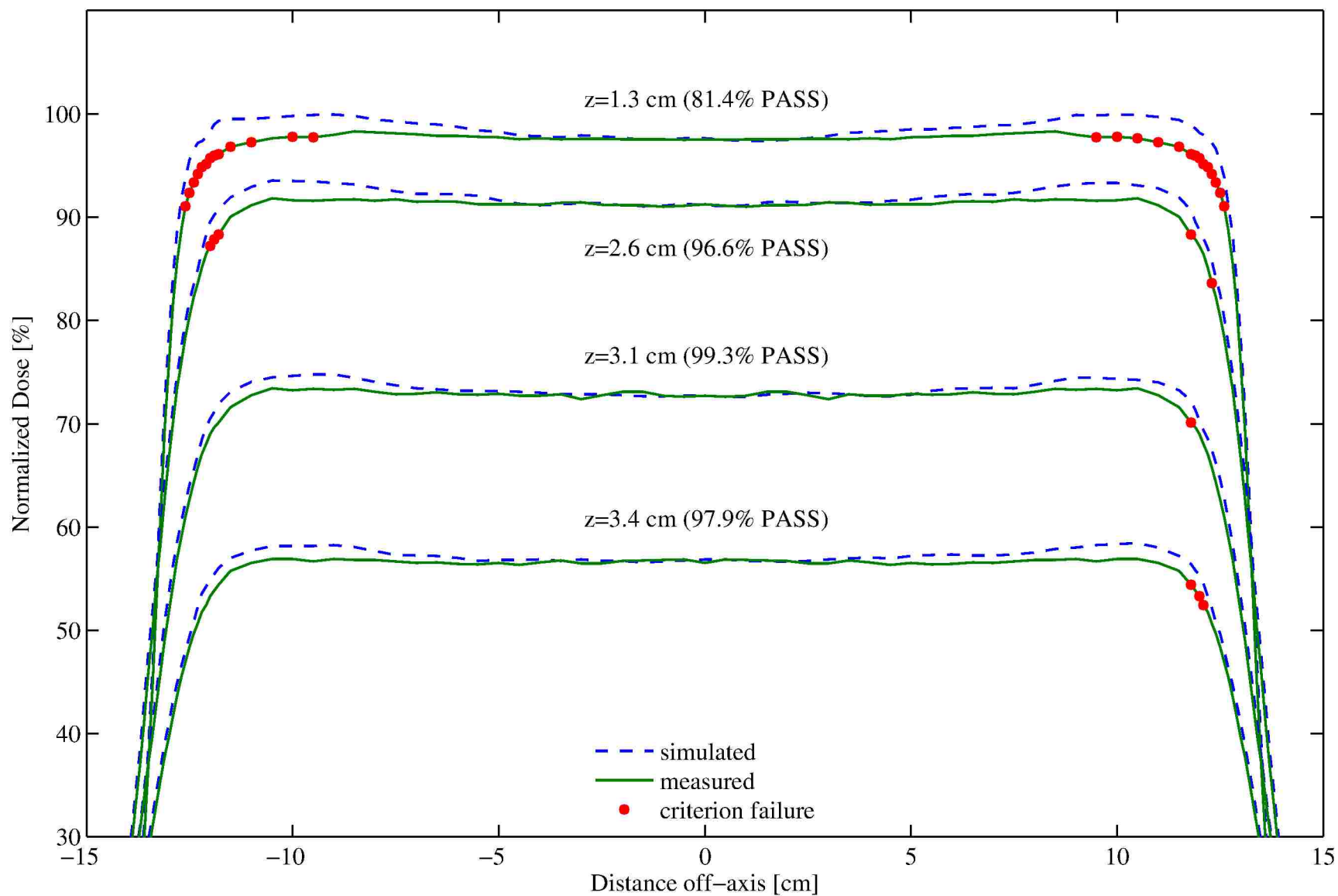
Figure 3.12: 9MeV-25x25 cm^2 in-plane (Y) profiles: zoomed view of Figure 3.11(a)-(d)
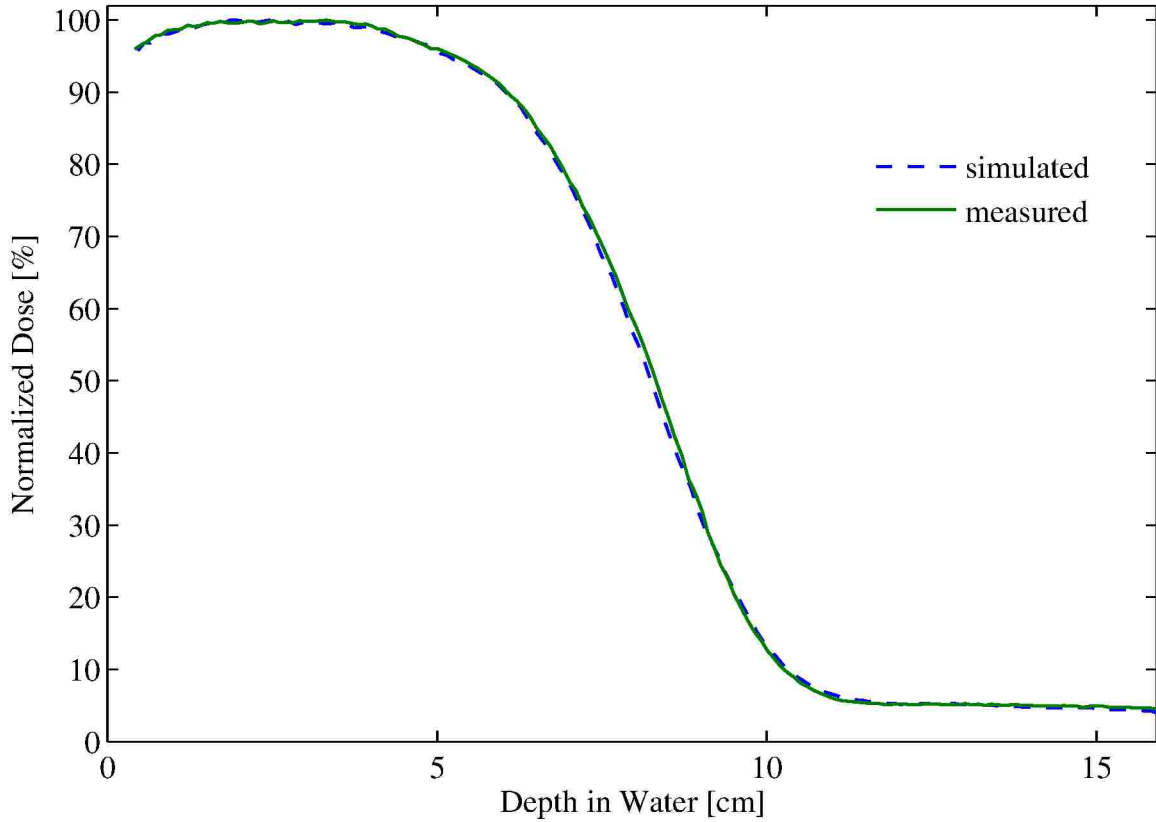
3.7 10-MeV Large-Field Results
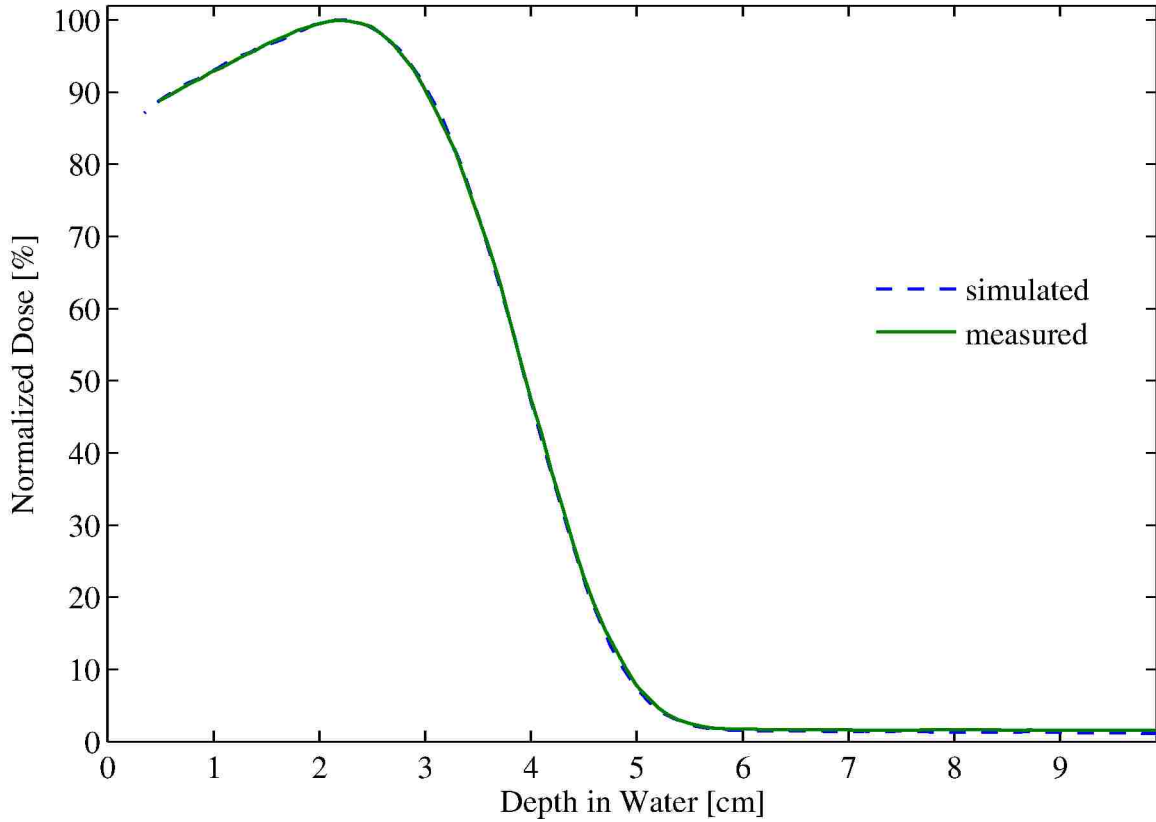
Figure 3.13: %DD: 10MeV - 25x25 cm^2 applicator

Table 3.4: 10MeV-25x25 cm^2 applicator comparison summary

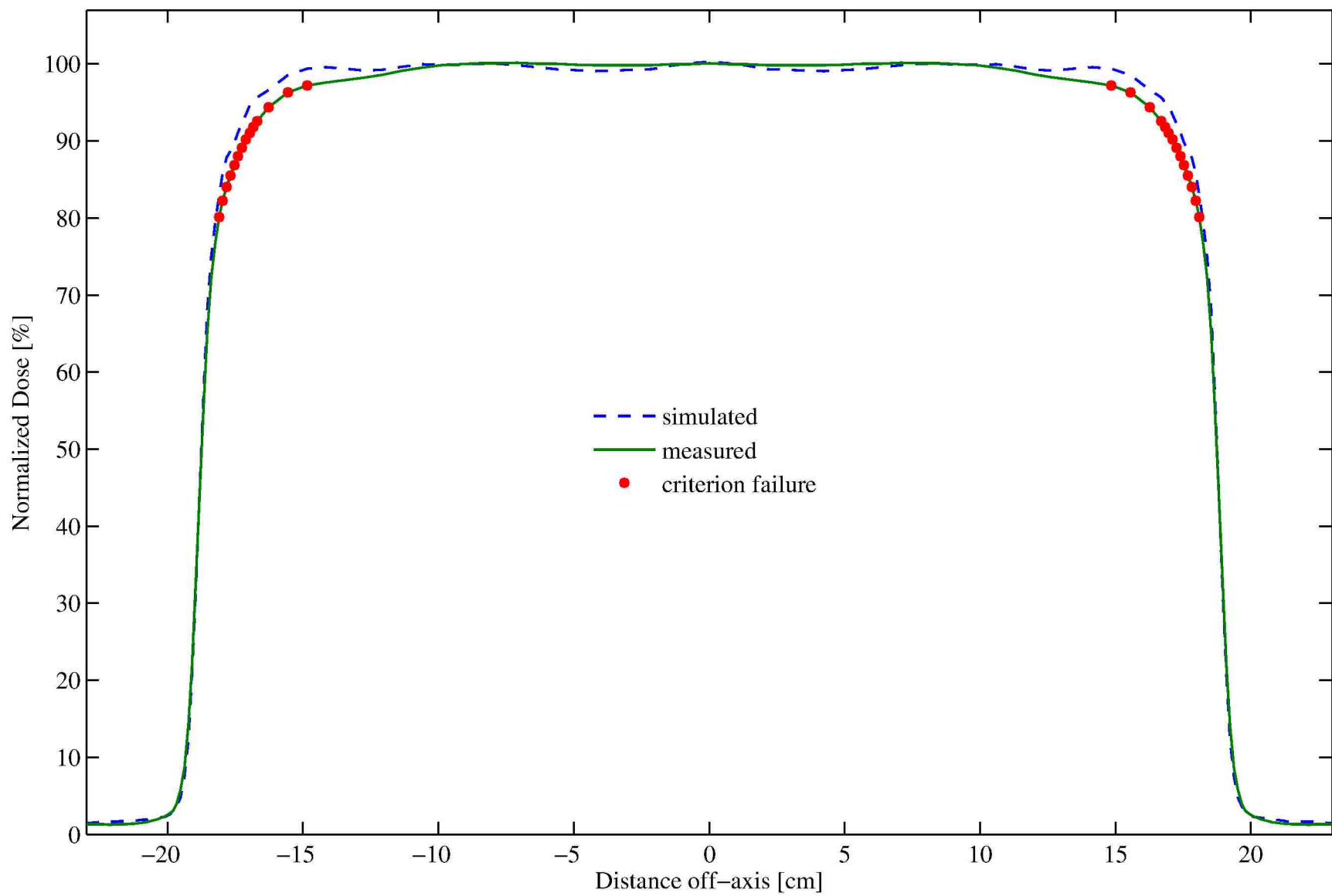| Profile type (%DD, X, Y)	Profile depth (cm)	Percent of points passing		
		2%/1mm	2%/2mm	3%/3mm
%DD	–	100.0%	–	–
Diagonal	1.0	83.2%	85.3%	97.9%
Cross-plane (X)	1.5	99.3%	100.0%	–
	3.0	94.6%	100.0%	–
	3.6	94.6%	100.0%	–
	4.0	100.0%	–	–
	6.9	100.0%	–	–
In-plane (Y)	1.5	100.0%	–	–
	3.0	99.3%	100.0%	–
	3.6	100.0%	–	–
	4.0	100.0%	–	–
	6.9	100.0%	–	–
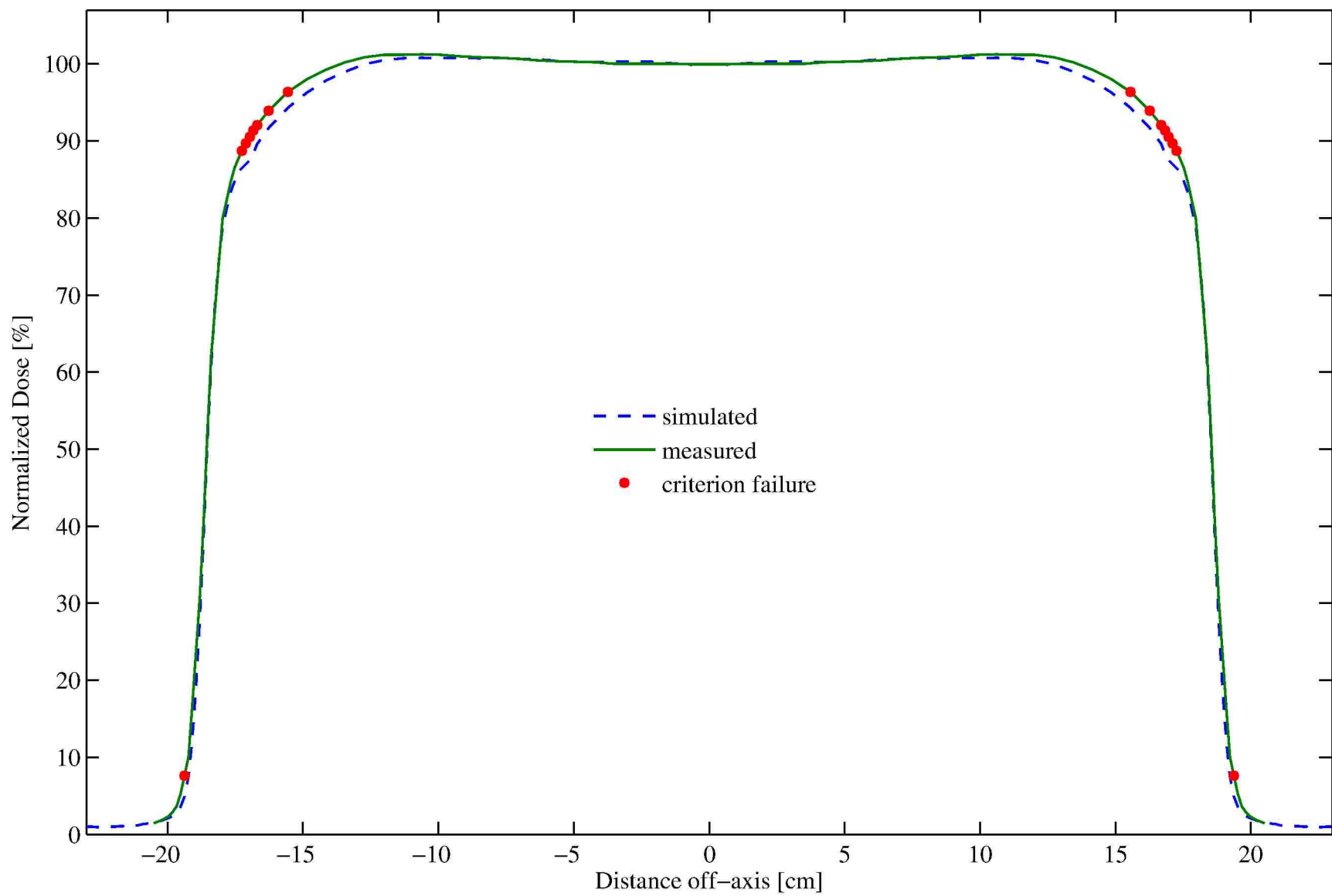
Figure 3.14: Diagonal profile: 10MeV - 25x25 cm^2 applicator at z=1 cm
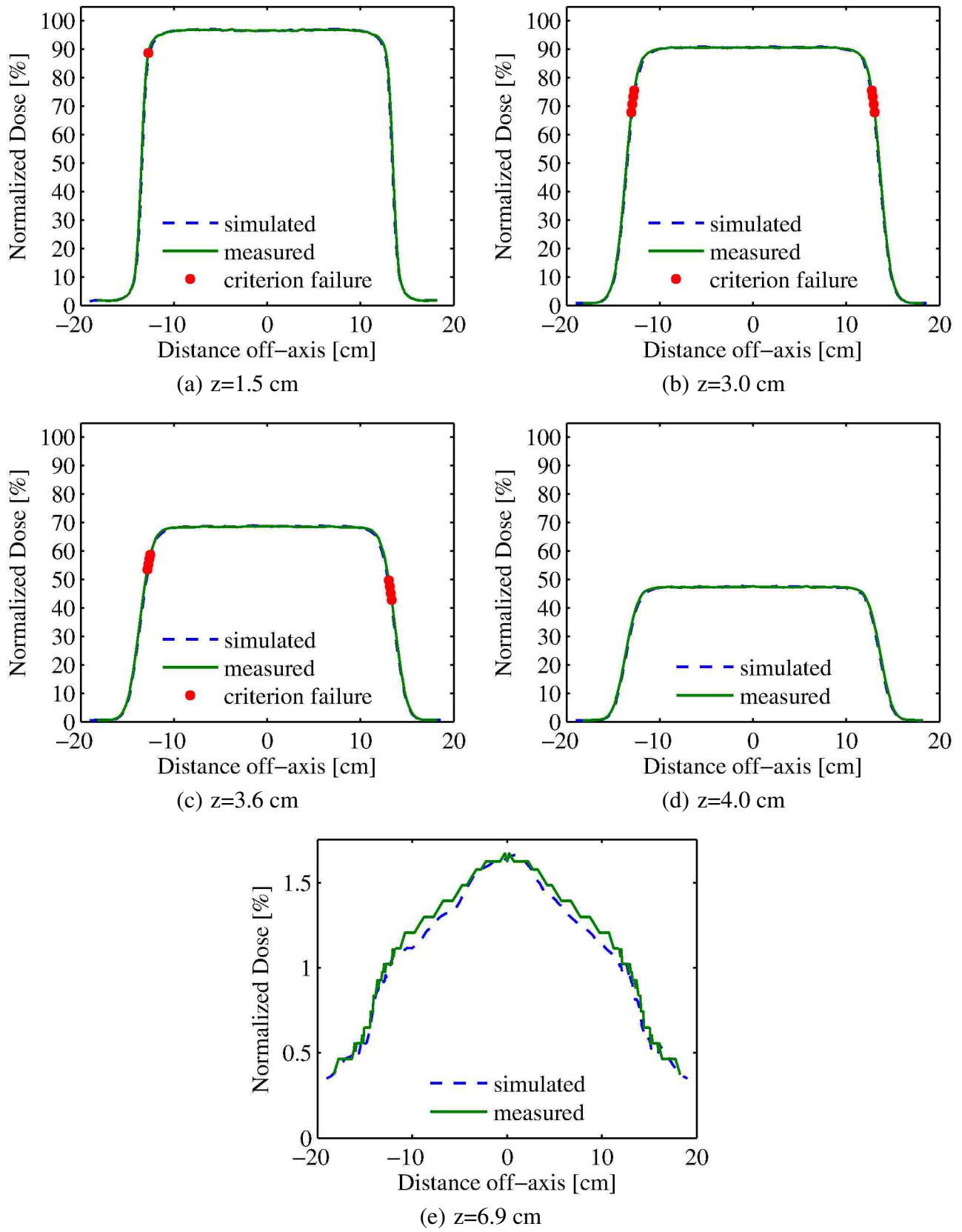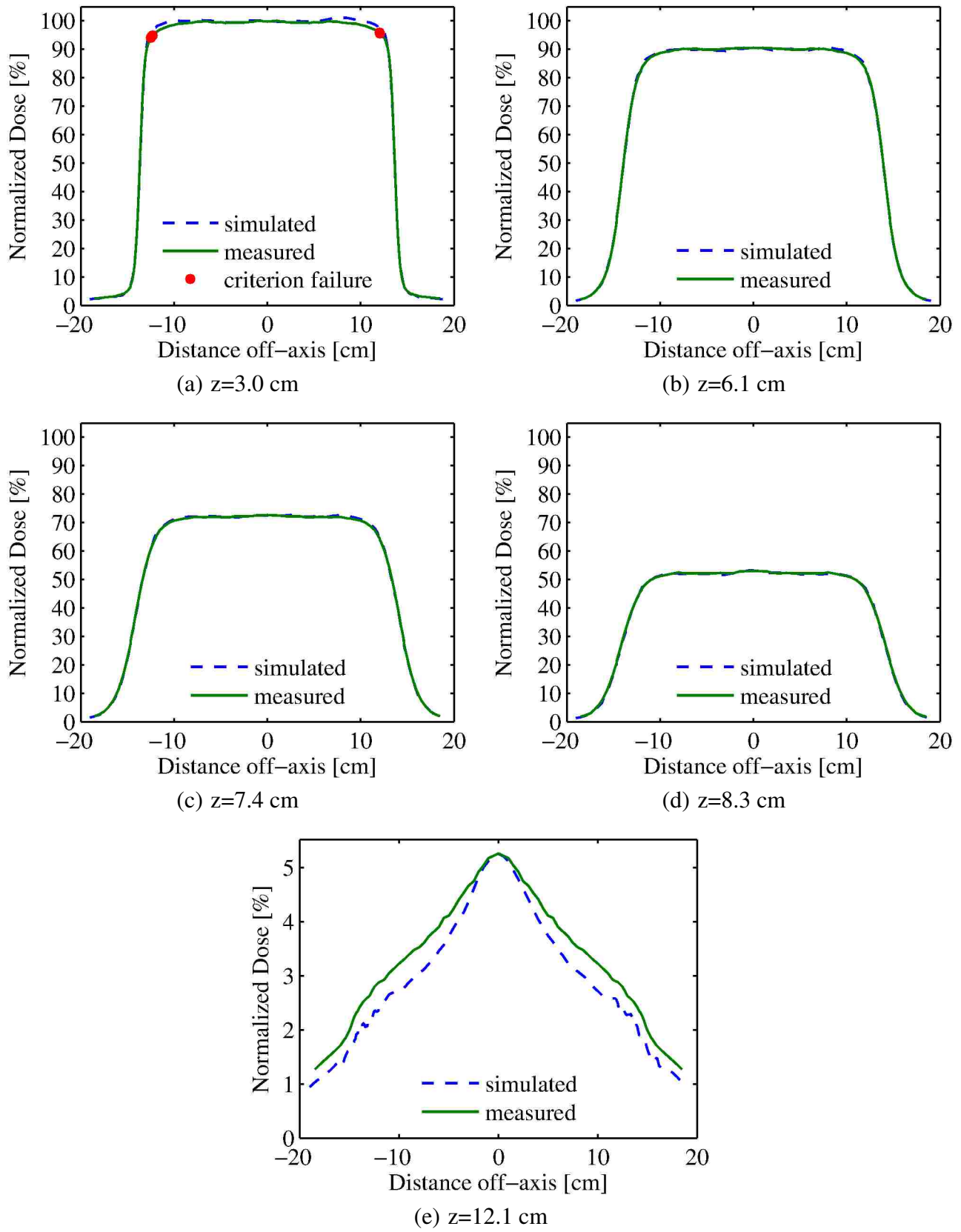
Figure 3.15: 10MeV-25x25 cm^2 cross-plane (X) profiles at five depths (1.5, 3.0, 3.6, 4.0, and 6.9 cm)
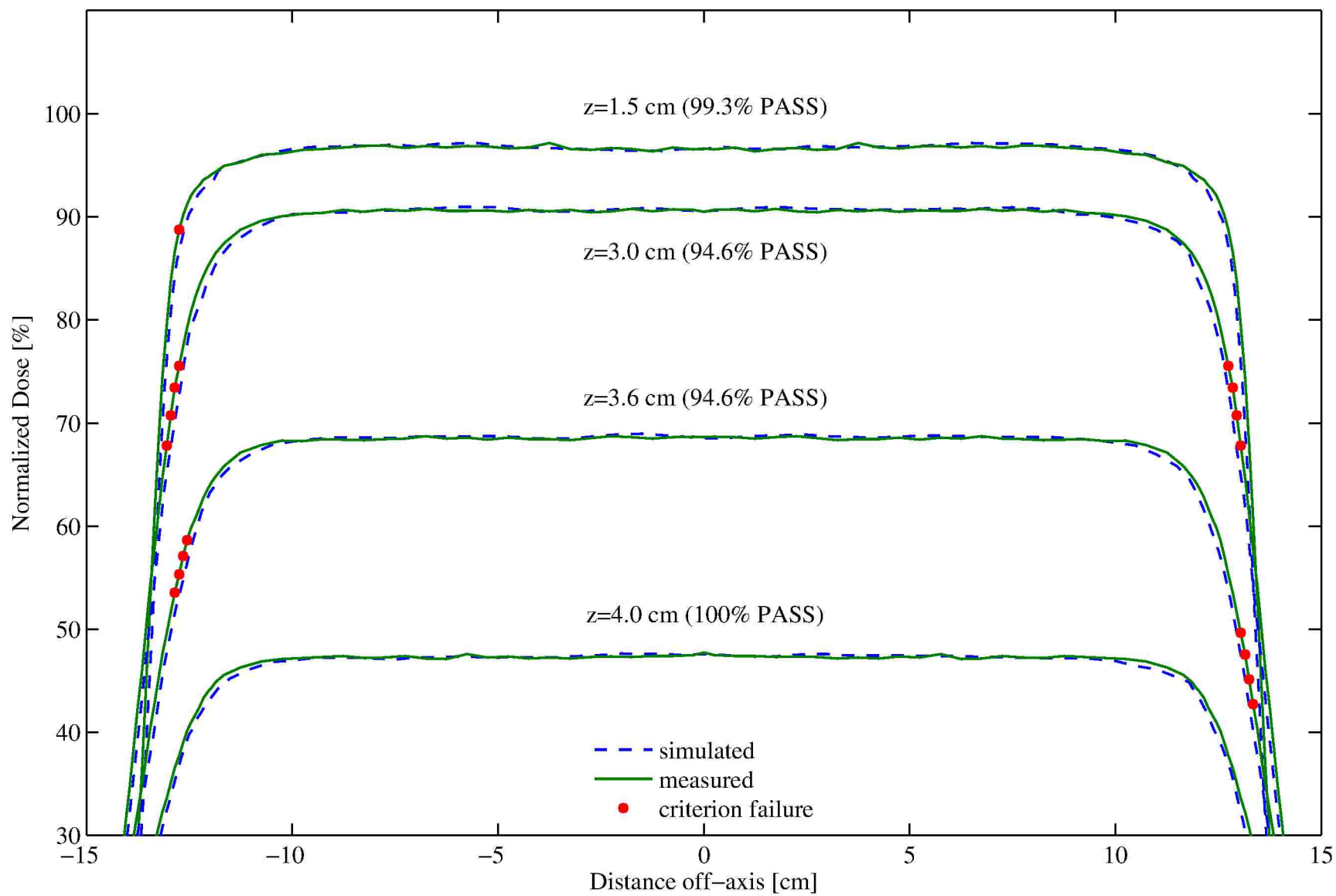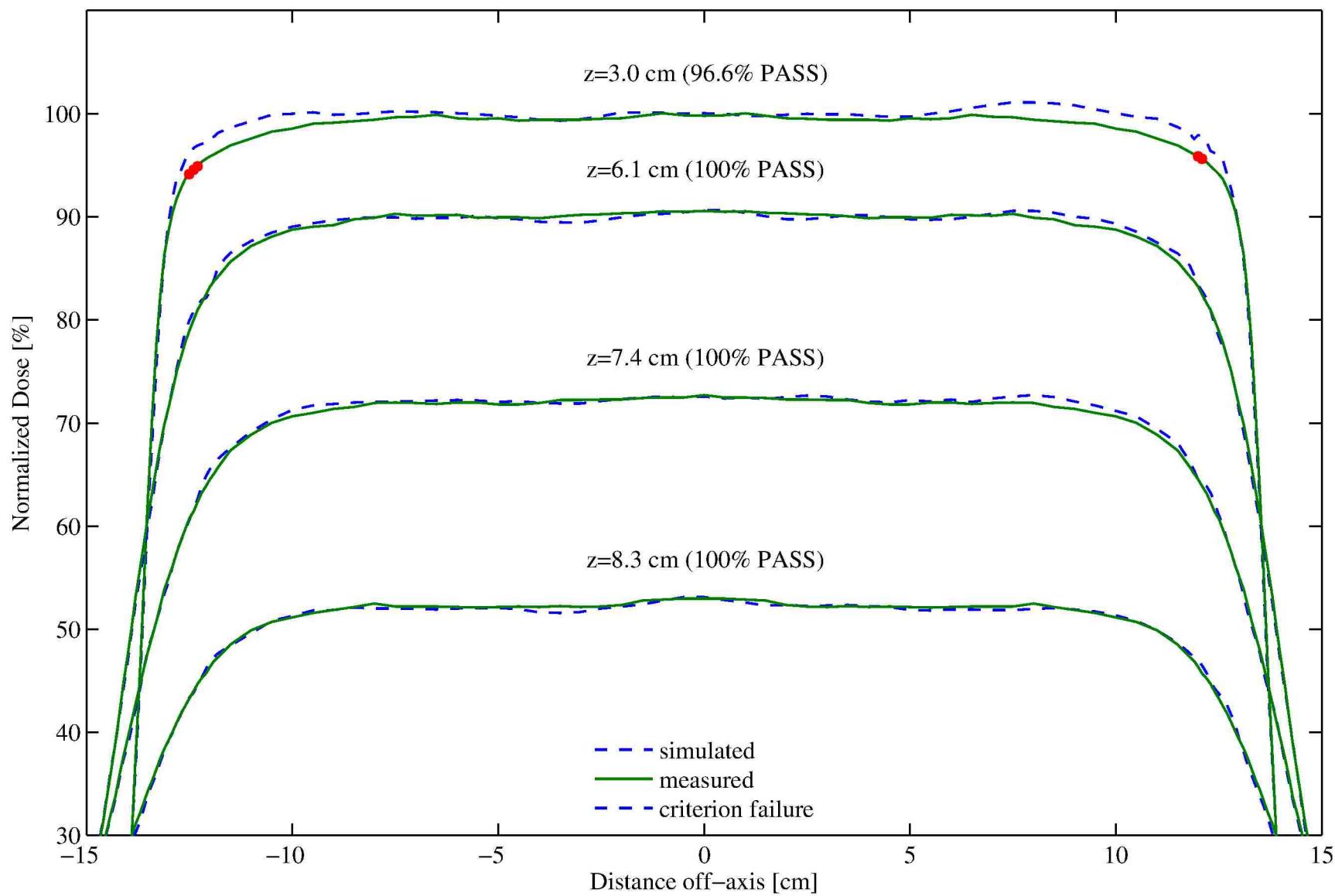
Figure 3.16: 10MeV-25x25 cm^2 cross-plane (X) profiles: zoomed view of Figure 3.15(a)-(d)
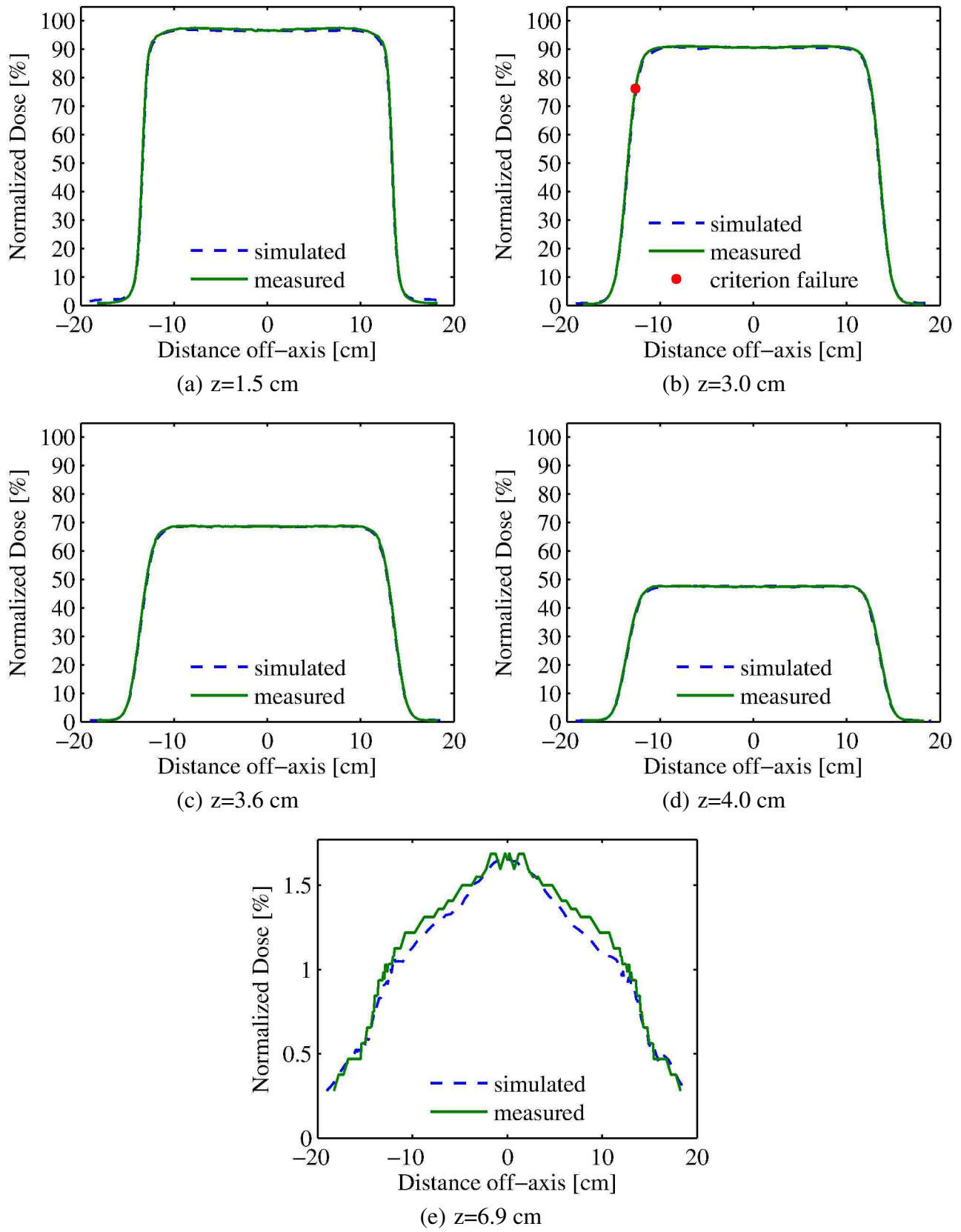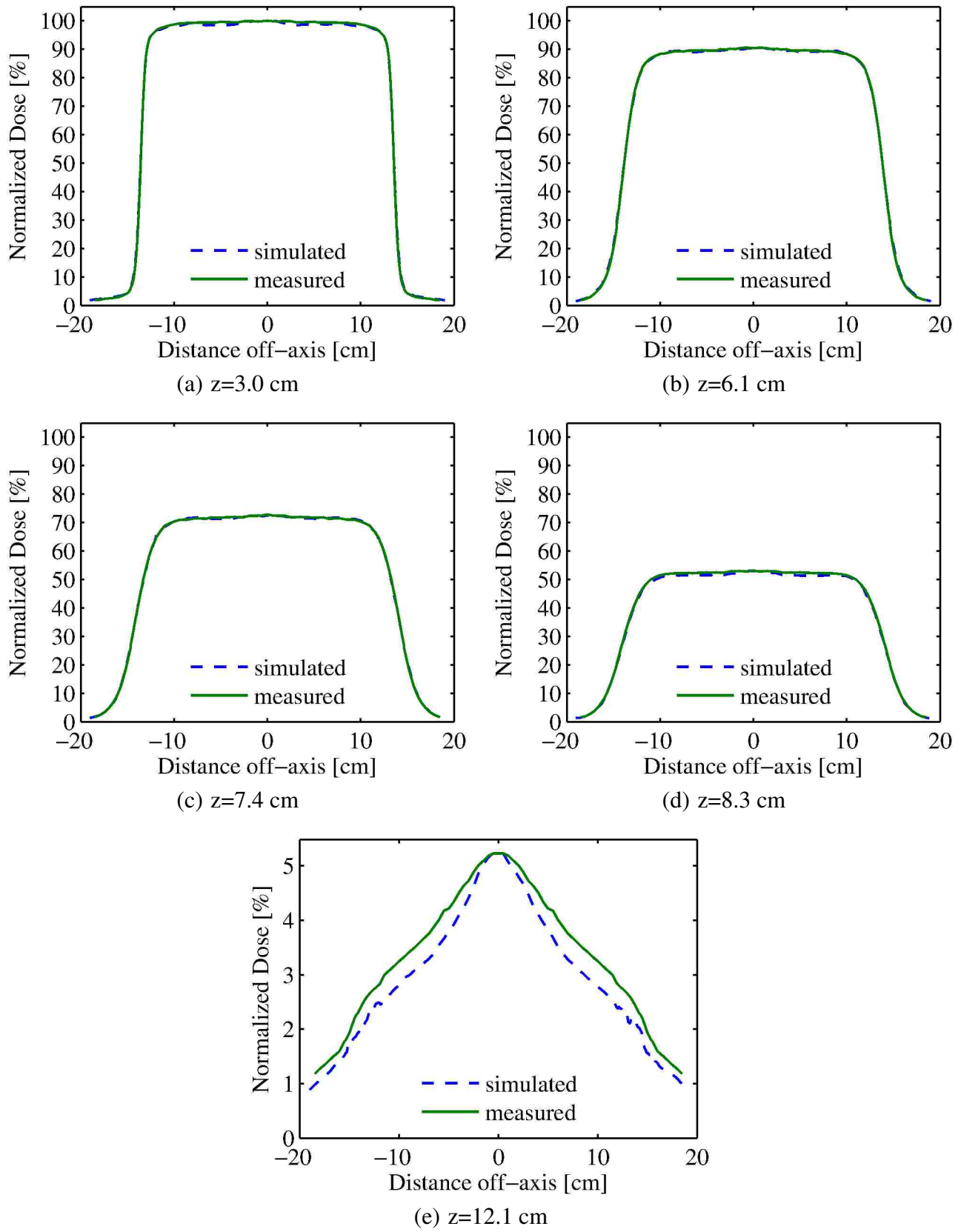
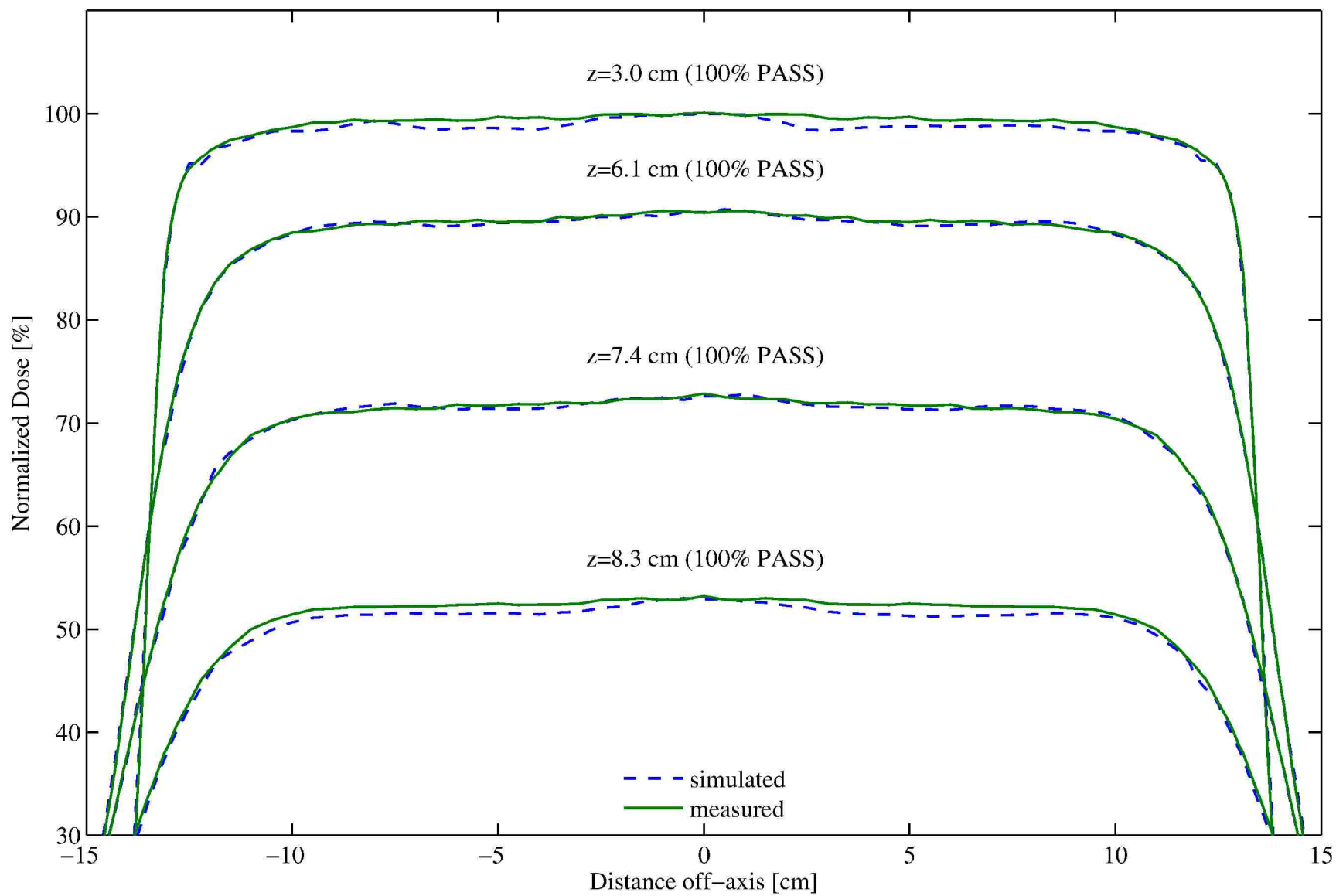Figure 3.17: 10MeV-25x25 cm^2 in-plane (Y) profiles at five depths (1.5, 3.0, 3.6, 4.0, and 6.9 cm)
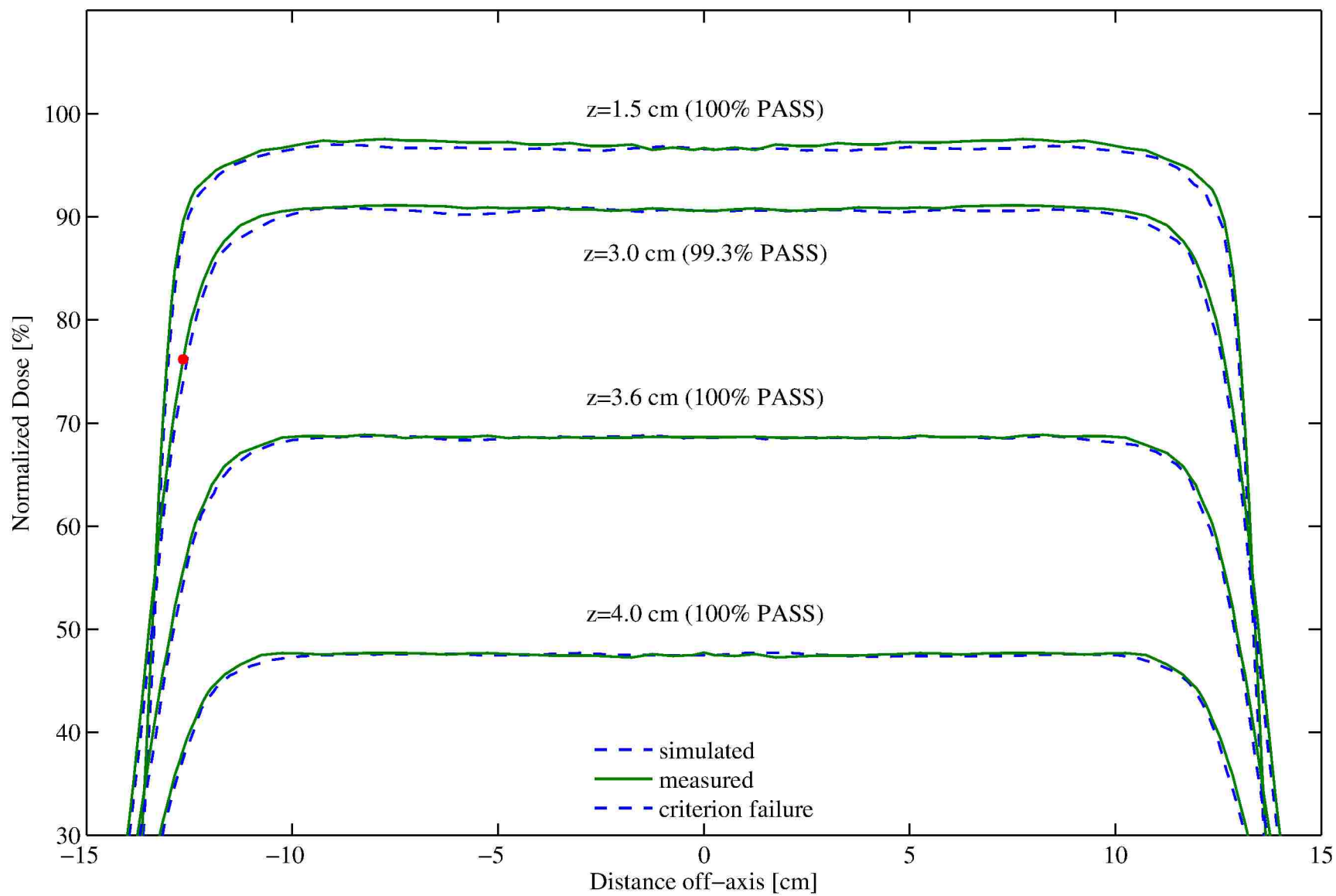
Figure 3.18: 10MeV-25x25 cm^2 in-plane (Y) profiles: zoomed view of Figure 3.17(a)-(d)

3.8   11-MeV Large-Field Results
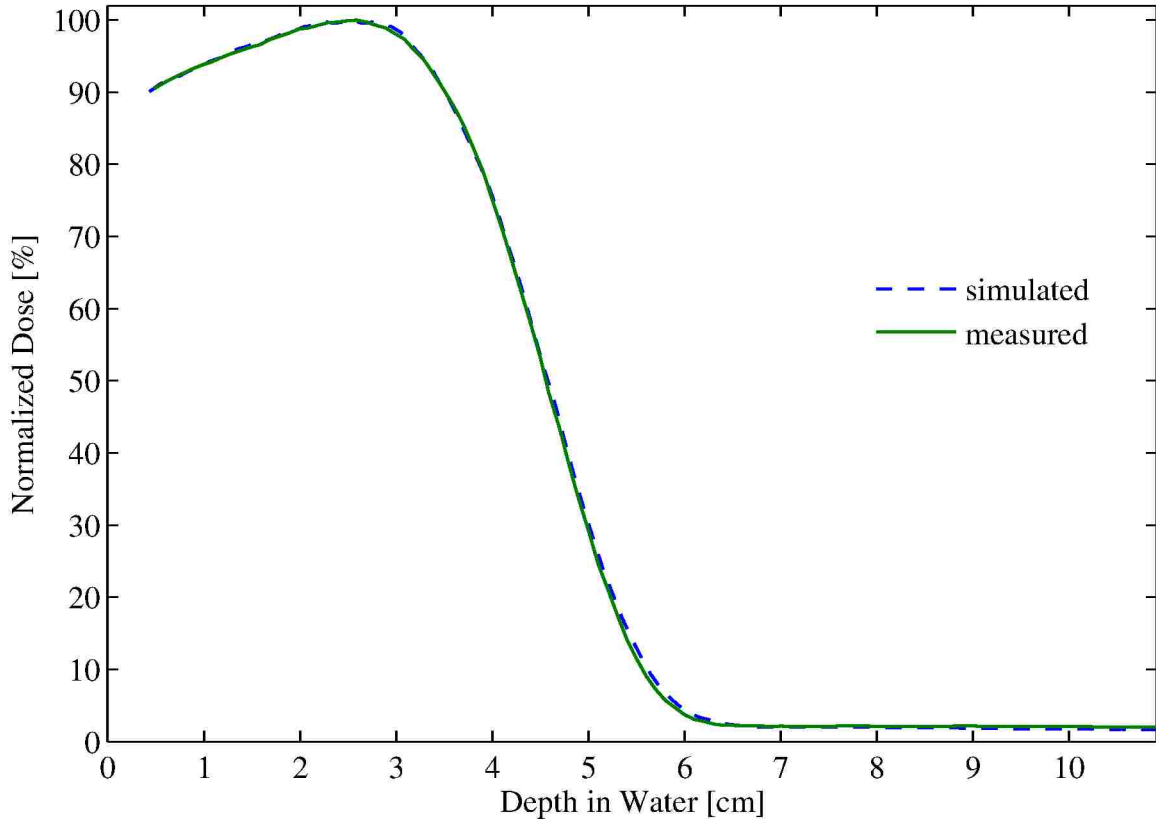
Figure 3.19: %DD: 11MeV - 25x25 cm^2 applicator

Table 3.5: 11MeV-25x25 cm^2 applicator comparison summary

Profile type (%DD, X, Y)	Profile depth (cm)	Percent of points passing		
		2%/1mm	2%/2mm	3%/3mm
%DD	–	100.0%	–	–
Diagonal	2.0	69.5%	71.4%	90.5%
Cross-plane (X)	1.7	93.9%	98.6%	100.0%
	3.5	89.1%	99.3%	100.0%
	4.1	91.2%	100.0%	–
	4.5	92.5%	100.0%	–
	7.6	100.0%	–	–
In-plane (Y)	1.7	87.8%	89.8%	98.6%
	3.5	87.8%	95.2%	100.0%
	4.1	95.9%	100.0%	–
	4.5	100.0%	–	–
	7.6	100.0%	–	–
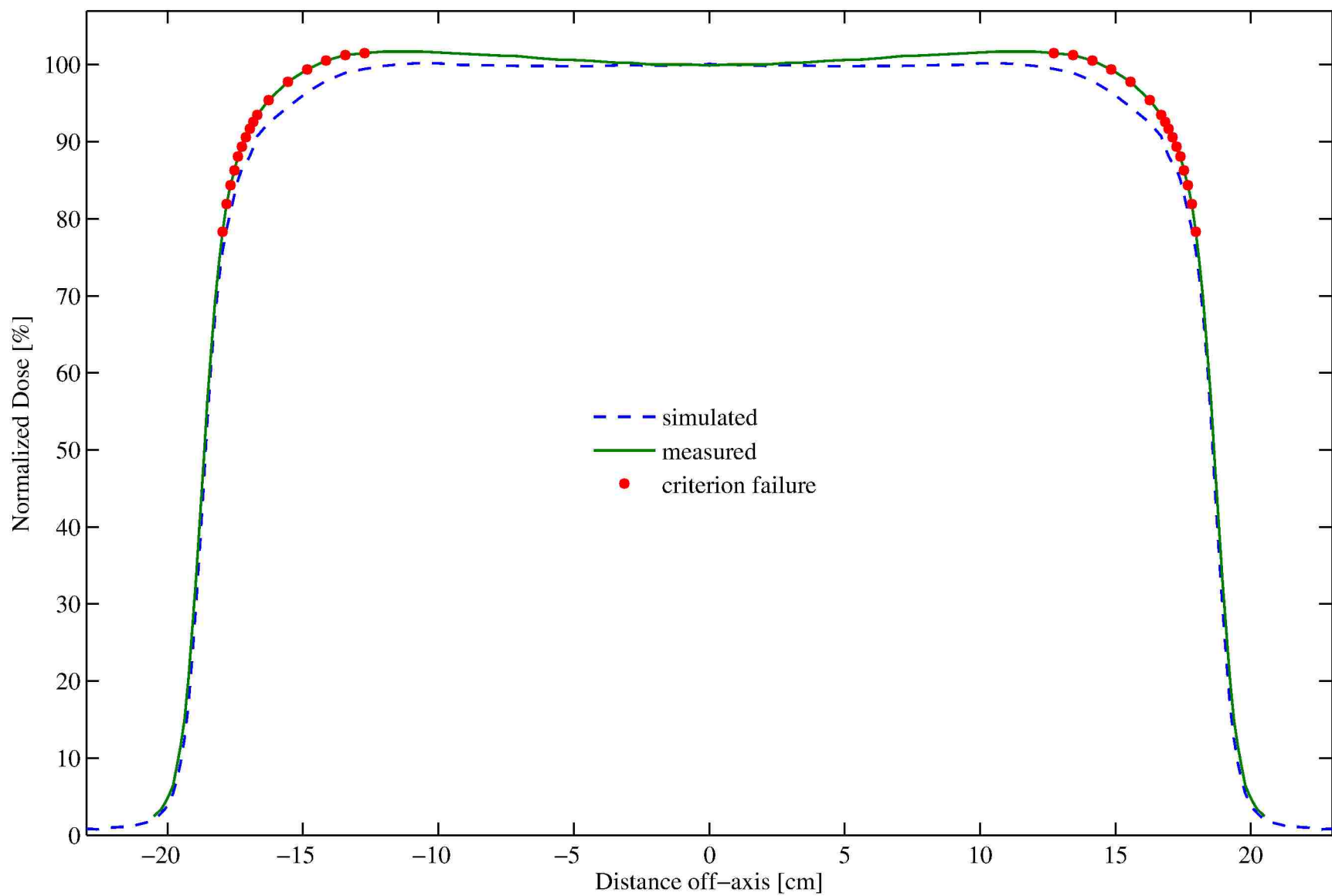
Figure 3.20: Diagonal profile: 11MeV - 25x25 cm^2 applicator at z=2 cm
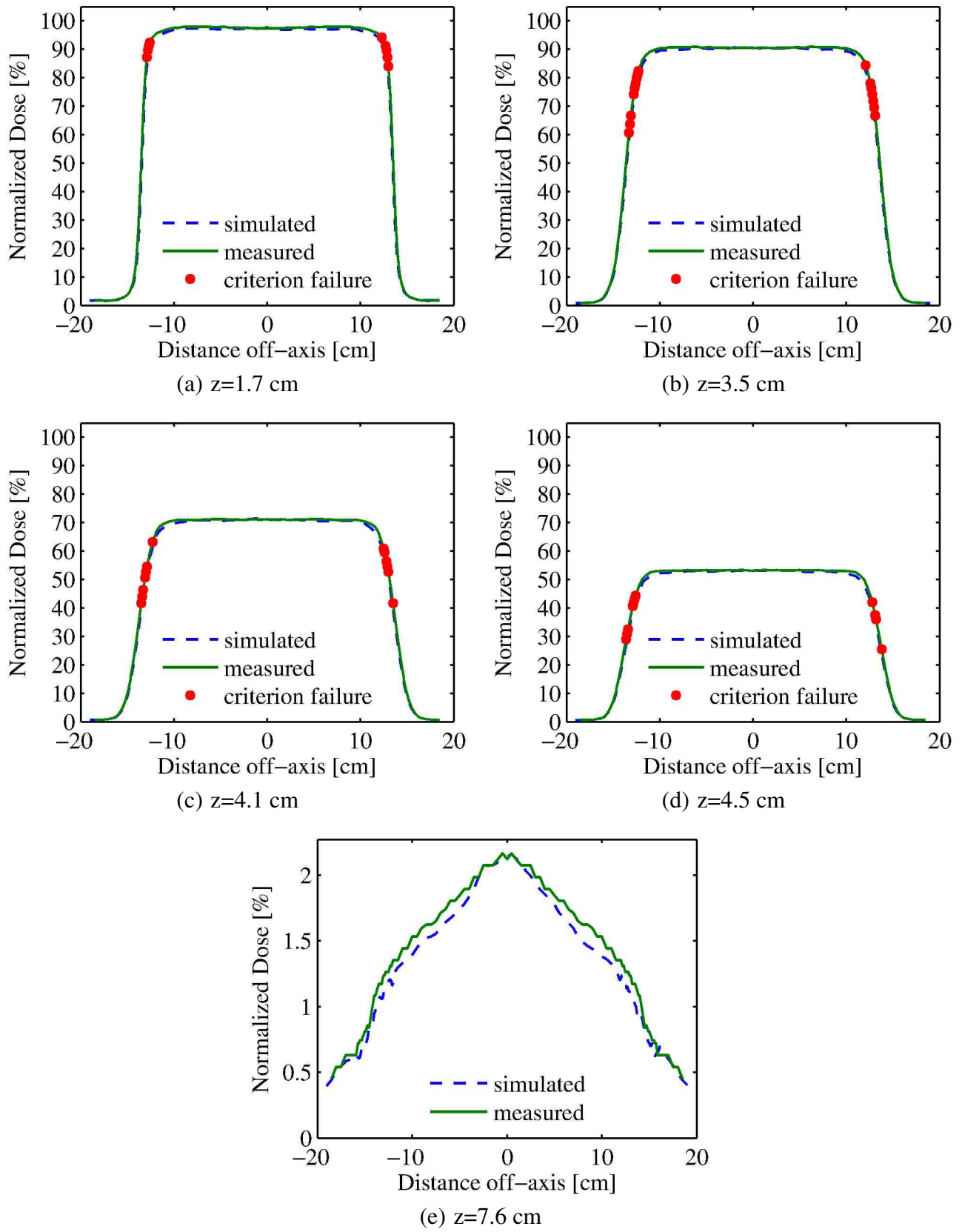
Figure 3.21: 11MeV-25x25 cm^2 cross-plane (X) profiles at five depths (1.7, 3.5, 4.1, 4.5, and 7.6 cm)
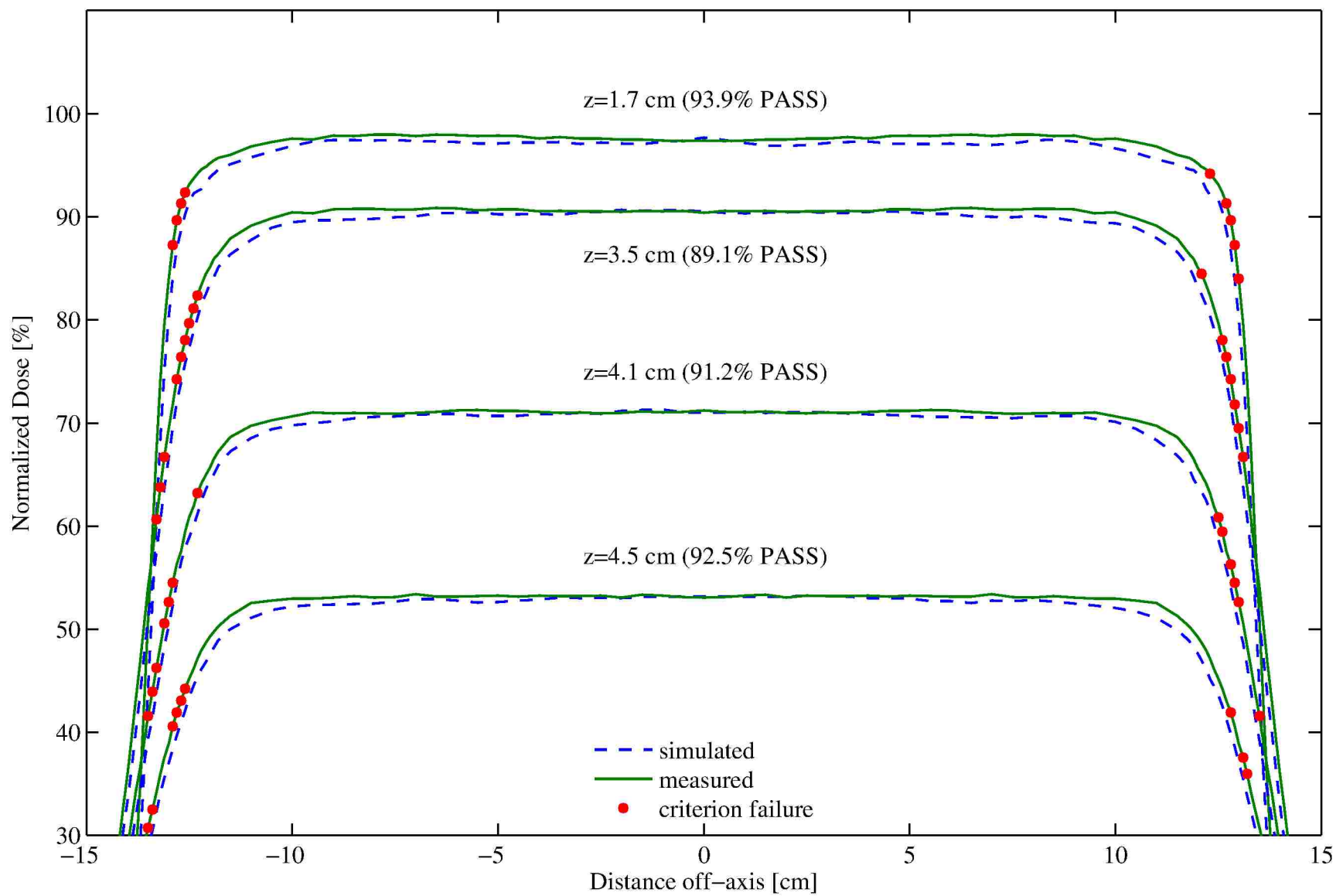
Figure 3.22: 11MeV-25x25 cm^2 cross-plane (X) profiles: zoomed view of Figure 3.21(a)-(d)

(a) z=1.7 cm

(b) z=3.5 cm

(c) z=4.1 cm

(d) z=4.5 cm

(e) z=7.6 cm
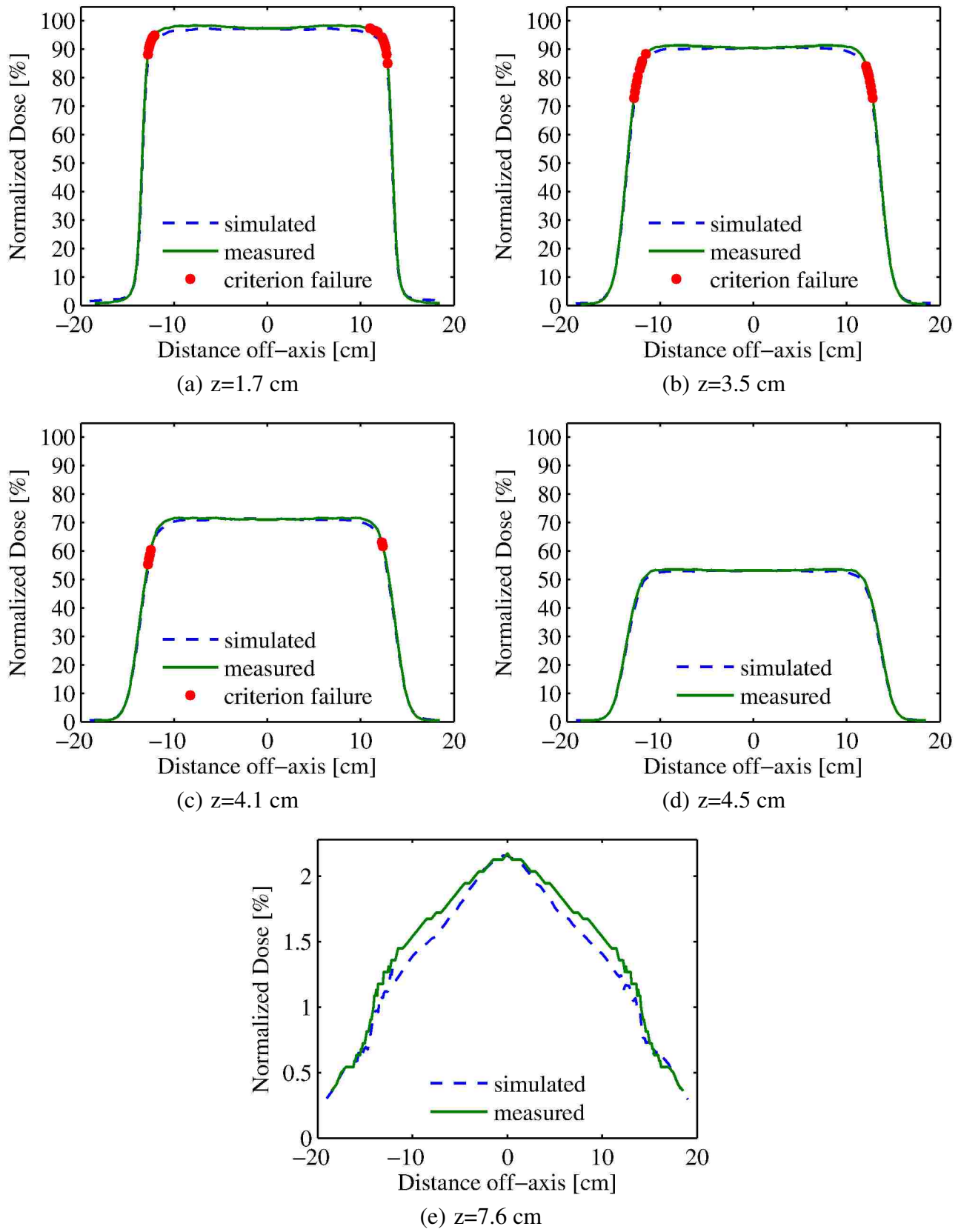
Figure 3.23: 11MeV-25x25 cm^2 in-plane (Y) profiles at five depths (1.7, 3.5, 4.1, 4.5, and 7.6 cm)
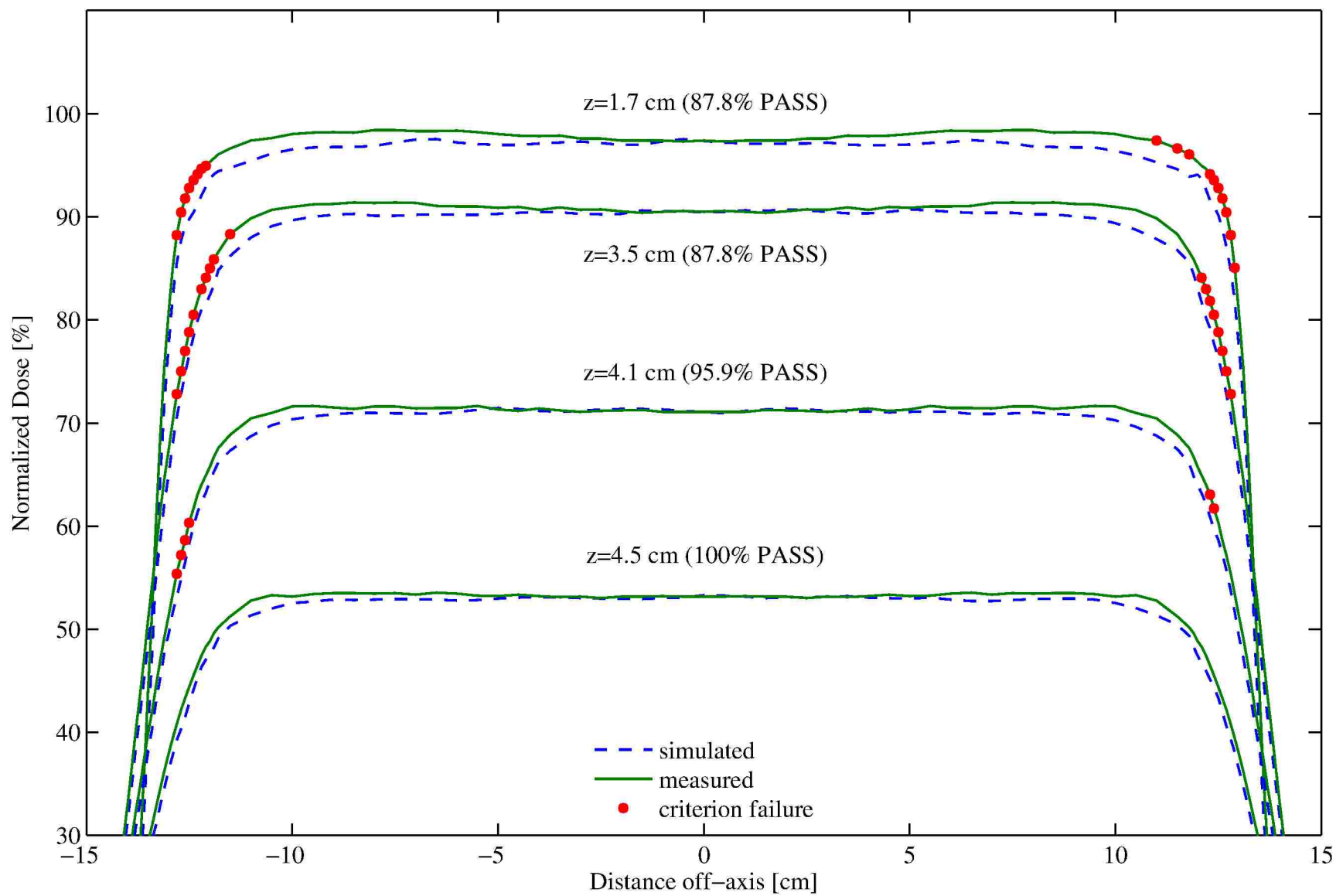
Figure 3.24: 11MeV-25x25 cm^2 in-plane (Y) profiles: zoomed view of Figure 3.23(a)-(d)

3.9 13-MeV Large-Field Results
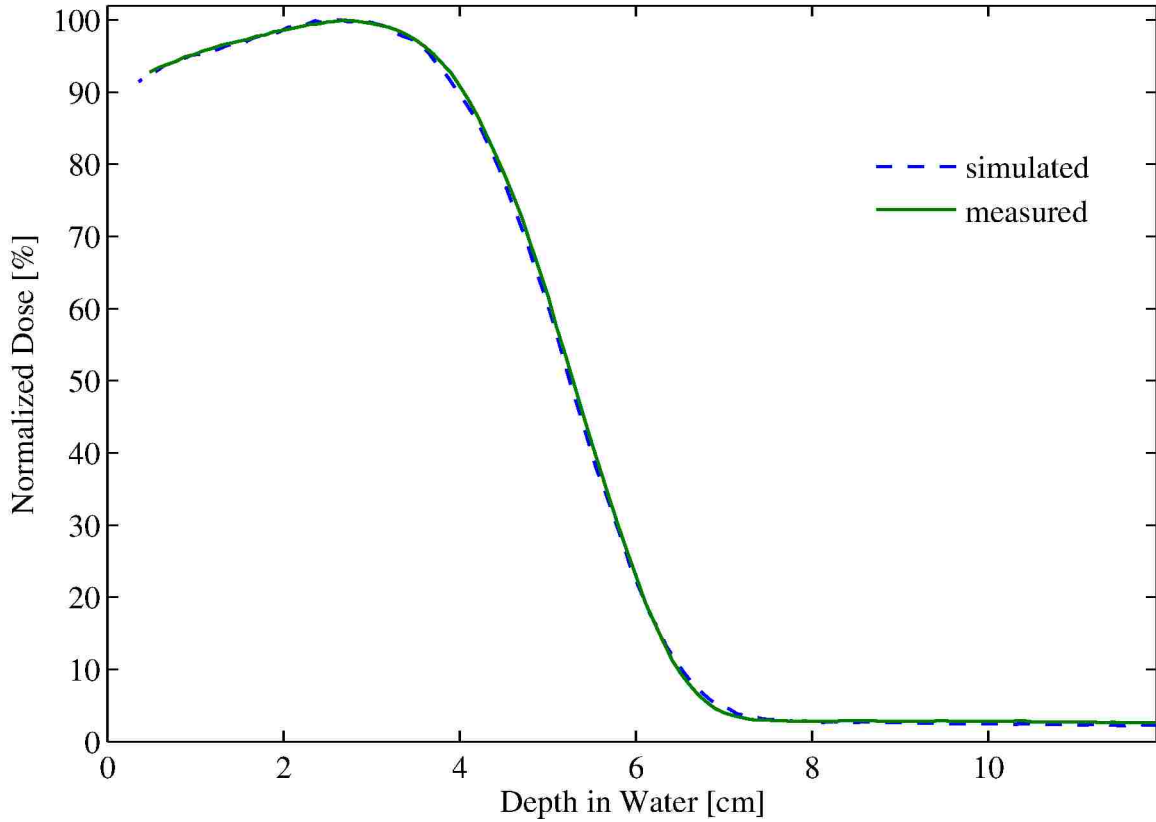
Figure 3.25: %DD: 13MeV - 25x25 cm^2 applicator

Table 3.6: 13MeV-25x25 cm^2 applicator comparison summary

Profile type (%DD, X, Y)	Profile depth (cm)	Percent of points passing 2%/1mm	2%/2mm	3%/3mm
%DD	–	100.0%	–	–
Diagonal	2.0	77.4%	82.6%	96.5%
Cross-plane (X)	2.0	95.2%	100.0%	–
	4.0	83.7%	99.3%	100.0%
	4.8	83.7%	98.6%	100.0%
	5.3	100.0%	–	–
	8.5	100.0%	–	–
In-plane (Y)	2.0	98.6%	100.0%	–
	4.0	89.8%	99.3%	100.0%
	4.8	95.9%	100.0%	–
	5.3	100.0%	–	–
	8.5	100.0%	–	–
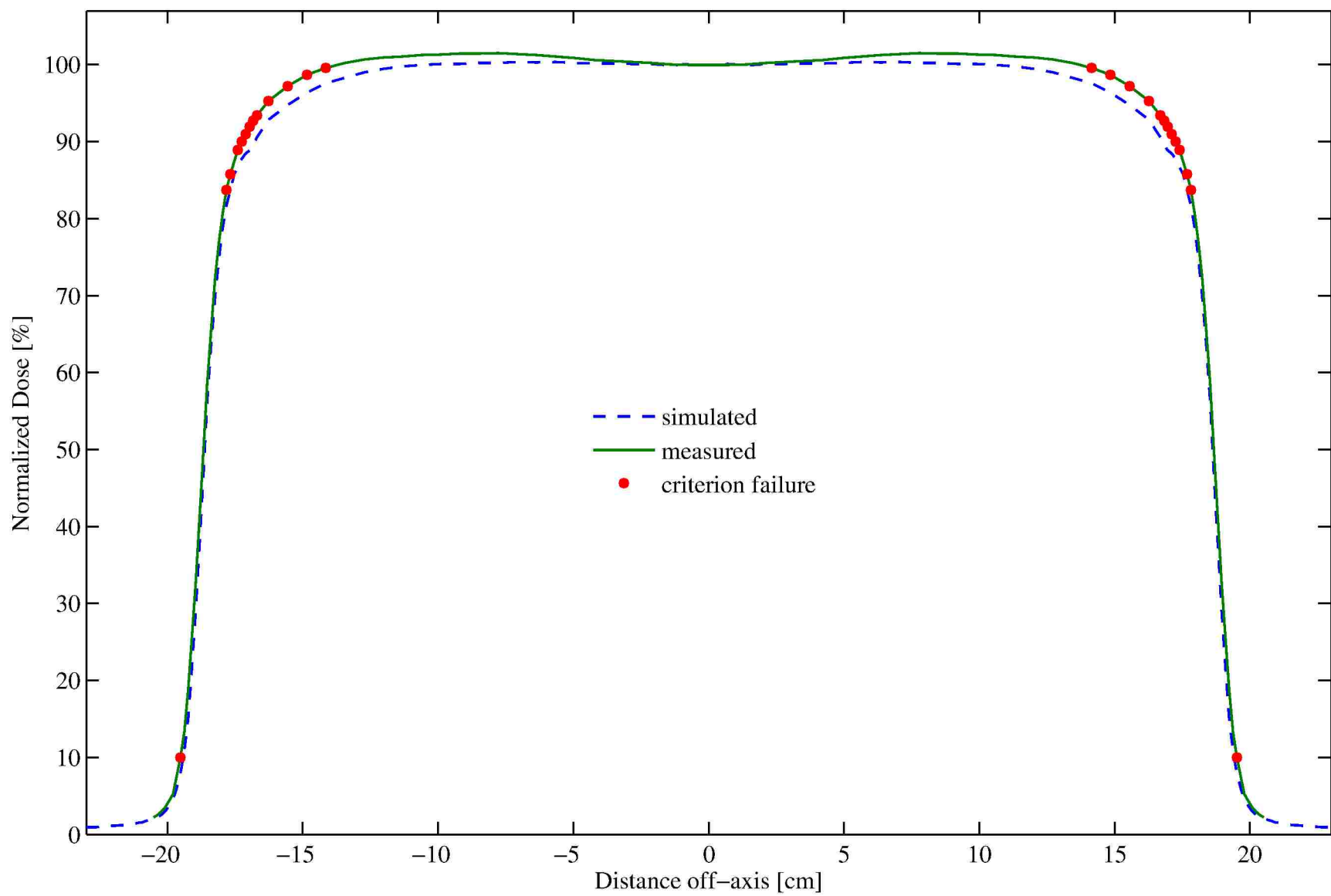
Figure 3.26: Diagonal profile: 13MeV - 25x25 cm^2 applicator at z=2 cm
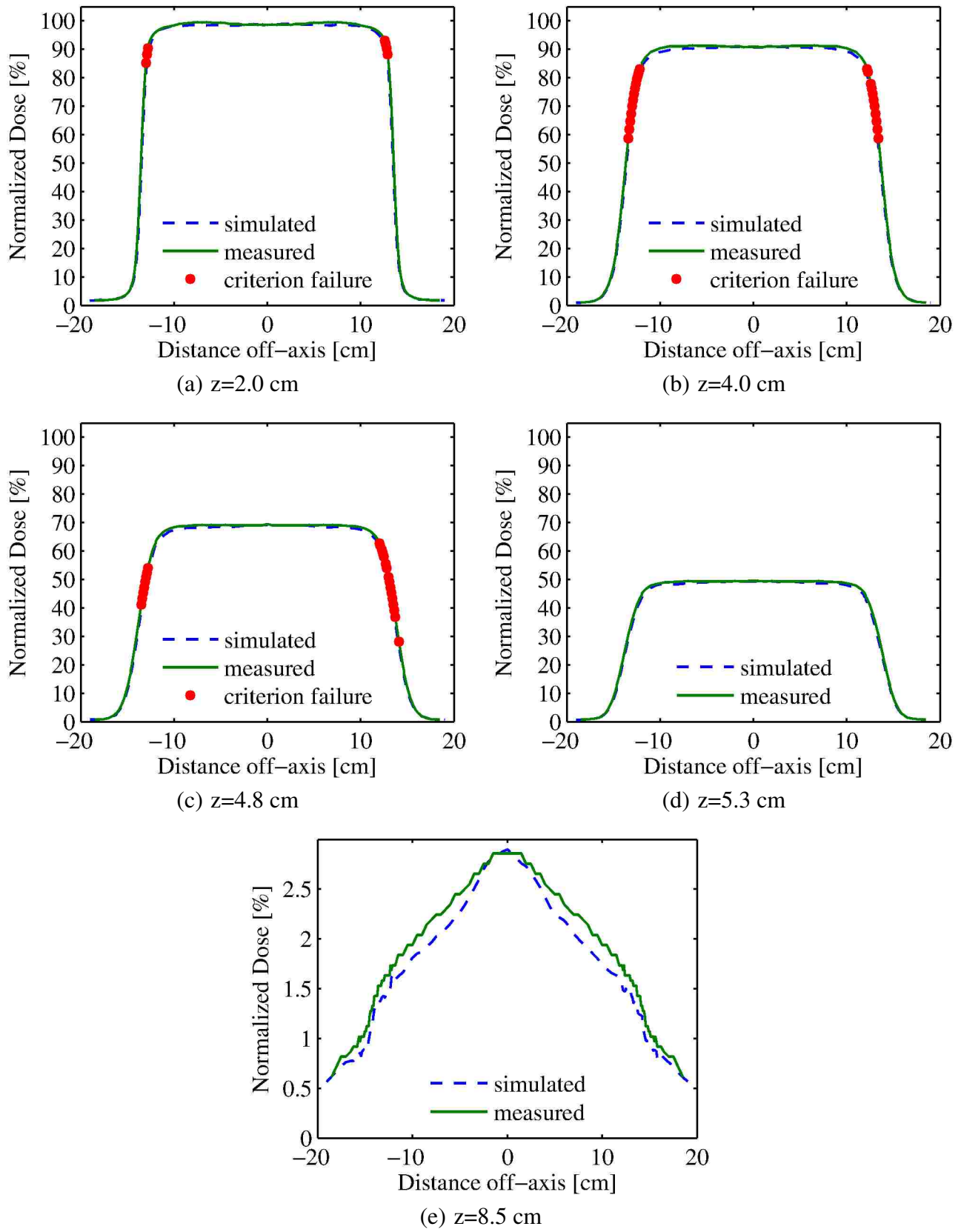
Figure 3.27: 13MeV-25x25 cm^2 cross-plane (X) profiles at five depths (2.0, 4.0, 4.8, 5.3, and 8.5 cm)
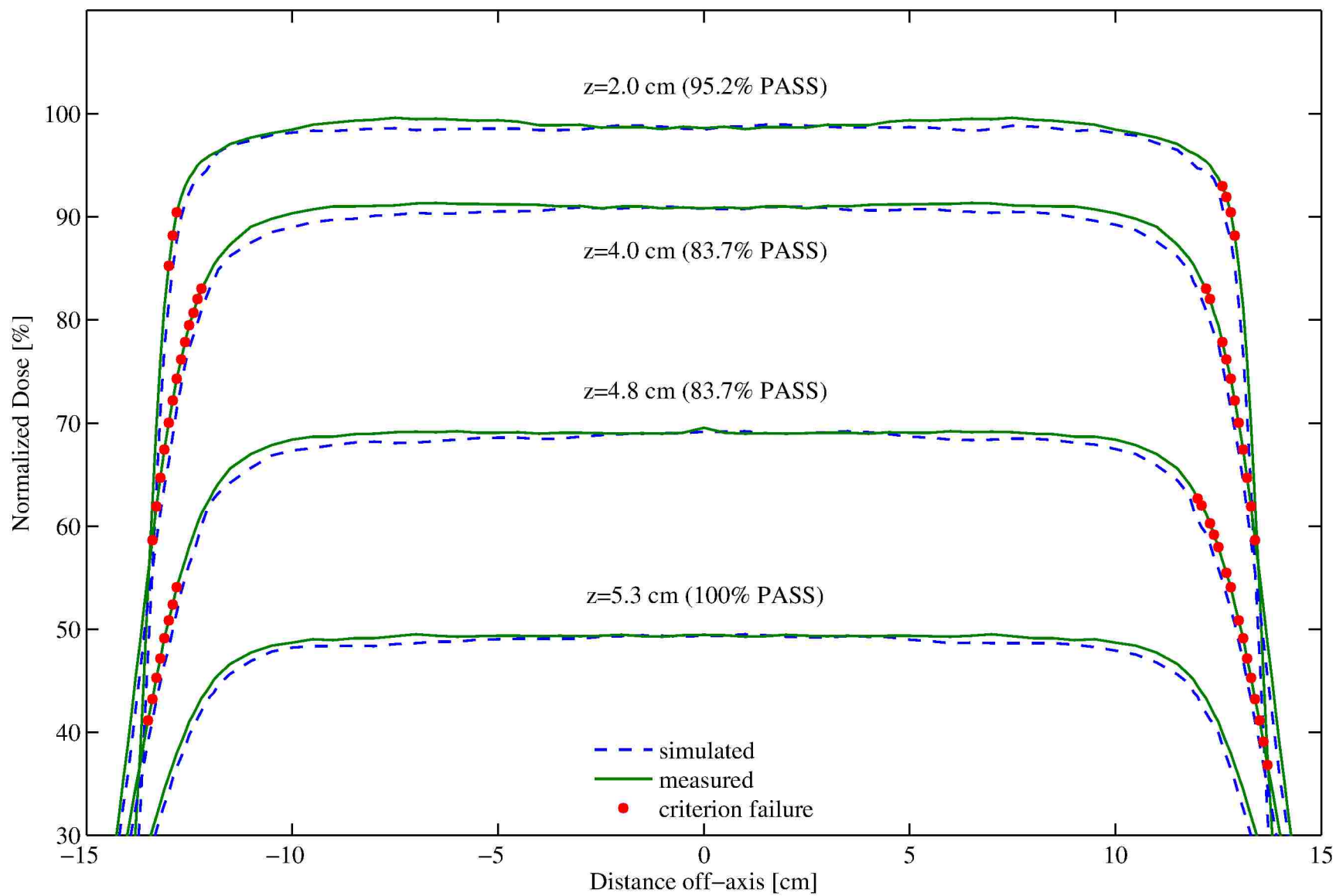
Figure 3.28: 13MeV-25x25 cm^2 cross-plane (X) profiles: zoomed view of Figure 3.27(a)-(d)

(a) z=2.0 cm

(b) z=4.0 cm

(c) z=4.8 cm

(d) z=5.3 cm

(e) z=8.5 cm
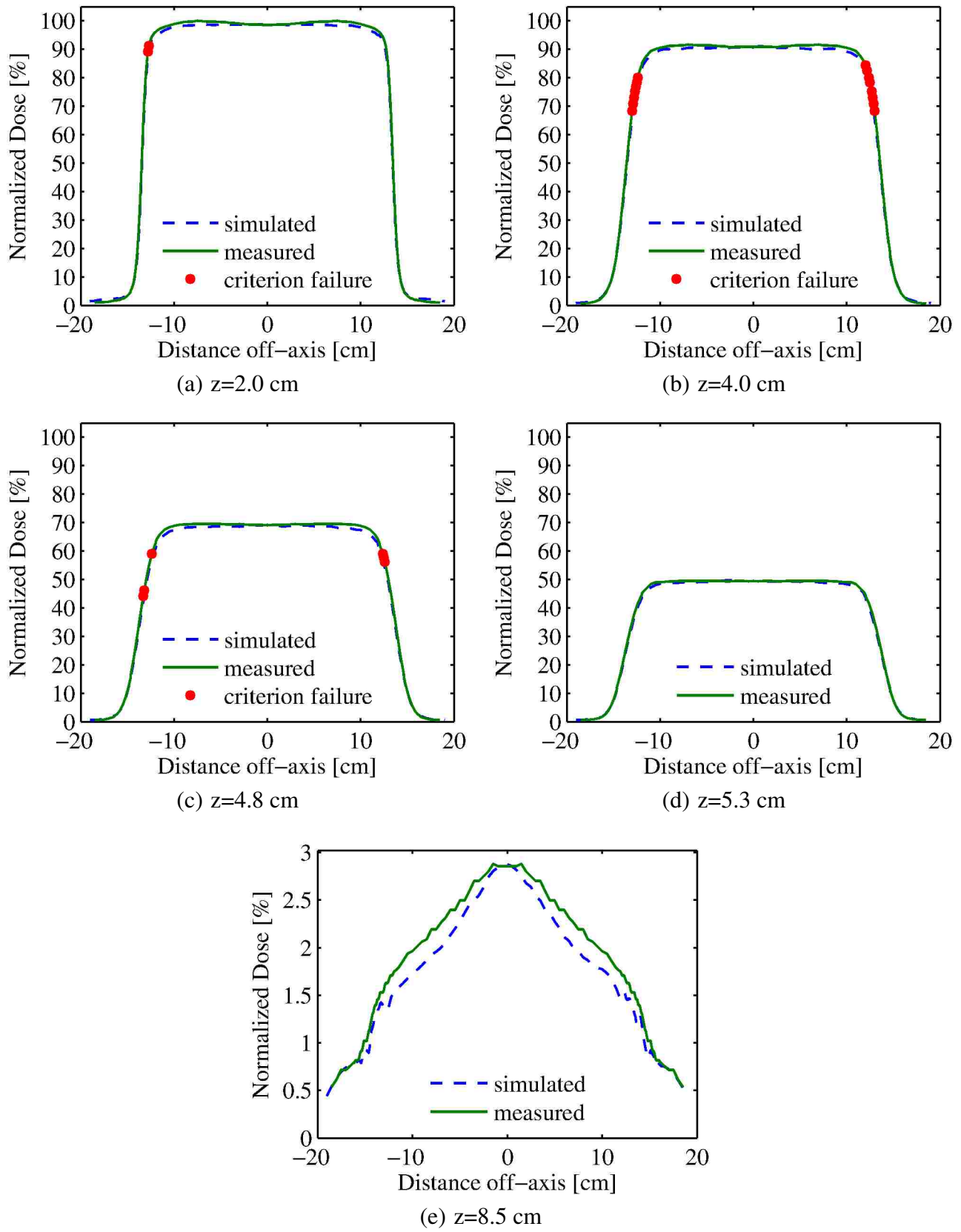
Figure 3.29: 13MeV-25x25 cm^2 in-plane (Y) profiles at five depths (2.0, 4.0, 4.8, 5.3, and 8.5 cm)
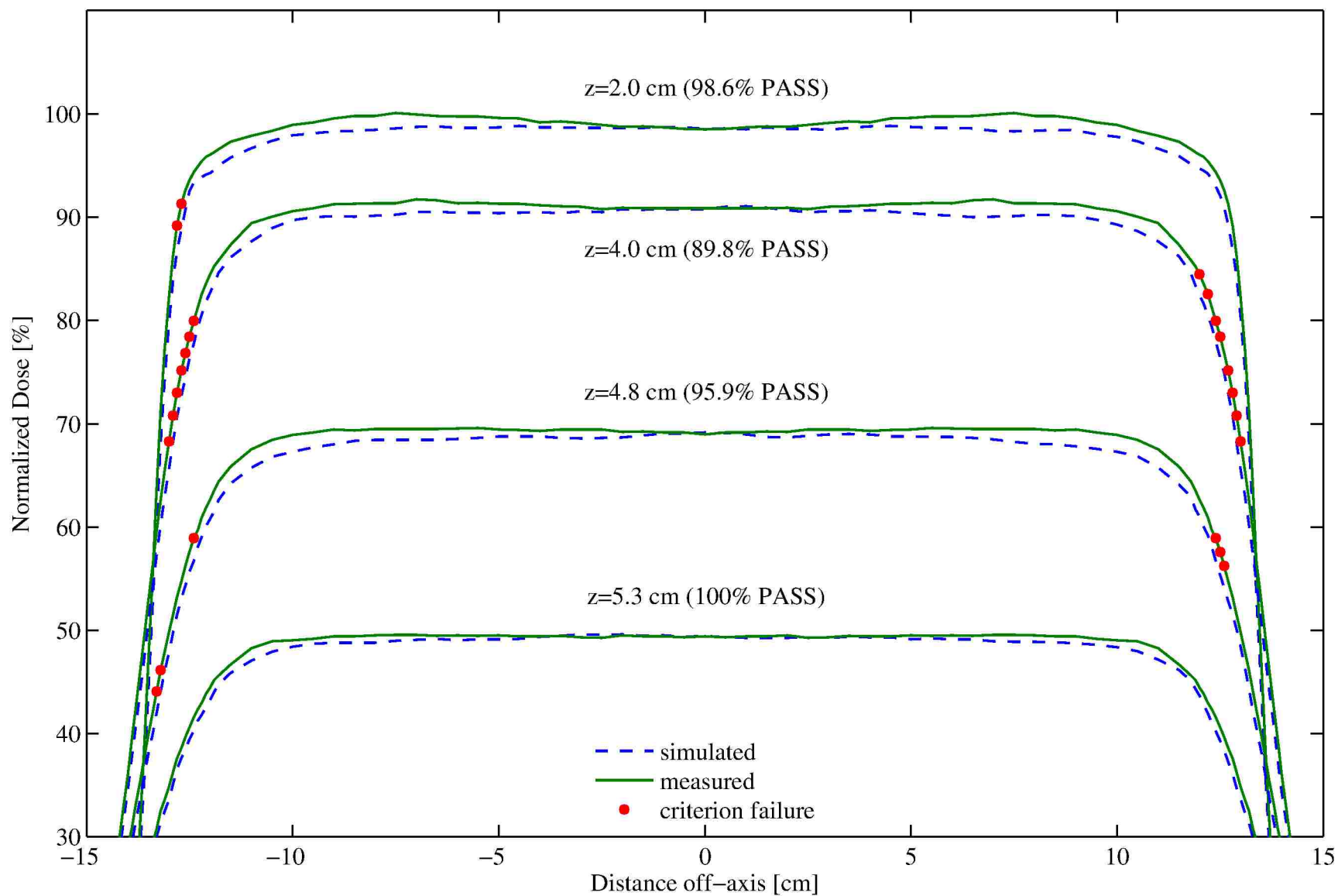
Figure 3.30: 13MeV-25x25 cm^2 in-plane (Y) profiles: zoomed view of Figure 3.29(a)-(d)

3.10   16-MeV Large-Field Results
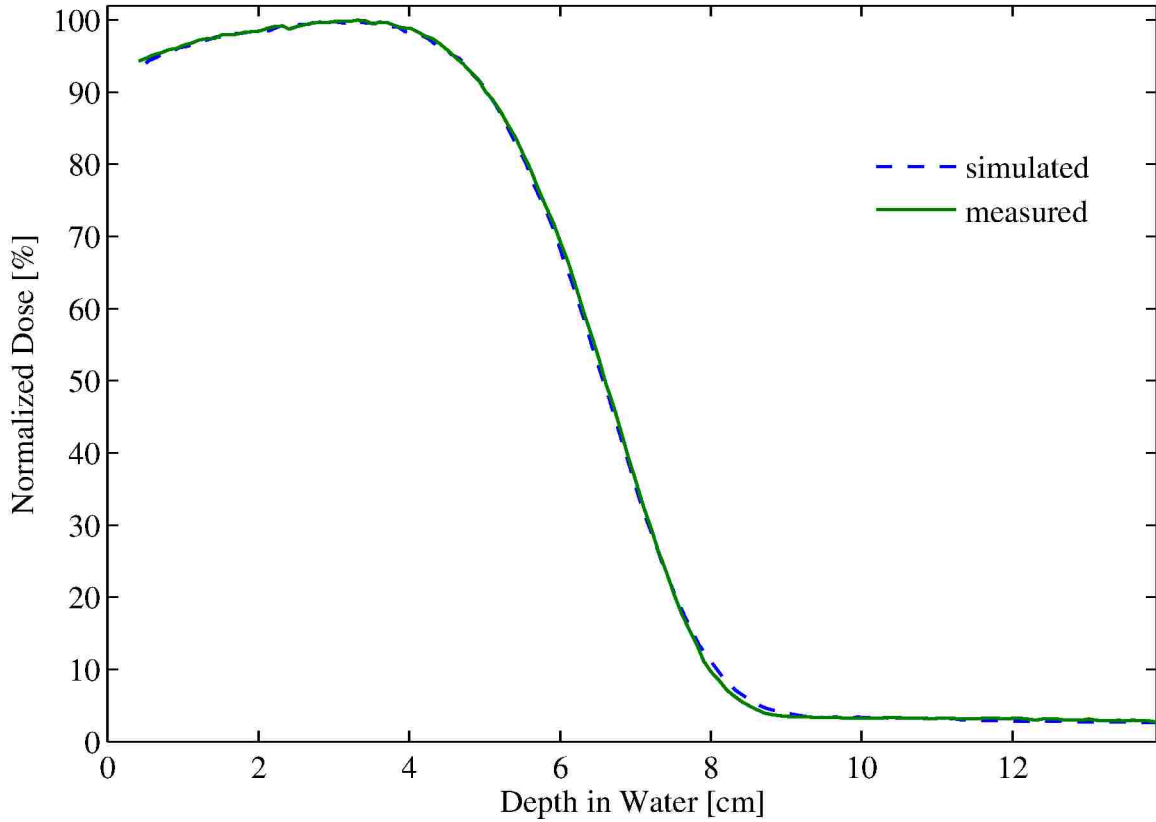
Figure 3.31: %DD: 16MeV - 25x25 cm^2 applicator

Table 3.7: 16MeV-25x25 cm^2 applicator comparison summary

Profile type (%DD, X, Y)	Profile depth (cm)	Percent of points passing		
		2%/1mm	2%/2mm	3%/3mm
%DD	–	100.0%	–	–
Diagonal	2.0	79.4%	82.4%	97.1%
Cross-plane (X)	10.0	100.0%	–	–
	2.5	99.3%	99.3%	100.0%
	5.0	100.0%	–	–
	6.0	100.0%	–	–
	6.6	100.0%	–	–
In-plane (Y)	10.0	100.0%	–	–
	2.5	100.0%	–	–
	5.0	100.0%	–	–
	6.0	100.0%	–	–
	6.6	100.0%	–	–
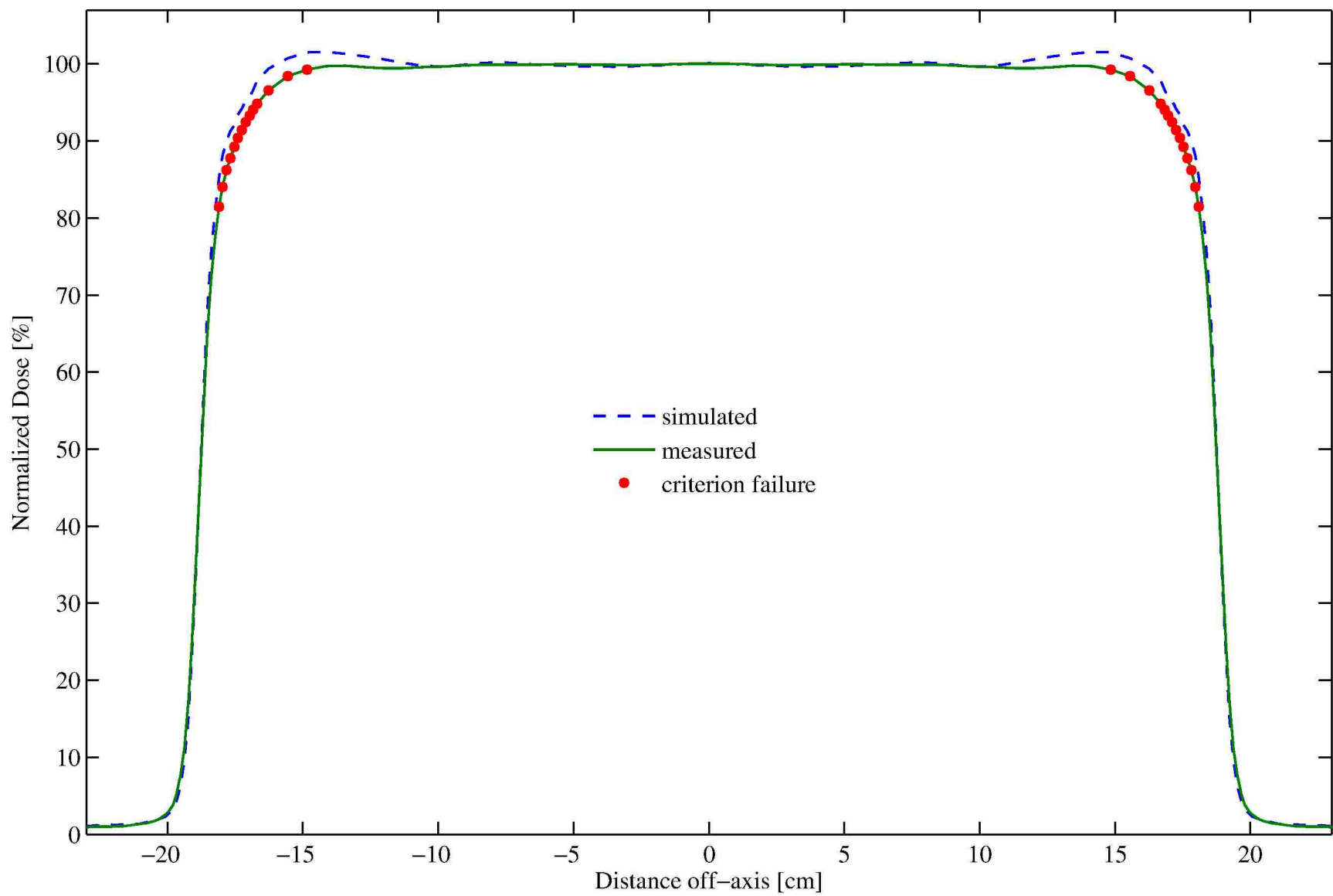
Figure 3.32: Diagonal profile: 16MeV - 25x25 cm^2 applicator at z=2 cm

(a) z=2.5 cm

(b) z=5.0 cm

(c) z=6.0 cm

(d) z=6.6 cm

(e) z=10.0 cm

Figure 3.33: 16MeV-25x25 cm^2 cross-plane (X) profiles at five depths (2.5, 5.0, 6.0, 6.6, and 10.0 cm)

Figure 3.34: 16MeV-25x25 cm^2 cross-plane (X) profiles: zoomed view of Figure 3.33(a)-(d)
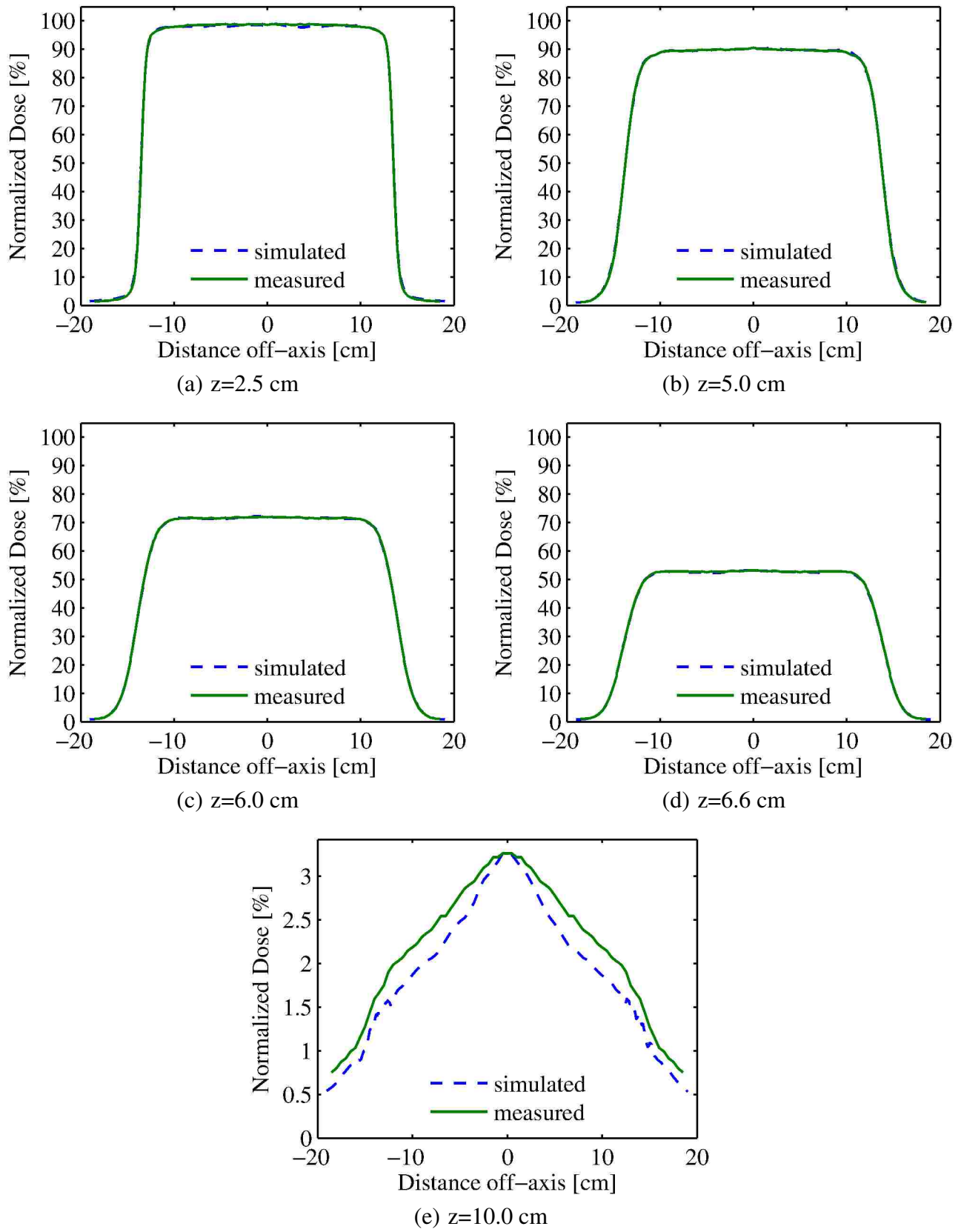
Figure 3.35: 16MeV-25x25 cm^2 in-plane (Y) profiles at five depths (2.5, 5.0, 6.0, 6.6, and 10.0 cm)
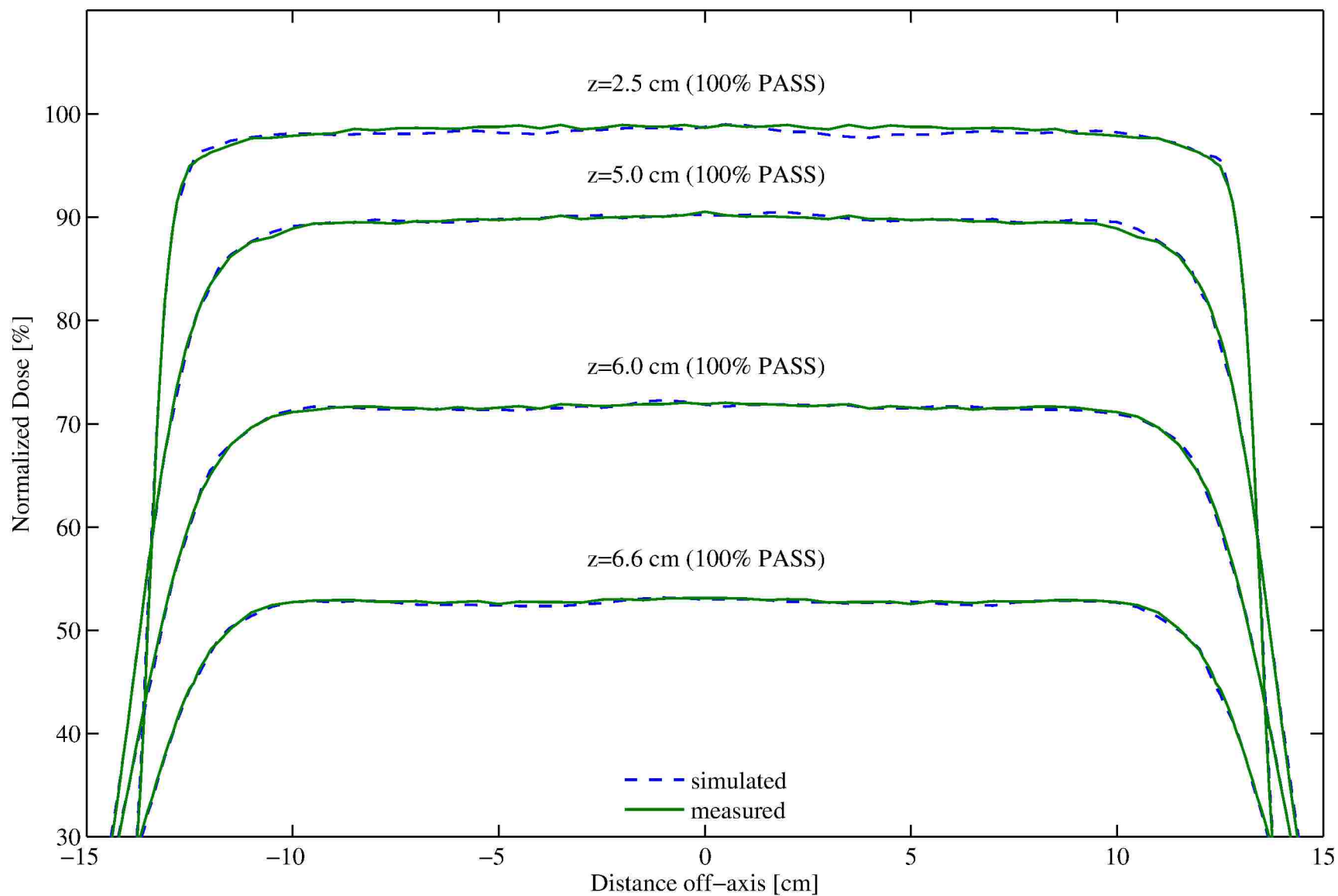
Figure 3.36: 16MeV-25x25 cm^2 in-plane (Y) profiles: zoomed view of Figure 3.35(a)-(d)

3.11   20-MeV Large-Field Results

Figure 3.37: %DD: 20MeV - 25x25 cm^2 applicator

Table 3.8: 20MeV-25x25 cm^2 applicator comparison summary

Profile type (%DD, X, Y)	Profile depth (cm)	Percent of points passing		
		2%/1mm	2%/2mm	3%/3mm
%DD	–	100.0%	–	–
Diagonal	2.0	82.1%	84.6%	92.3%
Cross-plane (X)	12.1	100.0%	–	–
	3.0	96.6%	96.6%	100.0%
	6.1	100.0%	–	–
	7.4	100.0%	–	–
	8.3	100.0%	–	–
In-plane (Y)	12.1	100.0%	–	–
	3.0	100.0%	–	–
	6.1	100.0%	–	–
	7.4	100.0%	–	–
	8.3	100.0%	–	–

Figure 3.38: Diagonal profile: 20MeV - 25x25 cm^2 applicator at z=2 cm

(a) z=3.0 cm

(b) z=6.1 cm

(c) z=7.4 cm

(d) z=8.3 cm

(e) z=12.1 cm

Figure 3.39: 20MeV-25x25 cm^2 cross-plane (X) profiles at five depths (3.0, 6.1, 7.4, 8.3, and 12.1 cm)

Figure 3.40: 20MeV-25x25 cm^2 cross-plane (X) profiles: zoomed view of Figure 3.39(a)-(d)

Figure 3.41: 20MeV-25x25 cm^2 in-plane (Y) profiles at five depths (3.0, 6.1, 7.4, 8.3, and 12.1 cm)

Figure 3.42: 20MeV-25x25 cm^2 in-plane (Y) profiles: zoomed view of Figure 3.41(a)-(d)

Chapter 4
Conclusions

4.1   Summary of Results

The goal of this work was to create a Monte Carlo model of the Elekta Infinity linear accelerator electron beam delivery system. The hypothesis of this work was that dose distributions of calculated by the Monte-Carlo model could reproduce measured cross-beam profiles and depth dose distributions to within 2% of D_{max} of 1 mm DTA for all field sizes. The model was tested for the large-field (25x25 cm^2 applicator) %DD curves and cross-beam profiles for all seven clinical beam energies (7-, 9-, 10-, 11-, 13-, 16-, and 20-MeV). The comparison of the calculated dose-distributions obtained from the BEAMnrc simulations against the measured commissioning data resulted in the following observations:

1. The model could reproduce %DD curves at 100 cm for the open-insert 25x25 cm^2 applicator within the specified criteria for all clinical energies.

2. The calculated cross-beam profiles did not produce results within the specified criteria at the commissioning depths for any clinical beam energy. The low energy(7-, 9-MeV) and the high energy(16-, 20-MeV) simulation results over-predicted the off-axis dose in the high-dose, low-gradient region of the beam. The medium energy (10-, 11- ,and 13-MeV) beams under-predicted the off-axis dose in the high-dose, low-gradient region of the beam.

3. The under-prediction of off-axis dose and the DTA failures observed in the middle electron energies (10-, 11-, and 13-MeV), which used the unmodified secondary scattering foil, can be rectified if some initial angular spread is added to the initial electron source that is incident on the nickel exit window.

Table 4.1: Pass rate for 25x25 cm^2 cross-beam results

Energy (MeV)	Pass rate at 2%/1mm	DTA to achieve 100%	% of D_{max} to achieve 100%
7	98.5	1mm	2.5%
9	96.3	1mm	3%
10	97.4	2.1mm	2%
11	94.0	2.5mm	3%
13	94.6	2.3mm	2%
16	100	1mm	2%
20	99.1	1mm	2.5%

4.2 Evaluation of Hypothesis

The results of this study do not support the initial hypothesis of the work. Using an arbitrarily defined energy spectrum incident on the vacuum exit window as the only free parameter, the Monte-Carlo model was unable to reproduce the cross-beam profiles within 2% or 1 mm DTA when compared against the large-field beam measurements from the commissioning data set. If the criteria were loosened to 3% of D_{max} or 2.5 mm DTA then the hypothesis would be supported for the cross-beam commissioned data. Diagonal profiles required the criteria to be loosened to 4% of D_{max} or 2.5 mm DTA for the hypothesis to be supported.

4.3 Utility of Results

Limited investigation of additional cross-beam profiles with smaller applicators (6x6 cm^2 and 14x14 cm^2) suggest the model can meet the specified criteria for smaller field-sizes at normal and extended SSDs. AAPM Task Group No. 105 cites Monte Carlo agreement with measured beam data within 2% or 2 mm as excellent for the purposes of commissioning a Monte Carlo treatment planning system (Chetty et al. 2007). Thus, the model could be used in its current state as a Monte Carlo treatment planning system for small field sizes. Additionally, given the dimensions of the photon flattening filters and the tungsten target, the model could be used to simulate the photon beams of the Elekta accelerator with minimal additional labor.

4.4 Future Work

The Monte Carlo model must be able to meet the tolerance criteria of the hypothesis for the large field beam data to serve as a benchmark for the redesign of beam-line components. Studies are currently underway to measure the electron energy spectrum at machine isocenter using a magnetic spectrometer (Hogstrom et al. 2012). This data will be mathematically de-convolved to reproduce the physical electron spectra as it is incident on the nickel exit window. Actual measured energy spectrum data could help to resolve some of the discrepancies between the model and the measured beam data.

The energy bandwidth of the bending magnet system of an Elekta accelerator should be approximately 9% (Björk, Knöös, and Nilsson 2002). Given this information, the energy spectra parameters required to model the measured %DD curves are potentially non-physical since the energies extend past outside of the maximum bandwidth of the bending magnet system. The actual bandwidth of the bending magnet system is questionable as Deasy, Almond, and McEllistrem (1994) reported Philips/Elekta accelerator energy spectra measurements with FWHM values as large as 20%. Further investigation into the truncating the energy spectra to create more physically valid energy spectrum should be considered.

This work focused on creating a simple model of the incident electron source with as few free parameters as possible. Further investigation into a sensitivity study of the initial source input parameters for each beam energy should be considered. Additional source options provided in the BEAMnrc package could also be investigated.

Additionally, further analysis of the accelerator could be performed by taking dosimetric measurements with critical beam-line components removed. Measurements for each clinical energy with one or both scattering foils taken out of the beam would allow further insights into the issues that caused the model to over-predict the off-axis dose for the low energy and high energy beams. Finally, radio-chromic film measurement in the empty carousel position (used in photon mode) of the primary foil holder could allow further quantification of the spatial distribution of the electron spot size for each beam energy.

References

Ali, O. A., C. A. Willemse, W. Shaw, F. H. J. O'Reilly, and F. C. P. du Plessis. 2011. "Monte Carlo electron source model validation for an Elekta Precise linac." *Medical Physics* 38 (5): 2366–2373.

Antolak, John A., Michael R. Bieda, and Kenneth R. Hogstrom. 2002. "Using Monte Carlo methods to commission electron beams: A feasibility study." *Medical Physics* 29 (5): 771–786.

Bieda, Michael R., John A. Antolak, and Kenneth R. Hogstrom. 2001. "The effect of scattering foil parameters on electron-beam Monte Carlo calculations." *Medical Physics* 28 (12): 2527–2534.

Bieda, M R. 1999. "A Monte Carlo method for commissioning electron beams." Master's thesis, The University of Texas Health Science Center at Houston, Houston, TX.

Björk, Peter, Tommy Knöös, and Per Nilsson. 2002. "Influence of initial electron beam characteristics on Monte Carlo calculated absorbed dose distributions for linear accelerator electron beams." *Physics in Medicine and Biology* 47 (22): 4019.

Chetty, Indrin J., Bruce Curran, Joanna E. Cygler, John J. DeMarco, Gary Ezzell, Bruce A. Faddegon, Iwan Kawrakow, Paul J. Keall, Helen Liu, C.-M. Charlie Ma, D. W. O. Rogers, Jan Seuntjens, and Daryoush Sheikh-Bagheri. 2007. "Report of the AAPM Task Group No. 105: Issues associated with clinical implementation of Monte Carlo-based photon and electron external beam treatment planning." *Medical Physics* 34 (12): 4818–4853.

Chibani, Omar, Belal Moftah, and C.-M. Charlie Ma. 2011. "On Monte Carlo modeling of megavoltage photon beams: A revisited study on the sensitivity of beam parameters." *Medical Physics* 38 (1): 188–201.

Das, Indra J., Chee-Wai Cheng, Ronald J. Watts, Anders Ahnesjo, John Gibbons, X. Allen Li, Jessica Lowenstein, Raj K. Mitra, William E. Simon, and Timothy C. Zhu. 2008. "Accelerator beam data commissioning equipment and procedures: Report of the TG-106 of the Therapy Physics Committee of the AAPM." *Medical Physics* 35 (9): 4186–4215.

Deasy, J., P. R. Almond, and M. T. McEllistrem. 1994. "The spectral dependence of electron central-axis depth-dose curves." *Medical Physics* 21 (9): 1369–1376.

Deasy, J. O., P. R. Almond, and M. T. McEllistrem. 1996. "Measured electron energy and angular distributions from clinical accelerators." *Medical Physics* 23 (5): 675–684.

Faddegon, Bruce A., Daren Sawkey, Tuathan O'Shea, Malcolm McEwen, and Carl Ross. 2009. "Treatment head disassembly to improve the accuracy of large electron field simulation." *Medical Physics* 36 (10): 4577–4591.

Gerbi, Bruce J., John A. Antolak, F. Christopher Deibel, David S. Followill, Michael G. Her-

man, Patrick D. Higgins, M. Saiful Huq, Dimitris N. Mihailidis, Ellen D. Yorke, Kenneth R. Hogstrom, and Faiz M. Khan. 2009. "Recommendations for clinical electron beam dosimetry: Supplement to the recommendations of Task Group 25." *Medical Physics* 36 (7): 3239–3279.

Green, A D. 1991. "Modeling of dual scattering systems for clinical electron beams." Master's thesis, The University of Texas Health Science Center at Houston, Houston, TX.

Guerra, A. Del, and Walter R. Nelson. 1988. "High-Energy Physics Applications of EGS." Technical Report SLAC PUB-4789, Stanford Linear Accelerator Center, Stanford University.

Hogstrom, Kenneth R, and Peter R Almond. 2006. "Review of electron beam therapy physics." *Physics in Medicine and Biology* 51 (13): R455.

Hogstrom, K R, A L Boyer, A S Shiu, T G Ochran, S M Kirsner, F Krispel, and Tyvin Richy. 1990. "Design of metallic electron beam cones for an intraoperative therapy linear accelerator." *International Journal of Radiation Oncology* 18 (5): 1223–1232.

Hogstrom, K R, D McLaughlin, J Gibbons, P Shikhaliev, T Clarke, A Henderson, D Taylor, P Shagin, and E Liang. 2012. "SU-D-BRCD-6: Measurement of Elekta Electron Energy Spectra Using a Small Magnetic Spectrometer." Volume 39. AAPM.

ICRU-35. 1984. "Radiation Dosimetry: Electron Beams with Energies Between 1 and 50 MeV." Technical Report, International Commission on Radiation Units and Measurements (ICRU), Bethesda, MD.

ICRU-37. 1984. "Stopping powers for electrons and positrons." Technical Report ICRU Report 37. Bethesda, MD, International Commission on Radiation Units and Measurements (ICRU).

IEC, 6061-2-1. 1998. Medical electrical equipment- Part 2-1: Particular requirements for the safety of electron accelerators in the range 1MeV to 50MeV.

Jiang, Steve B., Ajay Kapur, and C.-M. Ma. 2000. "Electron beam modeling and commissioning for Monte Carlo treatment planning." *Medical Physics* 27 (1): 180–191.

Kainz, K K, J A Antolak, P R Almond, C D Bloch, and K R Hogstrom. 2005. "Dual scattering foil design for poly-energetic electron beams." *Physics in Medicine and Biology* 50 (5): 755.

Karzmark, C. J. 1984. "Advances in linear accelerator design for radiotherapy." *Medical Physics* 11 (2): 105–128.

Karzmark, C.J. 1993. *Medical electron accelerators*. 1st. New York: McGraw-Hill, Inc., Health Professions Division.

Kawrakow, I, E Mainegra-Hing, D W O Rogers, F Tessier, and B R B Walters. 2011. "The EGSnrc code system: Monte Carlo simulation of electron and photon transport." Technical Report PIRS-701, National Research Council of Canada (NRCC).

Khan, Faiz M. 2010. *The Physics of Radiation Therapy*. 4th. Philadelphia: Lippincott Williams & Wilkins.

Khan, Faiz M., Karen P. Doppke, Kenneth R. Hogstrom, Gerald J. Kutcher, Ravinder Nath, Satish C. Prasad, James A. Purdy, Martin Rozenfeld, and Barry L. Werner. 1991. "Clinical electron-beam dosimetry: Report of AAPM Radiation Therapy Committee Task Group No. 25." *Medical Physics* 18 (1): 73–109.

Kim, S, L Ren, J Jin, J Kim, B Movsas, and I Chetty. 2011. "SU-E-J-21: Verification of a Monte Carlo Model of CBCT Flat Panel Detector Using BEAMnrc/EGSnrc Code." Volume 38. AAPM, 3446–3446.

Kim, Sangroh, Haijun Song, Benjamin Movsas, and Indrin J. Chetty. 2012. "Characteristics of x-ray beams in two commercial multidetector computed tomography simulators: Monte Carlo simulations." *Medical Physics* 39 (1): 320–329.

Lax, I, and A Brahme. 1980. "Collimation of high energy electron beams." *Acta Radiologica Oncology* 19 (3): 199–207.

Loevinger, R, C J Karzmark, and M Weissbluth. 1961. "Radiation therapy with high-energy electrons." *Radiology* 77:906.

Nelson, Walter R., Hideo Hirayama, and David W. 0. Rogers. 1985. "The EGS4 Code System." Technical Report SLAC-265, Stanford Linear Accelerator Center, Stanford University.

Rogers, D. W. O., B. A. Faddegon, G. X. Ding, C.-M. Ma, J. We, and T. R. Mackie. 1995. "BEAM: A Monte Carlo code to simulate radiotherapy treatment units." *Medical Physics* 22 (5): 503–524.

Rogers, D W O. 2006. "Fifty years of Monte Carlo simulations for medical physics." *Physics in Medicine and Biology* 51 (13): R287.

Rogers, D W O, B Walters, and I Kawrakow. 2011. "BEAMnrc Users Manual." Technical Report PIRS-0509 revL, National Research Council of Canada (NRCC).

Schreiber, E C, and B A Faddegon. 2005. "Sensitivity of large-field electron beams to variations in a Monte Carlo accelerator model." *Physics in Medicine and Biology* 50 (5): 769.

Waldron, T. 2002, July. The Theory and Operation of Computer-Controlled Medical Linear Accelerators. Session at 44th annual AAPM meeting.

Walters, B, I Kawrakow, and D W O Rogers. 2011. "DOSXYZnrc Users Manual." Technical Report PIRS-794 revB, National Research Council of Canada (NRCC).

Appendix A
Parallel Run Submission Script

The BEAMnrc code was modified to achieve parallel operation on Red Hat Linux Enterprise (RHEL) computing clusters. The basic structure of the BASH script necessary to submit the parallel jobs is as follows:

```bash
#!/bin/bash

#PBS -q checkpt
#PBS -l walltime=2:00:00
#PBS -l nodes=5:ppn=4
#PBS -N Parallel_run_example

pegs=pegs4dat file
input=$input_file(.egsinp)
output=$phase_space_name(.egsphsp1)
user_code=BEAM_$module_file(.module)

cd $PBS_O_WORKDIR
cd ..
newhome=`pwd`
cd $PBS_O_WORKDIR

#Get the nubmer of available processors.
nprocs=`wc -l $PBS_NODEFILE | awk 'print $1'`

#Build a host list
count=0
HOSTLIST=
for host in `cat $PBS_NODEFILE`
  do
    HOSTLIST[$count]=$host
    count=$(( $count + 1 ))
done

#Run the modified pprocess script to get the splitted input files.

EGS_HOME=$newhome /home/$USER/HEN_HOUSE/scripts/pprocess $user_code $input $pegs $nprocs

#Launch one job for each input file.
count=0
for id in `cat 13`
  do
    remotehost=$HOSTLIST[$count]
    cat > childjob_$id.sh << EOF
#!/bin/bash
cd $PBS_O_WORKDIR
EGS_HOME=$newhome $user_code -i $id -p $pegs
EOF
    chmod 755 childjob_$id.sh
    echo "Connecting to $remotehost..."
    ssh -n $remotehost $PBS_O_WORKDIR/childjob_$id.sh &
    count=$(( $count + 1 ))
done
wait

#add parallel run phase-space files together
addphsp $input $output $nprocs
```

Appendix B
Comparisons of Energy Spectra
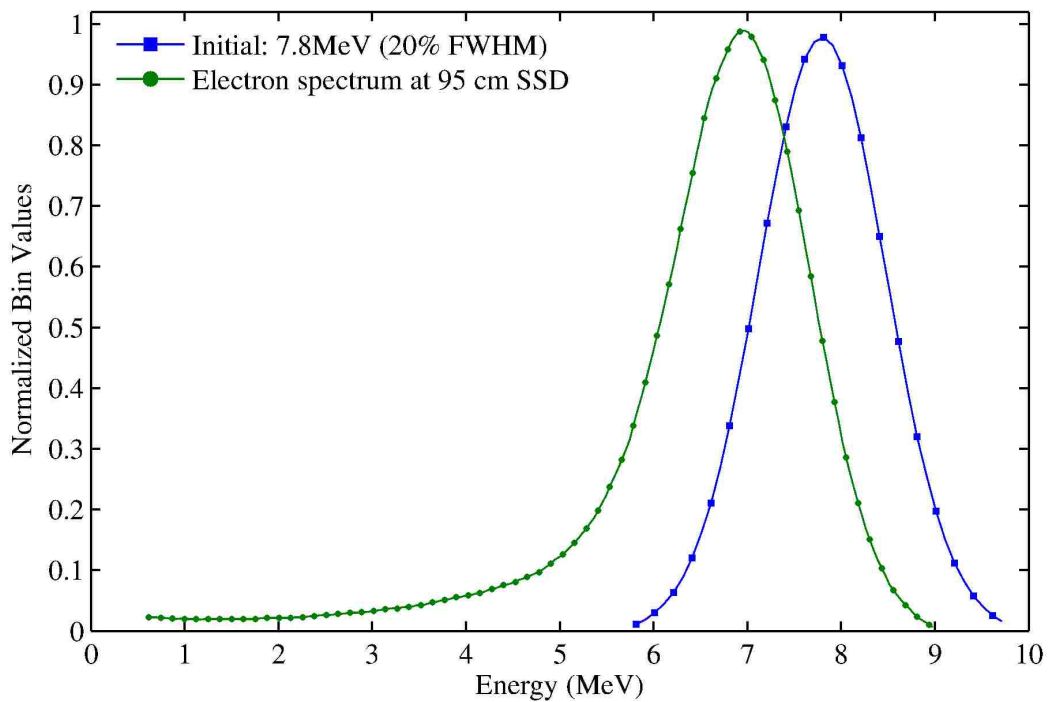
Figure B.1: 7MeV - 14x14 cm^2 applicator - incident energy spectra compared with BEAMDP spectrum at the field insert (95 cm SSD)
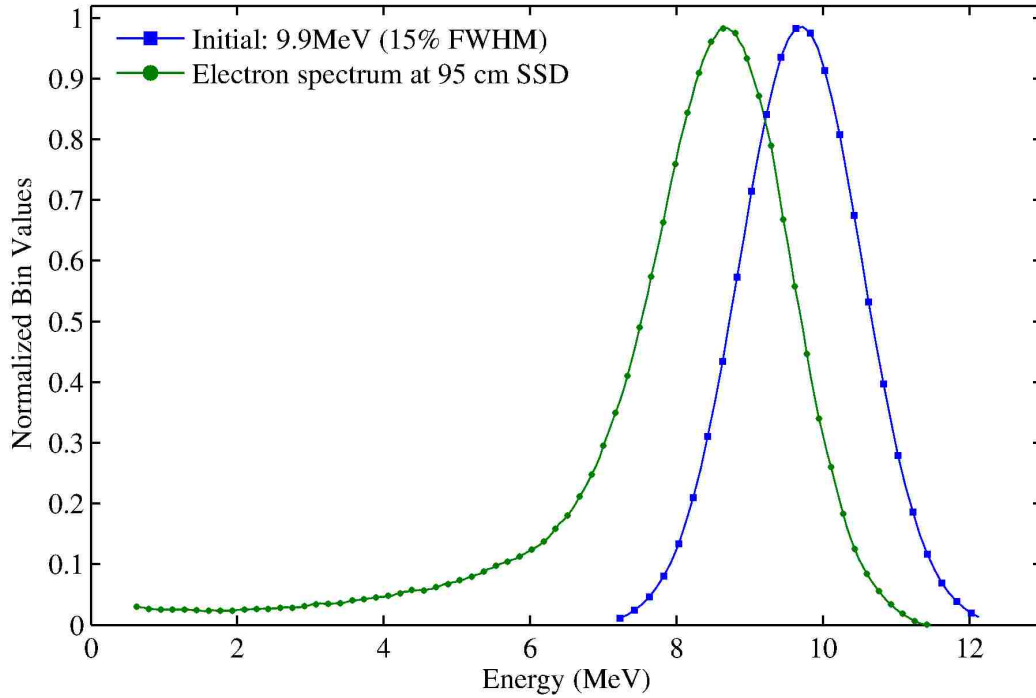
Figure B.2: 9MeV - 14x14 cm^2 applicator - incident energy spectra compared with BEAMDP spectrum at the field insert (95 cm SSD)
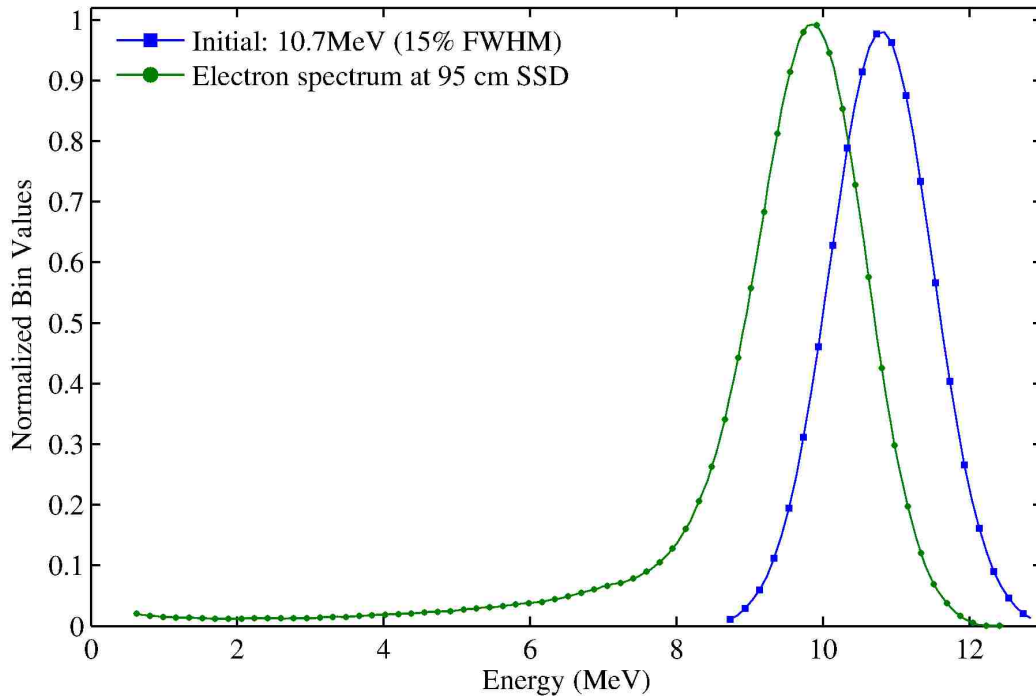
Figure B.3: 10MeV - 14x14 cm^2 applicator - incident energy spectra compared with BEAMDP spectrum at the field insert (95 cm SSD)
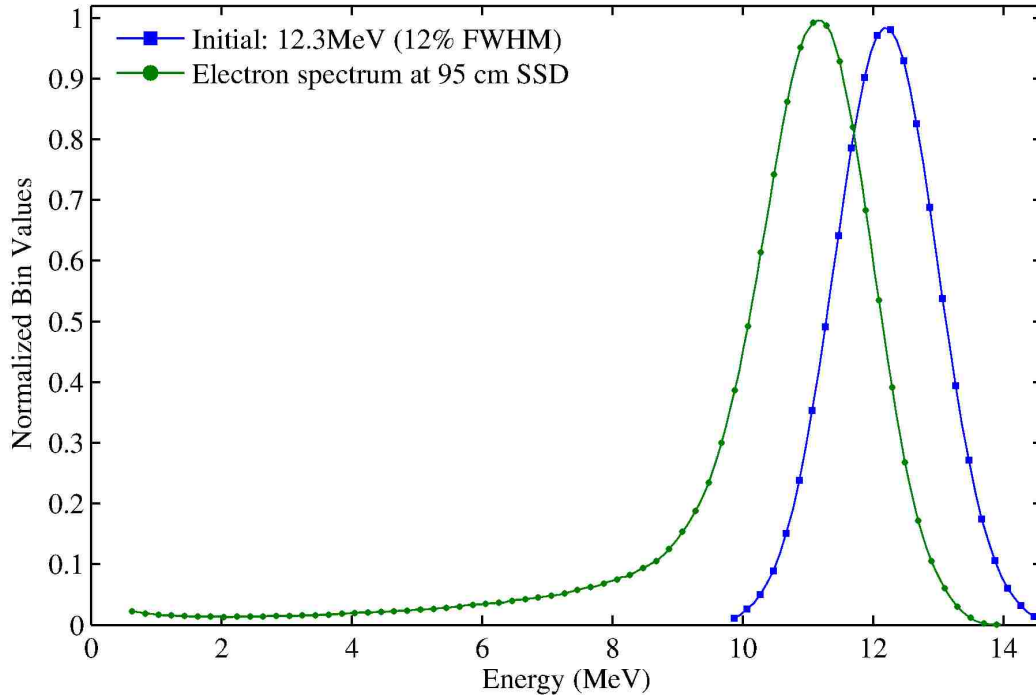
Figure B.4: 11MeV - 14x14 cm^2 applicator - incident energy spectra compared with BEAMDP spectrum at the field insert (95 cm SSD)
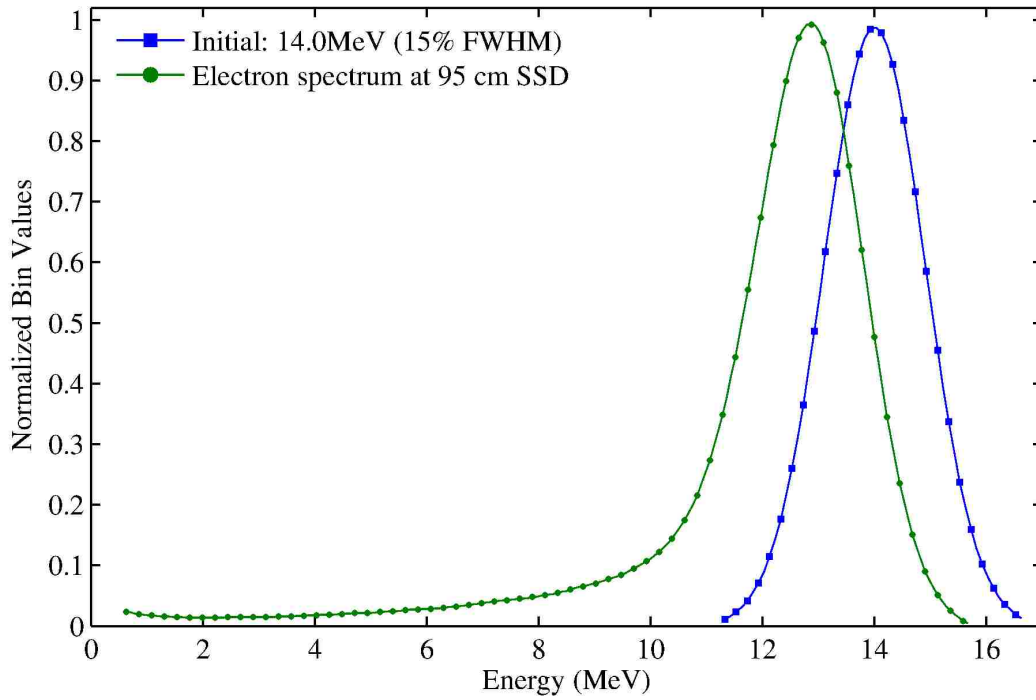
Figure B.5: 13MeV - 14x14 cm^2 applicator - incident energy spectra compared with BEAMDP spectrum at the field insert (95 cm SSD)
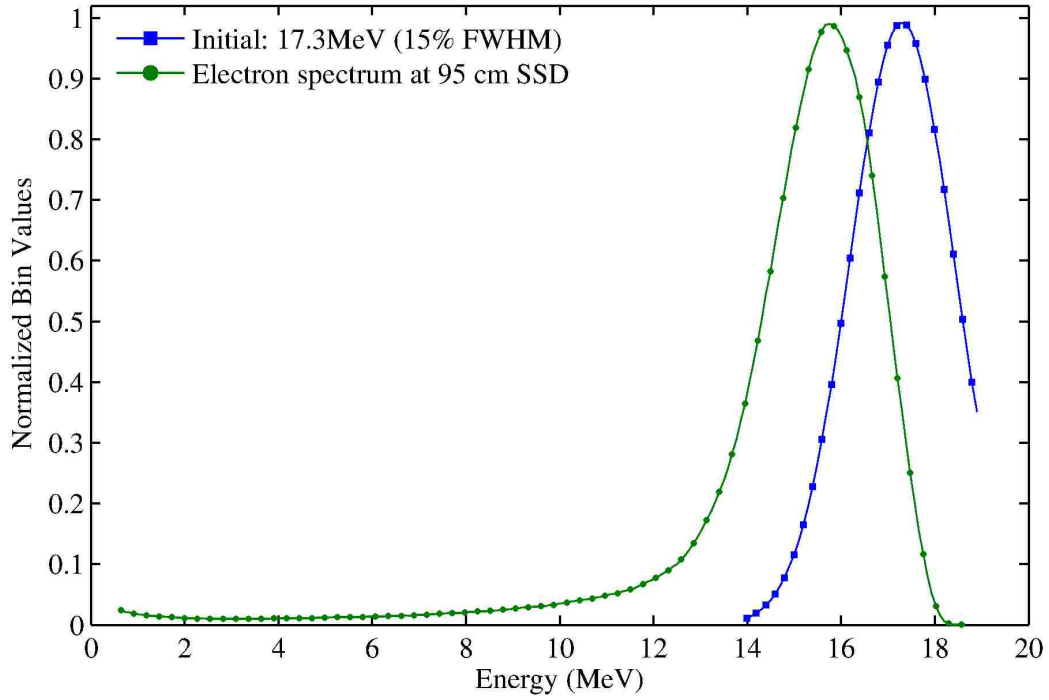
Figure B.6: 16MeV - 14x14 cm^2 applicator - incident energy spectra compared with BEAMDP spectrum at the field insert (95 cm SSD)
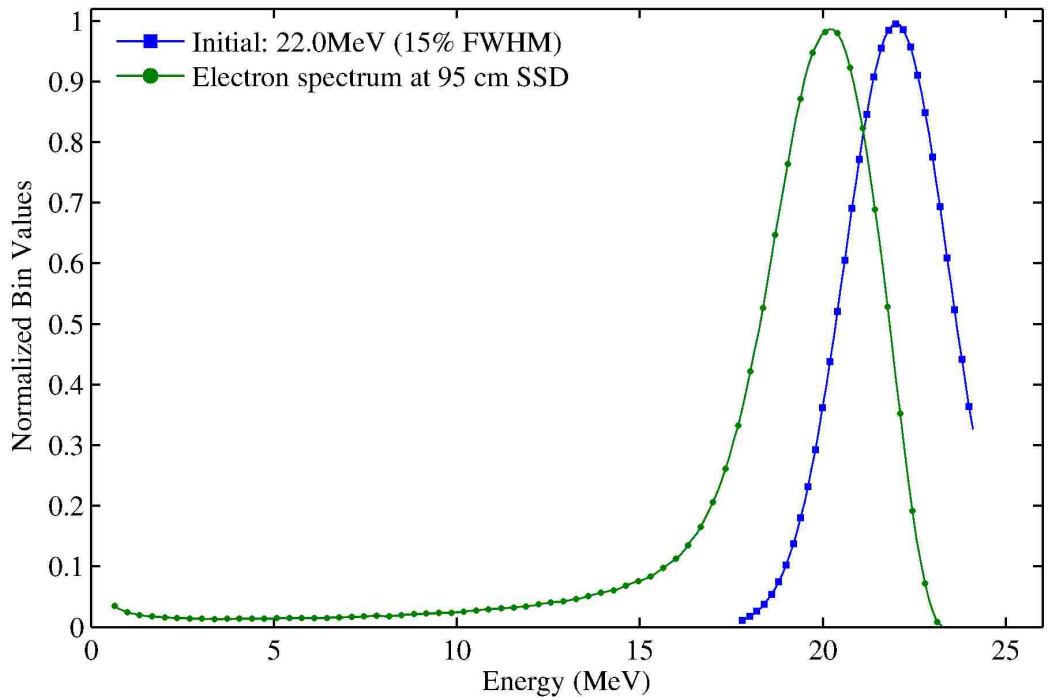
Figure B.7: 20MeV - 14x14 cm^2 applicator - incident energy spectra compared with BEAMDP spectrum at the field insert (95 cm SSD)

Appendix C
Additional Small-Field Results

C.1 7-MeV 6x6 cm^2 Applicator - 100 cm SSD
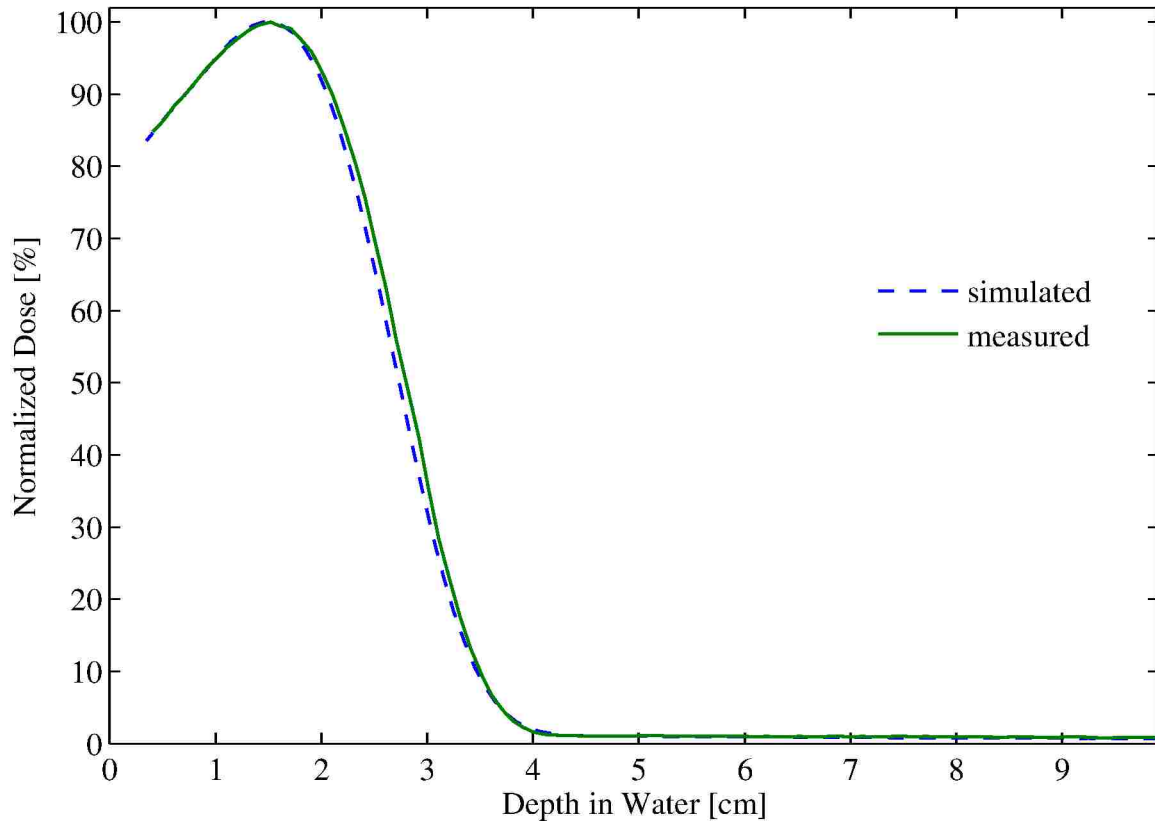
Figure C.1: %DD: 7MeV - 06x06 cm^2 applicator

Table C.1: 7MeV-06x06 cm^2 applicator comparison summary

| Profile type (%DD, X)	Profile depth (cm)	Percent of points passing 2%/1mm	2%/2mm	3%/3mm
%DD	–	100.0%	–	–
Cross-plane (X)	0.5	100.0%	–	–
	1.0	100.0%	–	–
	2.0	100.0%	–	–
	2.5	100.0%	–	–
	2.8	100.0%	–	–
	3.5	100.0%	–	–
	5.5	100.0%	–	–
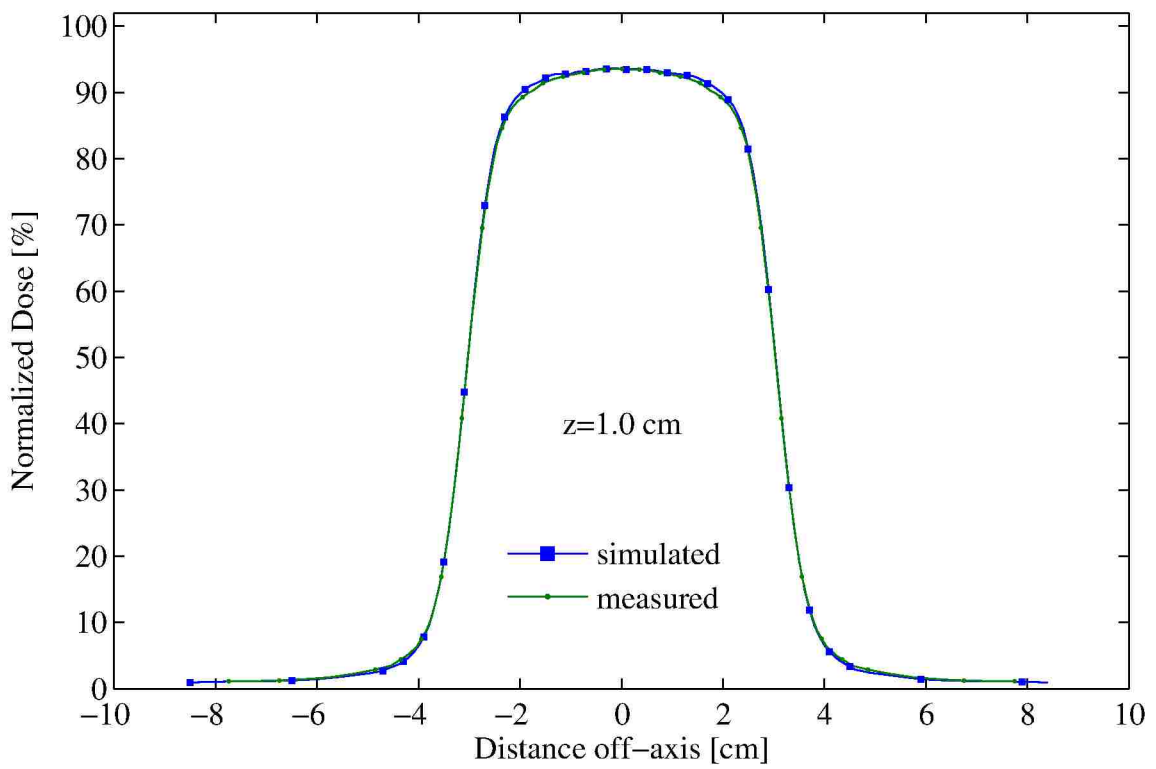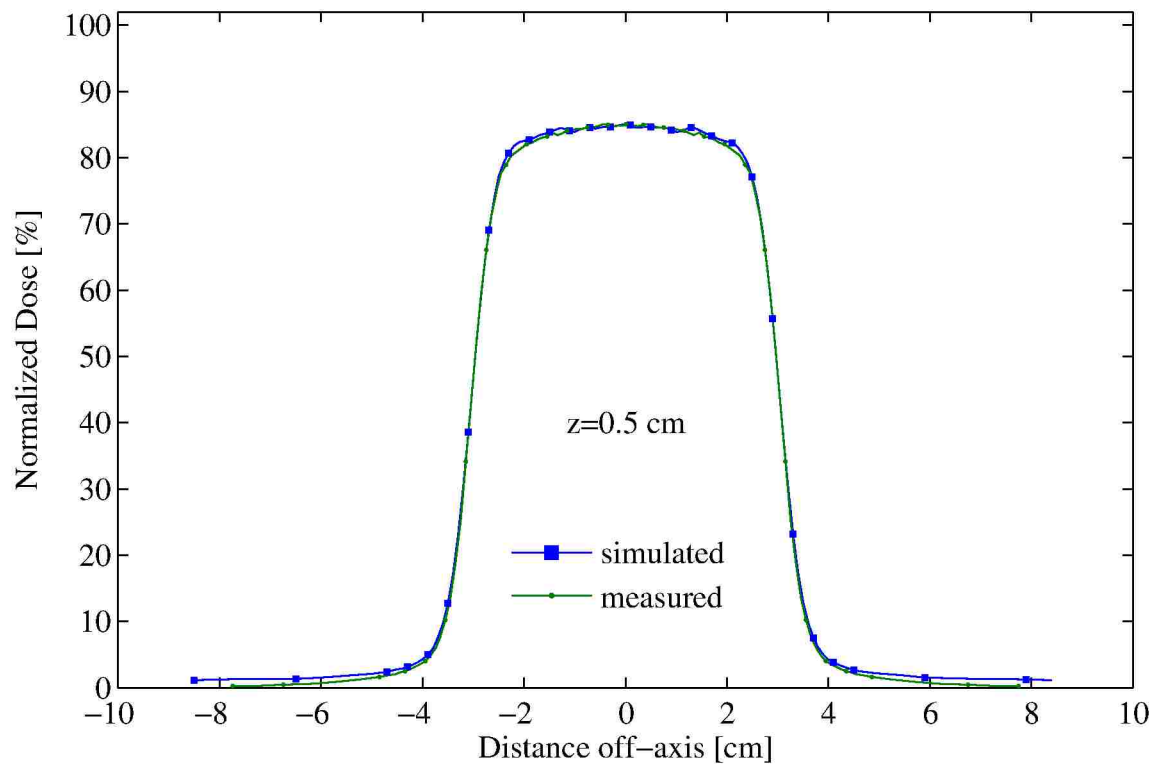
Figure C.2: 7MeV-6x6 cm^2 100cm SSD - cross-plane profiles at depths, z=0.5 and 1.0 cm
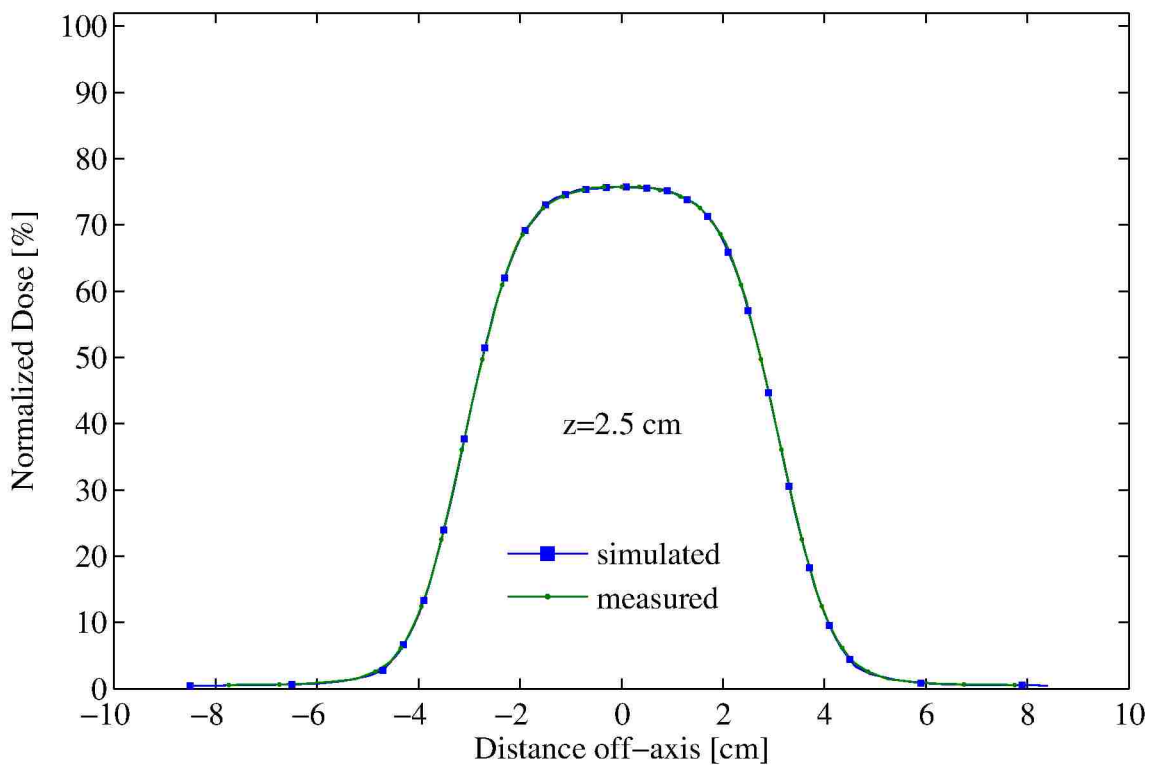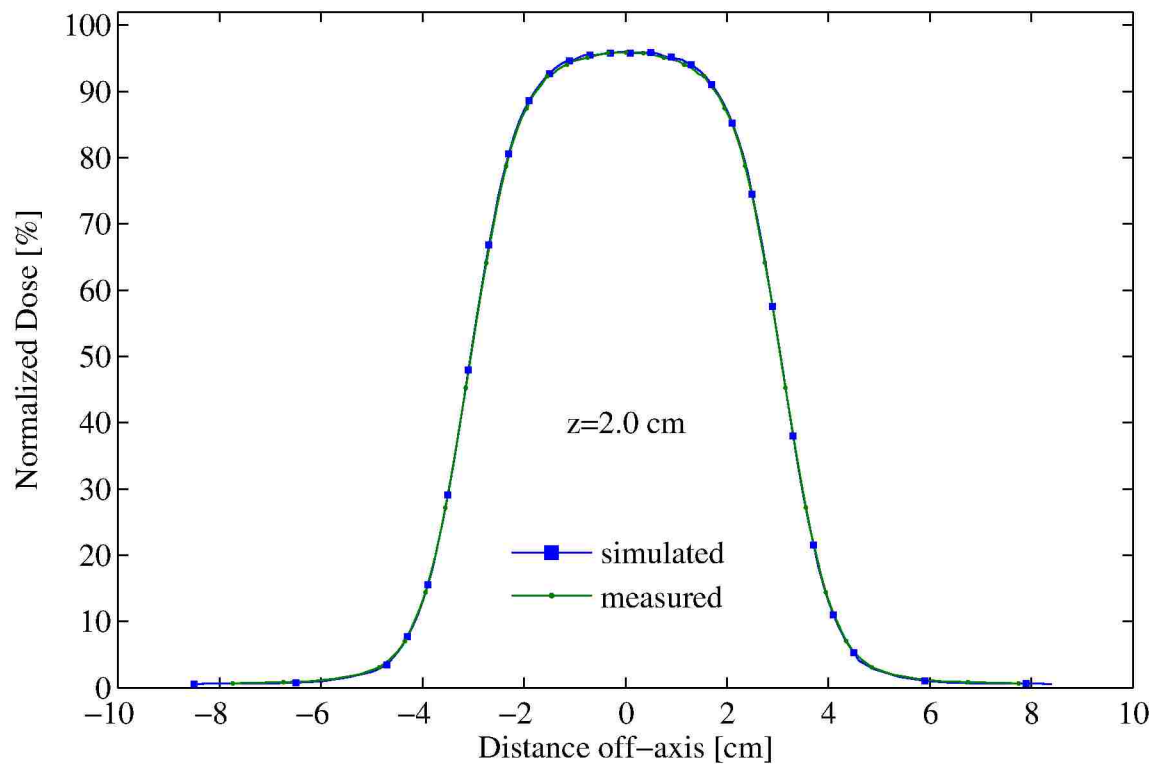
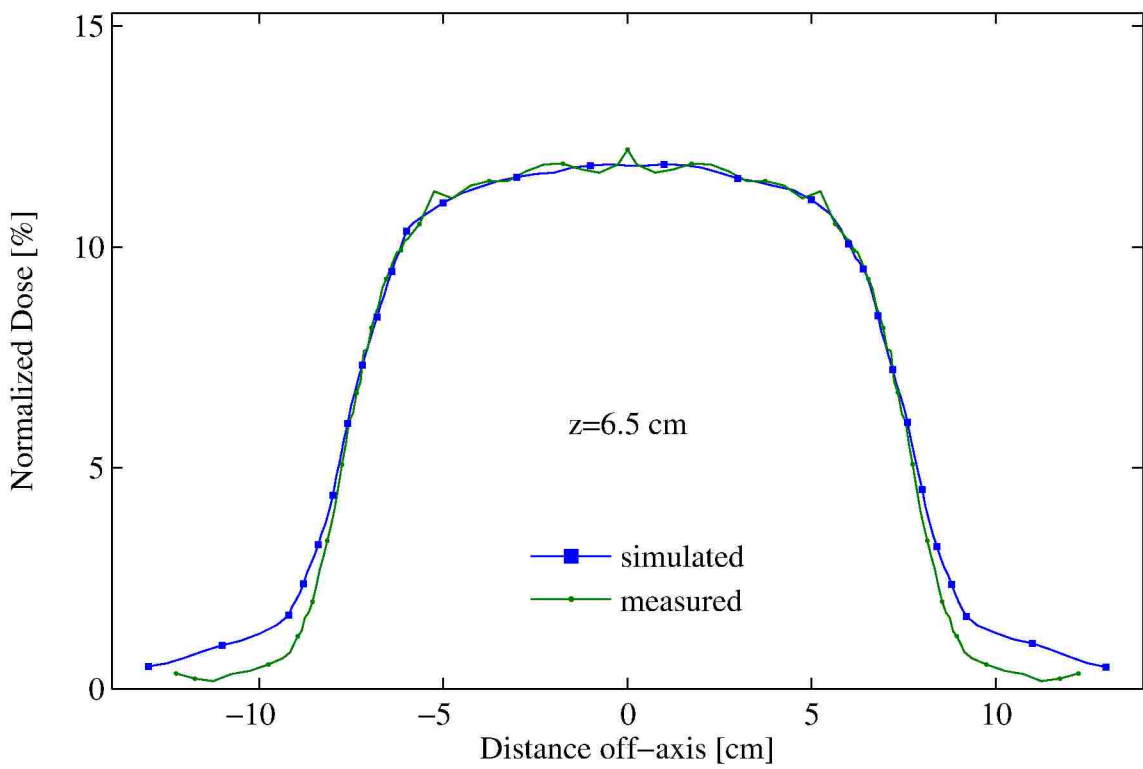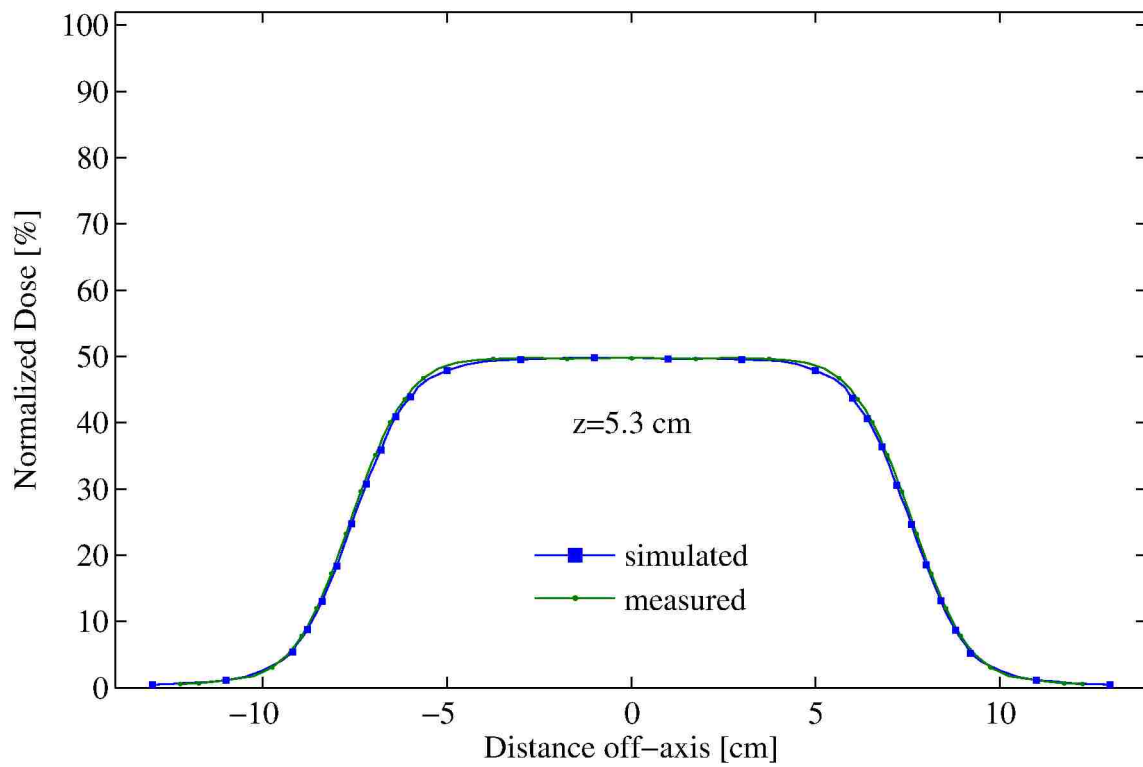Figure C.3: 7MeV-6x6 cm^2 100cm SSD - cross-plane profiles at depths, z=2.0 and 2.5 cm
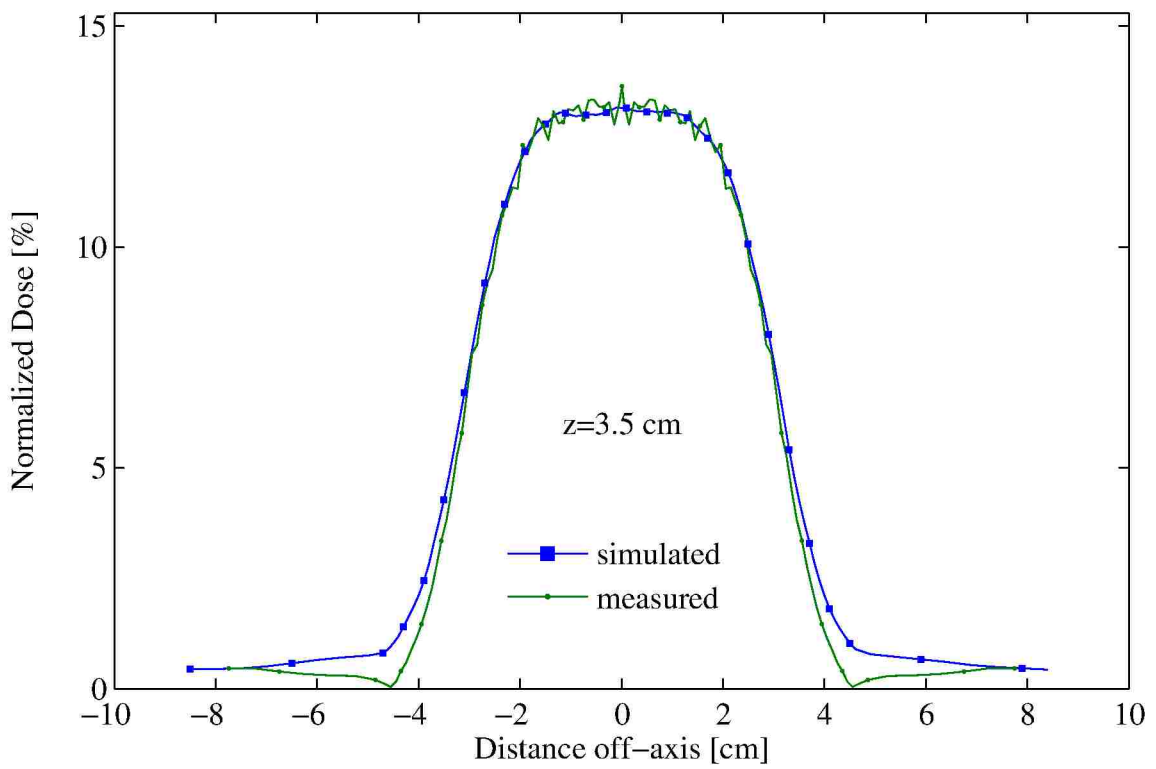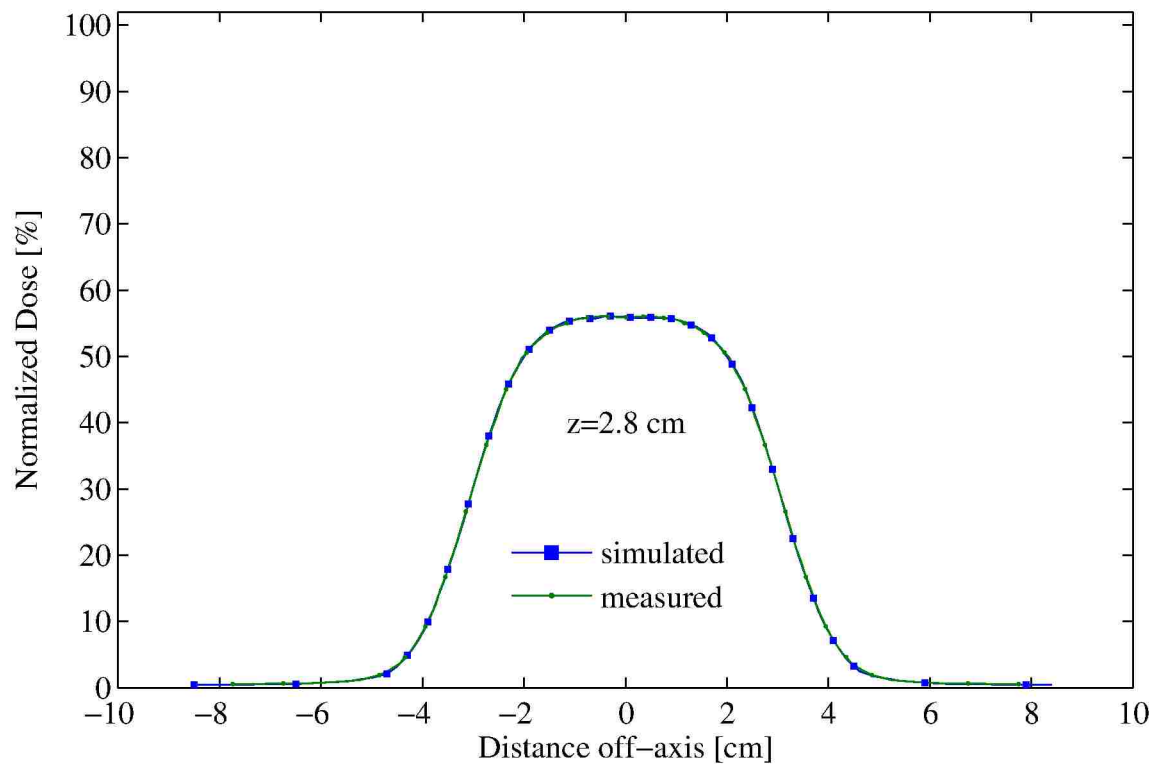
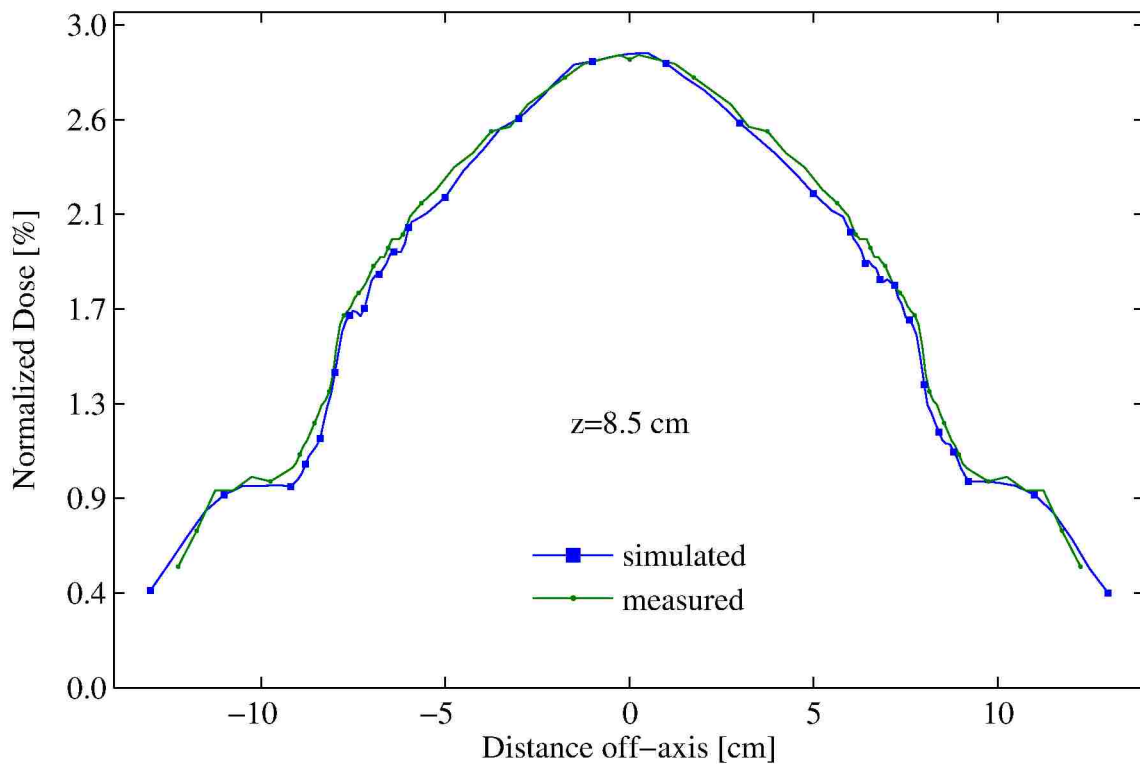Figure C.4: 7MeV-6x6 cm^2 100cm SSD - cross-plane profiles at depths, z=2.8 and 3.5 cm
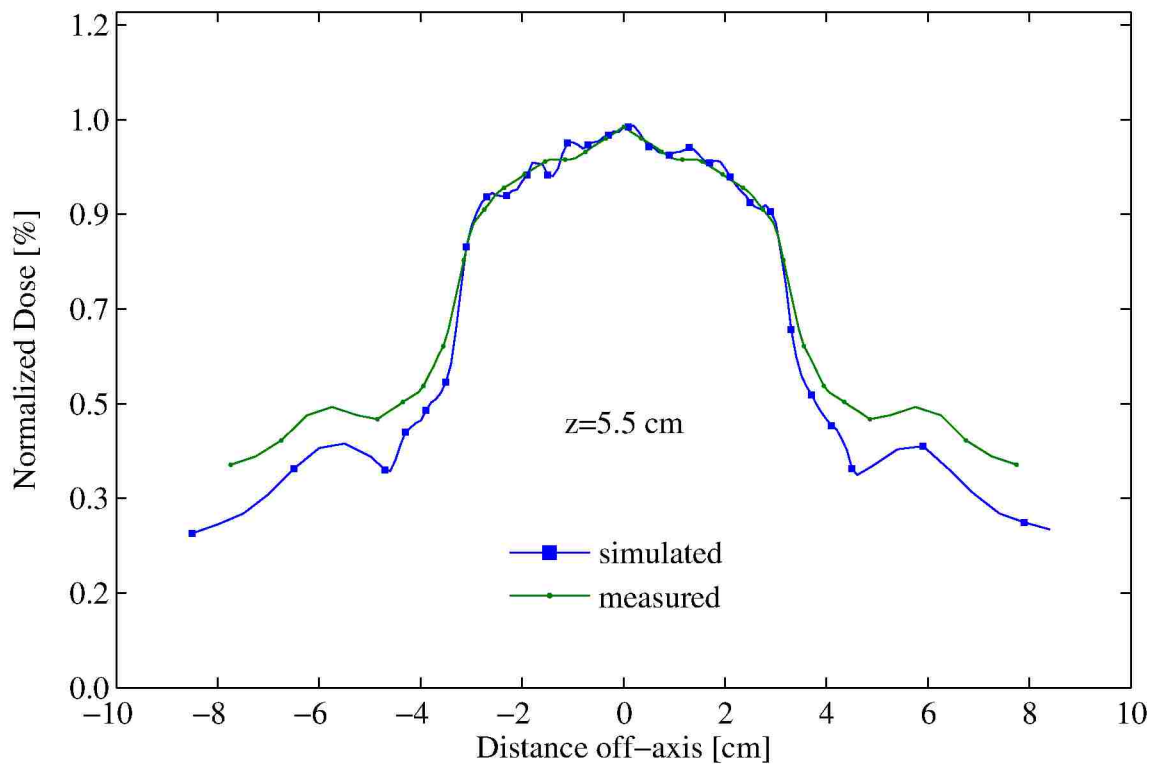
Figure C.5: 7MeV-6x6 cm^2 100cm SSD - cross-plane profiles at depth, z=5.5 cm

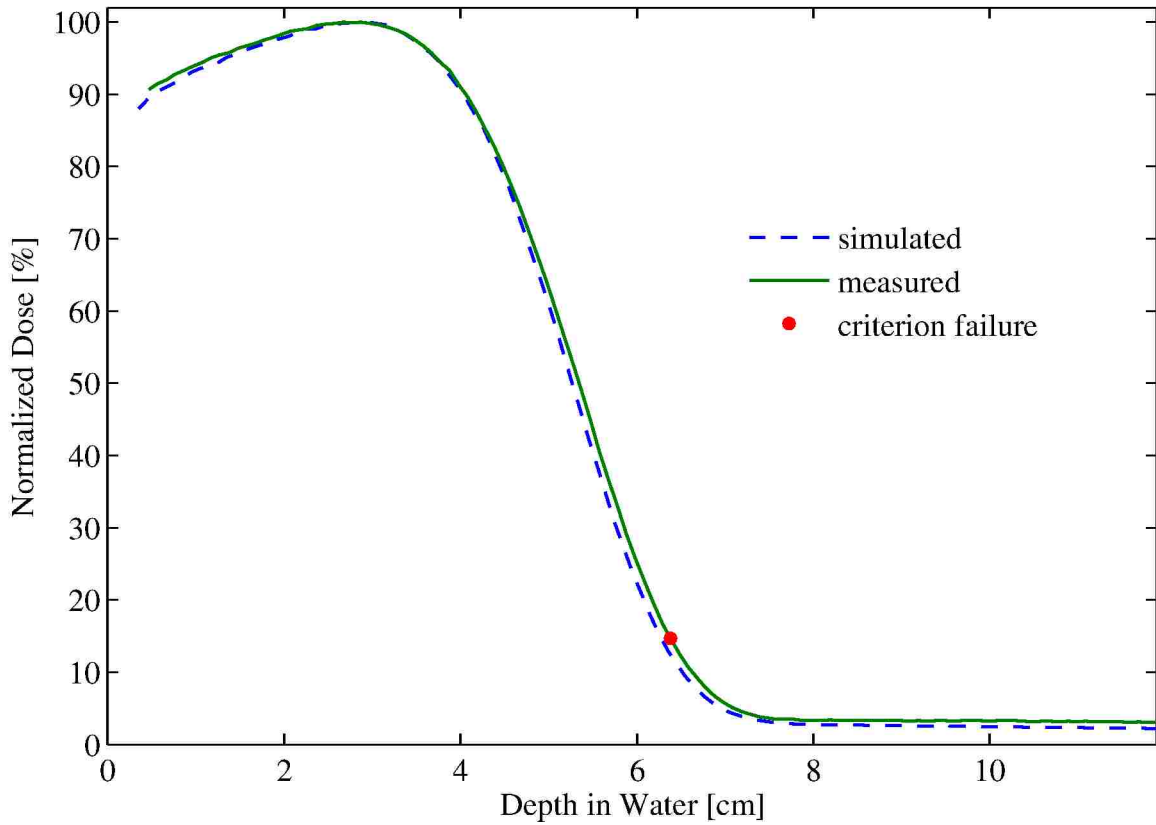## C.2 7-MeV 14x14 cm^2 Applicator - 100 cm SSD
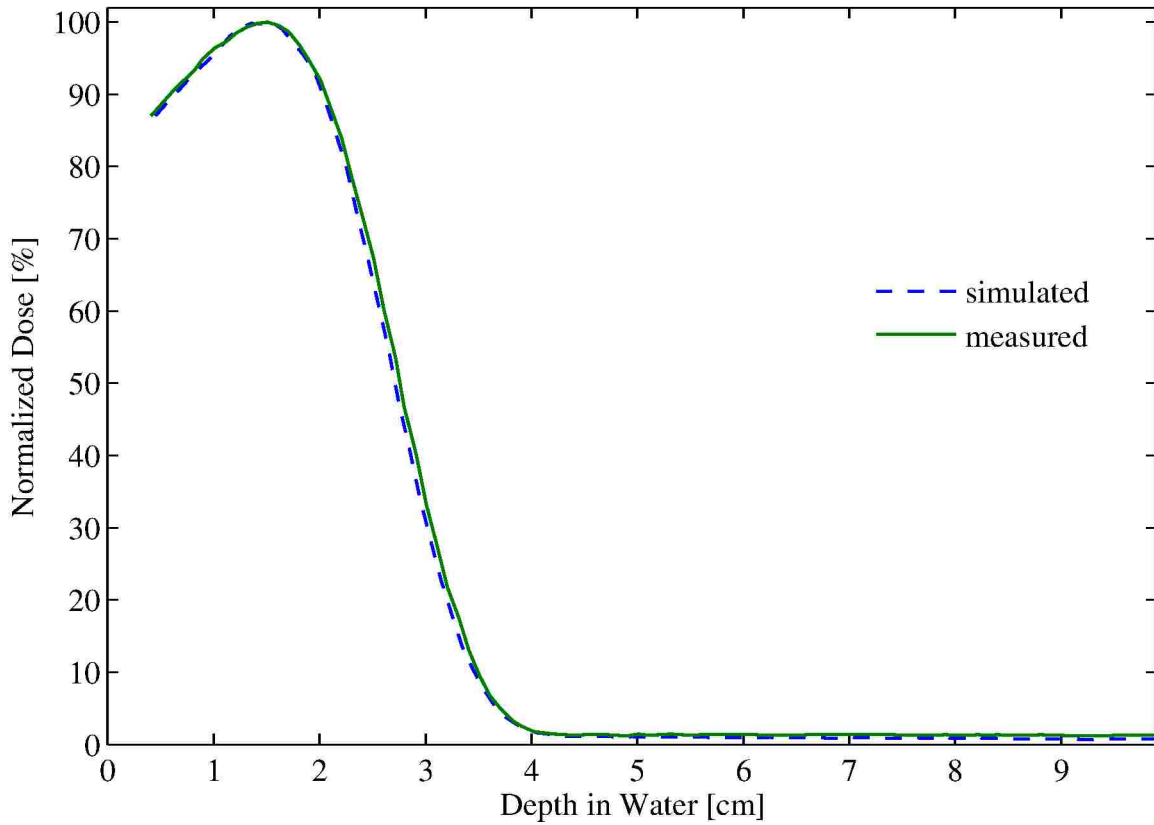
Figure C.6: %DD: 7MeV - 14x14 cm^2 applicator

Table C.2: 7MeV-14x14 cm^2 applicator comparison summary

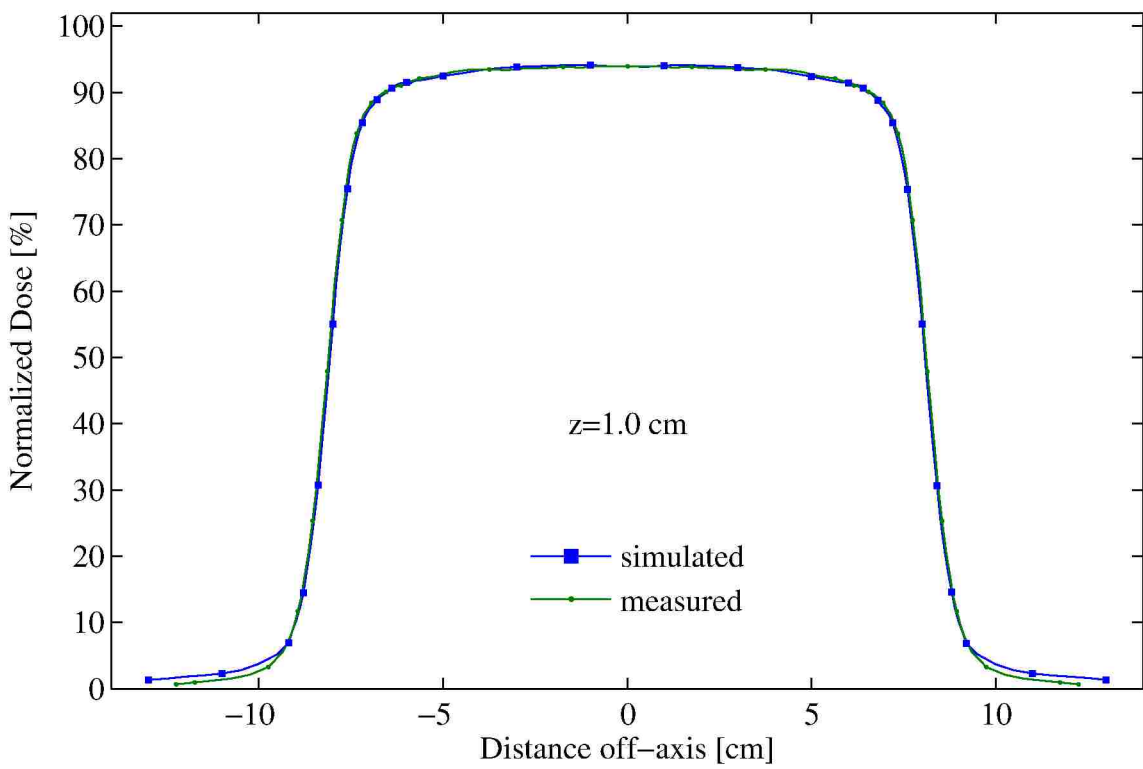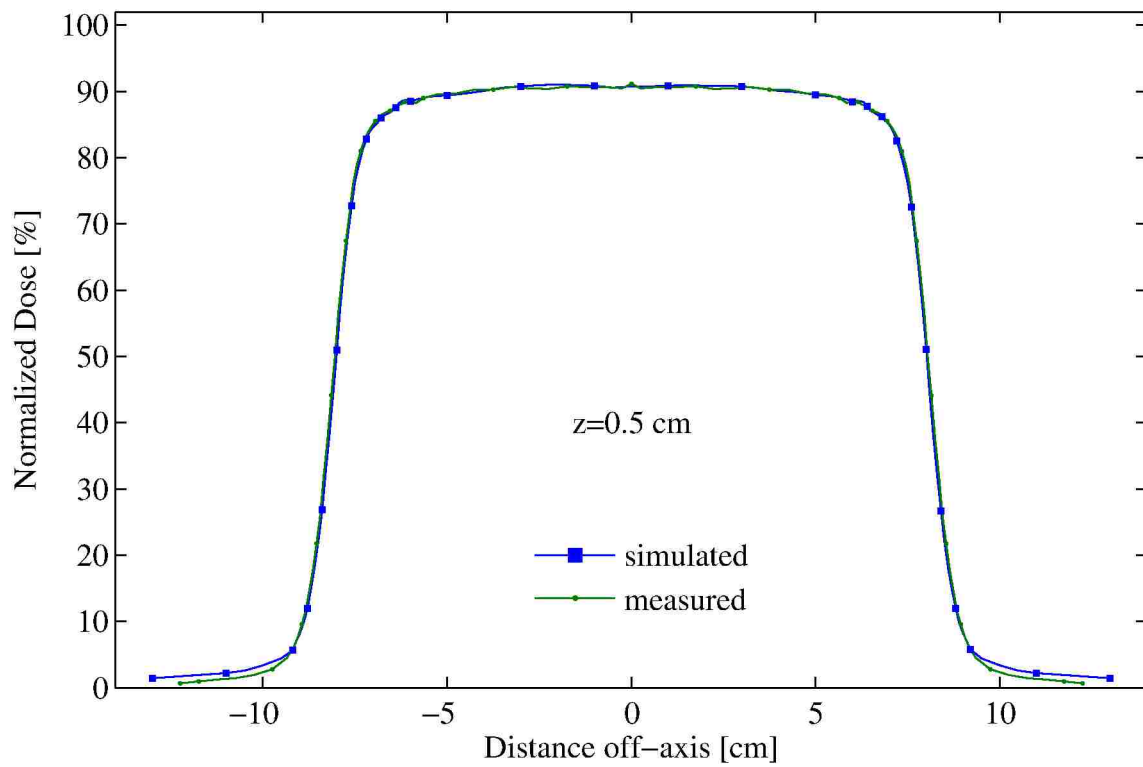| Profile type (%DD, X)	Profile depth (cm)	Percent of points passing		
		2%/1mm	2%/2mm	3%/3mm
%DD	–	100.0%	–	–
Cross-plane (X)	0.5	100.0%	–	–
	1.0	100.0%	–	–
	2.1	100.0%	–	–
	2.5	100.0%	–	–
	2.8	100.0%	–	–
	3.5	100.0%	–	–
	5.5	100.0%	–	–

Figure C.7: 7MeV-14x14 cm^2 100cm SSD - cross-plane profiles at depths, z=0.5 and 1.0 cm
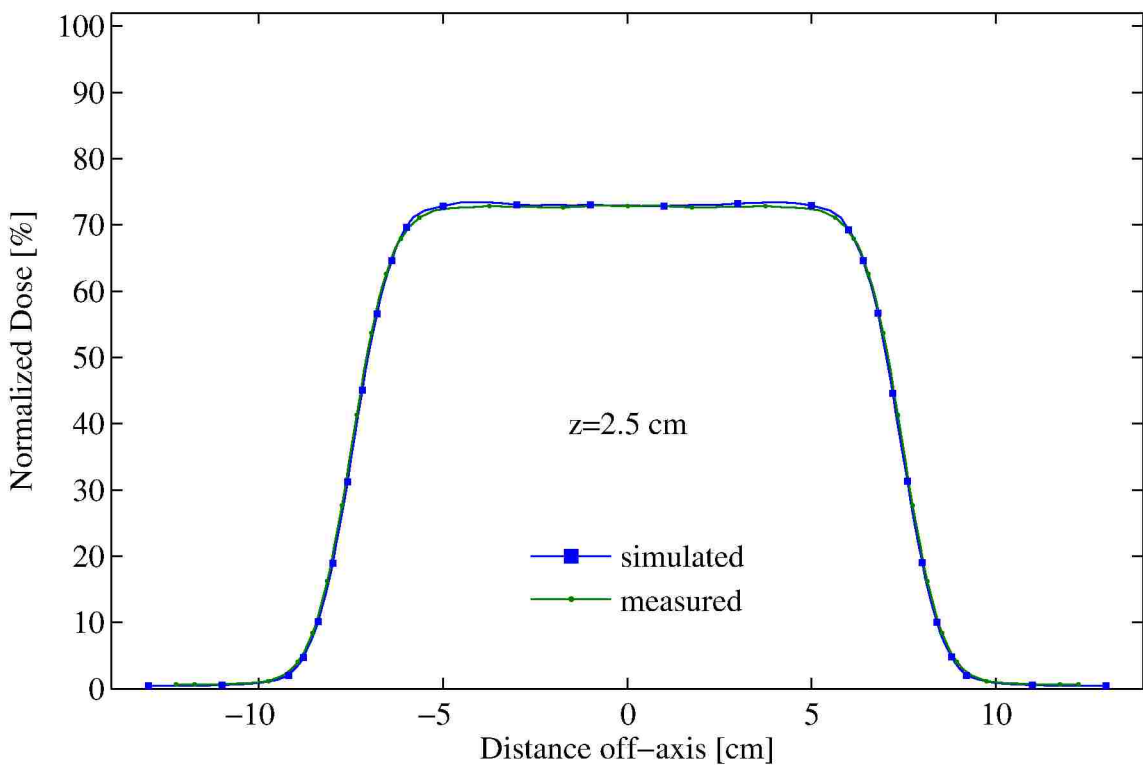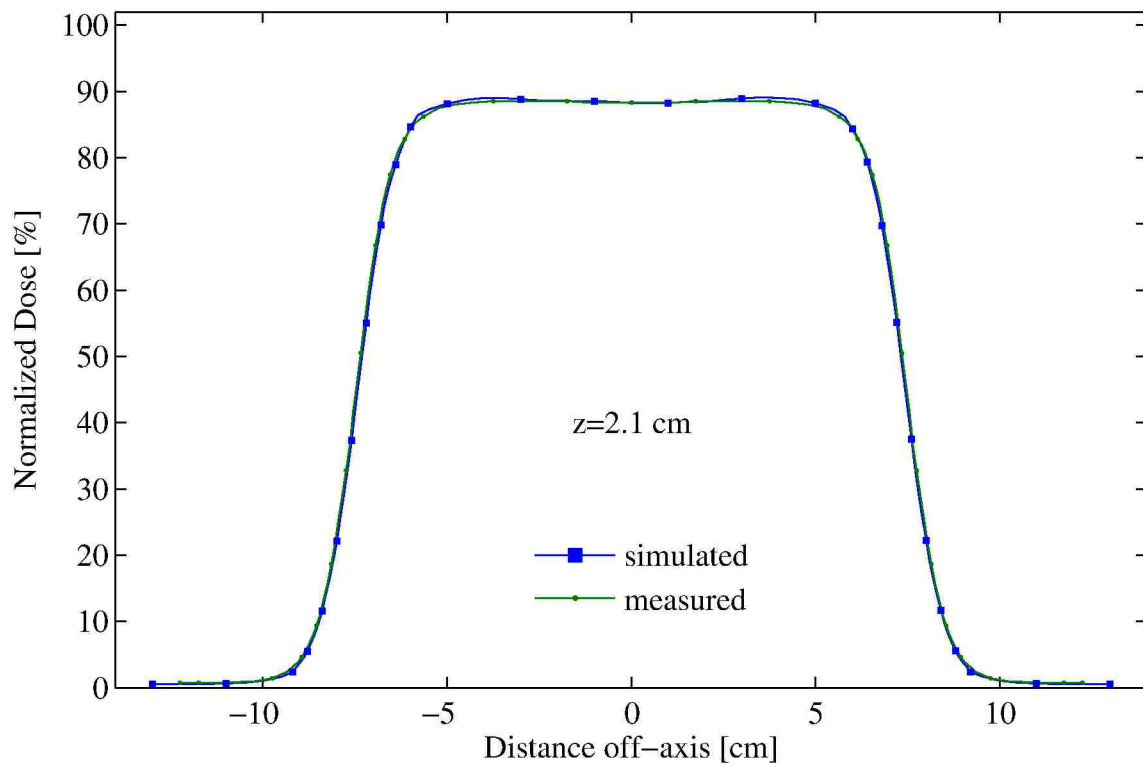
Figure C.8: 7MeV-14x14 cm^2 100cm SSD - cross-plane profiles at depths, z=2.1 and 2.5 cm
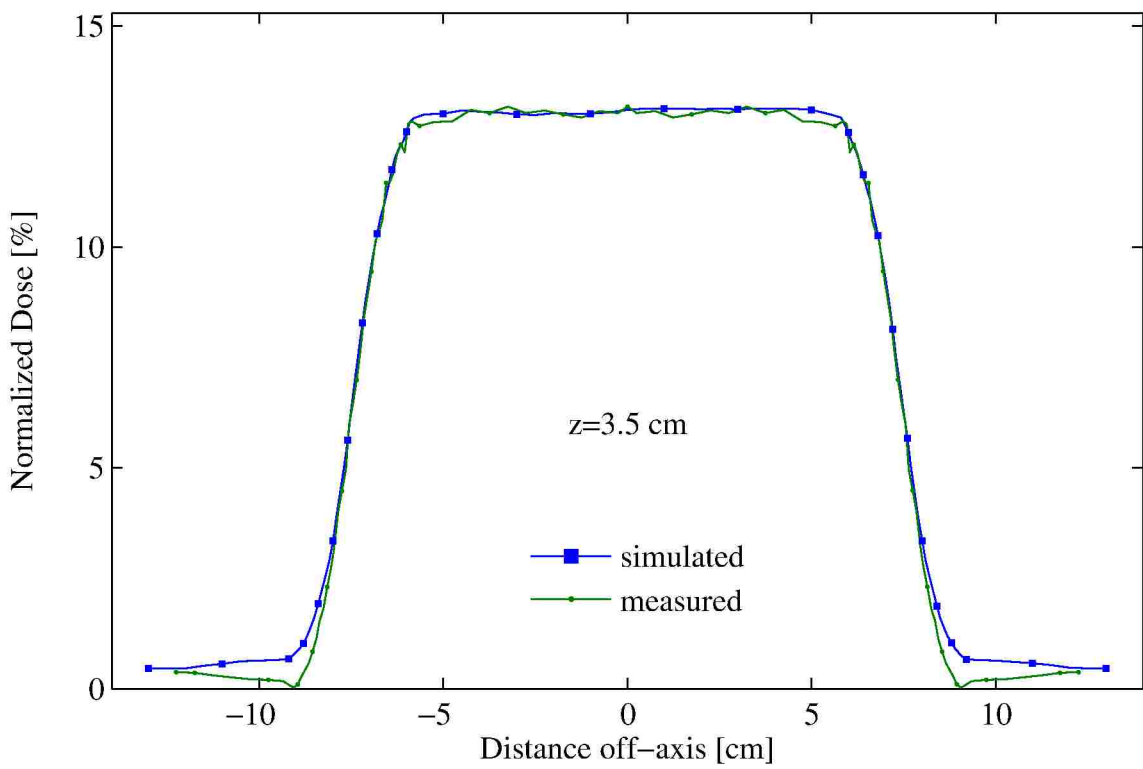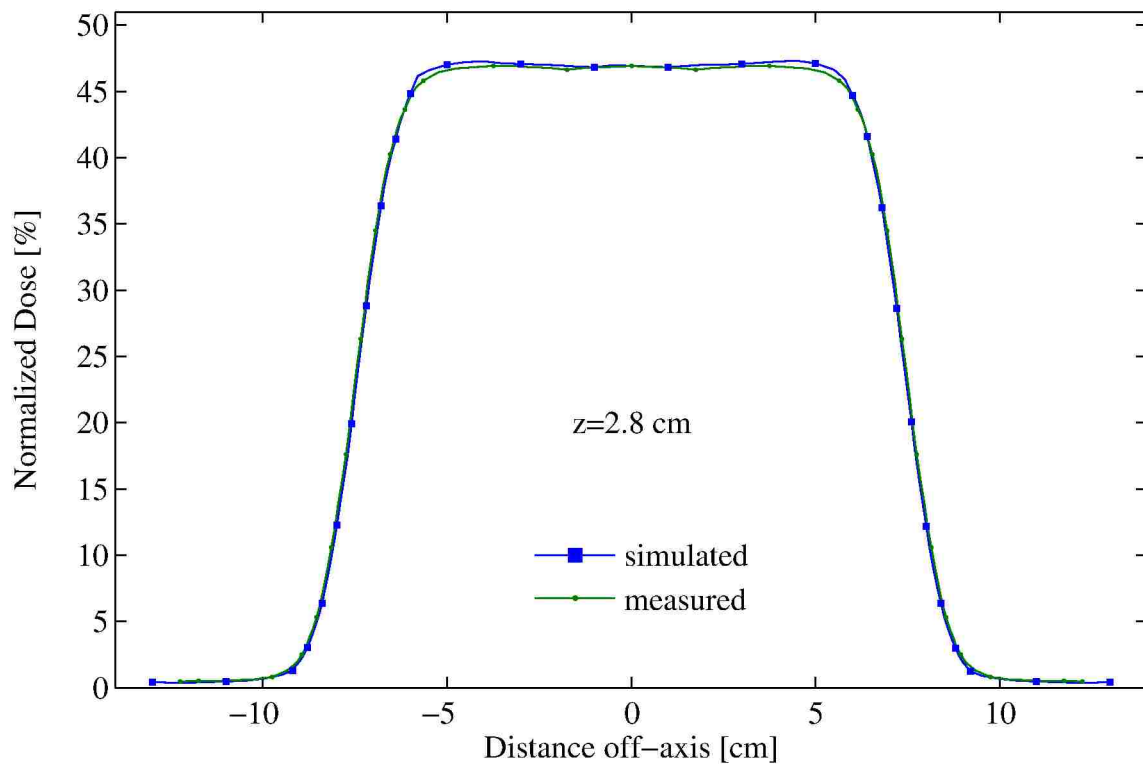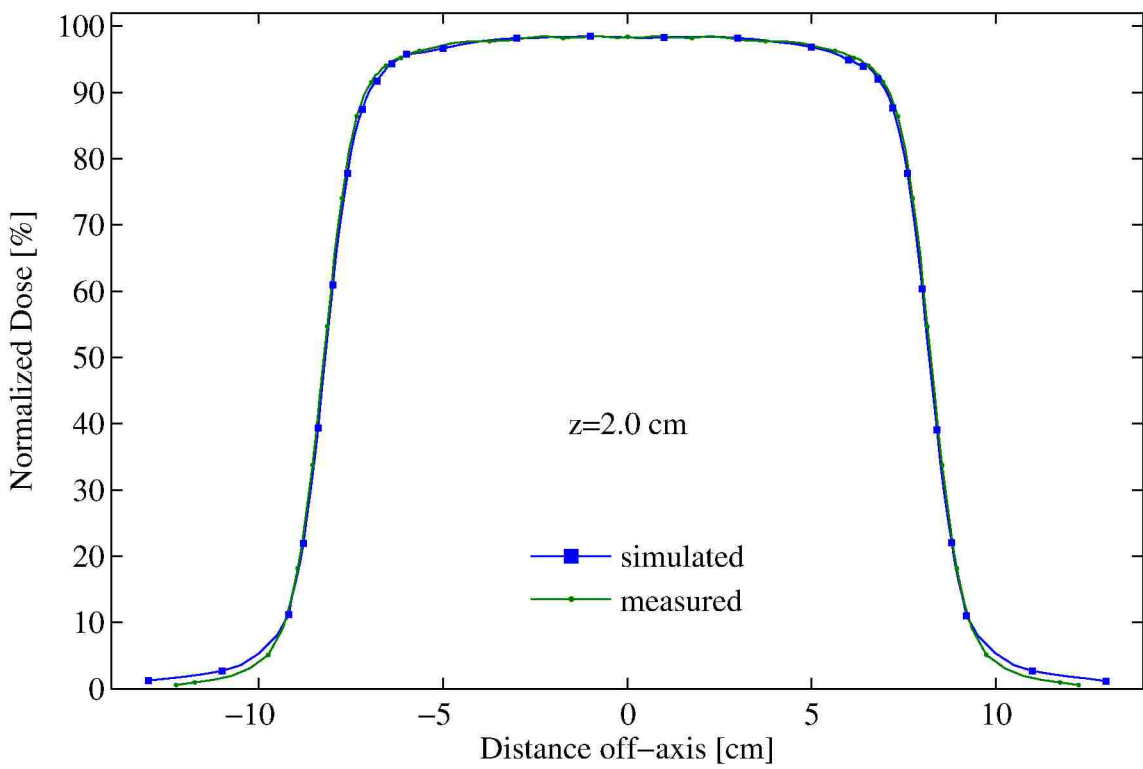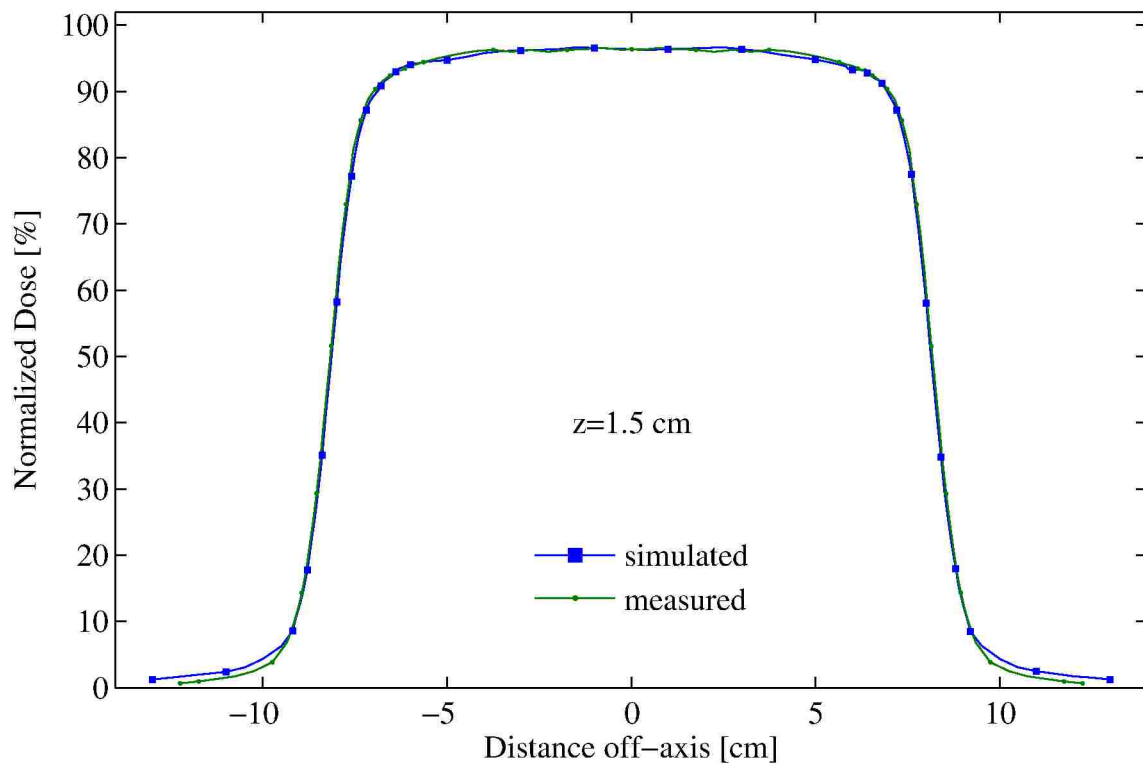
Figure C.9: 7MeV-14x14 cm^2 100cm SSD - cross-plane profiles at depths, z=2.8 and 3.5 cm
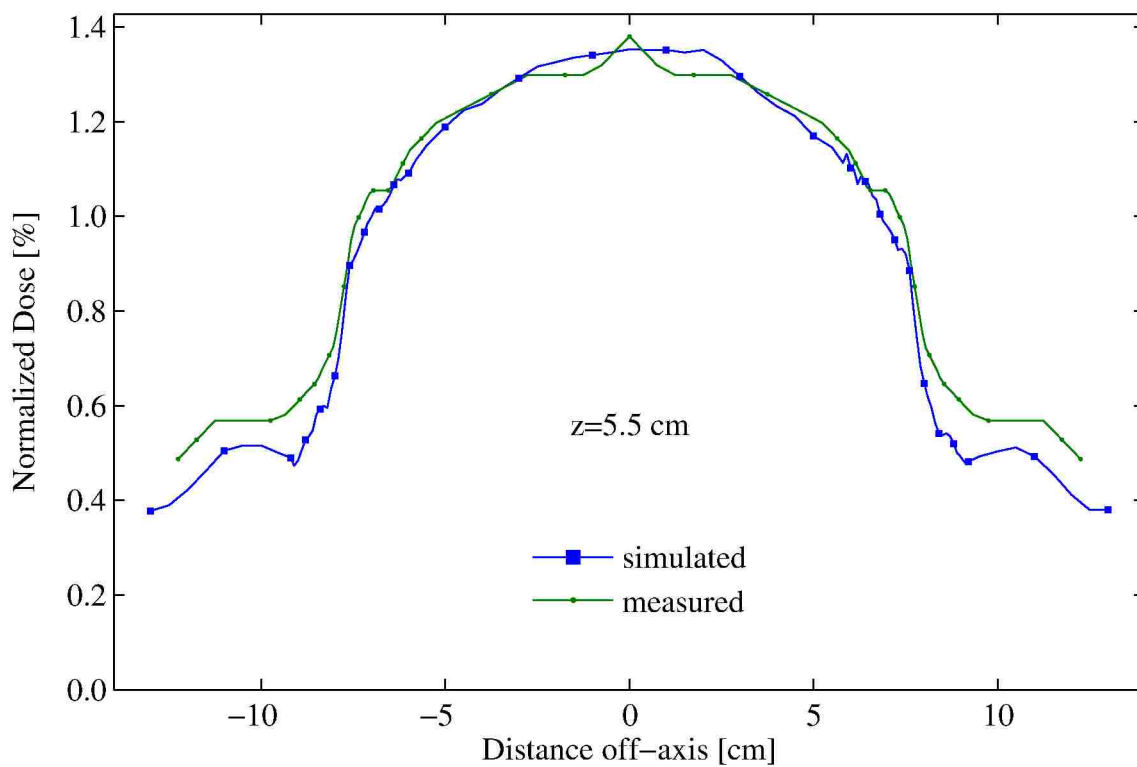
Figure C.10: 7MeV-14x14 cm^2 100cm SSD - cross-plane profiles at depth, z=5.5 cm

C.3 7-MeV 14x14 cm^2 Applicator - 110 cm SSD
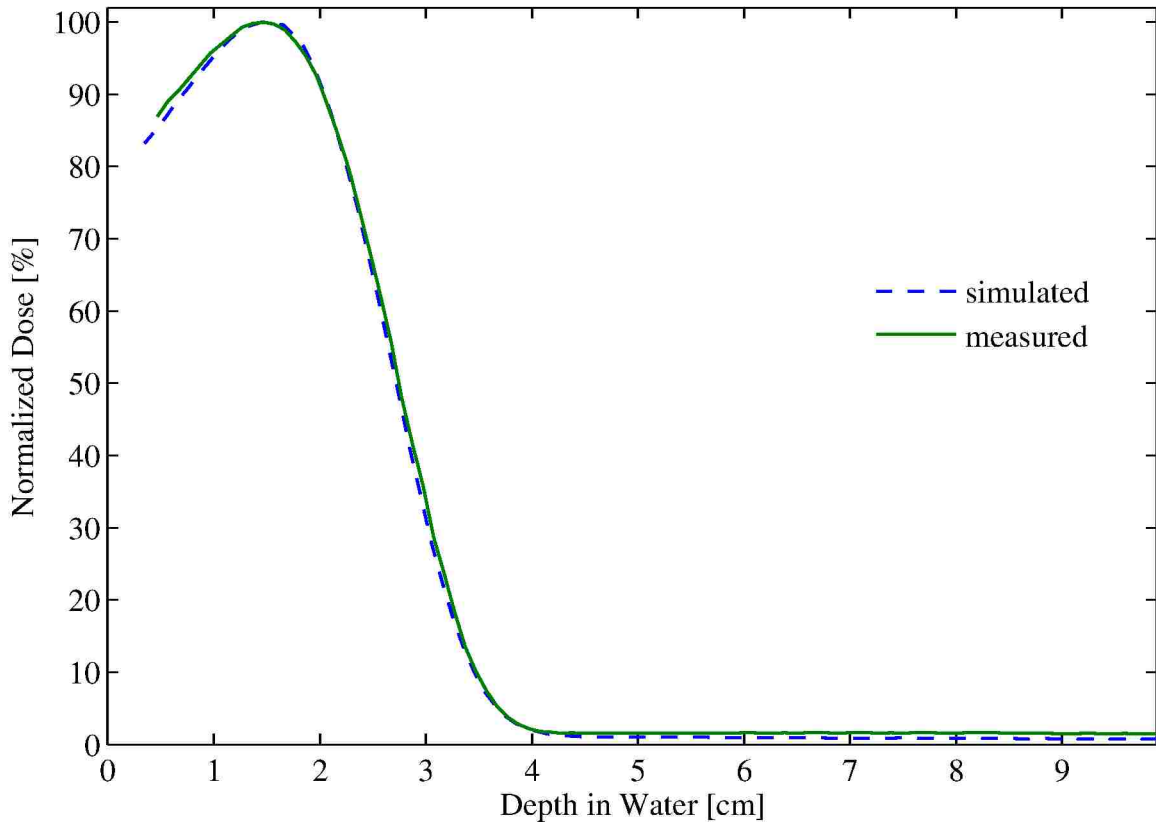
Figure C.11: %DD: 7MeV - 14x14 cm^2 applicator

Table C.3: 7MeV-14x14 cm^2 applicator comparison summary

Profile type (%DD, X)	Profile depth (cm)	Percent of points passing		
		2%/1mm	2%/2mm	3%/3mm
%DD	–	100.0%	–	–
Cross-plane (X)	0.5	100.0%	–	–
	1.0	100.0%	–	–
	2.1	100.0%	–	–
	2.5	100.0%	–	–
	2.8	100.0%	–	–
	3.5	100.0%	–	–
	5.5	83.2%	83.2%	98.1%
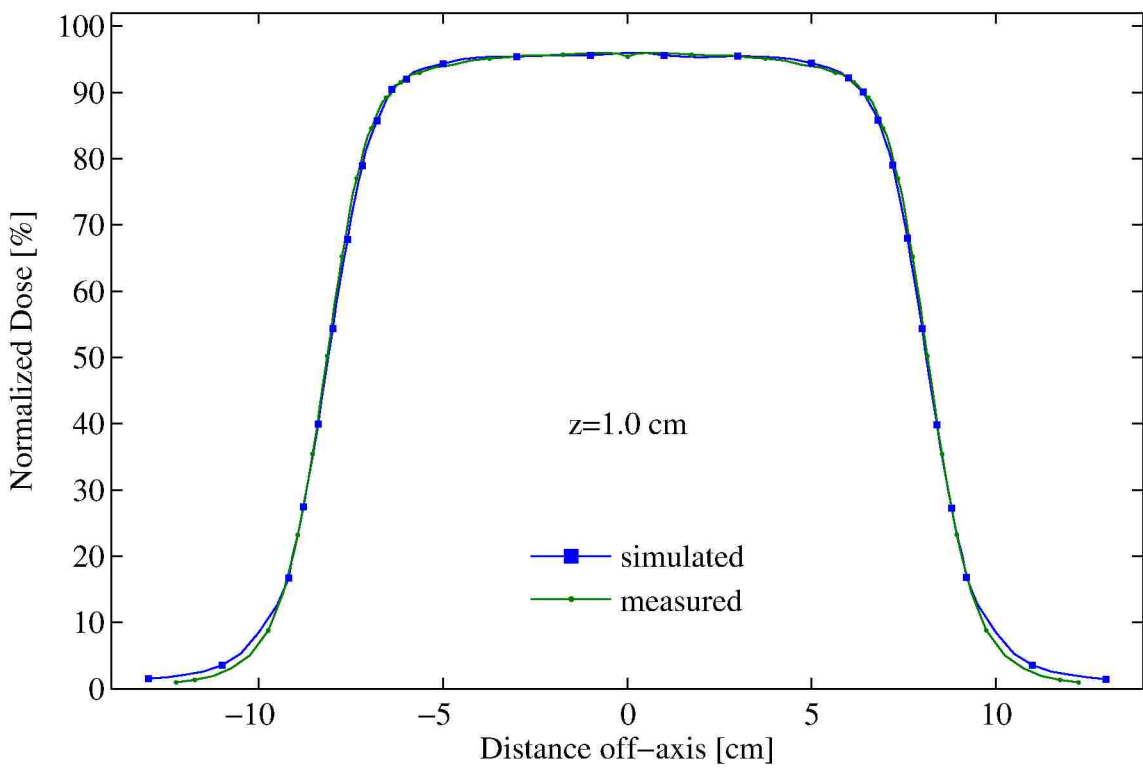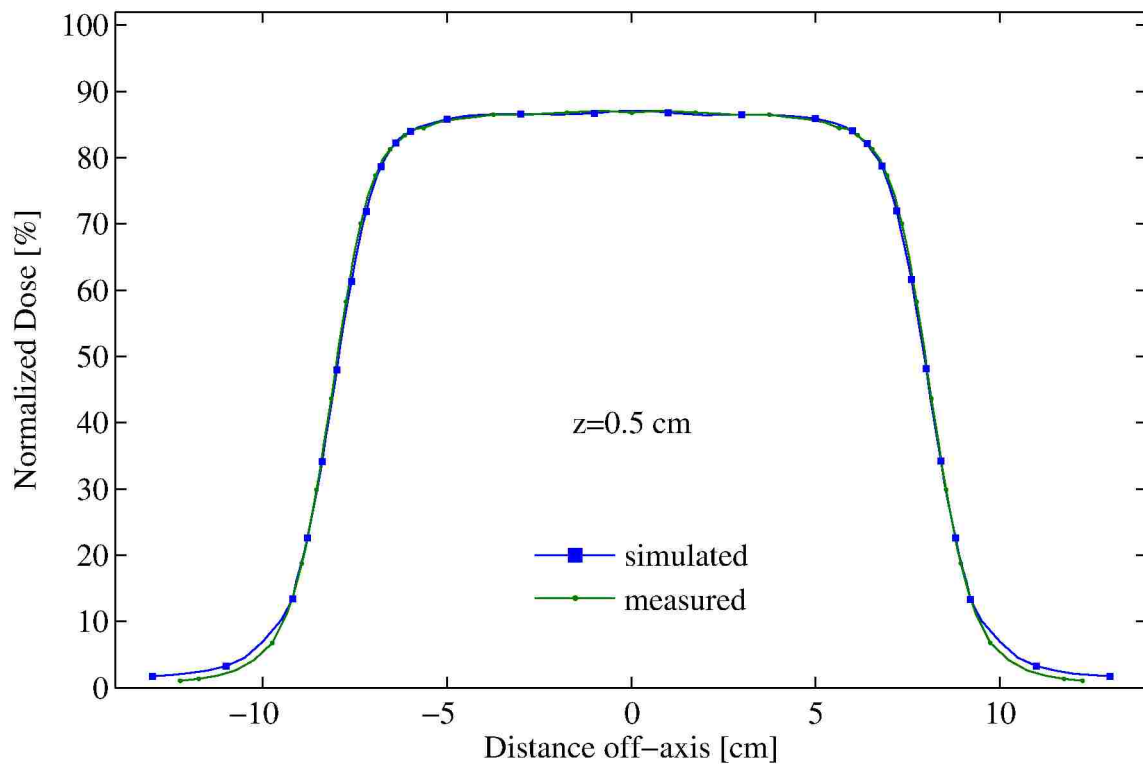
Figure C.12: 7MeV-14x14 cm^2 110cm SSD - cross-plane profiles at depths, z=0.5 and 1.0 cm
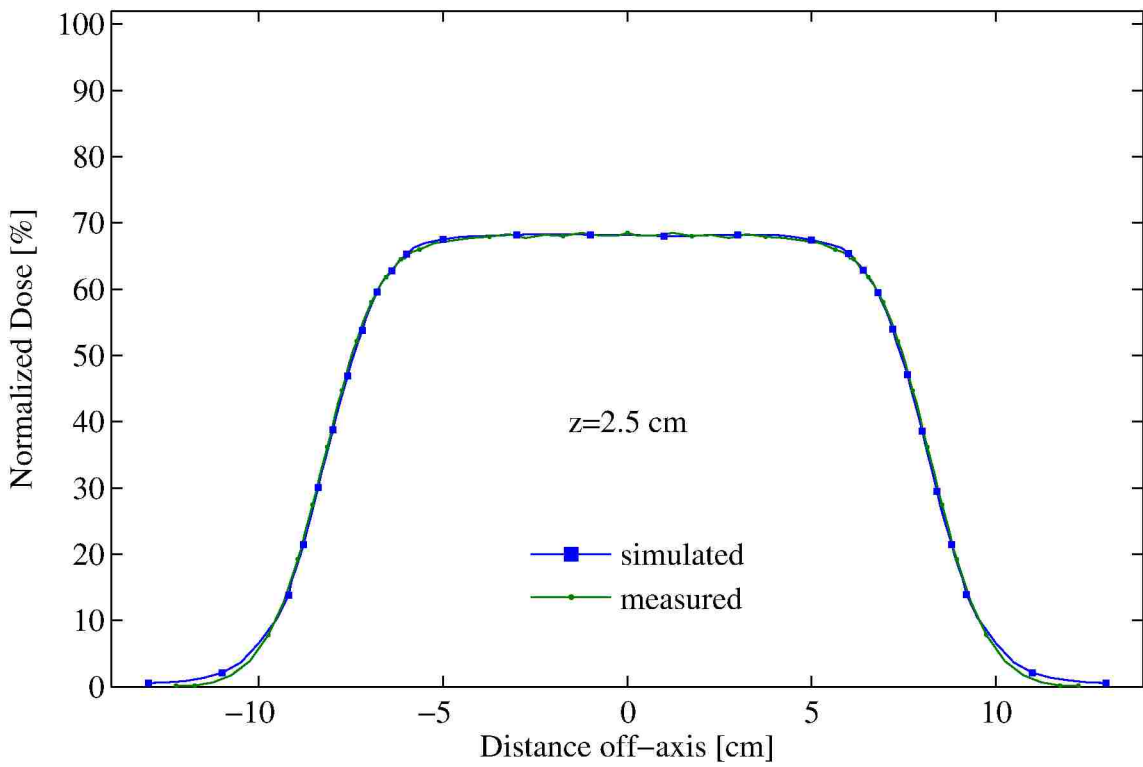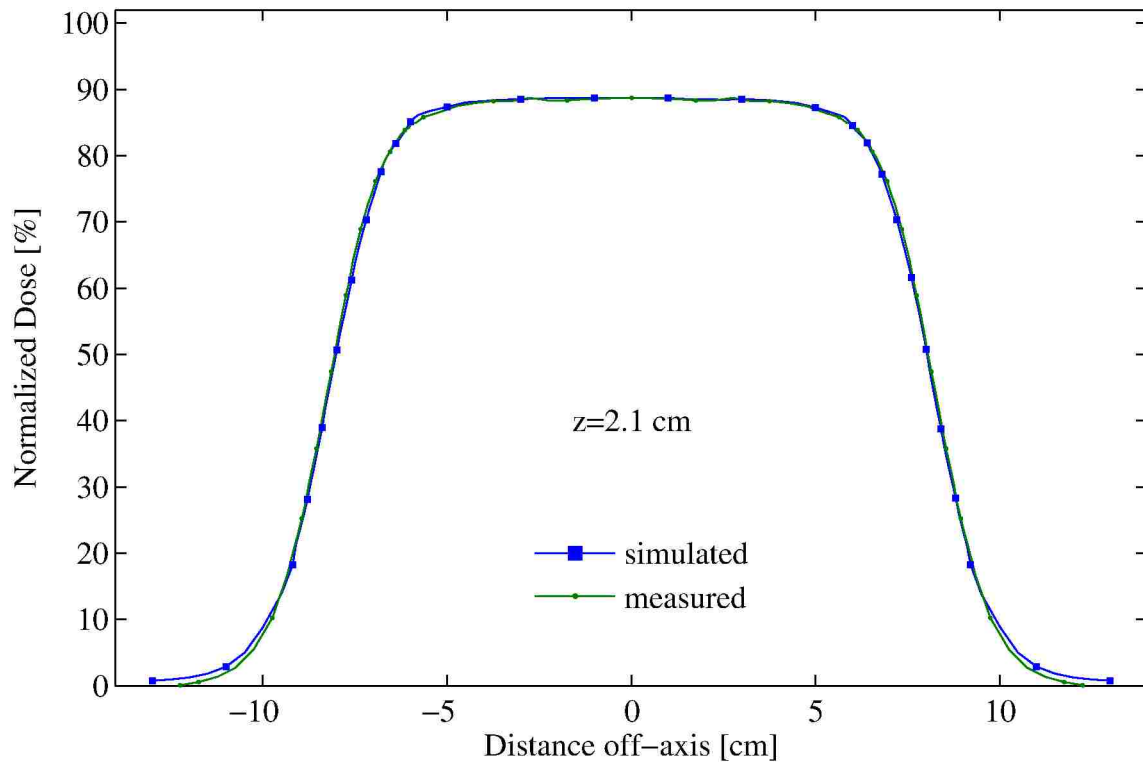
Figure C.13: 7MeV-14x14 cm^2 110cm SSD - cross-plane profiles at depths, z=2.1 and 2.5 cm
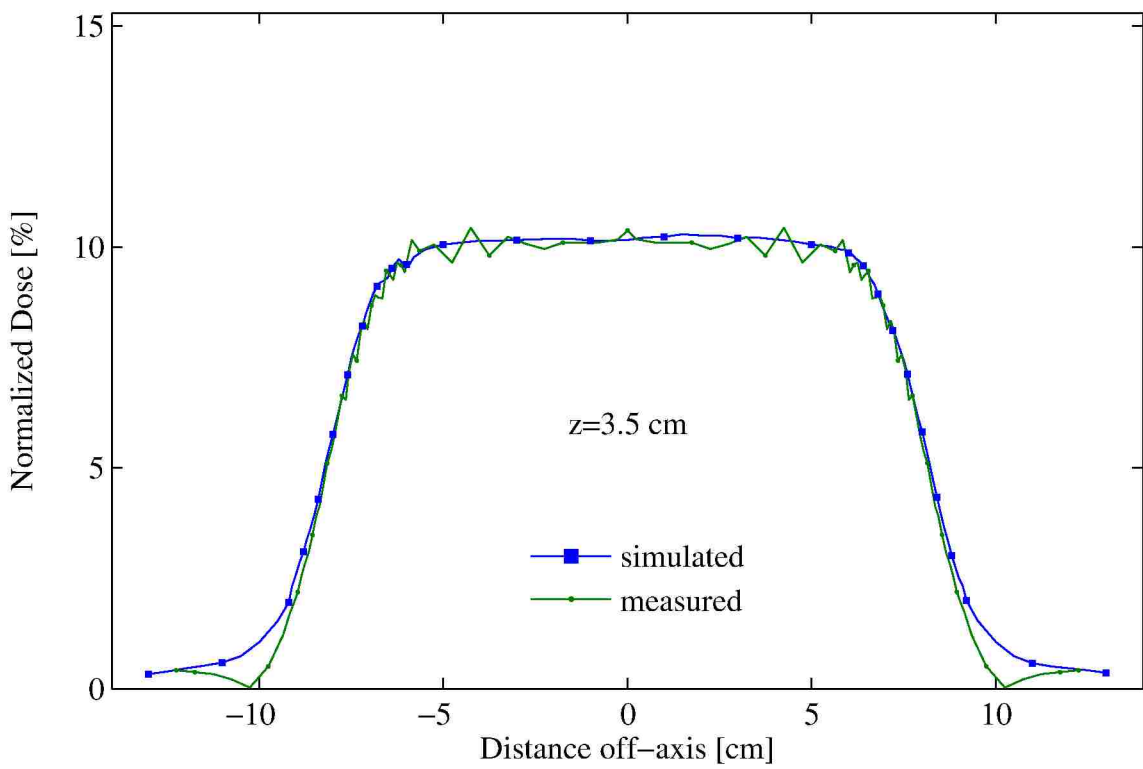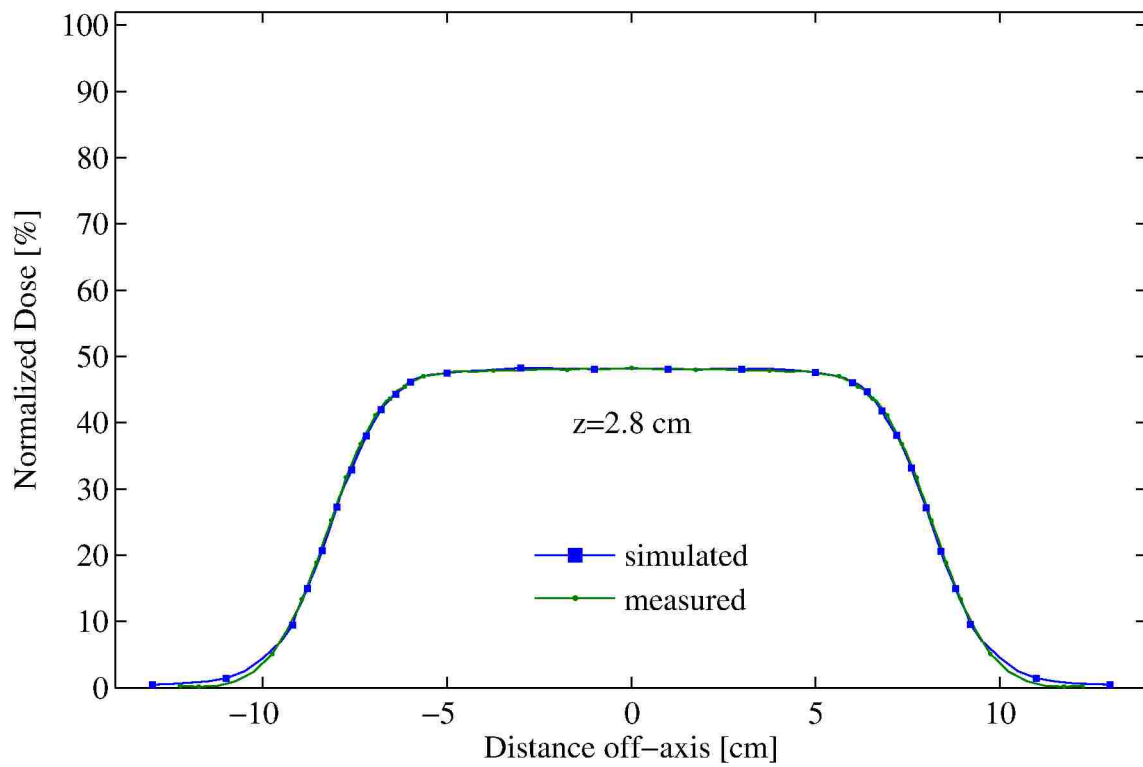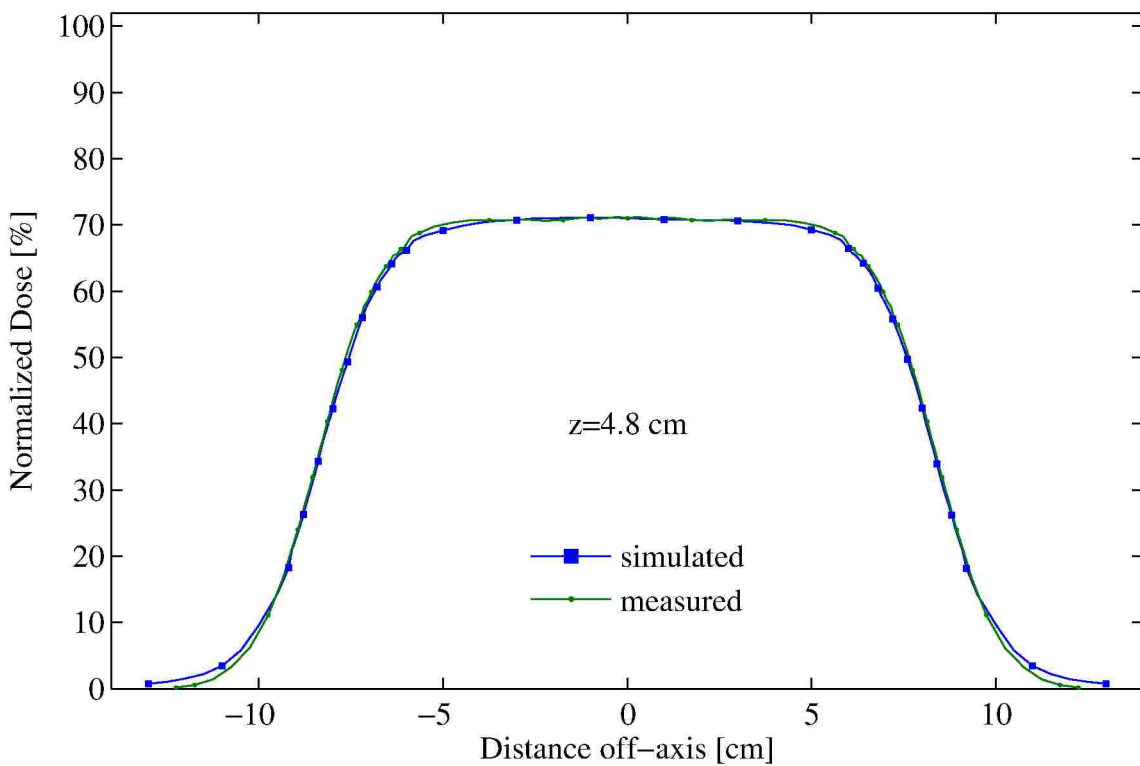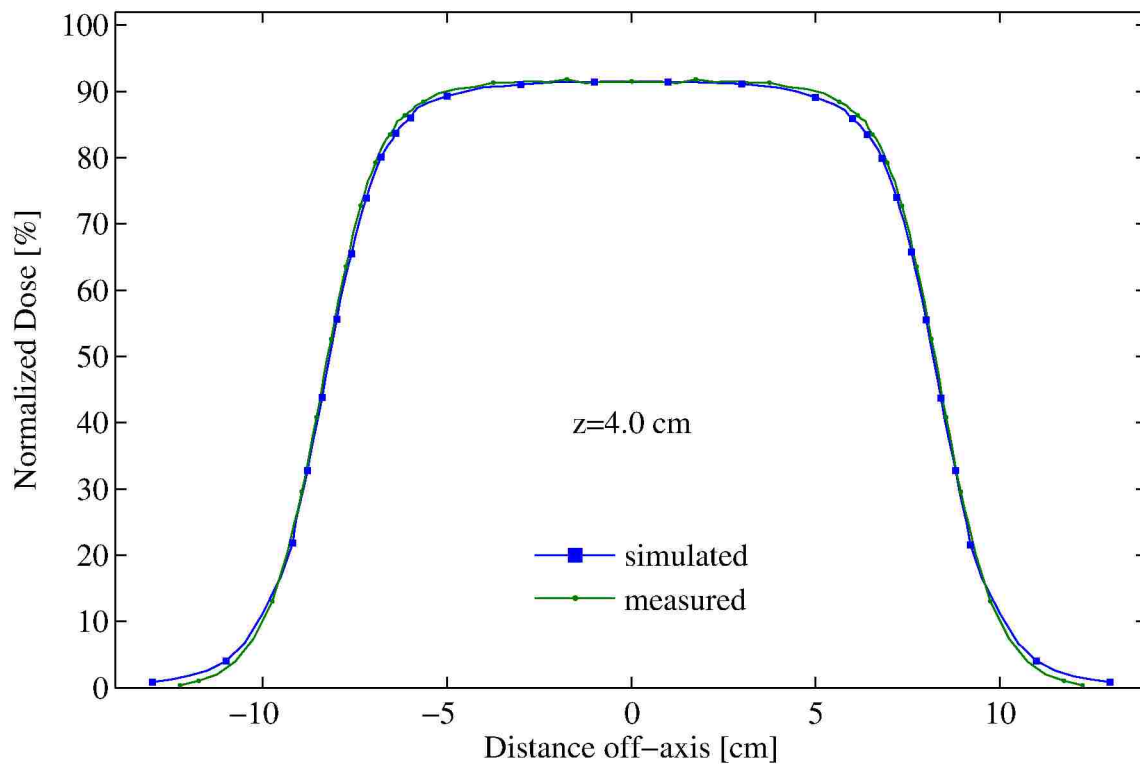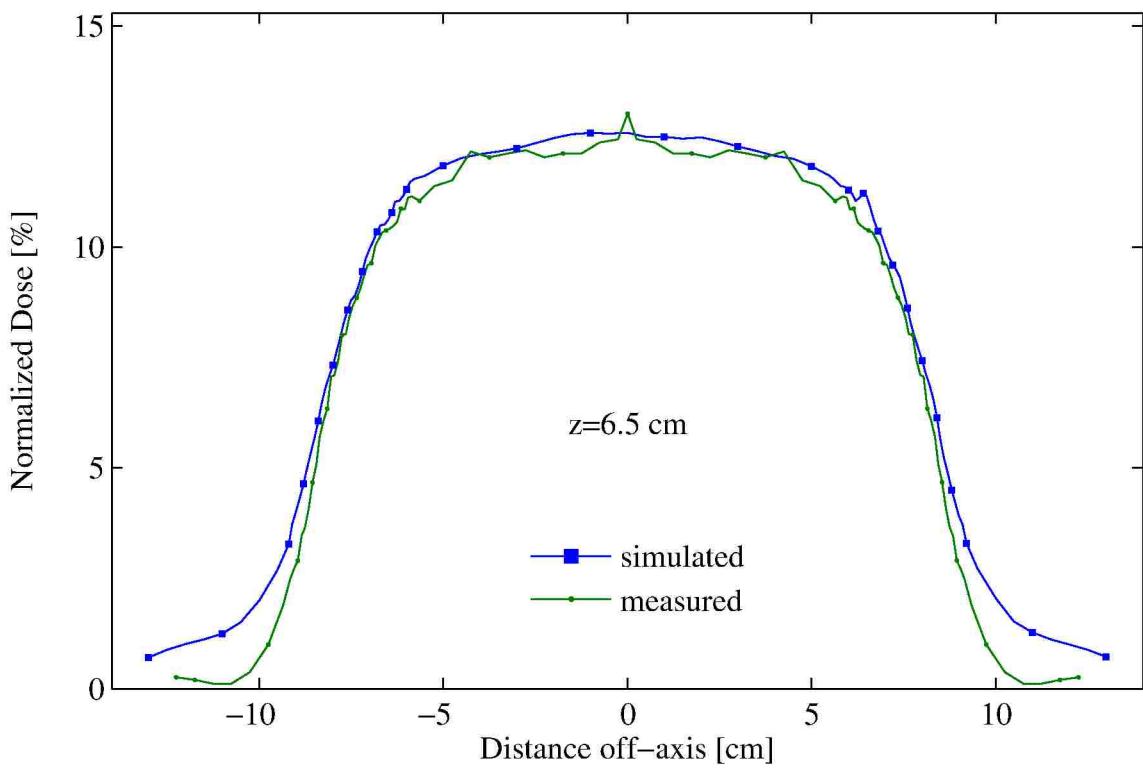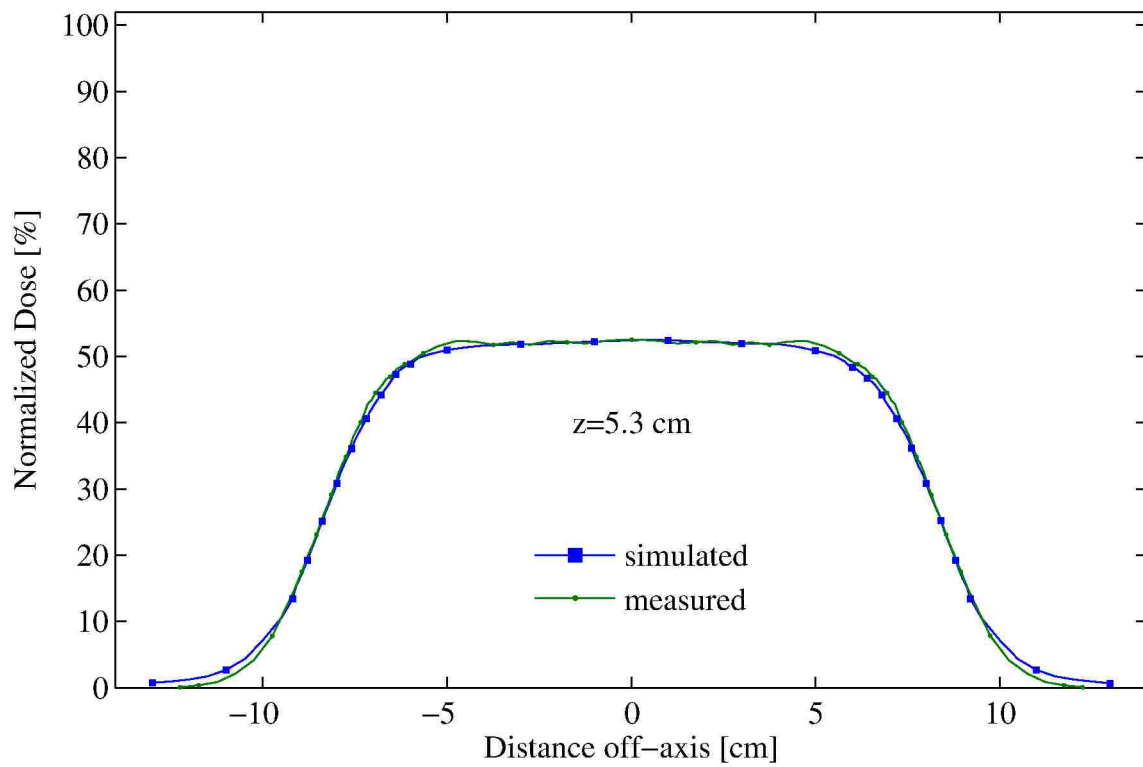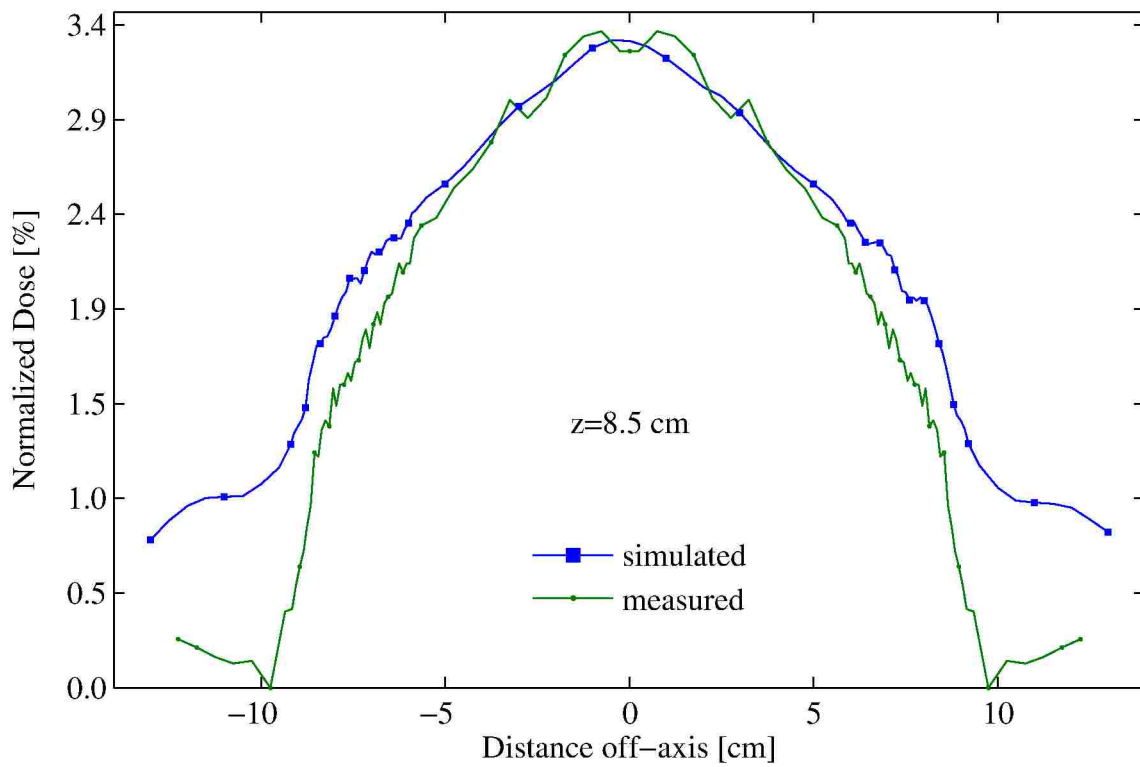
Figure C.14: 7MeV-14x14 cm^2 110cm SSD - cross-plane profiles at depths, z=2.8 and 3.5 cm
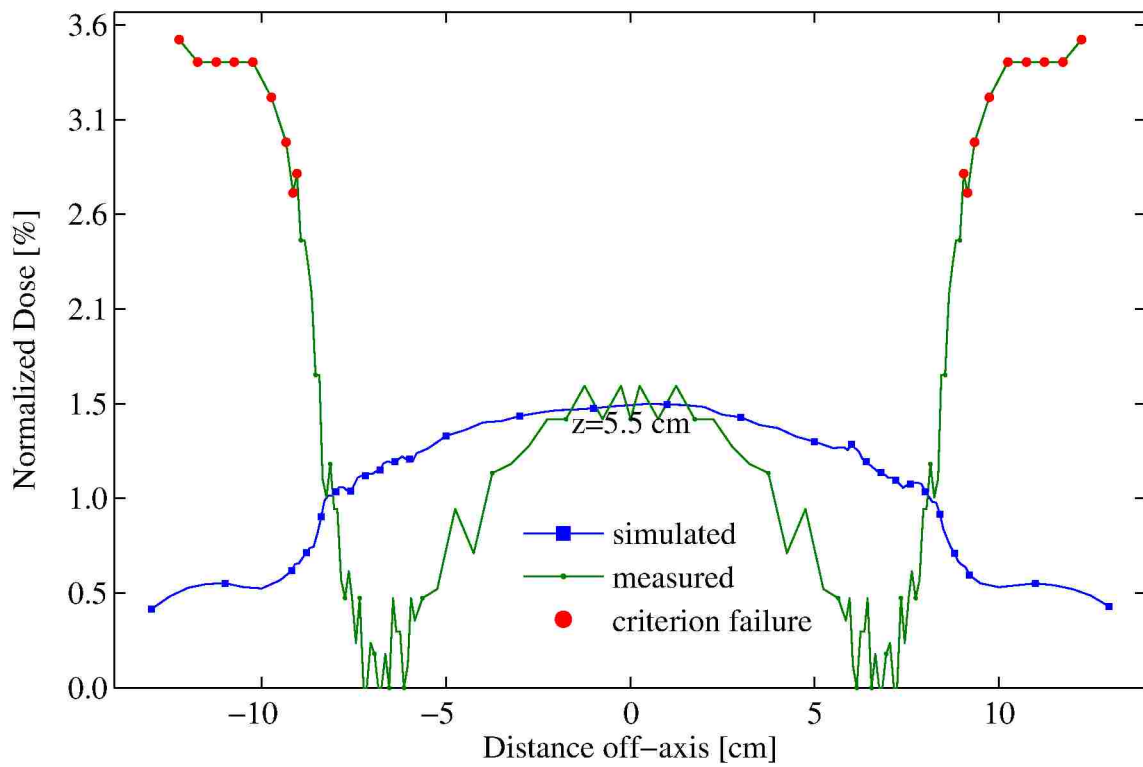
Figure C.15: 7MeV-14x14 cm^2 110cm SSD - cross-plane profiles at depth, z=5.5 cm
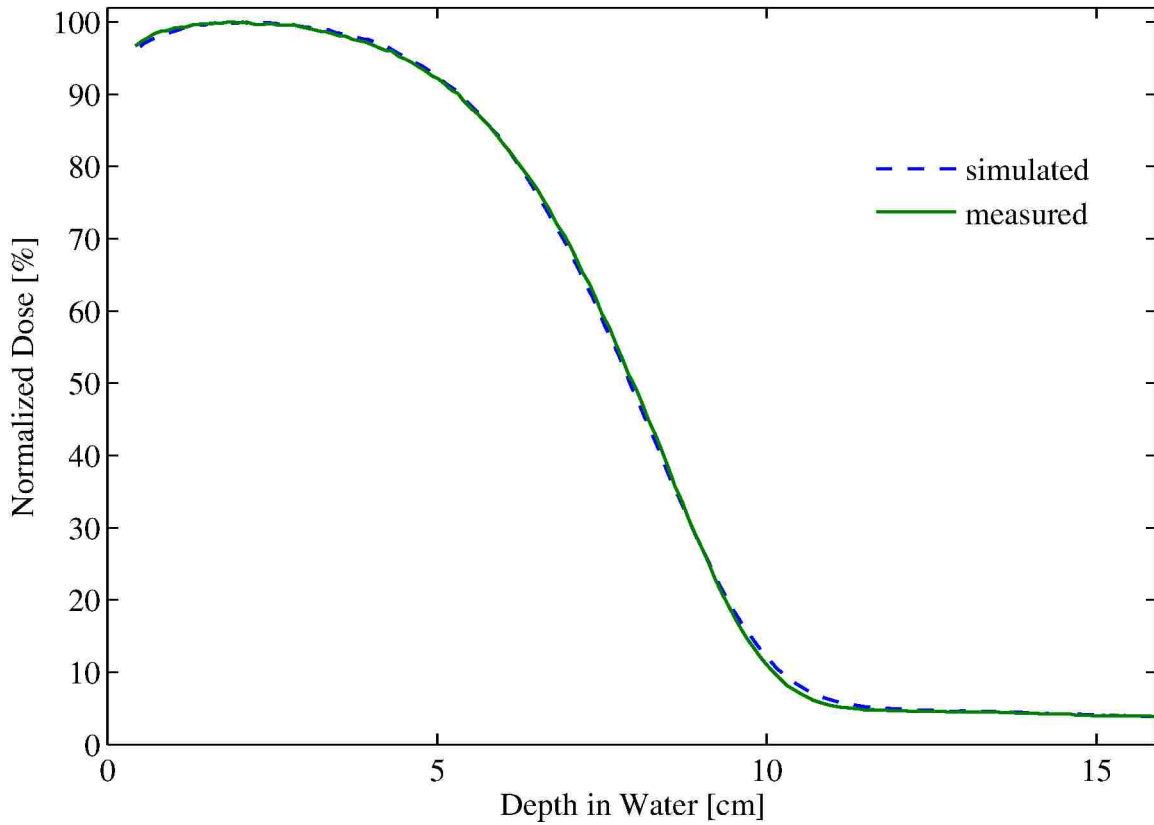
C.4   13-MeV 6x6 cm^2 Applicator - 100 cm SSD
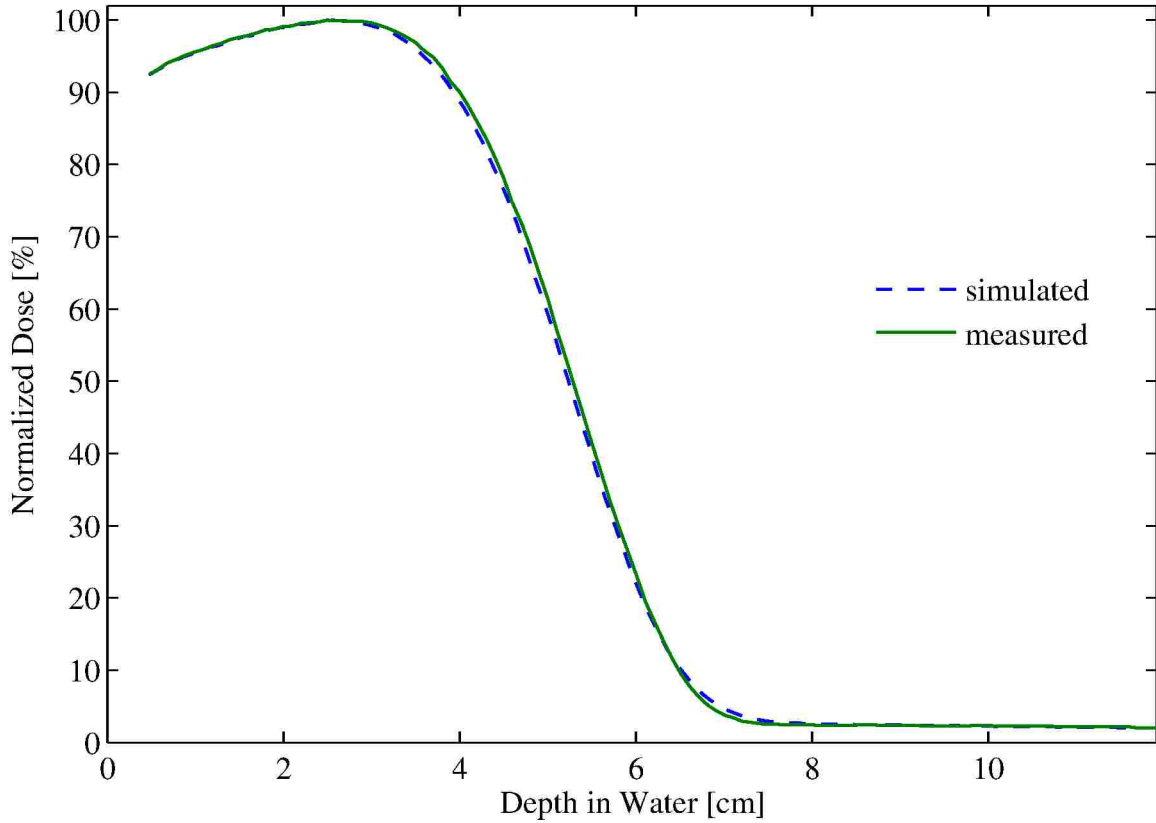
Figure C.16: %DD: 13MeV - 06x06 cm^2 applicator

Table C.4: 13MeV-06x06 cm^2 applicator comparison summary

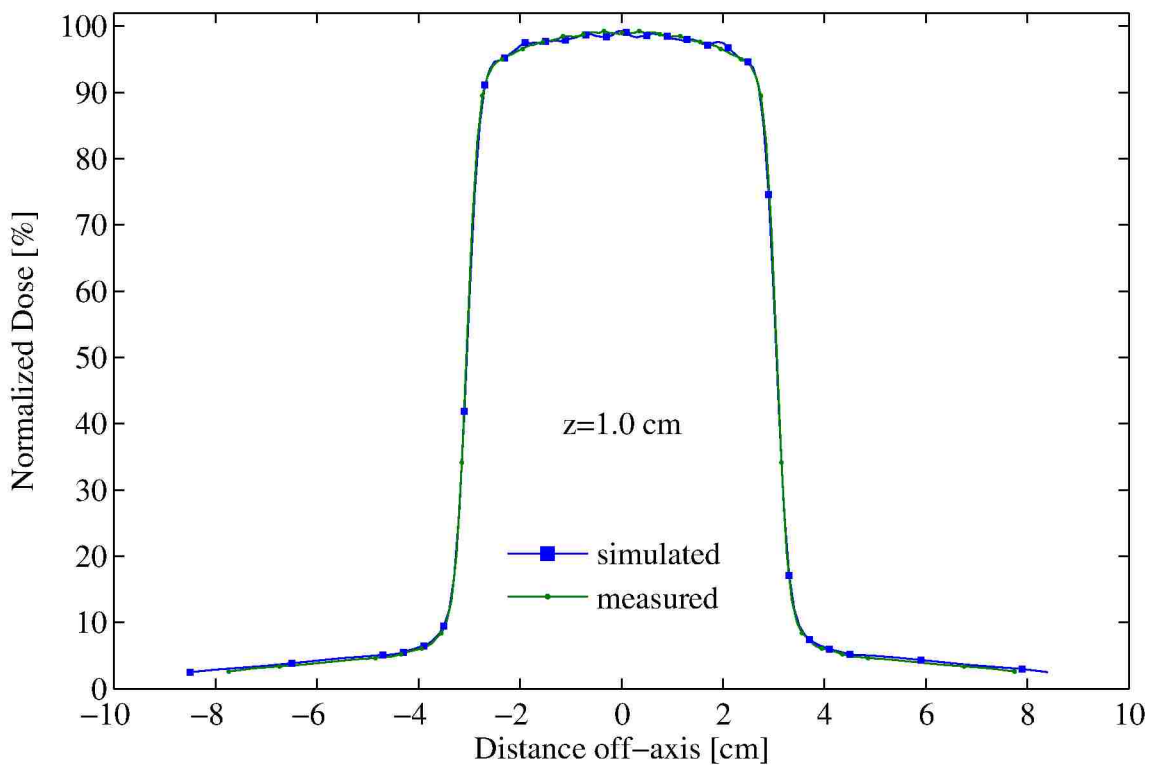| Profile type (%DD, X)	Profile depth (cm)	Percent of points passing		
		2%/1mm	2%/2mm	3%/3mm
%DD	–	100.0%	–	–
Cross-plane (X)	0.5	100.0%	–	–
	1.0	100.0%	–	–
	1.5	100.0%	–	–
	2.0	100.0%	–	–
	4.0	100.0%	–	–
	4.8	100.0%	–	–
	5.3	100.0%	–	–
	6.5	100.0%	–	–
	8.5	100.0%	–	–

Figure C.17: 13MeV-6x6 cm^2 100cm SSD - cross-plane profiles at depths, z=0.5 and 1.0 cm
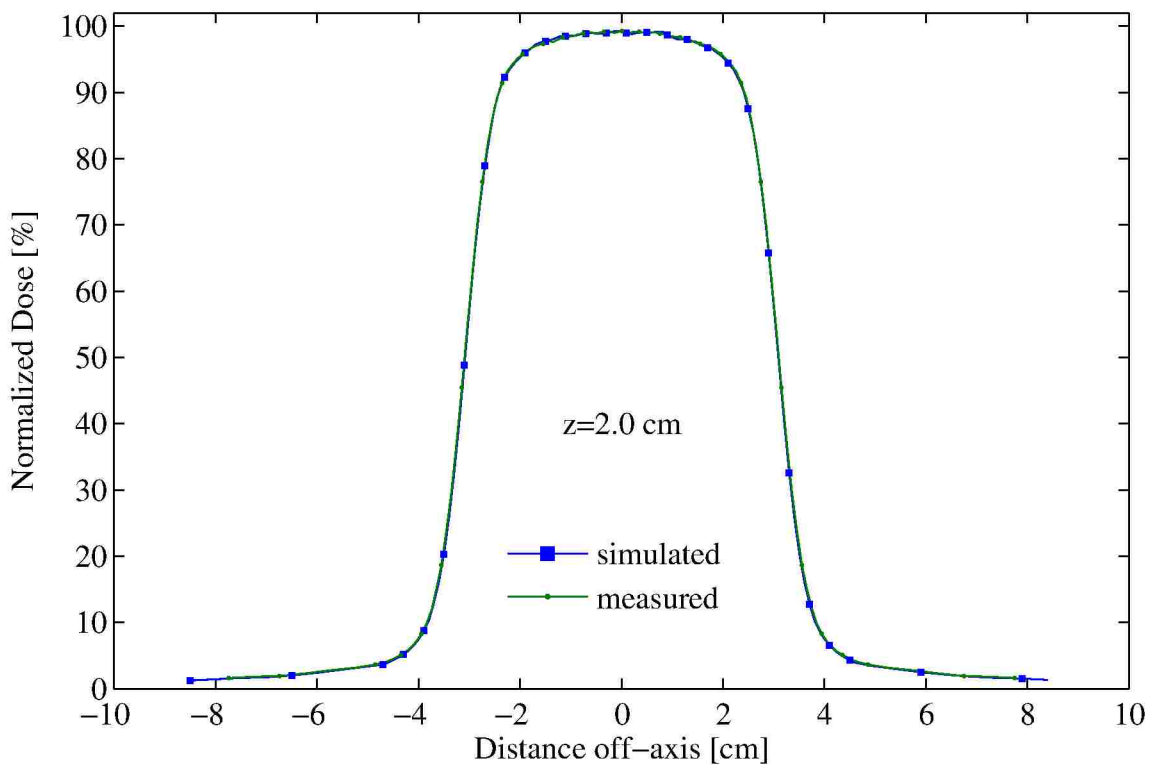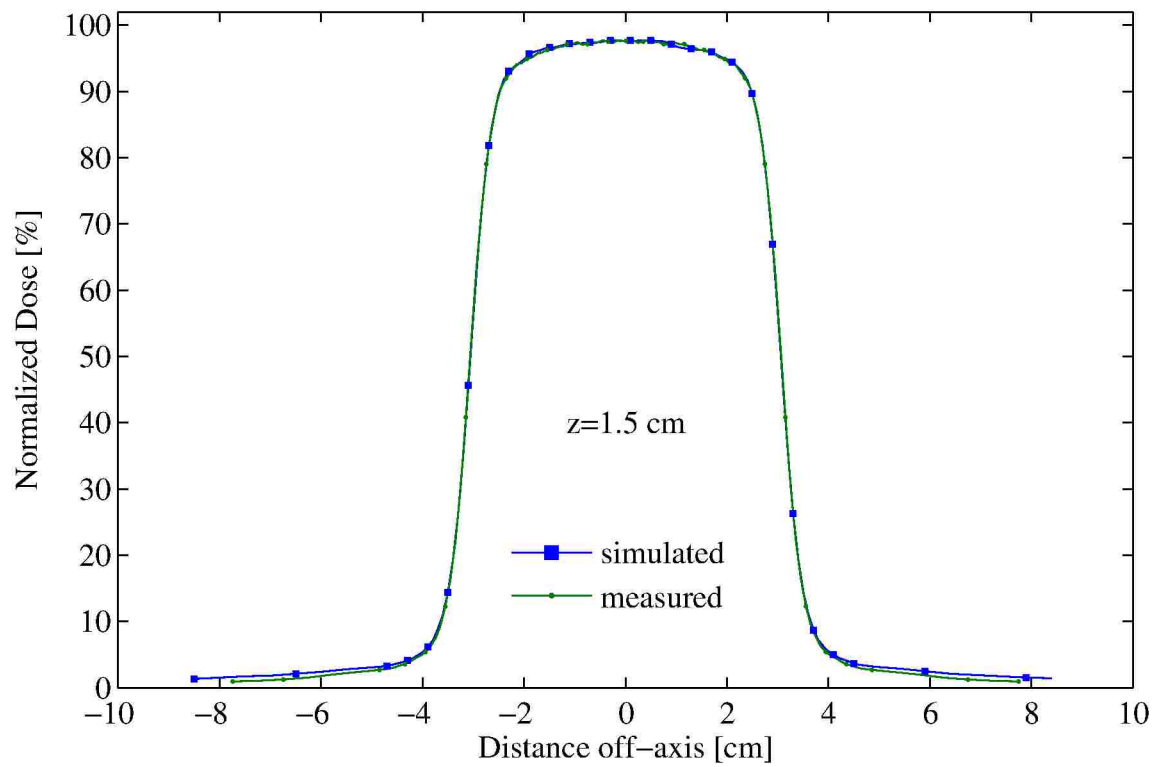
Figure C.18: 13MeV-6x6 cm^2 100cm SSD - cross-plane profiles at depths, z=1.5 and 2.0 cm
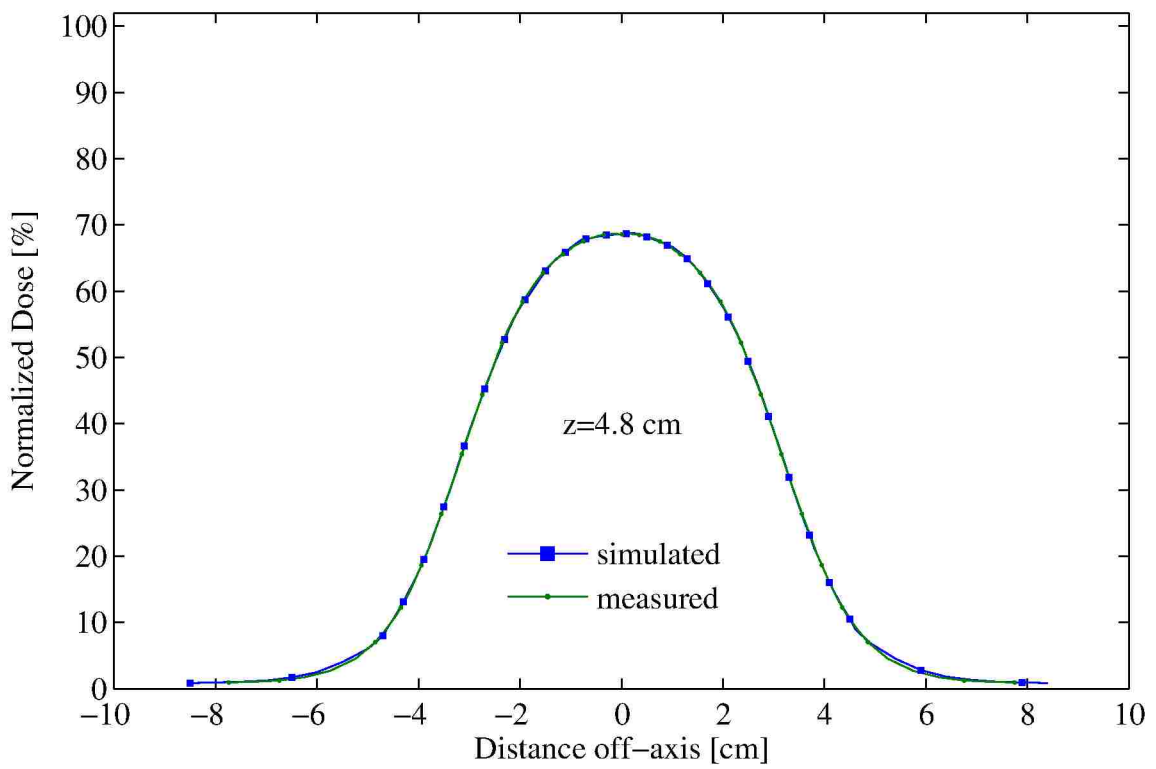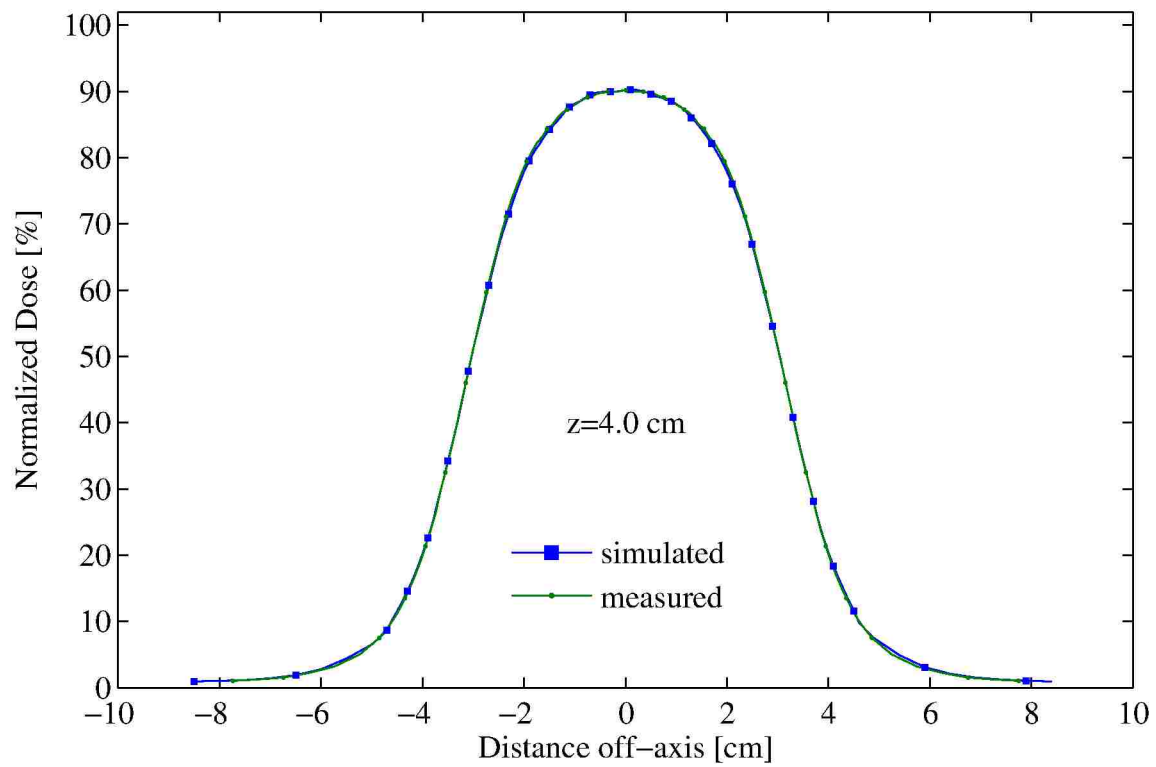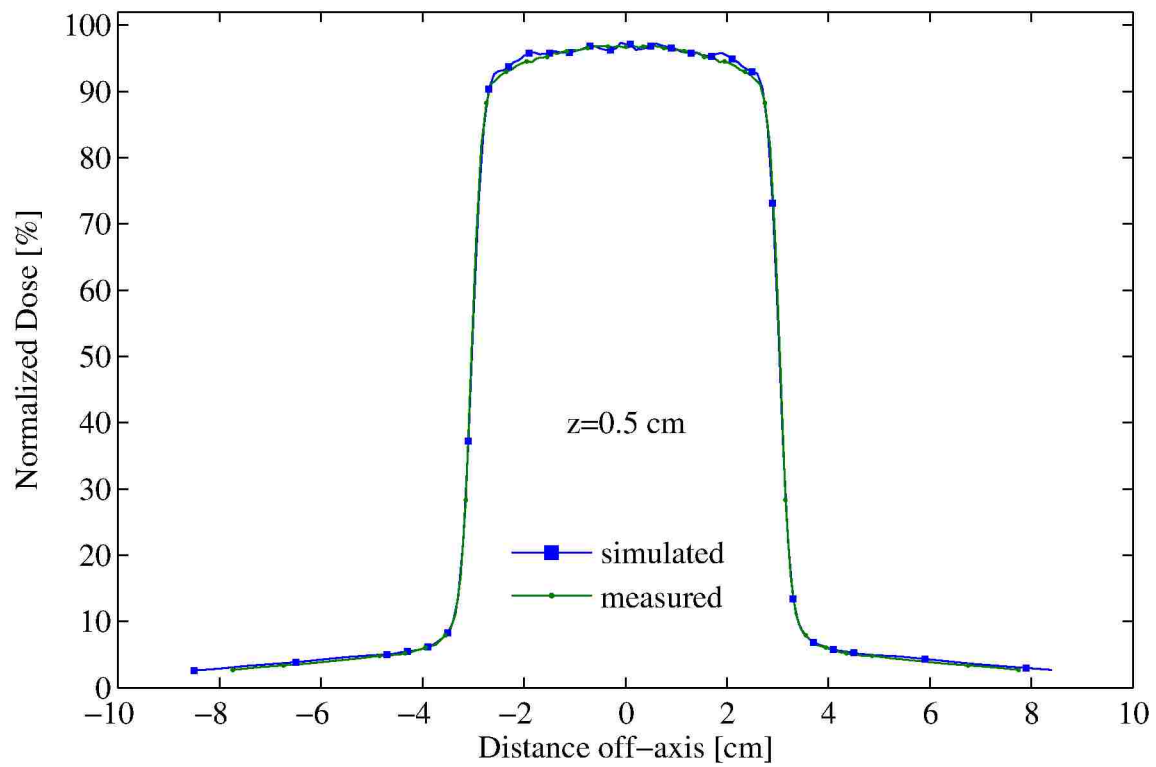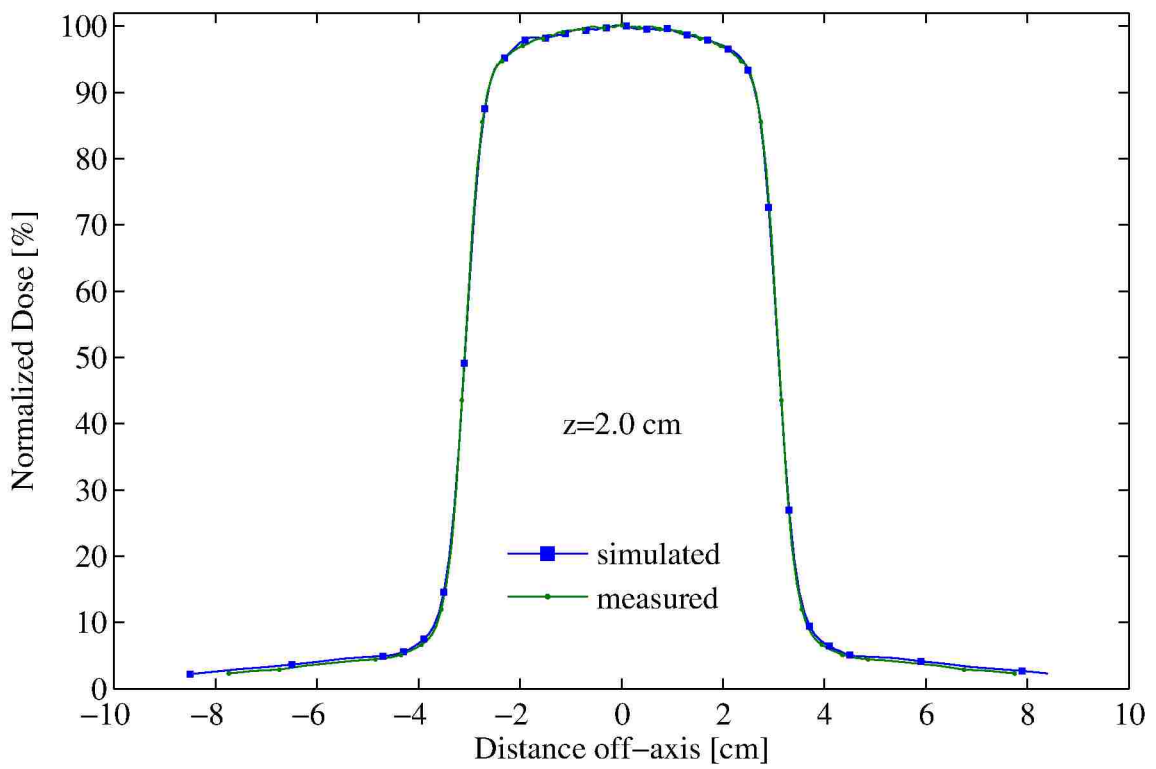
Figure C.19: 13MeV-6x6 cm^2 100cm SSD - cross-plane profiles at depths, z=4.0 and 4.8 cm
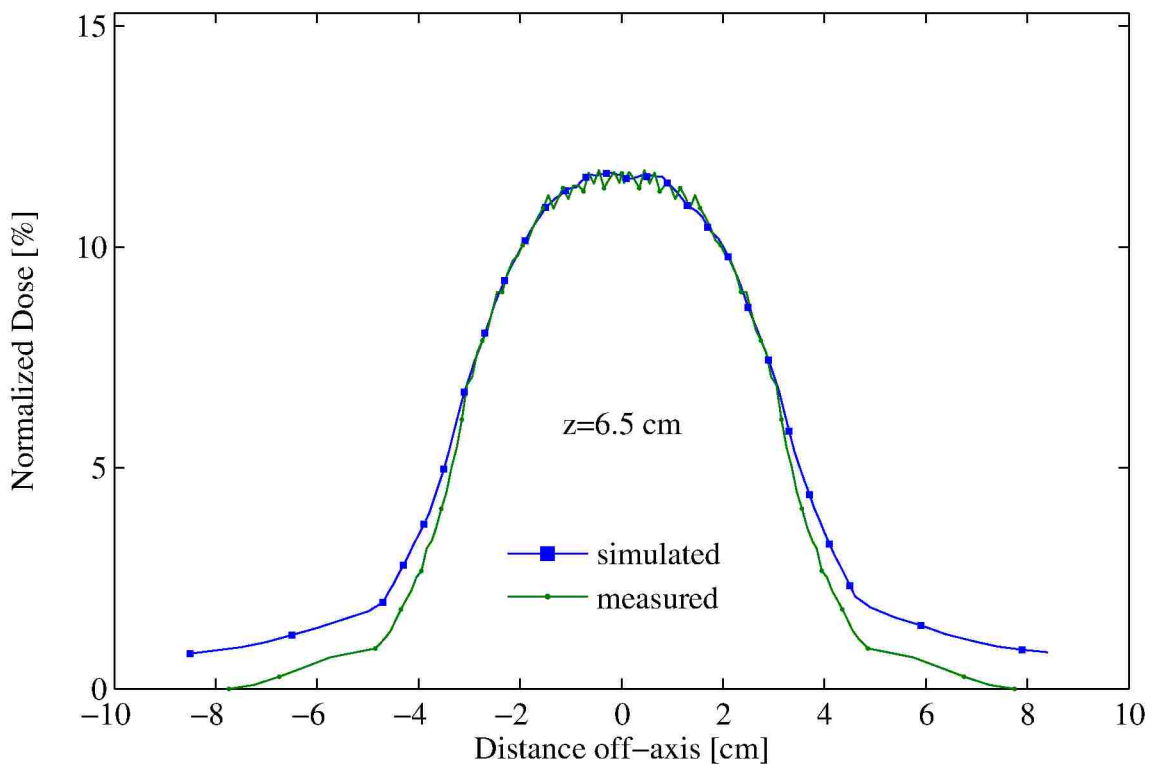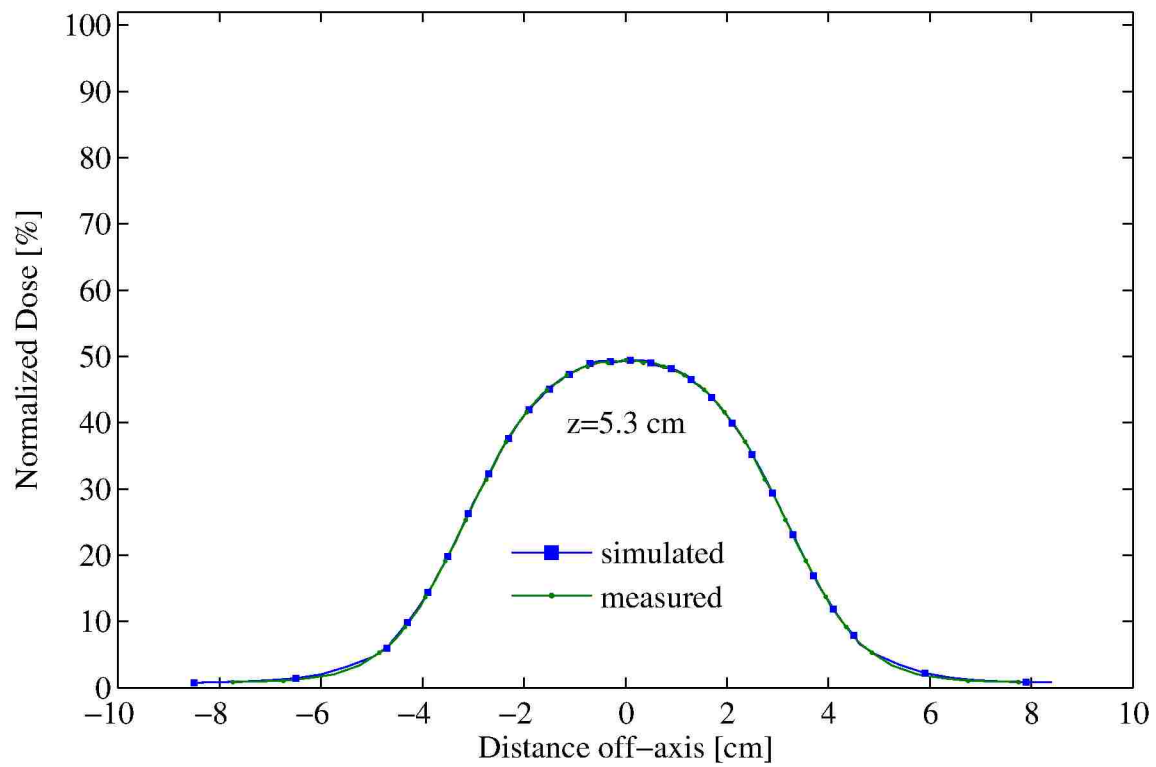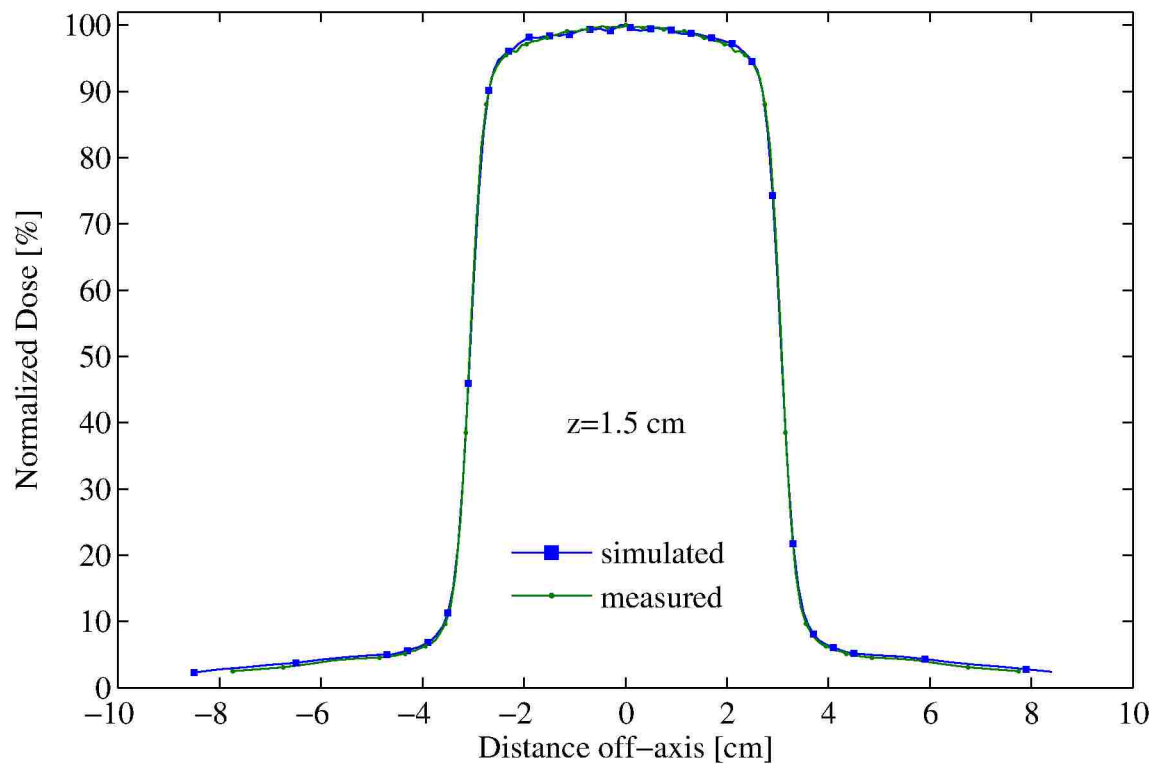
Figure C.20: 13MeV-6x6 cm^2 100cm SSD - cross-plane profiles at depths, z=5.3 and 6.5 cm
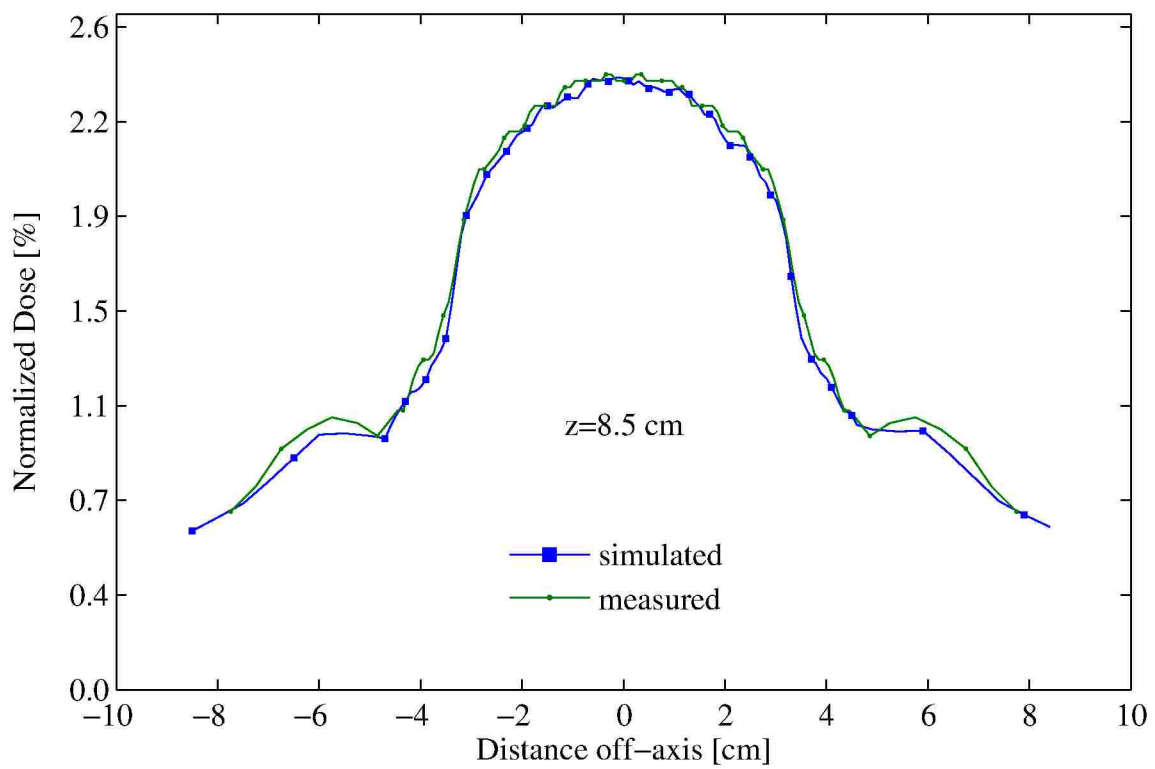
Figure C.21: 13MeV-6x6 cm^2 100cm SSD - cross-plane profiles at depth, z=8.5 cm

C.5 13-MeV 14x14 cm^2 Applicator - 100 cm SSD
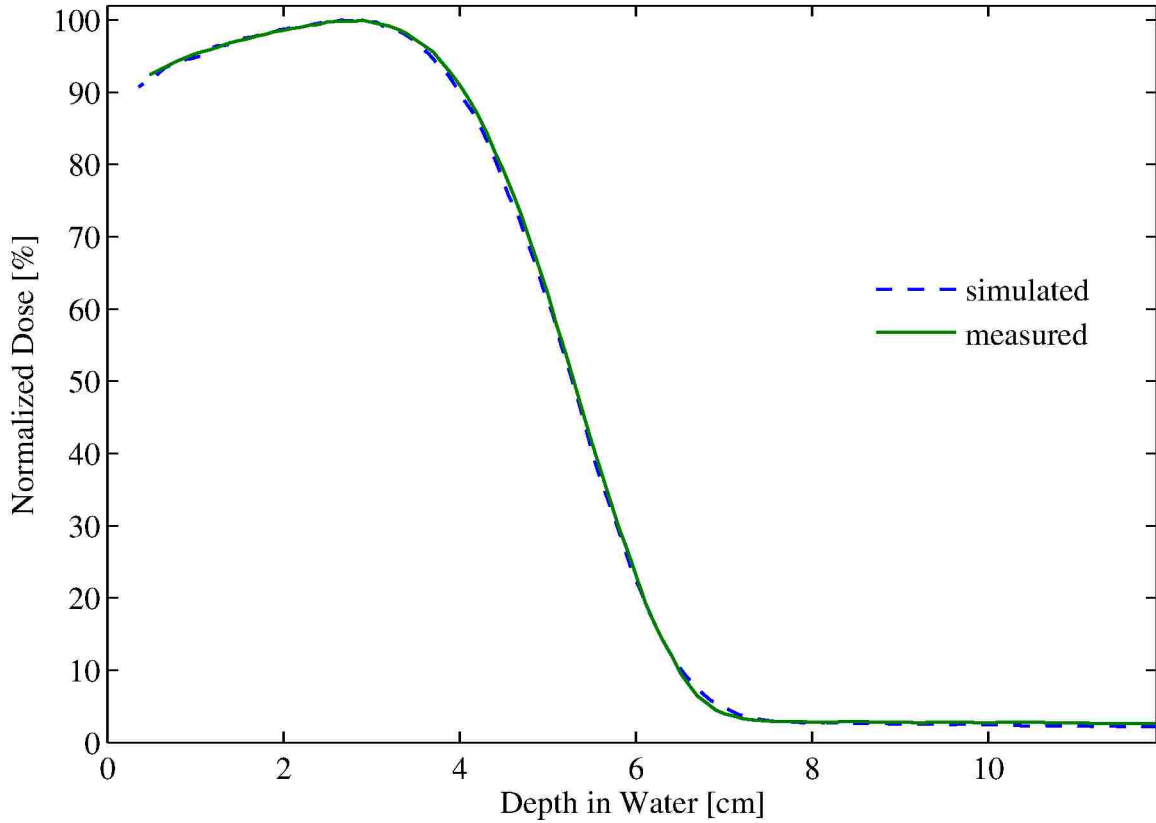
Figure C.22: %DD: 13MeV - 14x14 cm^2 applicator

Table C.5: 13MeV-14x14 cm^2 applicator comparison summary

Profile type (%DD, X)	Profile depth (cm)	Percent of points passing		
		2%/1mm	2%/2mm	3%/3mm
%DD	–	100.0%	–	–
Cross-plane (X)	0.5	100.0%	–	–
	1.0	100.0%	–	–
	1.5	100.0%	–	–
	2.0	100.0%	–	–
	4.0	97.2%	100.0%	–
	4.8	100.0%	–	–
	5.3	100.0%	–	–
	6.5	100.0%	–	–
	8.5	100.0%	–	–
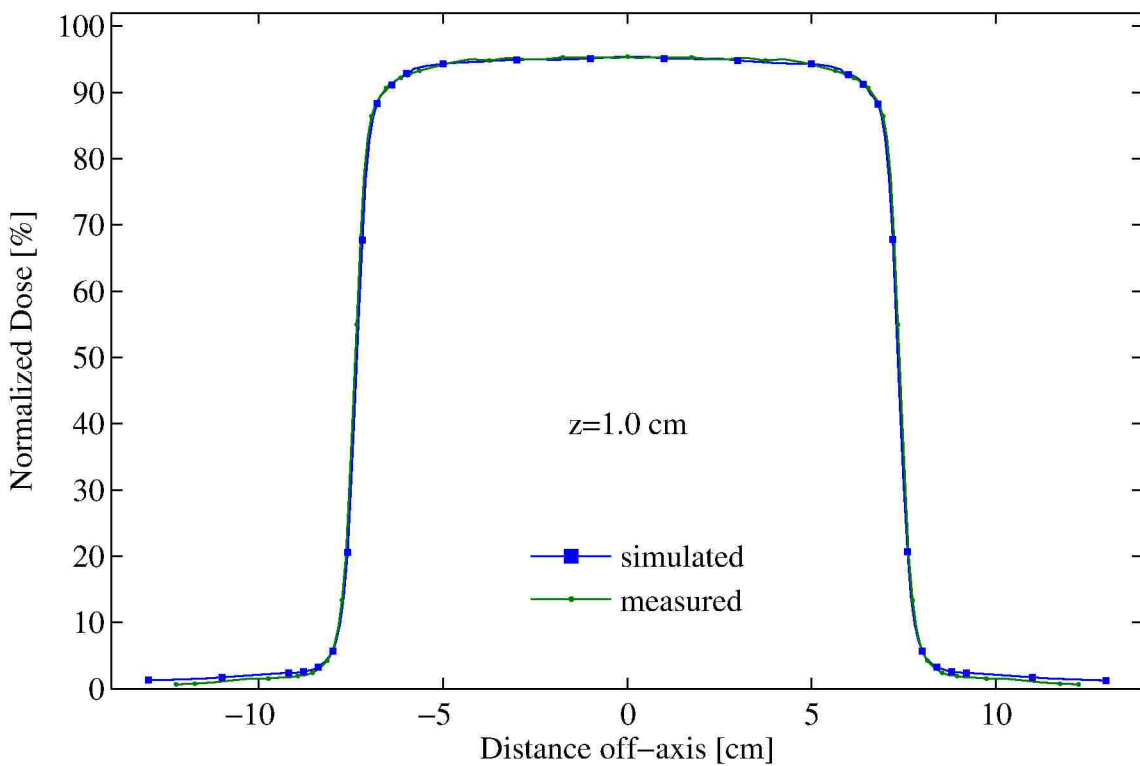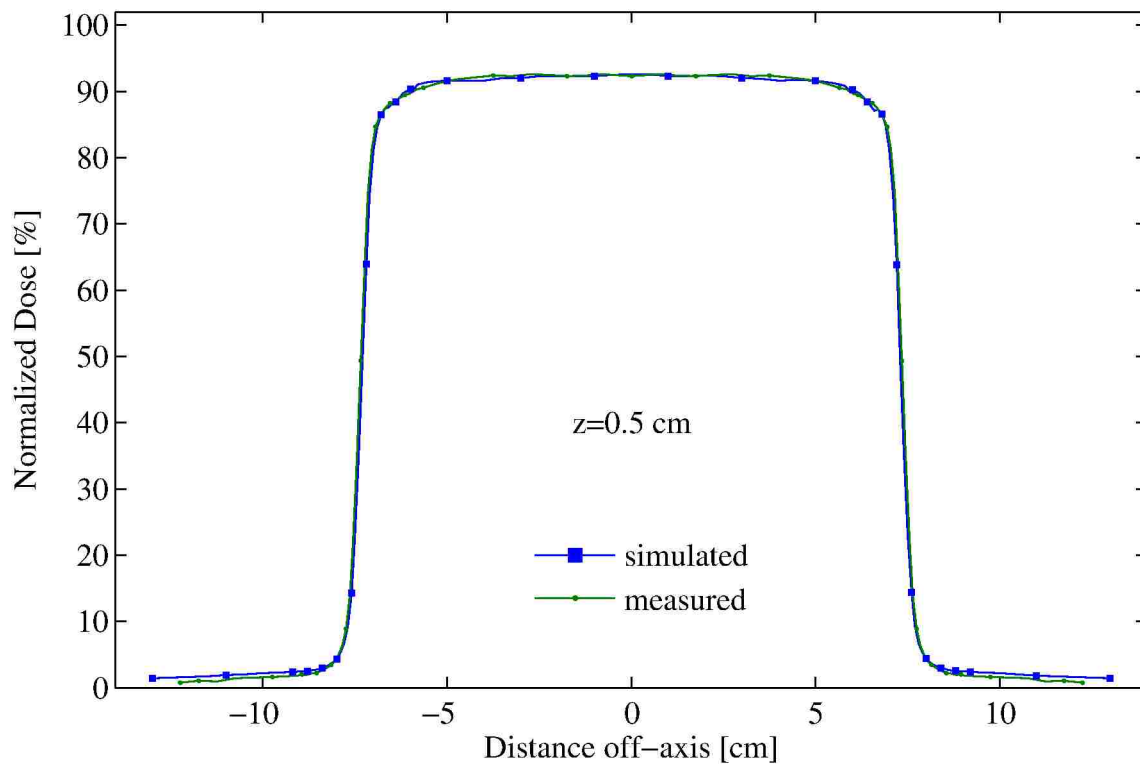
Figure C.23: 13MeV-14x14 cm^2 100cm SSD - cross-plane profiles at depths, z=0.5 and 1.0 cm
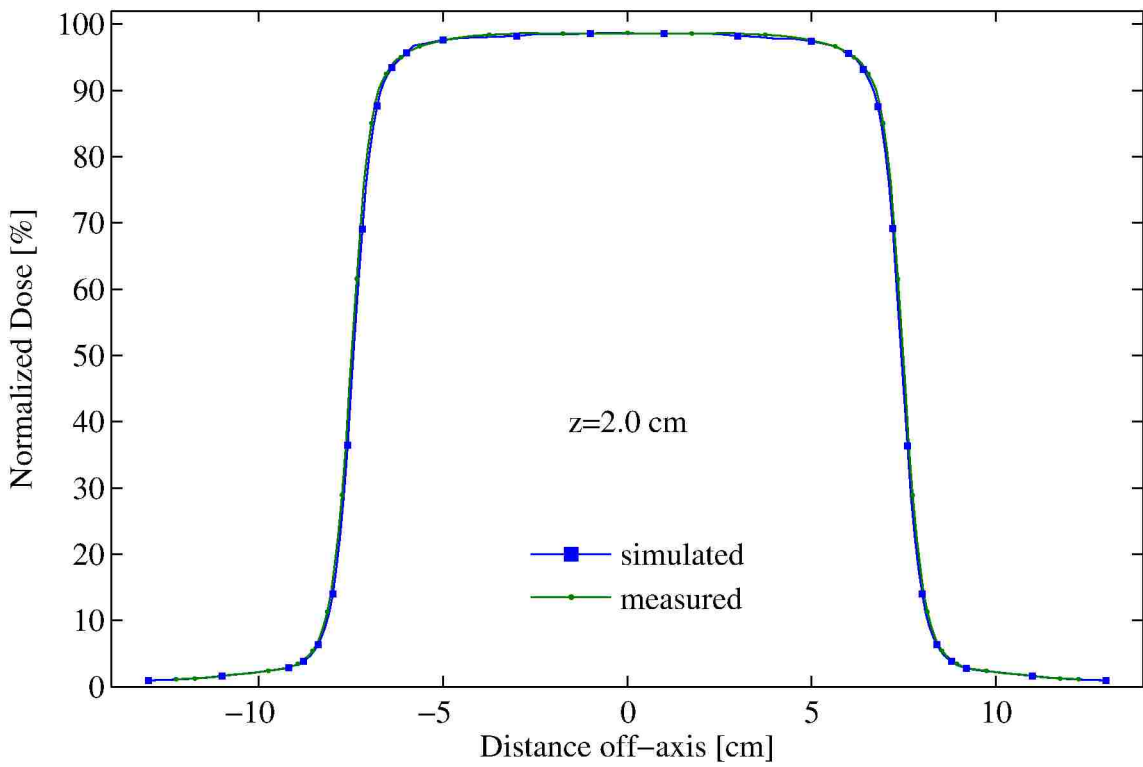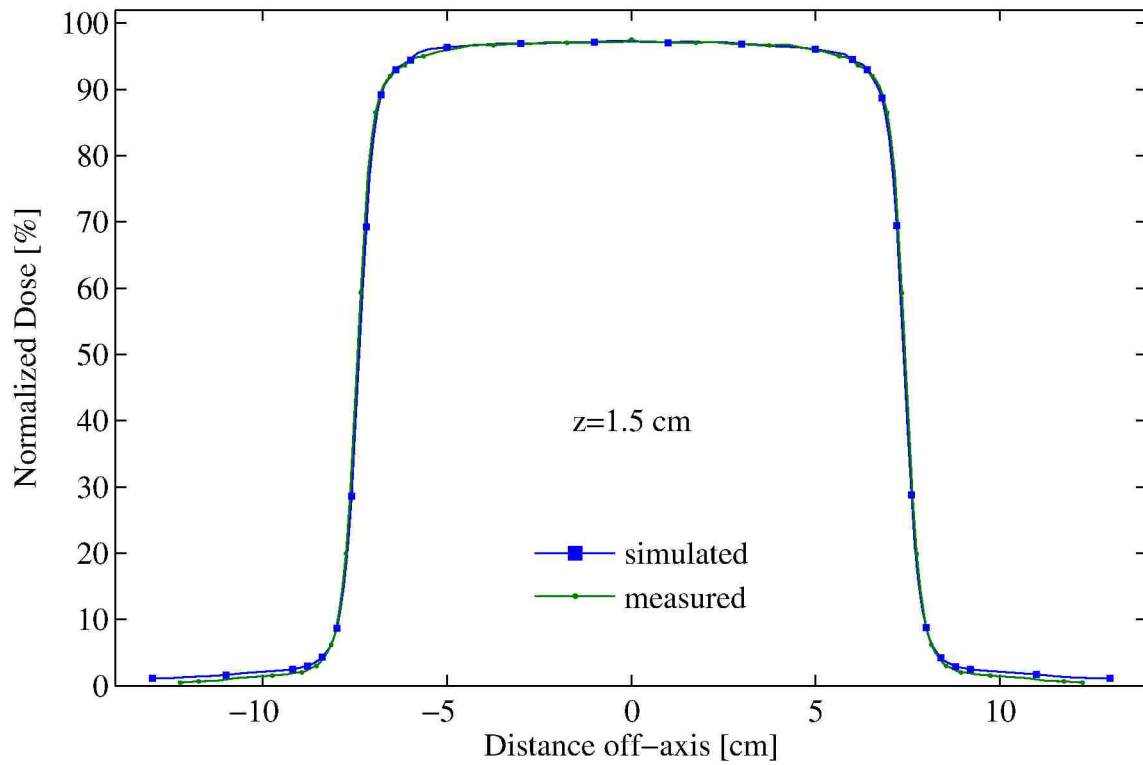
Figure C.24: 13MeV-14x14 cm^2 100cm SSD - cross-plane profiles at depths, z=1.5 and 2.0 cm
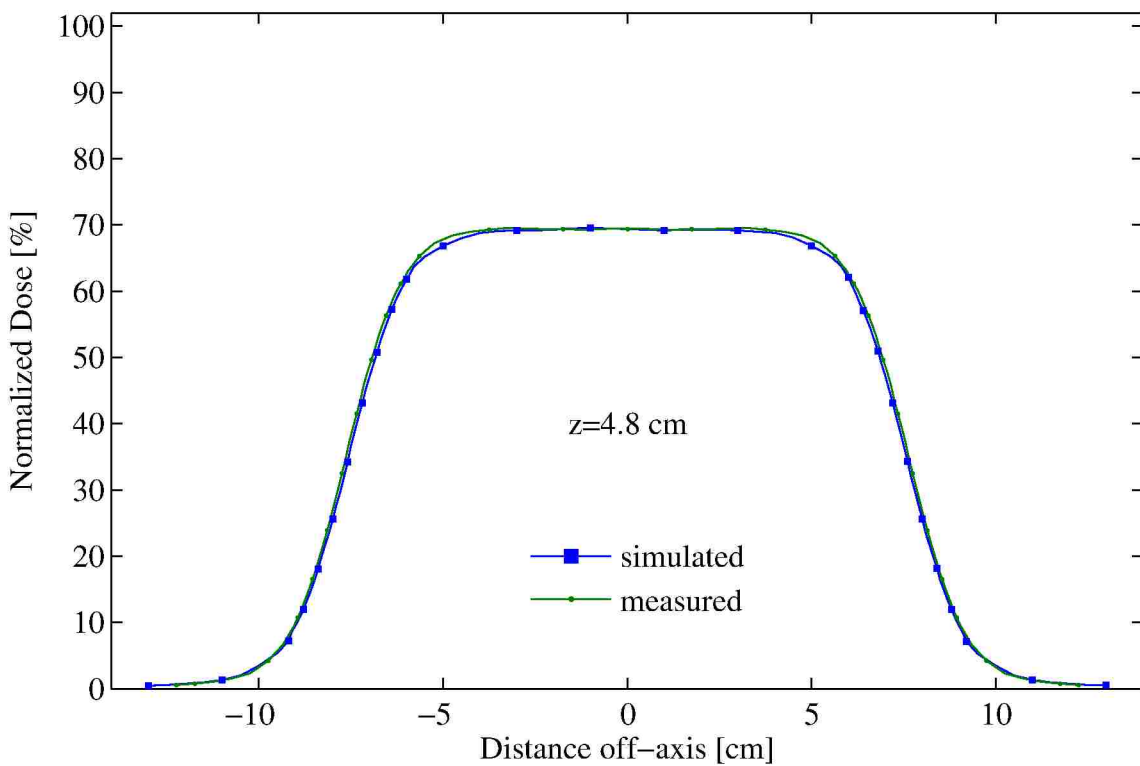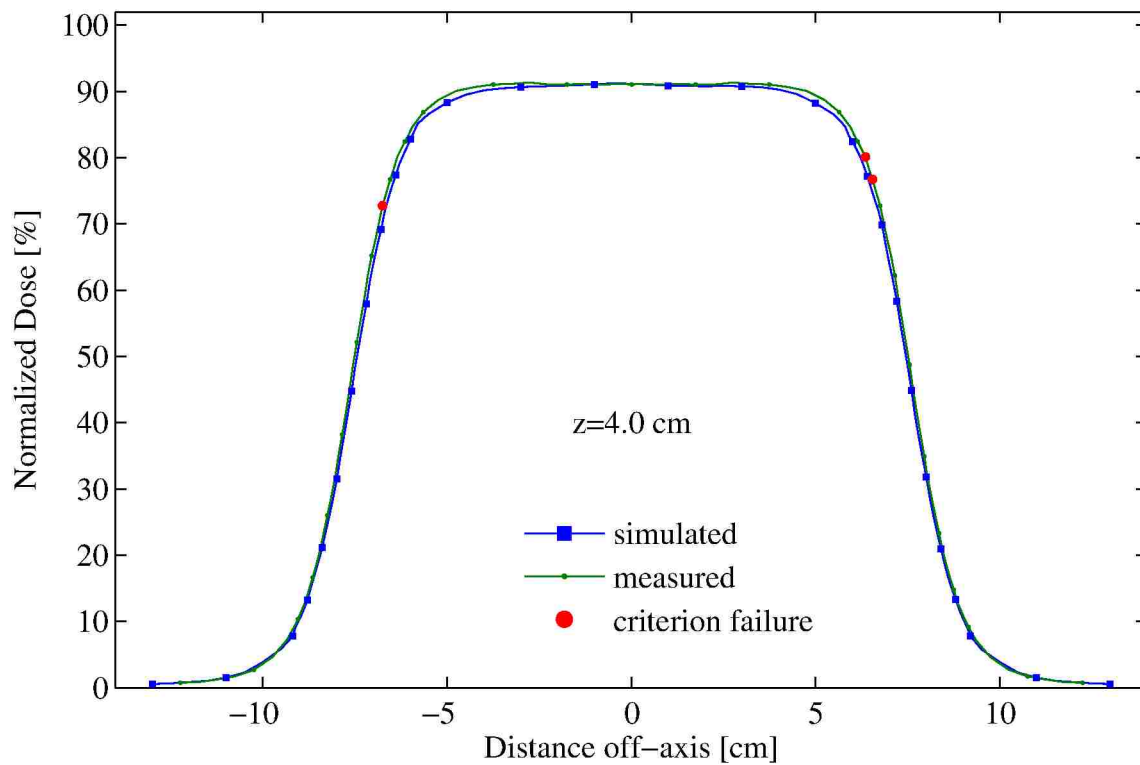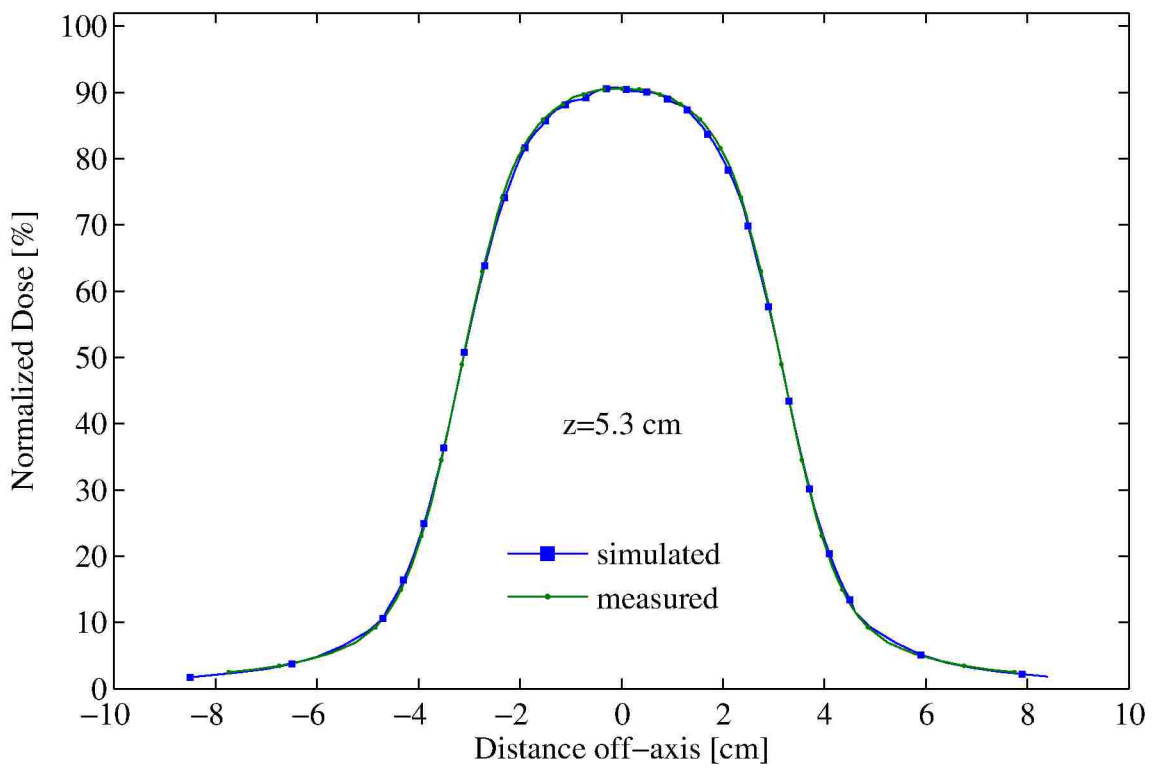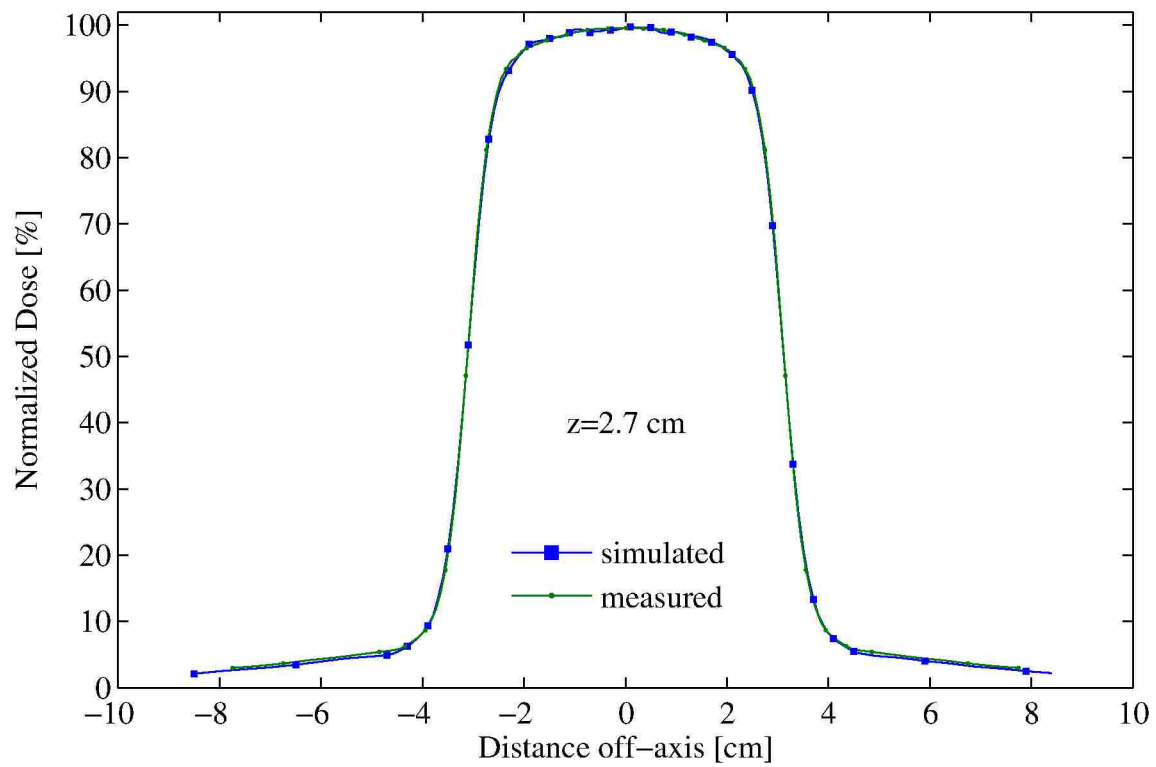
Figure C.25: 13MeV-14x14 cm^2 100cm SSD - cross-plane profiles at depths, z=4.0 and 4.8 cm
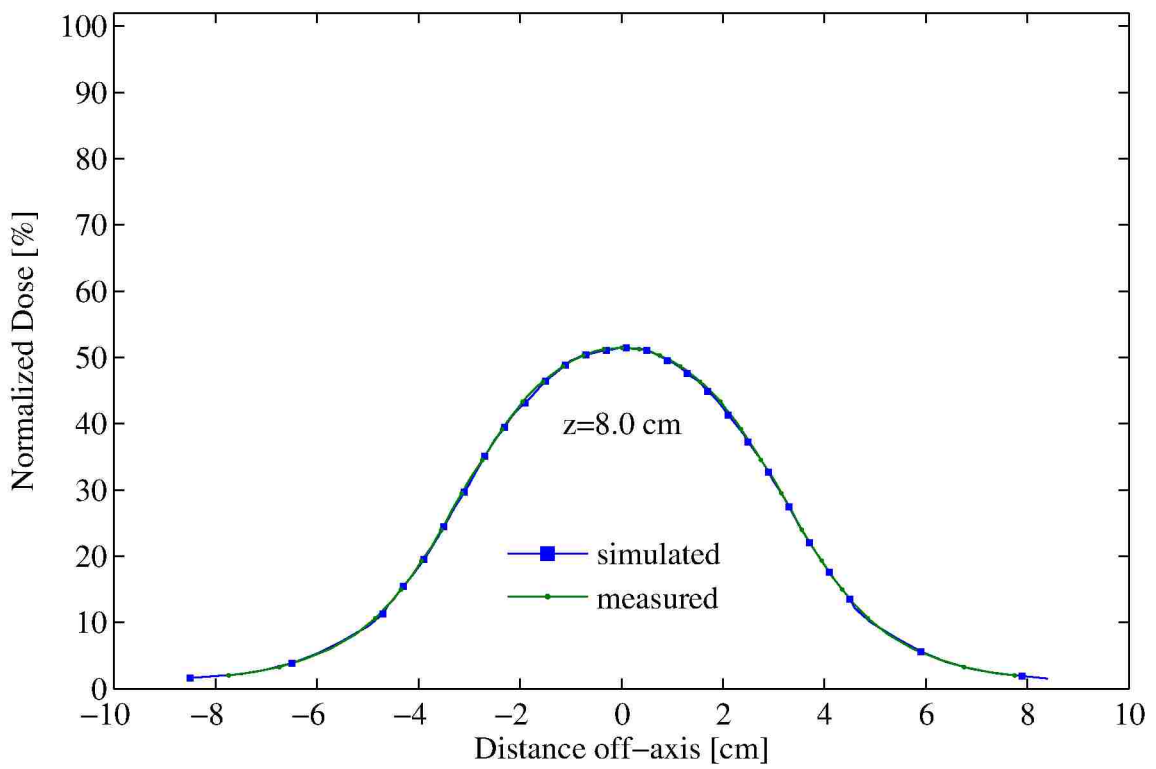
Figure C.26: 13MeV-14x14 cm^2 100cm SSD - cross-plane profiles at depths, z=5.3 and 6.5 cm
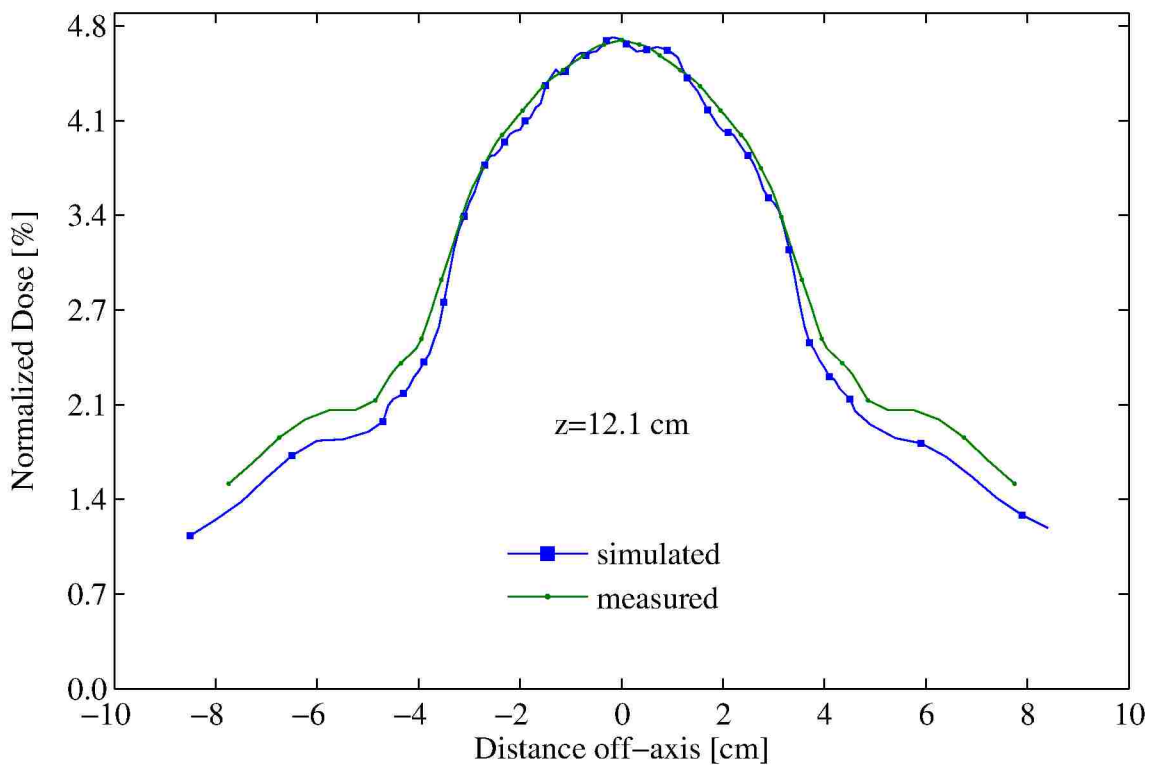
Figure C.27: 13MeV-14x14 cm^2 100cm SSD - cross-plane profiles at depth, z=8.5 cm

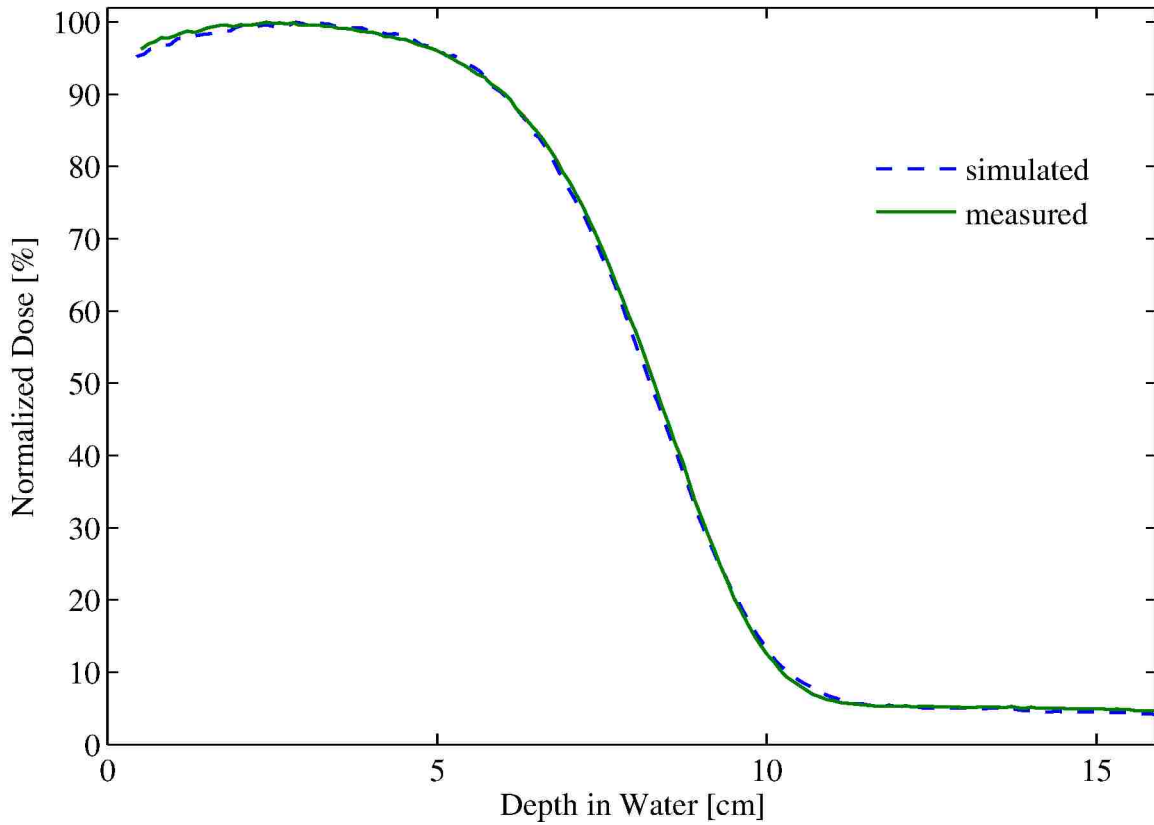## C.6 13-MeV 14x14 cm^2 Applicator - 110 cm SSD

Figure C.28: %DD: 13MeV - 14x14 cm^2 applicator

Table C.6: 13MeV-14x14 cm^2 applicator comparison summary

Profile type (%DD, X)	Profile depth (cm)	Percent of points passing 2%/1mm	2%/2mm	3%/3mm
%DD	–	99.1%	100.0%	–
Cross-plane (X)	0.5	100.0%	–	–
	1.0	100.0%	–	–
	1.5	100.0%	–	–
	2.0	100.0%	–	–
	4.0	100.0%	–	–
	4.8	100.0%	–	–
	5.3	100.0%	–	–
	6.5	100.0%	–	–
	8.5	100.0%	–	–

Figure C.29: 13MeV-14x14 cm^2 110cm SSD - cross-plane profiles at depths, z=0.5 and 1.0 cm

Figure C.30: 13MeV-14x14 cm^2 110cm SSD - cross-plane profiles at depths, z=1.5 and 2.0 cm
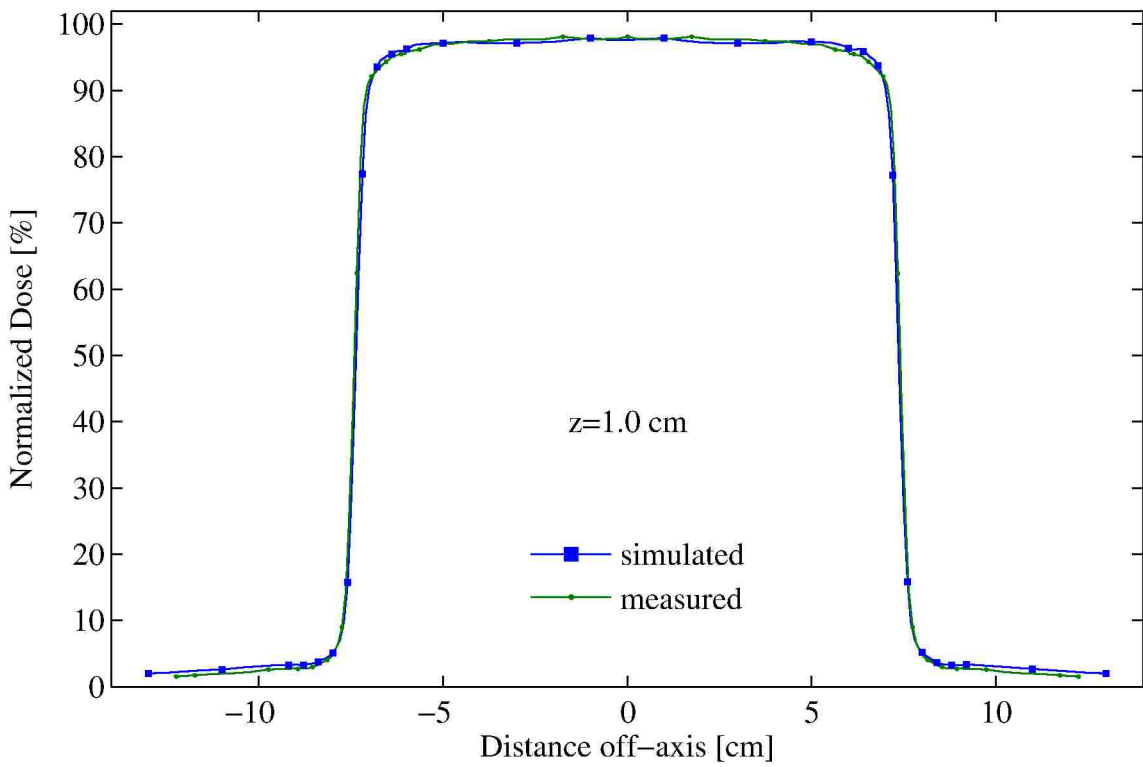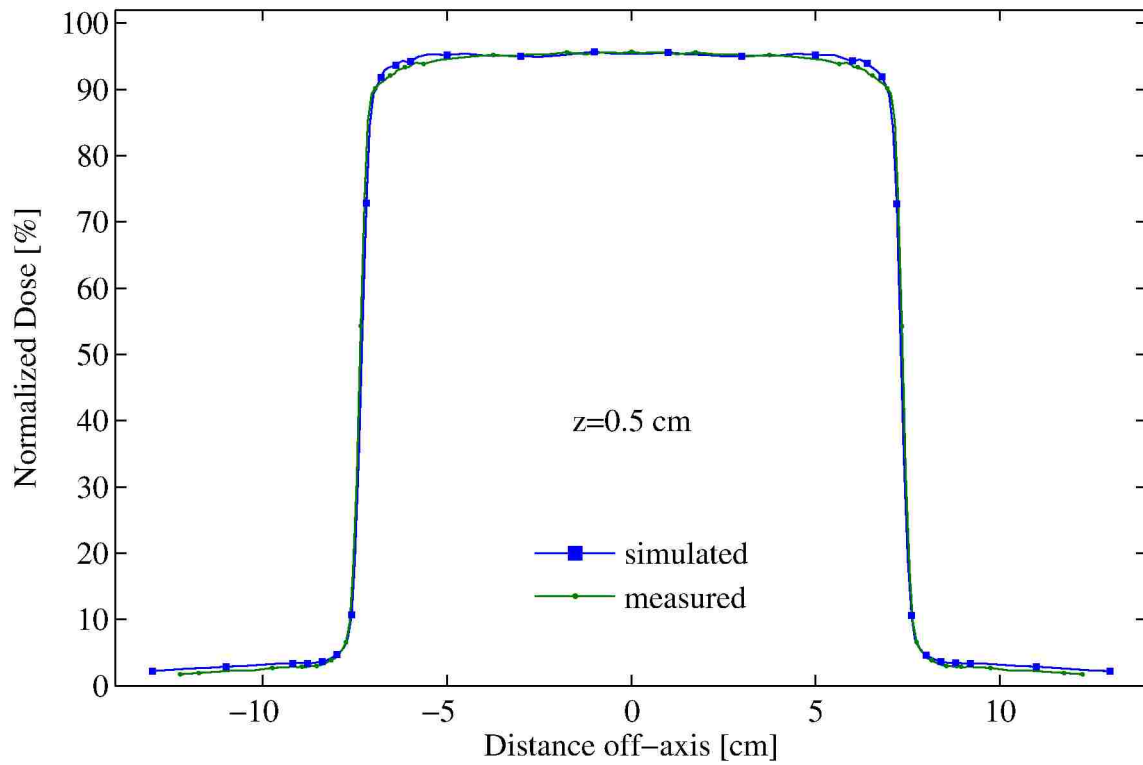
Figure C.31: 13MeV-14x14 cm^2 110cm SSD - cross-plane profiles at depths, z=4.0 and 4.8 cm
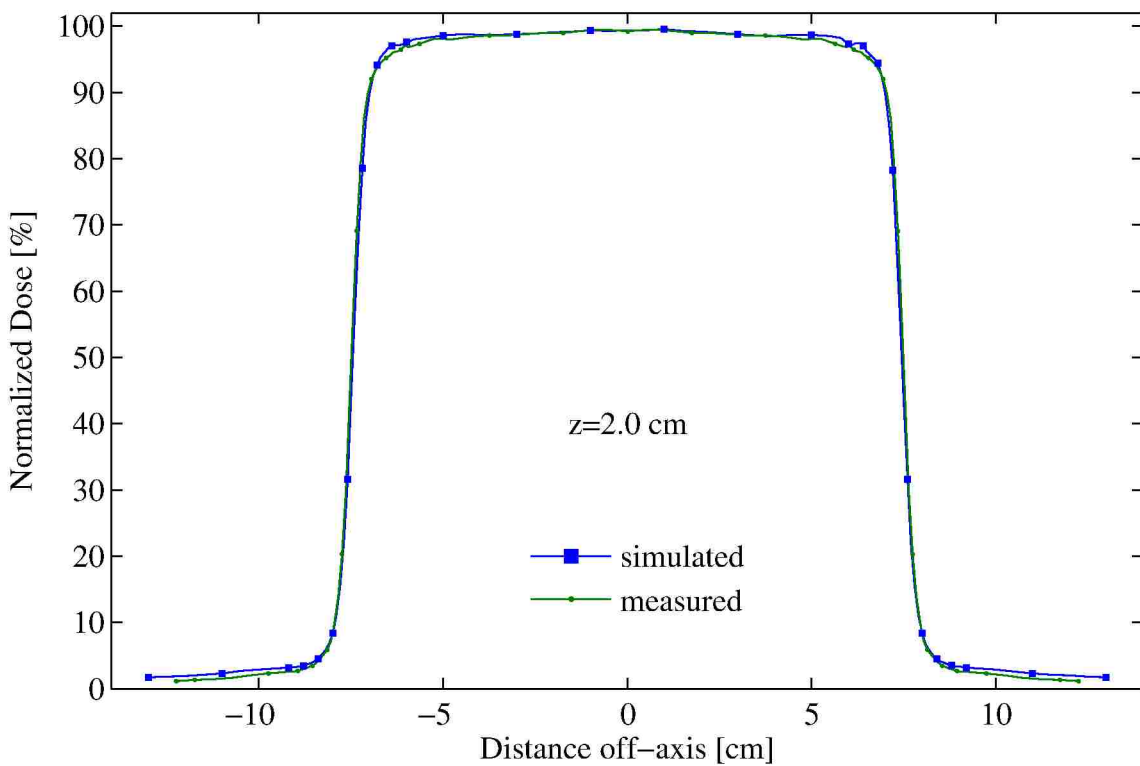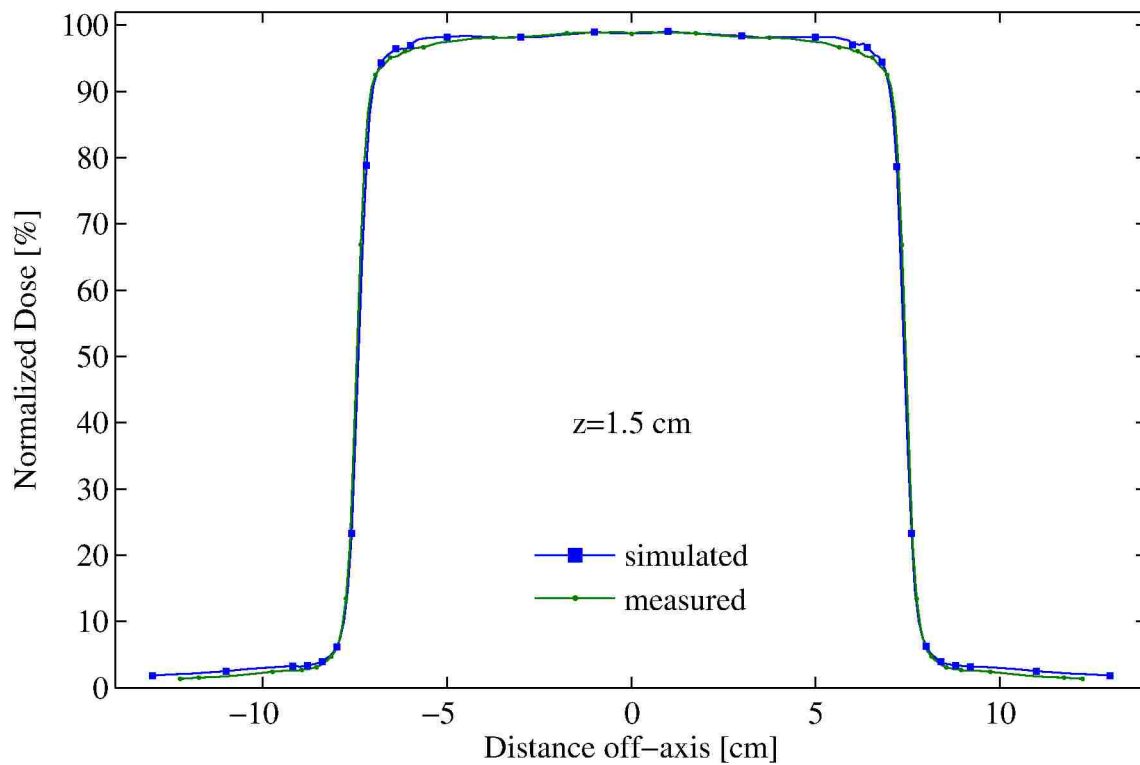
Figure C.32: 13MeV-14x14 cm^2 110cm SSD - cross-plane profiles at depths, z=5.3 and 6.5 cm

Figure C.33: 13MeV-14x14 cm^2 110cm SSD - cross-plane profiles at depth, z=8.5 cm

C.7 20-MeV 6x6 cm^2 Applicator - 100 cm SSD

Figure C.34: %DD: 20MeV - 06x06 cm^2 applicator

Table C.7: 20MeV-06x06 cm^2 applicator comparison summary

Profile type (%DD, X)	Profile depth (cm)	Percent of points passing		
		2%/1mm	2%/2mm	3%/3mm
%DD	–	100.0%	–	–
Cross-plane (X)	0.5	100.0%	–	–
	10.1	100.0%	–	–
	1.0	100.0%	–	–
	12.1	100.0%	–	–
	1.5	100.0%	–	–
	2.0	100.0%	–	–
	2.7	100.0%	–	–
	5.3	100.0%	–	–
	7.0	100.0%	–	–
	8.0	100.0%	–	–

Figure C.35: 20MeV-6x6 cm^2 100cm SSD - cross-plane profiles at depths, z=0.5 and 1.0 cm

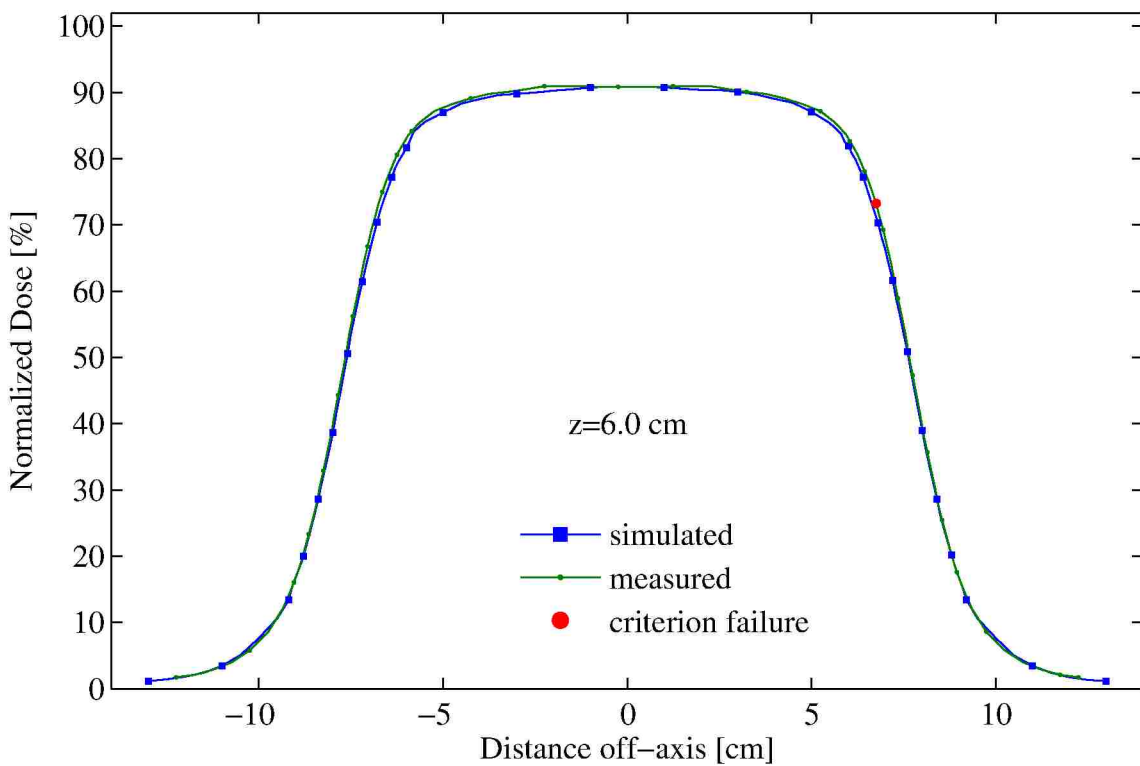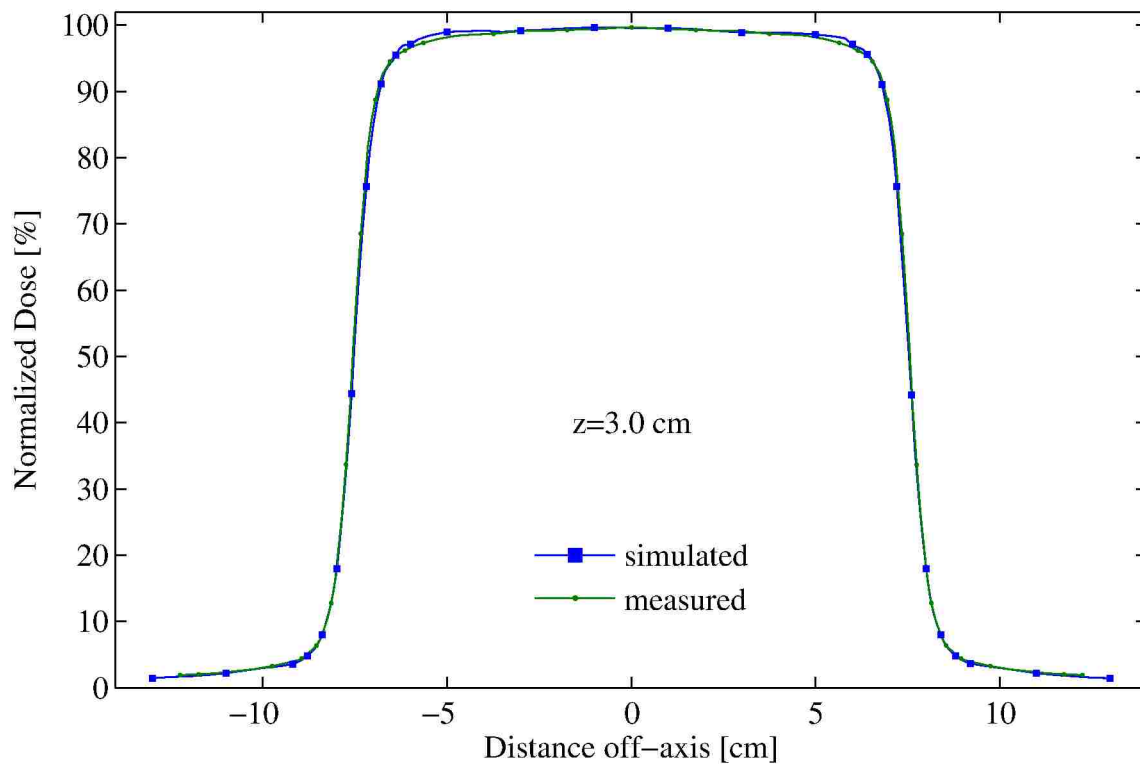Figure C.36: 20MeV-6x6 cm^2 100cm SSD - cross-plane profiles at depths, z=1.5 and 2.0 cm

Figure C.37: 20MeV-6x6 cm^2 100cm SSD - cross-plane profiles at depths, z=2.7 and 5.3 cm
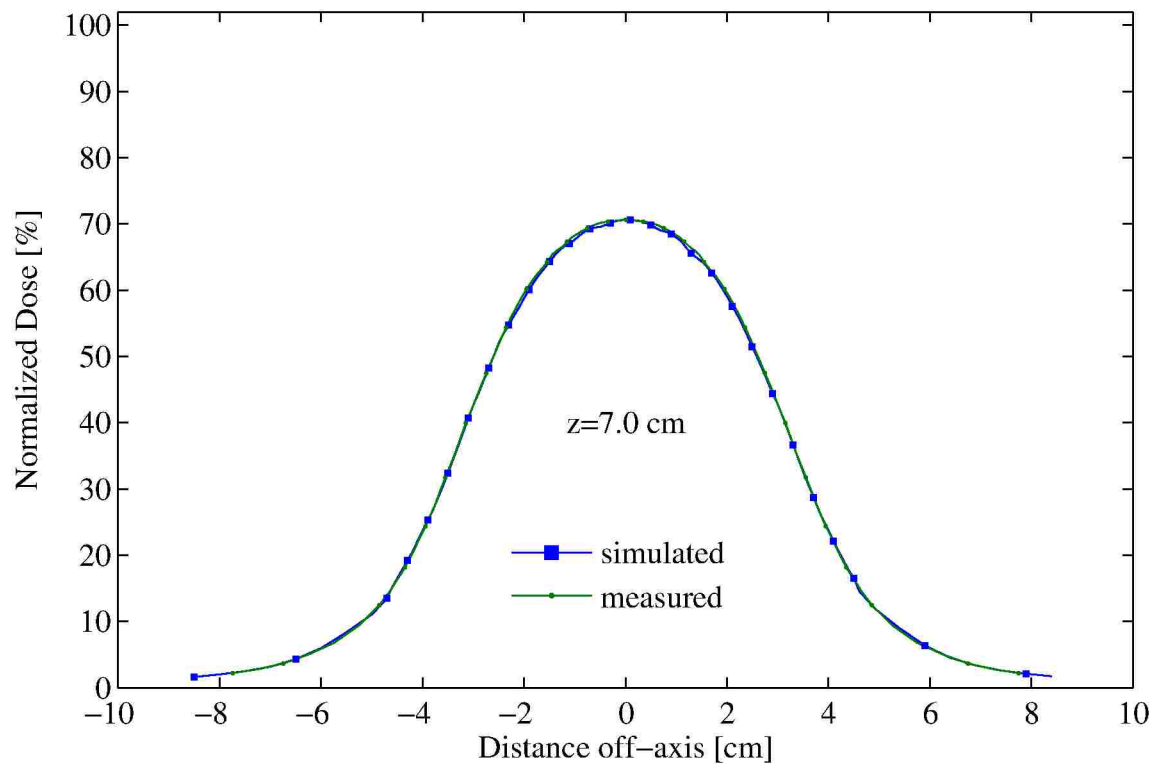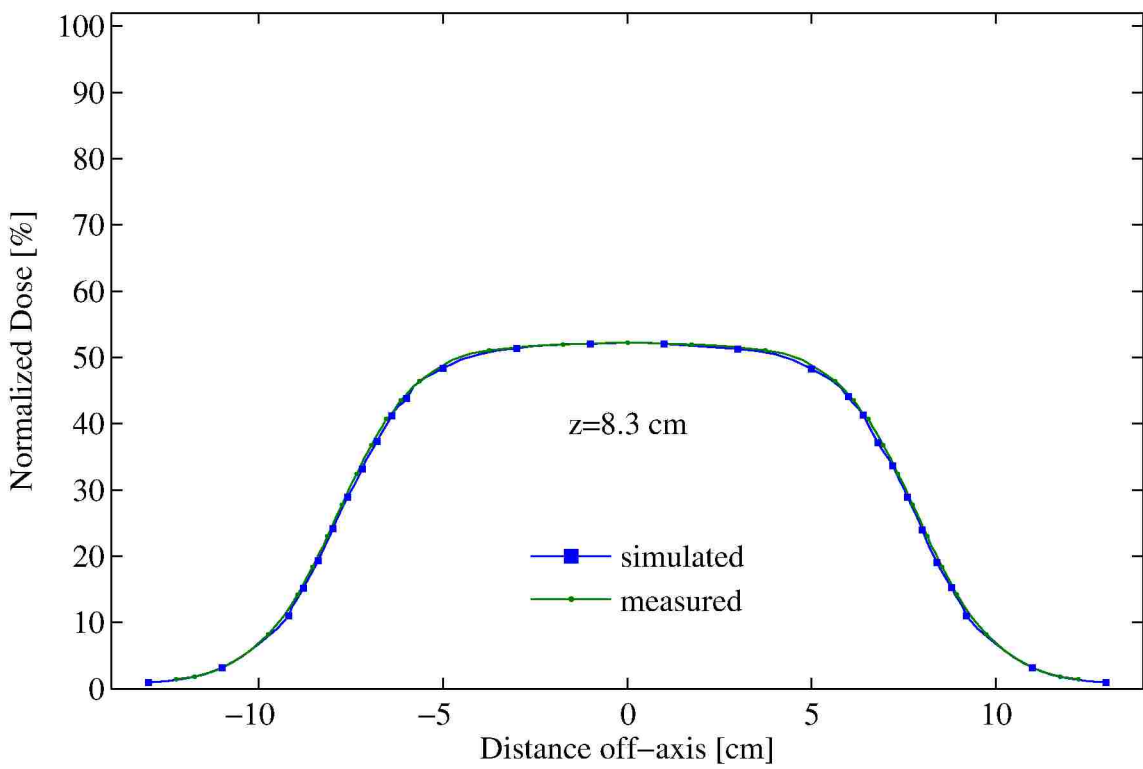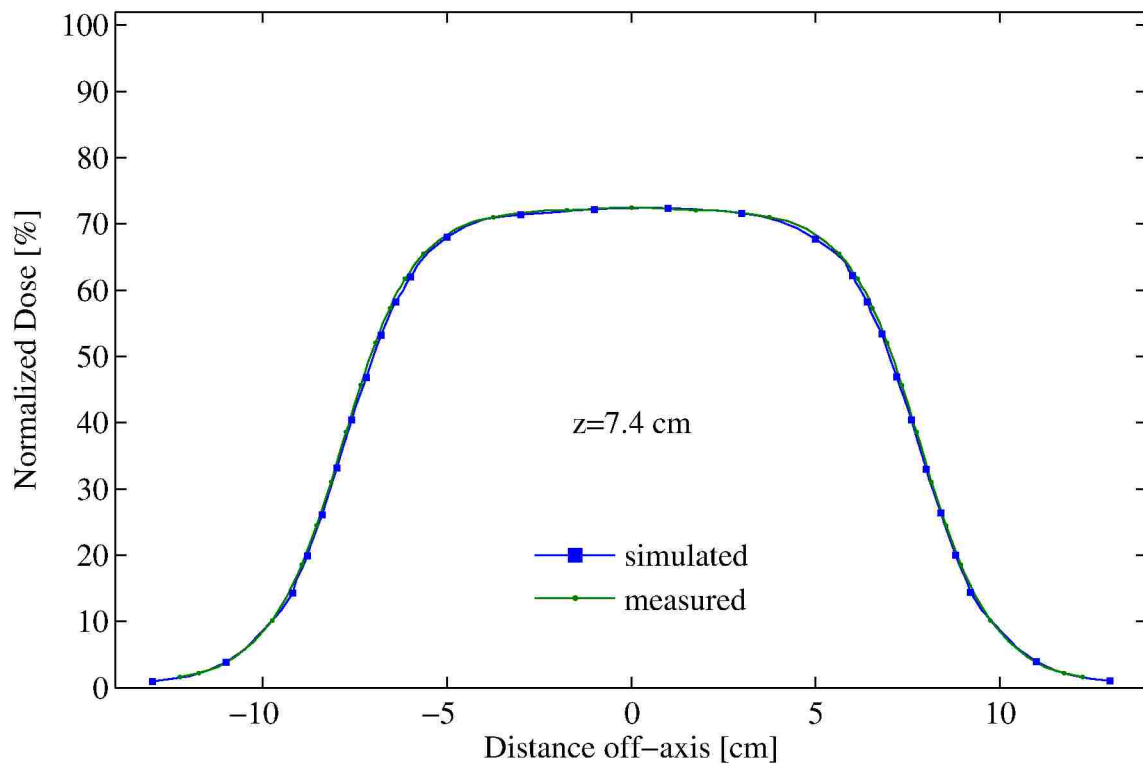
Figure C.38: 20MeV-6x6 cm^2 100cm SSD - cross-plane profiles at depths, z=7.0 and 8.0 cm
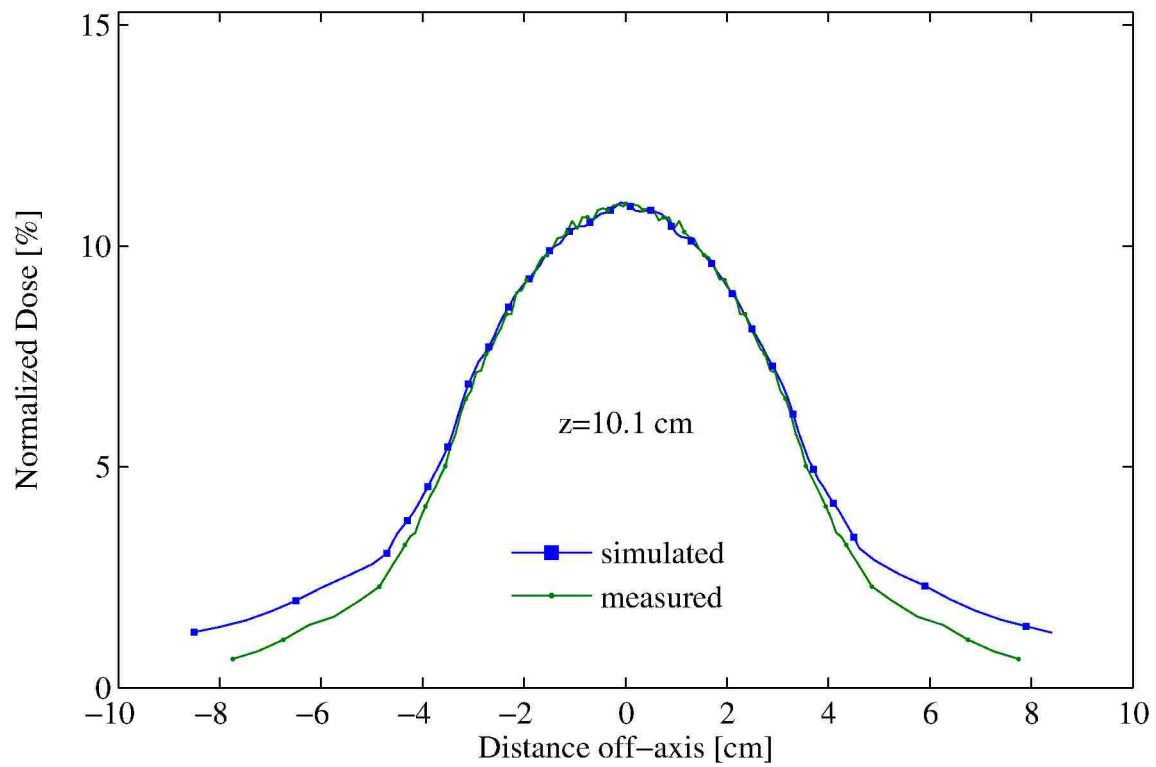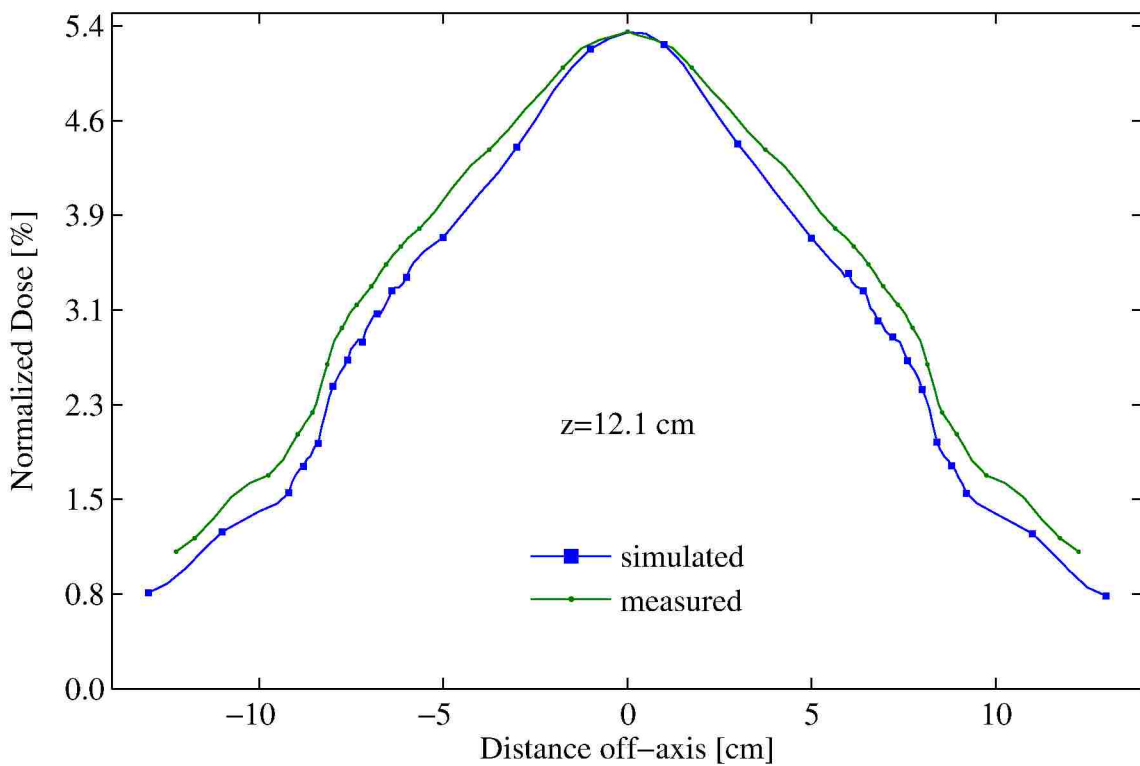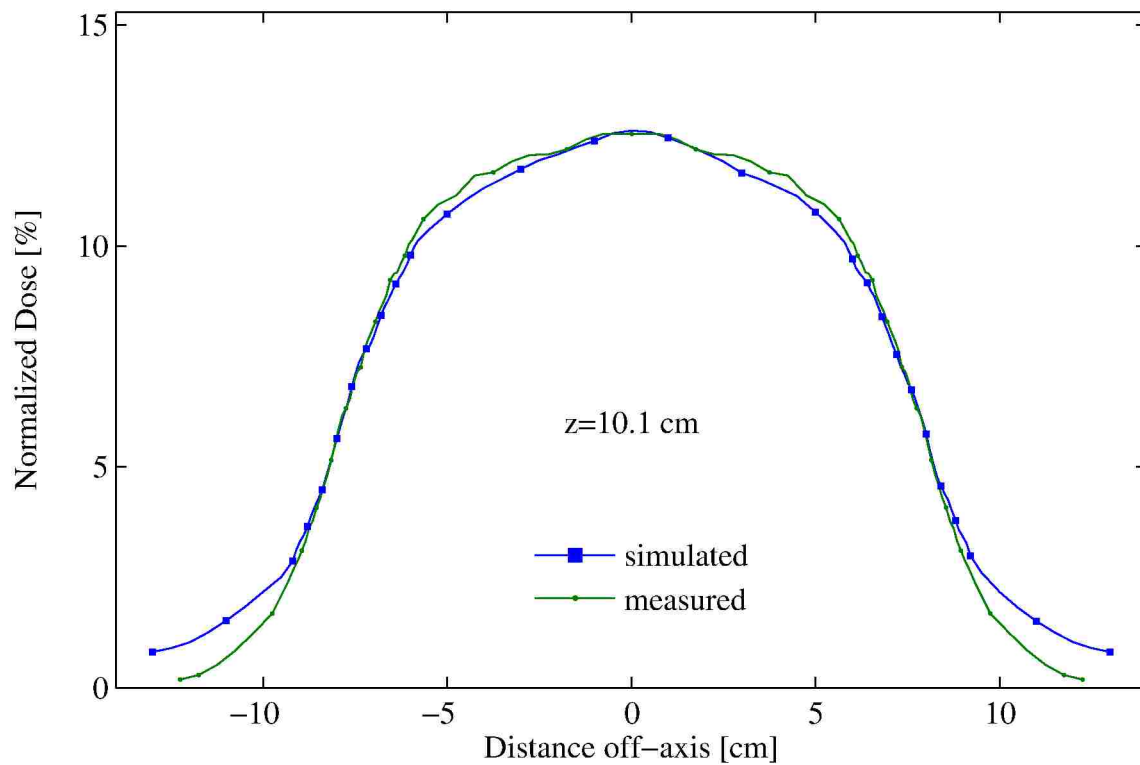
Figure C.39: 20MeV-6x6 cm^2 100cm SSD - cross-plane profiles at depths, z=10.1 and 12.1 cm

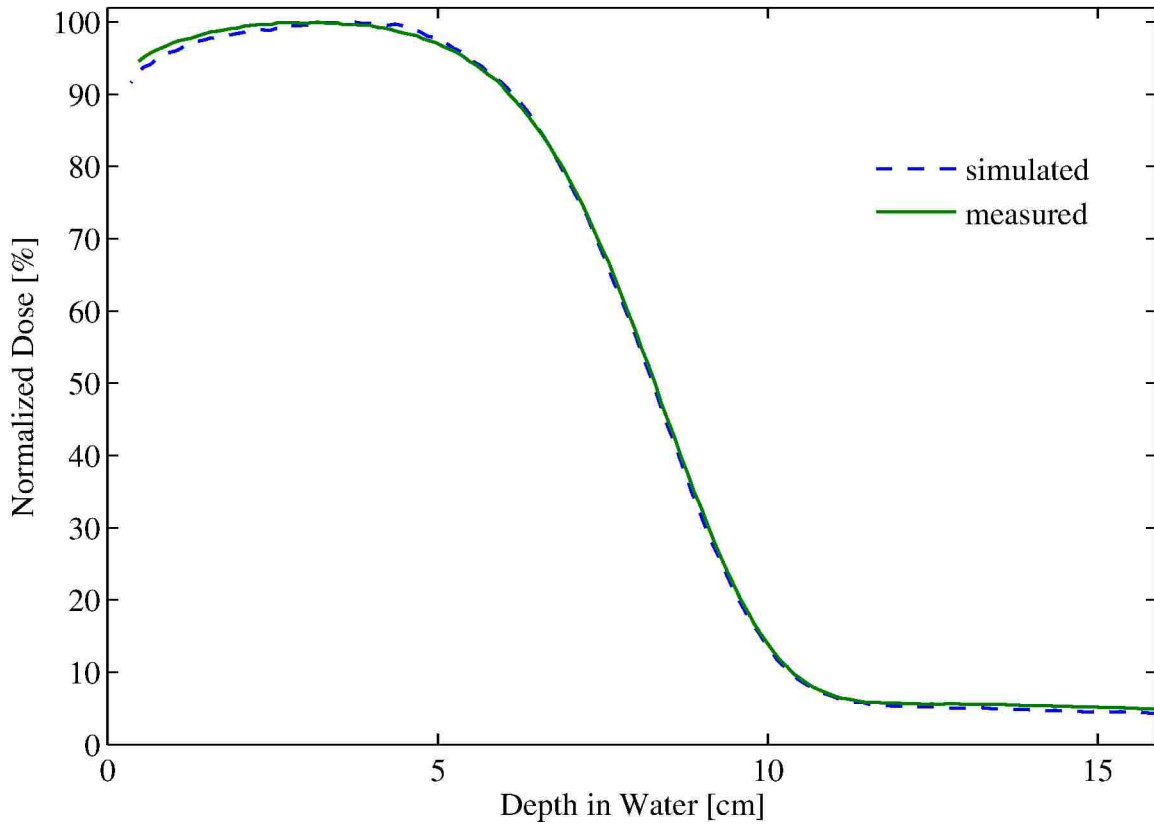## C.8   20-MeV 14x14 cm^2 Applicator - 100 cm SSD

Figure C.40: %DD: 20MeV - 14x14 cm^2 applicator

Table C.8: 20MeV-14x14 cm^2 applicator comparison summary

Profile type (%DD, X)	Profile depth (cm)	Percent of points passing		
		2%/1mm	2%/2mm	3%/3mm
%DD	–	100.0%	–	–
Cross-plane (X)	0.5	100.0%	–	–
	10.1	100.0%	–	–
	1.0	100.0%	–	–
	12.1	100.0%	–	–
	1.5	100.0%	–	–
	2.0	100.0%	–	–
	3.0	100.0%	–	–
	6.0	99.1%	100.0%	–
	7.4	100.0%	–	–
	8.3	100.0%	–	–

Figure C.41: 20MeV-14x14 cm^2 100cm SSD - cross-plane profiles at depths, z=0.5 and 1.0 cm

Figure C.42: 20MeV-14x14 cm^2 100cm SSD - cross-plane profiles at depths, z=1.5 and 2.0 cm
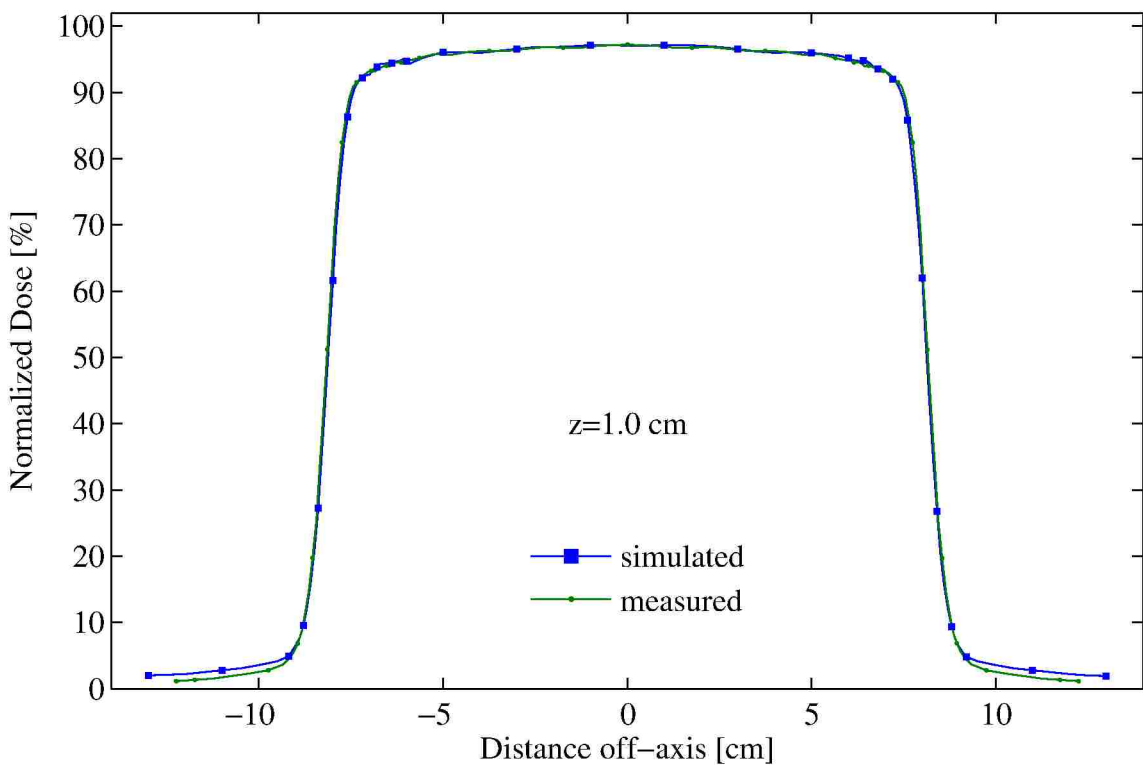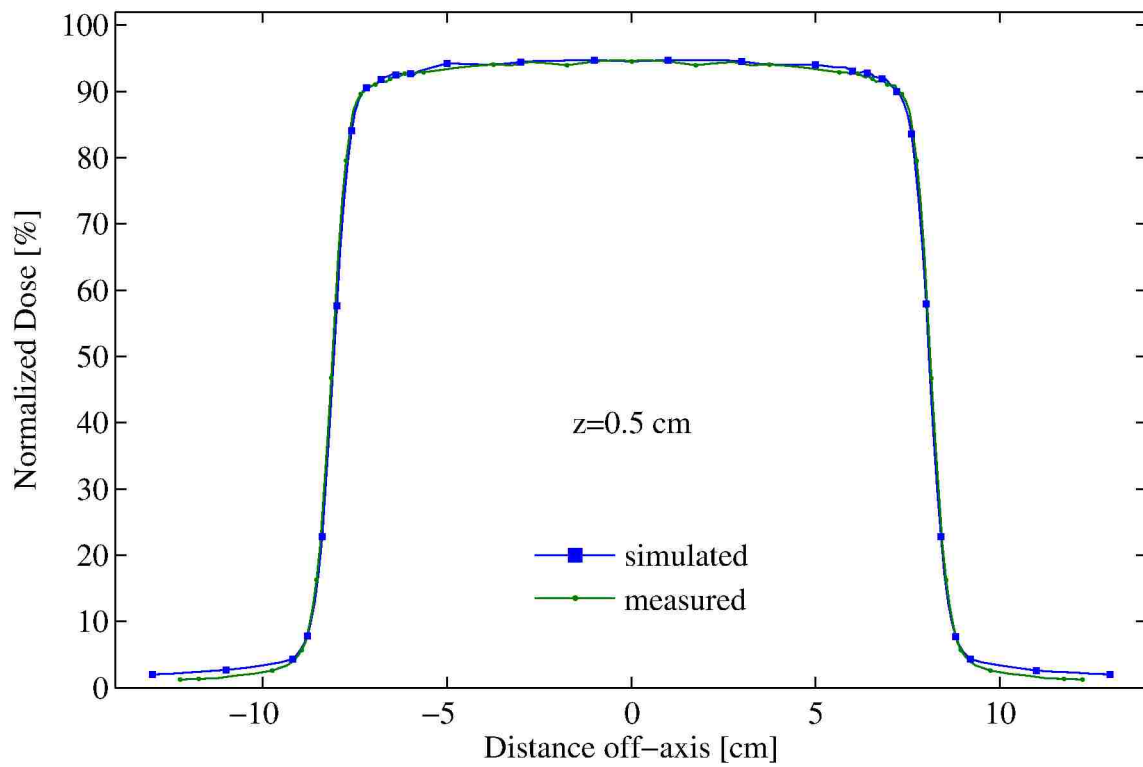
Figure C.43: 20MeV-14x14 cm^2 100cm SSD - cross-plane profiles at depths, z=3.0 and 6.0 cm

Figure C.44: 20MeV-14x14 cm^2 100cm SSD - cross-plane profiles at depths, z=7.4 and 8.3 cm
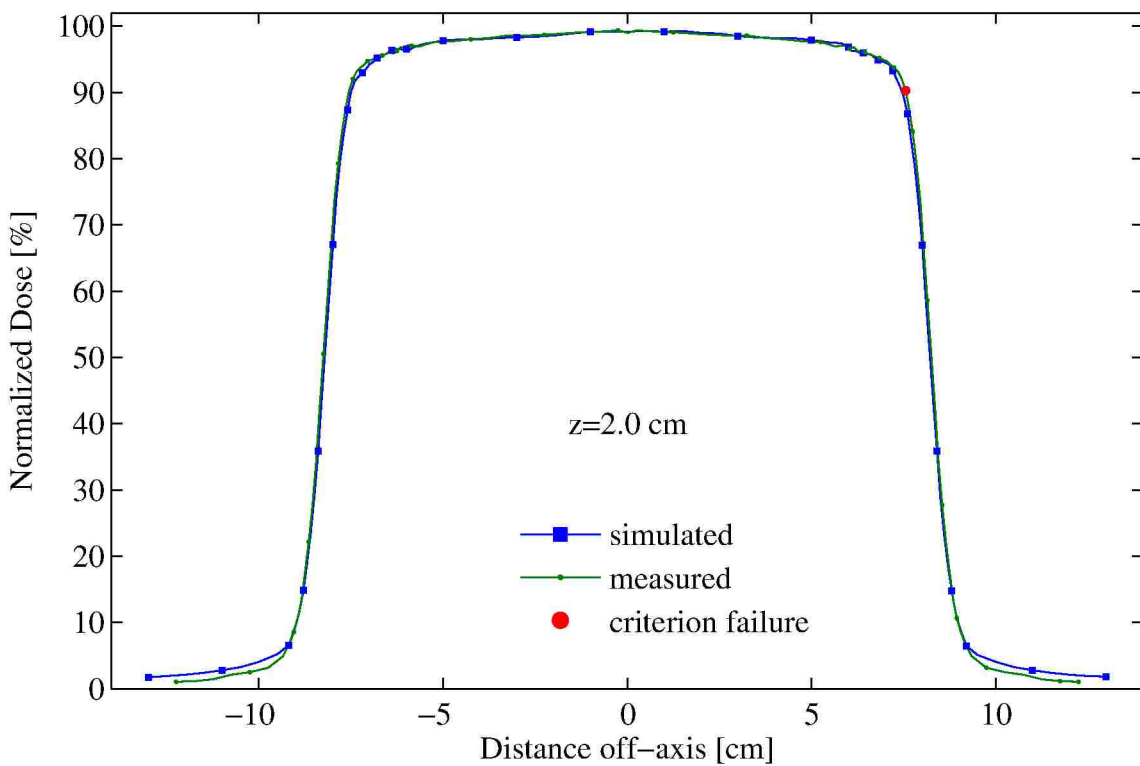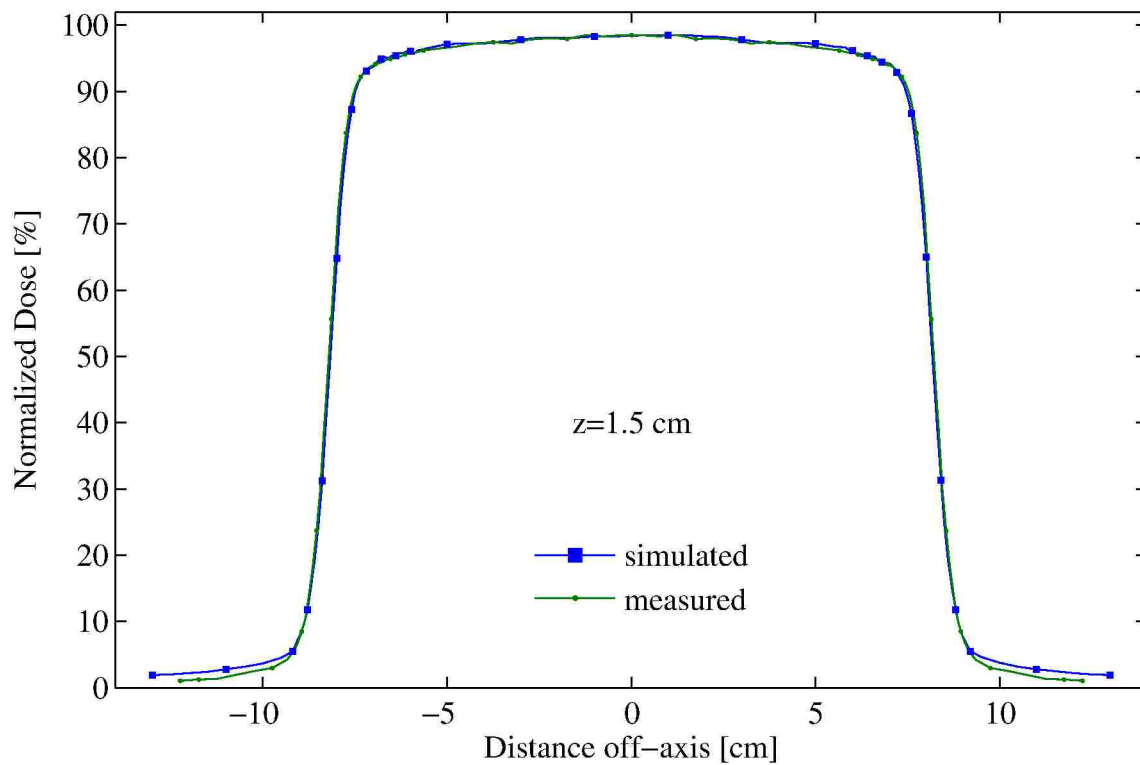
Figure C.45: 20MeV-14x14 cm^2 100cm SSD - cross-plane profiles at depths, z=10.1 and 12.1 cm

C.9   20-MeV 14x14 cm^2 Applicator - 110 cm SSD

Figure C.46: %DD: 20MeV - 14x14 cm^2 applicator

Table C.9: 20MeV-14x14 cm^2 applicator comparison summary

Profile type (%DD, X)	Profile depth (cm)	Percent of points passing 2%/1mm	2%/2mm	3%/3mm
%DD	–	100.0%	–	–
Cross-plane (X)	0.5	100.0%	–	–
	10.1	100.0%	–	–
	1.0	100.0%	–	–
	12.1	100.0%	–	–
	1.5	100.0%	–	–
	2.0	99.1%	100.0%	–
	3.0	100.0%	–	–
	6.0	99.1%	100.0%	–
	7.4	100.0%	–	–
	8.3	100.0%	–	–

Figure C.47: 20MeV-14x14 cm^2 110cm SSD - cross-plane profiles at depths, z=0.5 and 1.0 cm

Figure C.48: 20MeV-14x14 cm^2 110cm SSD - cross-plane profiles at depths, z=1.5 and 2.0 cm
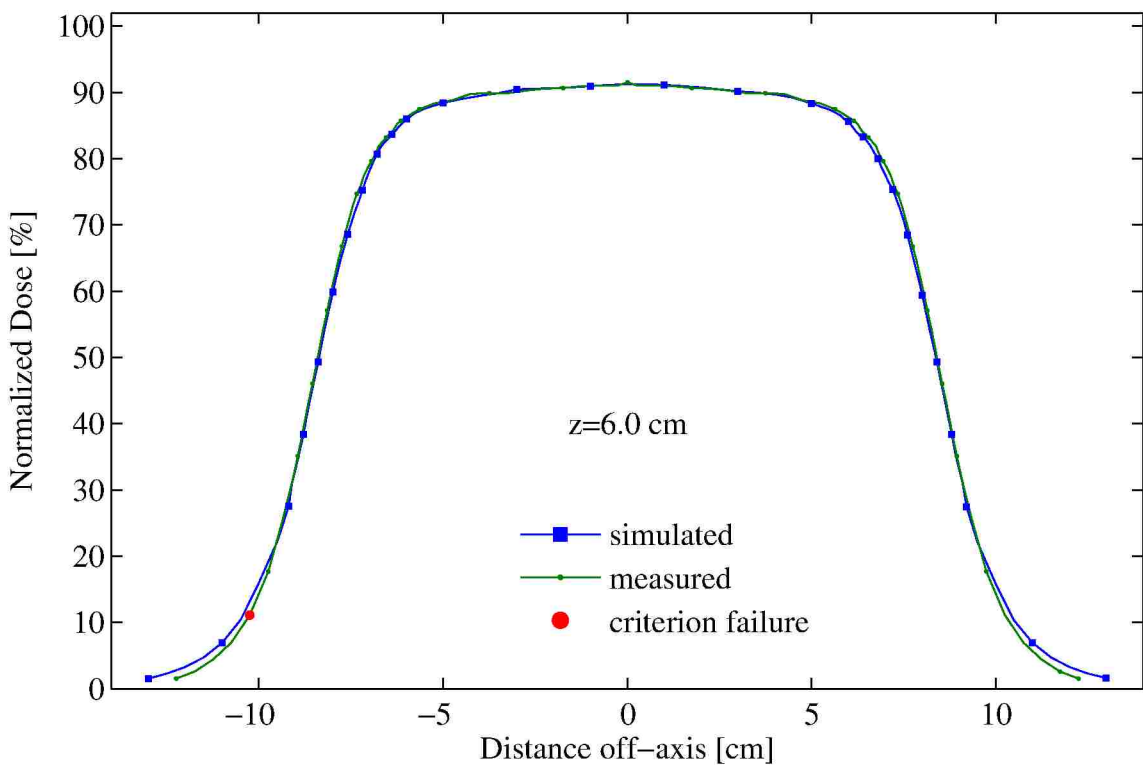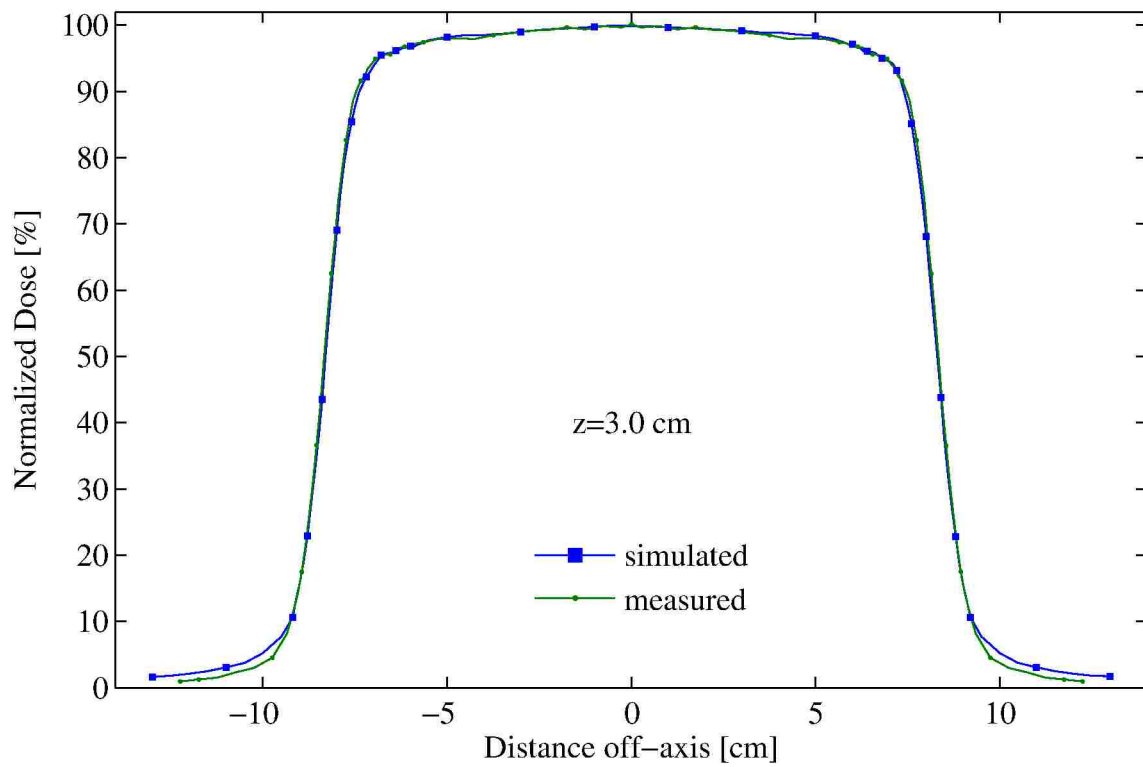
Figure C.49: 20MeV-14x14 cm^2 110cm SSD - cross-plane profiles at depths, z=3.0 and 6.0 cm
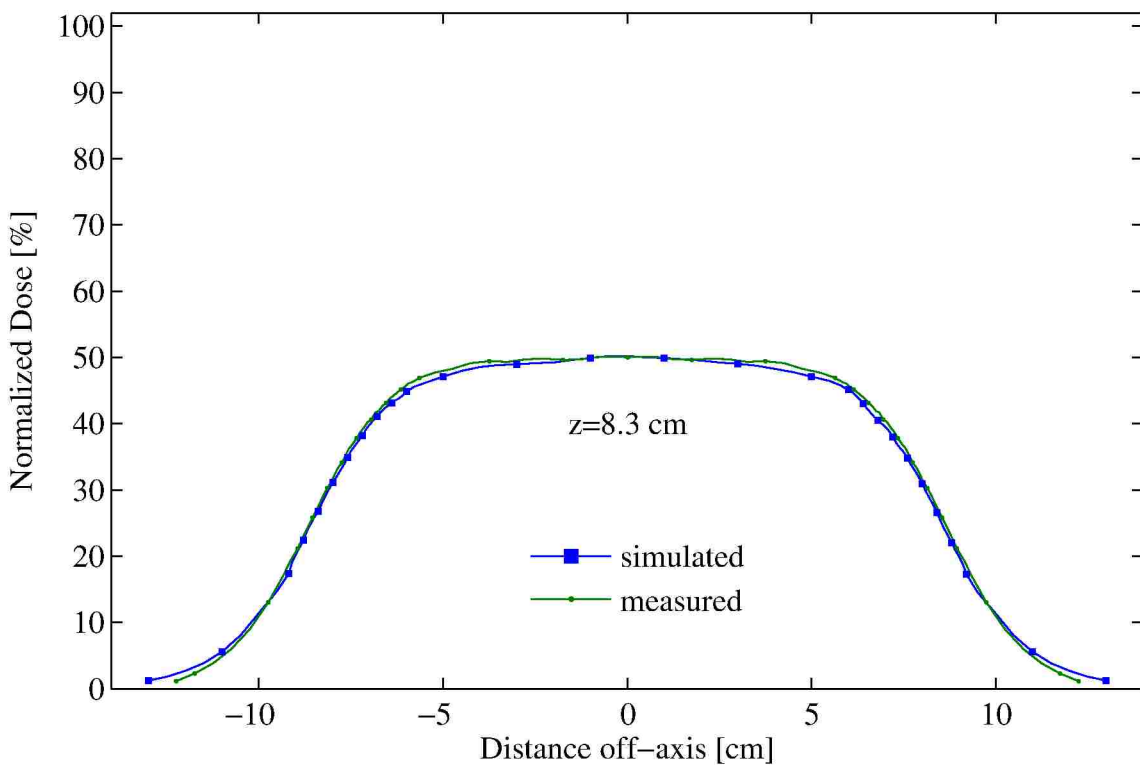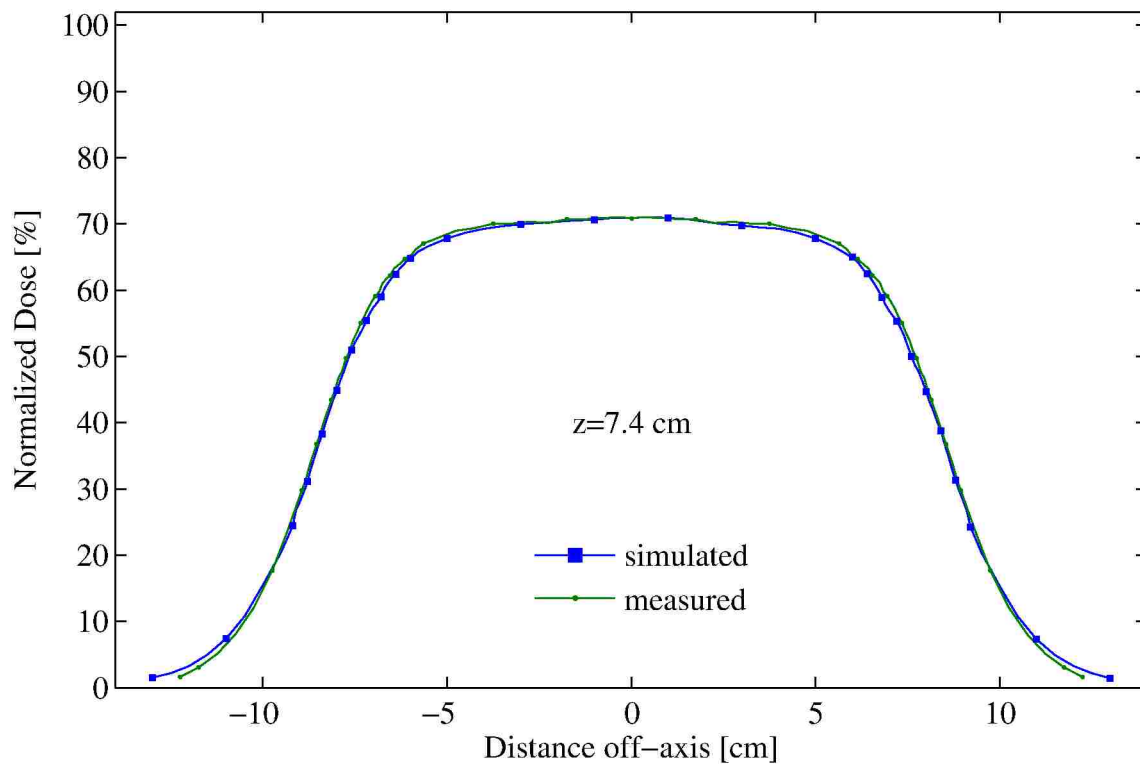
Figure C.50: 20MeV-14x14 cm^2 110cm SSD - cross-plane profiles at depths, z=7.4 and 8.3 cm
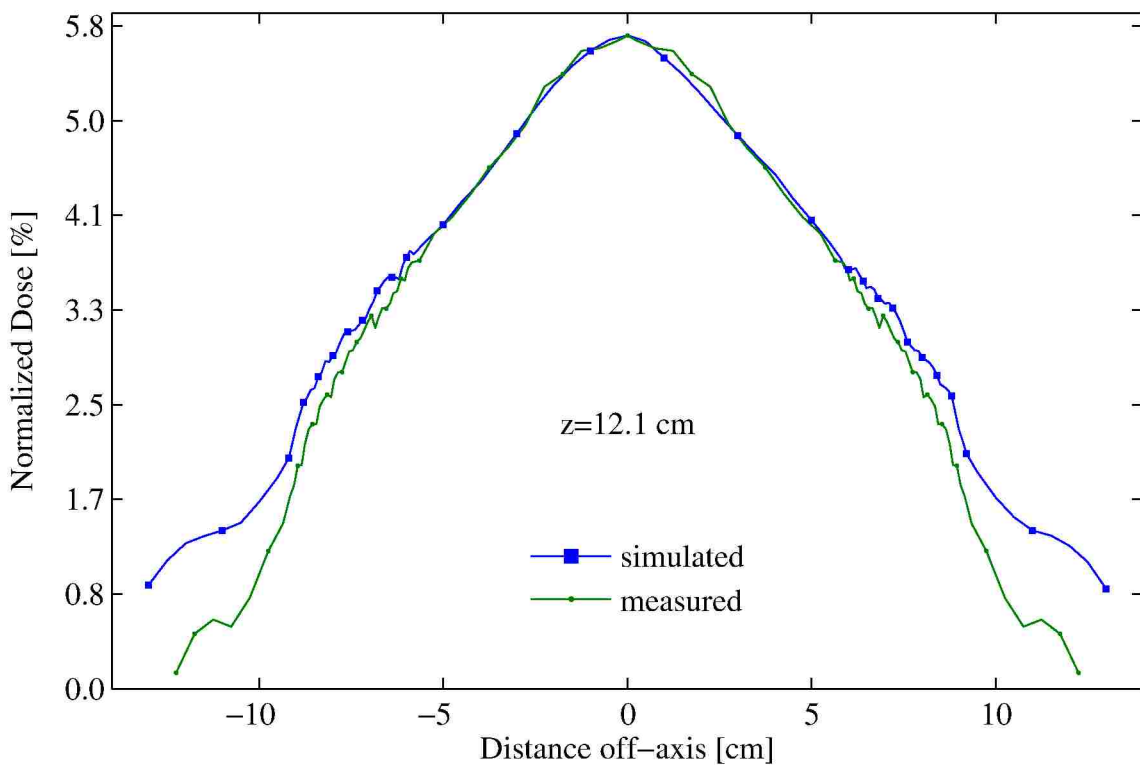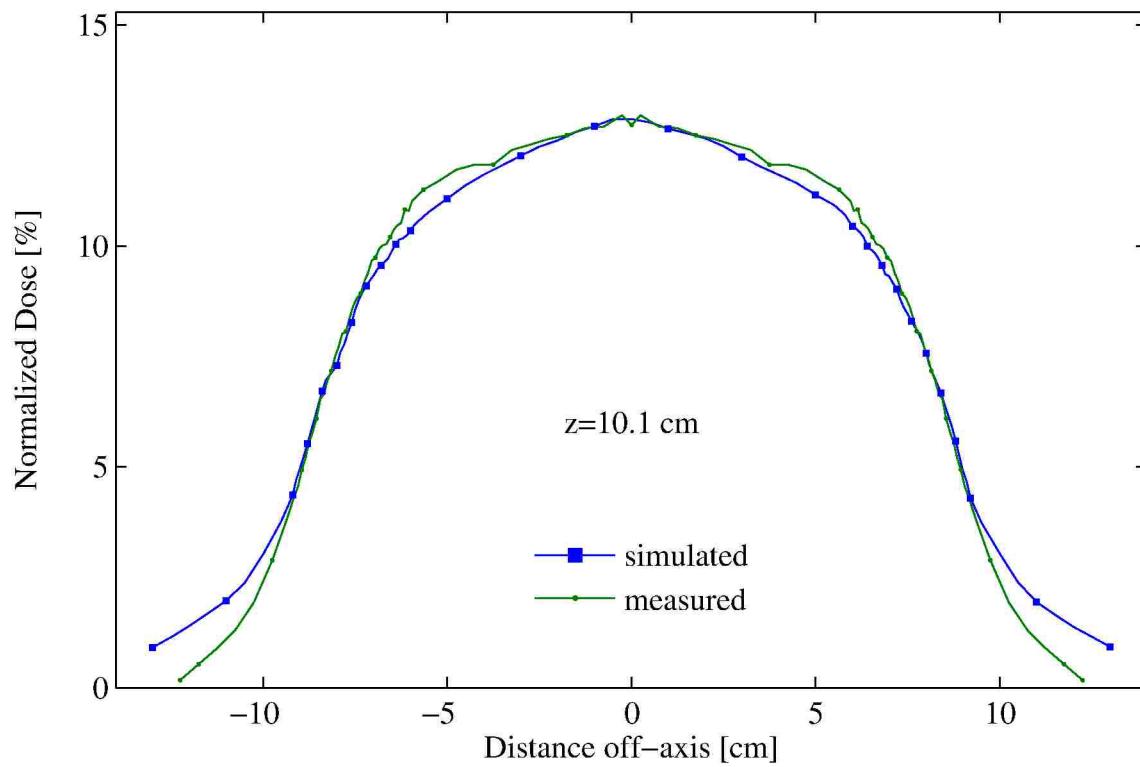
Figure C.51: 20MeV-14x14 cm^2 110cm SSD - cross-plane profiles at depths, z=10.1 and 12.1 cm

Vita

Guy Harris was born in Atlanta, Georgia in 1986. He grew up on a small farm outside of the city and received his B.S. in Physics from the Georgia Institute of Technology in 2009. After deciding to pursue a career in the field of medicine, Guy moved to Baton Rouge, Louisiana to work towards a Masters of Science in Medical and Health Physics at Louisiana State University. During the three years spent in Baton Rouge, Guy spent two years working at the program's clinical affiliate, Mary Bird Perkins Cancer Center. The clinical environment of Mary Bird Perkins Cancer influenced him to continue his education in translational research between basic and clinical sciences at Virginia Commonwealth University in Richmond, Virginia.